SLAC – 282
UC-34D
(E)

RADIATIVE DECAYS OF THE PSI PRIME TO ALL-PHOTON FINAL STATES*

Roger Alan Lee

Stanford Linear Accelerator Center
Stanford University
Stanford, California 94305

May 1985

Prepared for the Department of Energy
under contract number DE-AC03-76SF00515

Printed in the United States of America. Available from the National Technical Information Service, U.S. Department of Commerce, 5285 Port Royal Road, Springfield, Virginia 22161. Price: Printed Copy A14, Microfiche A01.

* Ph.D. Thesis.

ABSTRACT

Results of studies of selected radiative decays of the ψ' to charmonium and non-charmonium states which decay into photons are presented. These studies were performed using a sample of 1.8×10^6 produced ψ''s collected by the Crystal Ball detector at the SPEAR electron-positron storage ring.

In the first study, the branching ratios of the χ_0, χ_2, and η_c' to two photons have been measured to be $(4.5 \pm 2.2 \pm 2.0) \times 10^{-4}$, $(9.5 \pm 2.9 \pm 4.5) \times 10^{-4}$ (first errors statistical, second systematic), and $< 1 \times 10^{-2}$ (90% C.L.), respectively. (The statistical significance of the χ_0 signal is slightly less than three standard deviations.) The signal from the decay chain $\psi' \rightarrow \gamma\chi_0$, $\chi_0 \rightarrow \pi^0\pi^0$ has been observed with essentially no background. Using the observed line shape of the radiative photon in this reaction, the full width of the χ_0 has been found to be $8.8 \pm 1.3 \pm 1.5$ MeV$/c^2$. In addition, the branching ratios of the χ_0 and χ_2 to $\pi^0\pi^0$ have been measured to be $(3.5 \pm 0.3 \pm 1.2) \times 10^{-3}$ and $(1.2 \pm 0.2 \pm 0.4) \times 10^{-3}$, respectively; the branching ratios of the χ_0 and χ_2 to $\eta\eta$ have been measured to be $(2.8 \pm 0.9 \pm 1.3) \times 10^{-3}$ and $(8.4 \pm 4.2 \pm 4.0) \times 10^{-4}$.

In the second study, the decays of the ψ' to four non-charmonium states have been investigated. The branching ratios and upper limits of these decays have been normalized to the branching ratios of the corresponding decays from the J/ψ which have been measured using a sample of 2.2×10^6 produced J/ψ's collected by the Crystal Ball detector. The ratios of the ψ' branching ratios to the J/ψ branching ratios for the final states $\gamma\eta$, $\gamma\eta'$, $\gamma\theta$, and γf have been measured to be <1.8%, <2.6%, <10-15%, and 9 ± 3%, respectively. (Upper limits are 90% confidence level. The upper limit for the radiative decay to the θ is poorly determined due to the uncertainty in the f' contribution in the J/ψ data.)

These results are compared with the theoretical expectations of lowest-order quantum chromodynamics potential models. Substantial disagreement is found

between theory and experiment for the χ_0 two photon branching r io and full width, and the ratio of branching ratios upper limits for the $\gamma\eta$ and $\gamma\eta'$ i l states.

ACKNOWLEDGEMENTS

A successful experiment in high energy physics requires a clever idea, cooperation from Nature, and a group of talented and enthusiastic individuals. For the past several years I have been fortunate to have been associated with the Crystal Ball collaboration where all these elements were found in conjunction. I was aided in all aspects of my research not only by the direct contact I had with the members of this group, but also by their extraordinary intellectual and technical efforts, many of which took place "before my time".

Of course, certain individuals stand out. John Tompkins led me by the hand through my first rudimentary analyses and was the source of answers to innumerable questions ranging from calibration procedures to curve fitting to the idiosyncrasies of IBM software. Ian Kirkbride showed me by example the necessity of paying close attention to detail in his care and management of the Crystal Ball detector. Kay Königsmann, Frank Porter, and Don Coyne all contributed their experience in physics analysis and statistics; Fred Gilman and Stan Brodsky of the SLAC Theory Group elucidated the fine points of charmonium theory. Special thanks go to my advisor, Alan Litke, who suggested this research project and who never let me lose sight of the physics in the maze of cables, FORTRAN bugs, and angular distribution calculations.

Working together in close quarters tends to develop a certain camaraderie, and I would like to thank my fellow residents of the HEPL trailer, Dave Gelphman, Roland Horisberger, and Al Osterheld, for their support and input over the past several years. A special \thanks goes to Ray Cowan who patiently explained to me the inner workings of TEX.

I would also like to thank the people who set me on this path and saw me along it. I was fortunate enough to be introduced to physics by George Marček whose clarity and lucid style first allowed me to see physics as the beautiful subject it is.

I would also like to acknowledge the superb physics faculty of Swarthmore College where teaching is recognized as an important undertaking, not just a sideline. Steve and Steve helped me over the rocky parts of the trail; I hope they will help me climb more mountains in the future. Finally, I want to express my deepest appreciation to Claire Brown, whose love and confidence sustained me over many years and two continents, and thank her for the contributions she made to my life and this thesis (especially when the two were indistinguishable.)

Table of Contents

List of Tables

List of Figures

Chapter 1

Introduction

Since its discovery, the group of particles known as the charmonium family has been the object of intense experimental and theoretical investigation. Simply the existence of the lowest-lying member of this family produced in e^+e^- collisions, the $J/\psi(3095)$,[1,2] was taken as striking evidence of the charm hypothesis of Glashow, Iliopoulos, and Maiani.[3,4] The decays of the J/ψ have since received considerable attention. In particular, studies of the radiative decays of the J/ψ have led to several important discoveries.[5,6,7]

The more massive charmonium states which have been observed below open charm threshold have not been studied as extensively, partly because some of them (the χ states and the singlet η_c and η_c' states) do not have the same quantum numbers as the photon and so cannot be directly produced in high-energy e^+e^- collisions. The only charmonium state other than the J/ψ below open charm threshold produced in e^+e^- collisions, the $\psi(3685)$ (or ψ'), has been studied primarily due to its decays to other states. The ψ' has several charmonium decay modes which are not available to the J/ψ, but the mechanism responsible for its non-charmonium decays is expected to be the same as that of the J/ψ.

However, it is by virtue of the fact that there exists a family of closely-related particles that many of the uncertainties in predicted widths and decay rates can be removed. We wish to compare experimental measurements with the predictions

of the candidate theory of strong interactions, quantum chromodynamics, or QCD. Typically, QCD predictions rely on some parameters which must be supplied from experiment, since the hadronization process of gluons to observable particles is not understood. In the charmonium family, phenomenological parameters obtained from the study of one state can be used to make theoretical predictions of decay rates for other states in which no adjustable parameters remain. In particular, potential model calculations, using as input the known energies of the J/ψ and ψ', can be used to calculate the full widths and two-photon partial widths of the intermediate χ states. Also, the branching ratio of the J/ψ to a given final state can be used to predict the branching ratio of the ψ' to the same final state.

In this report we describe an investigation of the radiative decays of the ψ' to both charmonium and non-charmonium states using a sample of 1.8×10^6 produced ψ''s collected by the Crystal Ball detector. Inasmuch as the Crystal Ball has excellent energy and position resolution for photons, we have chosen to study those decays which contain only photons in the final state. Due to the odd C-parity of the ψ', all-photon final states typically contain an odd number of photons* and are of the form

$$\gamma + m\pi^0 + n\eta \qquad [1.1]$$

Thus, by selecting a sample of all-photon decays we are assured of having a large fraction of radiative ψ' decays.† In the category of charmonium decays, all-photon radiative decays include $\psi' \to \gamma\chi_{0,2}$, $\chi_{0,2} \to \pi^0\pi^0, \gamma\gamma$, and $\eta\eta$. The signal of the decay $\psi' \to \gamma\chi_0$, $\chi_0 \to \pi^0\pi^0$ is sufficiently free from background that we have used it to make a measurement of the full width of the χ_0. We have also set upper limits for the decay $\eta_c' \to \gamma\gamma$.

---

* Exceptions are decays in which one of the intermediate decay products decays weakly, i.e., $\psi' \to \phi\eta, \phi \to K_S^0 K_L^0$.

† Note that some decays of the form of reaction [1.1] may not be radiative decays of the ψ' (such as $\psi' \to \omega\pi^0\pi^0, \omega \to \gamma\pi^0$).

In the category of non-charmonium decays, we have measured the branching ratios / upper limits of the decays $\psi' \to \gamma f$, $\psi' \to \gamma\theta$, $\psi' \to \gamma\eta$, and $\psi' \to \gamma\eta'$. Since the quantities of most interest are the ratios of these branching ratios to the branching ratios of the same final states from the J/ψ, we have performed a parallel study of J/ψ decays using a sample of 2.2×10^6 produced J/ψ's taken by the Crystal Ball in virtually the same configuration as that used to take the ψ' sample. This allows us not only to check the results of our analysis against J/ψ branching ratios measured in previous experiments, but also reduces the systematic errors in the ratios of branching ratios.

Since the decays under study have been selected to exploit the unique capabilities of the Crystal Ball detector, we begin in Chapter 2 with a description of this device. In Chapter 3 we describe the analysis techniques which have been developed to study all-photon decays. In Chapters 4-6 we describe applications of these techniques to studies of all-photon decays and review the theoretical expectations for the decay channels we have studied. Chapter 4 details the study of decays to charmonium states. Chapter 5 describes the study of non-charmonium decays accessible to a standard exclusive analysis, namely, J/ψ, $\psi' \to \gamma f$ and $\gamma\theta$. Chapter 6 describes non-charmonium decays studies via the "global shower technique" which was developed to examine the decays $J/\psi, \psi' \to \gamma\eta$ and $\gamma\eta'$. Chapter 7 summarizes our results.

References

1) J. Aubert *et. al.*, *Phys. Rev. Lett.* **33** (1974) 1404.

2) J.-E. Augustin *et. al.*, *Phys Rev. Lett.* **33** (1974) 1406.

3) S. L. Glashow, J. Iliopoulos, J. Maiani, *Phys. Rev.* **D2** (1970) 1285.

4) T. Appelquist and H. D. Politzer, *Phys. Rev. Lett.* **34** (1975) 43.

5) D. L. Scharre *et. al.*, *Phys. Lett* **97B** (1980) 329.

6) C. Edwards *et. al.*, *Phys. Rev. Lett.* **48** (1982) 458.

7) K. E. Einsweiler, Ph.D. thesis, Stanford University, 1984, and SLAC-Report 272 (unpublished).

Chapter 2

The Crystal Ball Detector

2.1 SPEAR

All the data used in these investigations were collected by the Crystal Ball while installed in the east pit of the SPEAR electron- positron storage ring. (See Fig. 2.1.) This facility was operational in April 1972 and was the first e^+e^- storage ring with sufficient energy and luminosity to search for narrow resonances between 3 and 5.6 GeV. The ring was renovated during the summer of 1974 to accommodate two additional rf cavities (bringing the total to four) so that center-of-mass energies up to 7.4 GeV could be attained.[1] The ring consists of ten standard cells (for bending and focussing the beam) and two insertion cells in which the beam parameters can be optimized to obtain large luminosity at the intersection points. The electrons and positrons orbit in opposite directions in the same evacuated beam pipe. Each beam is concentrated into a single bunch with transverse dimension 1 mm and a Gaussian longitudinal density distribution with a σ of $\approx$ 3 cm.

The circumference of the ring is 234.4 meters.[2] Since the beams travel at virtually the speed of light, the orbital frequency is 1.28 MHz so that the beams collide at a given intersection point every 780 ns. As the bunches circulate, they give off synchrotron radiation at a rate of[3]

$$U = \frac{4\pi}{3} \frac{r_e}{(mc^2)^3} \frac{{E_b}^4}{\rho} \qquad [2.1]$$

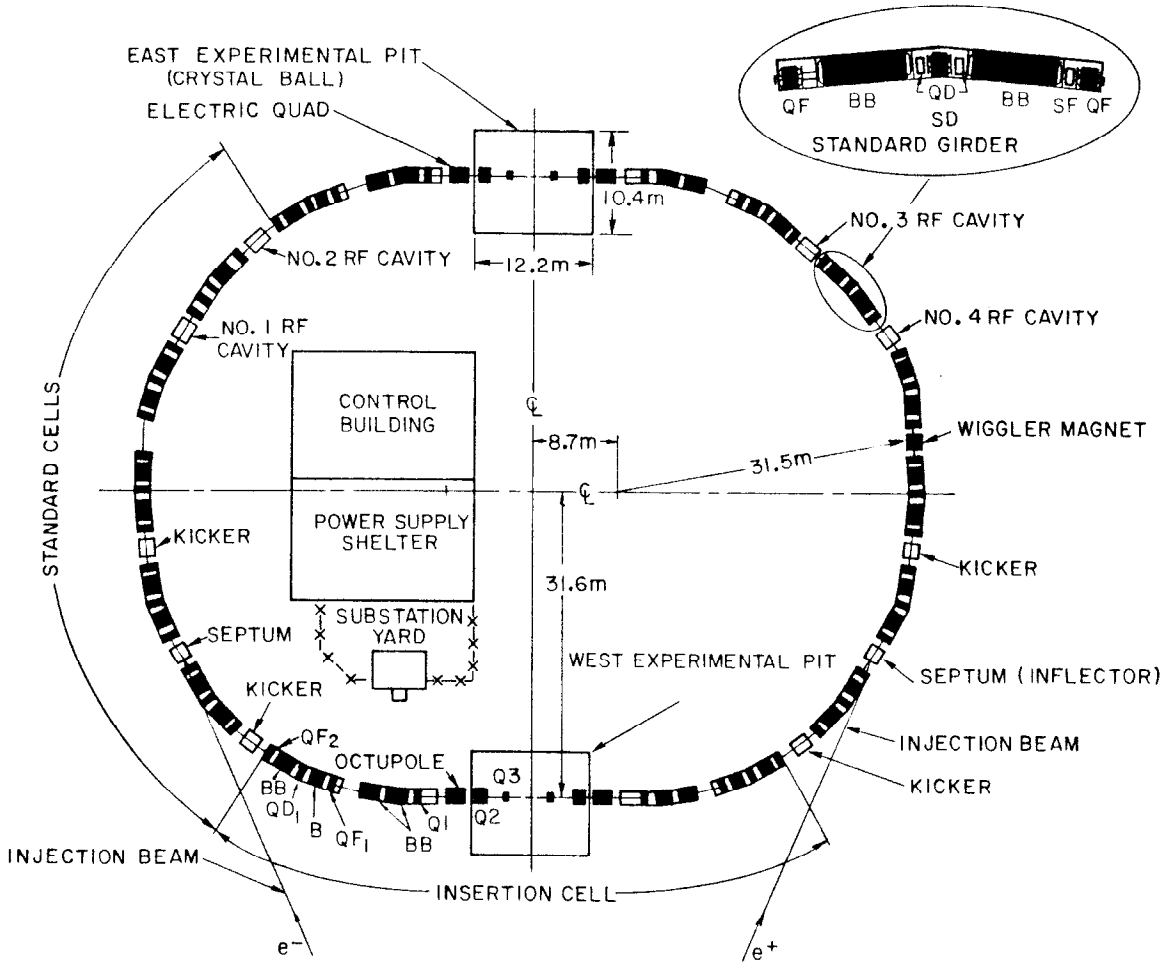

Fig. 2.1 Schematic representation of the SPEAR storage ring.

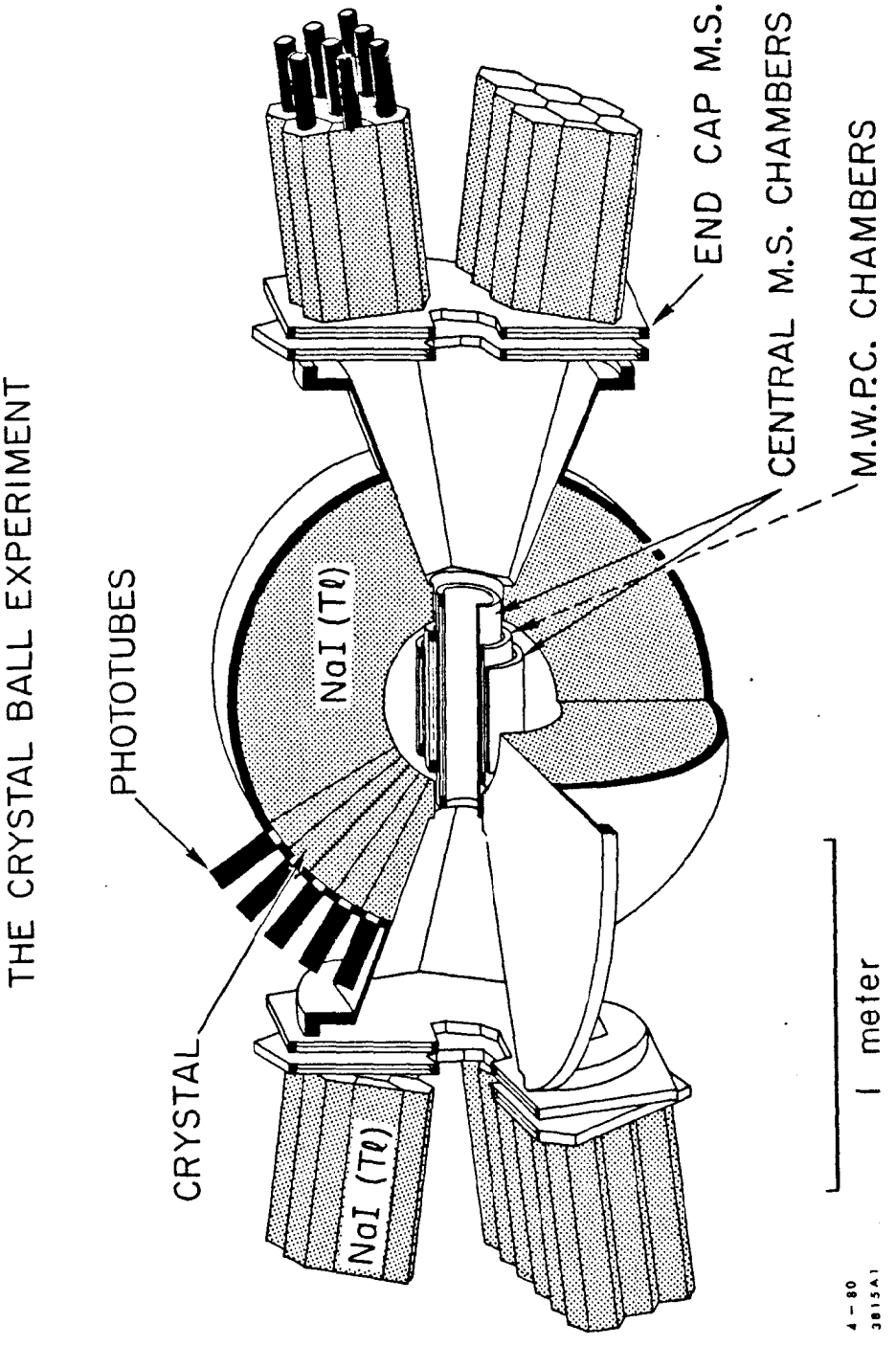

Fig. 2.2 Overview of the Crystal Ball detector.

where U is the energy loss per turn, r_e and m are the classical radius and mass of the electron, E_b is the beam energy, and ρ is the bending radius of the storage ring. At SPEAR, this works out to be 1.2 MeV per turn at $E_b = 1.8$ GeV. This has several consequences. First, the quantum fluctuations in this radiation introduce a spread in the energy of the beam $\approx$ 1 MeV. Thus, the spread in the energies of the beams is far larger than the exceptionally narrow widths of the J/ψ and ψ'. However, this spread is a small fraction of the mass of the J/ψ or ψ' , so it can be assumed that these particles are produced at rest.

Second, this synchrotron radiation induces a transverse polarization in the beam. In the absence of depolarizing effects, this polarization builds up exponentially with a time constant given by[4]

$$T_0 = 98\text{sec} \times \frac{\rho^3}{E_b^5}\frac{R}{\rho} \qquad [2.2]$$

where ρ and E_b are as defined previously (here measured in meters and GeV, respectively), and R is the circumference of the ring divided by 2π (measured in meters). Using the SPEAR parameters, this yields a time constant of approximately 8 hours at the ψ' energy, which is long compared to the average time between fills of two hours. Thus, we may treat the beams as unpolarized for the purposes of calculating angular distributions.

Finally, the flux of synchrotron photons is important to the experimental apparatus, since NaI(Tl) (of which a large part of the experiment is constructed) can be damaged by radiation. The integrated dose on the main detector was measured to be $\approx$ 300 rad during the entire time the Crystal Ball was at SPEAR.[5](This includes periods in which SPEAR was run solely to produce synchrotron radiation as well as high energy physics running.) The energy response and uniformity of that section of the detector closest to the beam line was measured several times during this period; no radiation damage was noted.

2.2 Detector Components

The Crystal Ball detector in its SPEAR configuration consisted of three main components:

1. Inner chambers for charged particle tagging and tracking,

2. Two hemispheres of NaI(Tl) crystals,

3. Supplemental detector components including a luminosity monitor and endcap NaI(Tl) arrays.

Figure 2.2 shows the arrangement of these various components. We describe each below. More detail can be found in the references.[6,7]

2.2.1 *Inner Detector*

The function of the inner detector was to identify charged particles (tagging) and measure their directions (tracking). (No measurement of the sign of the charge of a particle was possible since there was no magnetic field.) In order to make maximum use of the limited space available inside the NaI(Tl) hemispheres, three sets of cylindrical chambers were installed with varying lengths dictated by the geometrical constraints. The inner and outer sets consisted of spark chambers, while the middle set consisted of multiwire proportional chambers. (See Fig. 2.3.)

The following table summarizes the configuration of the inner detector:

	Type	Distance from Beam	Solid Angle Coverage	% Rad. Lengths*
Beam Pipe (Aluminum)	–	59 mm	100 %	1.9
Chamber 1	Spark	79	94	2.0
Chamber 2	MWPC	100	83	0.35
Chamber 3	Spark	137	71	2.0
Inner Ball Shell	–	254	94	4.3

*Normal Incidence

Table 2.1 Parameters of inner detector.

Each set of spark chambers contained two double gap chambers, giving 8 spark chambers total. Each layer of the spark chambers consisted of 0.3 mm diameter wires separated by 1 mm which were read out by one magnetostrictive wire perpendicular to the wires. Thus, each layer could give one angular coordinate of a track, but there was no way to establish a correspondence between coordinates measured by one layer with the coordinates measured by another. In order to reduce these combinatorial ambiguities, the chambers were wound with varying pitch angles.

The two multiwire proportional chambers[8] complemented the spark chambers in that they were less noisy and did not need to be pulsed; for these reasons they were included in the trigger logic. However, their spatial resolution was inferior to that of the spark chambers, and as such they were not used in the determination of the directions of charged tracks. Each chamber consisted of a stripped cathode

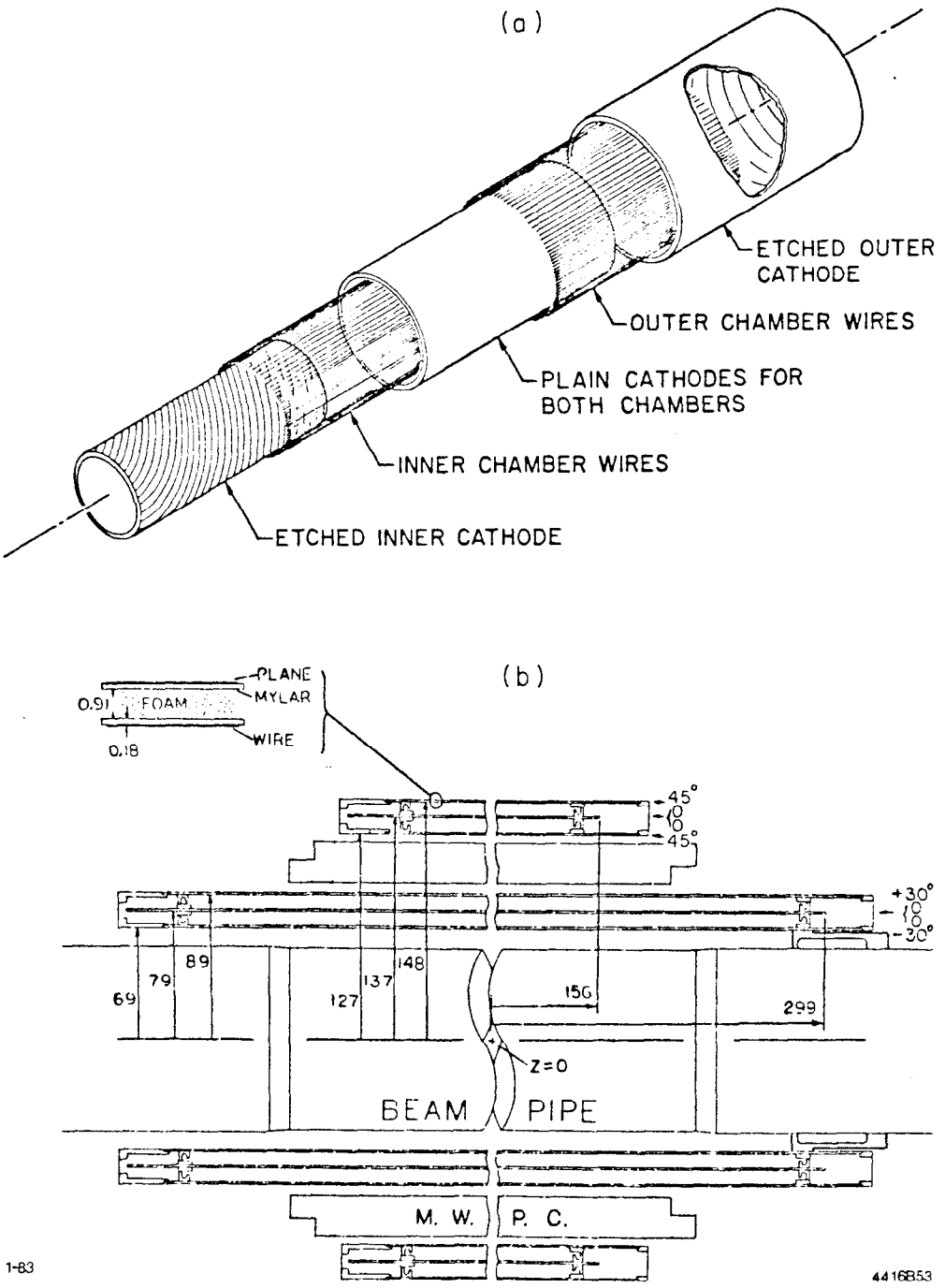

Fig. 2.3 Central tracking chambers. (a) Multiwire proportional chambers. (b) Spark chambers.

plane and 144 signal wires. Again, in order to reduce possible ambiguities, the strips of the cathode plane were constructed at different angles (62° and 90°) to the beam axis. In addition to the spark and multiwire proportional chambers, a layer of proportional wire tube chambers was installed inside the innermost spark chamber for the second half of the ψ' data taking (i.e., those data taken during 1981). These chambers were for test purposes only and were not used for either tagging or tracking. However, they did add 1.3% radiation lengths of material through which photons had to pass and so increased the conversion probability.

In the present analysis we study final states containing no charged particles. Thus, we do not use the tracking capabilities of the chambers but rather use them only to reject events which contained one or more tracks tagged as charged. The specifics of the chamber design affect the cuts used in the analysis only in the solid angle limit which is determined in part by the angular coverage of the chambers. We reject any event which has a track beyond $|\cos\theta| > 0.90$ (where θ is the angle between the track and the beam direction). The efficiency of the chambers in determining the charge of a track enters the Monte Carlo efficiency calculations and is discussed in Appendix B.

2.2.2 *Main Detector*

The main detector consisted of 672 thallium-doped sodium iodide (NaI(Tl)) crystals, each of which was triangular in cross section and 16 radiation lengths long. (See Fig. 2.4.) NaI(Tl) was chosen as a photon detector due to its superior energy resolution and high detection efficiency over a wide range of energies. As discussed in Appendices A and B, the energy resolution for photons as measured at SPEAR is well-described by the relation

$$\frac{\sigma_E}{E} = \frac{\sigma_0}{E(\text{ GeV})^{1/4}} \qquad [2.3]$$

where σ_0 = 2.4-2.8%. Also, the angular resolution for photons is expected from Monte Carlo studies to be between one and two degrees, depending on energy.

This is consistent with the angular errors determined from kinematic fits to well-constrained final states. (See Appendix B.)

During the assembly of the Ball, each crystal was alternately sanded or polished as necessary to achieve a uniform response to a Cs^{137} source placed along its axis.* Next, the crystals were wrapped in 0.005 inch thick paper and 0.0005 to 0.0015 inch thick aluminum foil to achieve optical isolation. The crystals were then stacked in two hemispheres in a projective geometry so that a line drawn from the center of the hemisphere to the face of a crystal would lie parallel to the axis of that crystal. NaI(Tl) is extremely hydroscopic and becomes discolored when exposed to even small levels of humidity. For this reason, each hemisphere was sealed in a metallic "can" which again had the shape of a hemispherical shell. For additional protection, the entire assembly was placed in a dryhouse in which the temperature and humidity was carefully controlled. Each crystal was viewed by an individual phototube through a 0.5 inch thick window and a two inch air gap.

The two hemispheres were installed above and below the SPEAR beampipe. The hemispheres were controlled by a hydraulic system so that they could be closed during normal running or moved away when the detector was not taking data (for instance, during synchrotron radiation running) in order to reduce the radiation dose on the NaI(Tl) crystals. The two hemispheres were not flush when in the closed position but rather were separated by a gap of 3.5 to 8.0 mm, depending on the radial distance from the center. This gap can be seen, for instance, in the angular distribution of $e^+e^- \to \gamma\gamma$ events (Fig. B.16). Crystals on either side of this gap are called "equator modules". In addition, there were gaps in each hemisphere to allow openings for the beam pipe and connections to the inner detector to enter and exit. (The missing volume is equivalent to 24 crystals for each opening, or 48 crystals total.) These gaps are called "tunnels", and the crystals surrounding the

* This process is referred to as "compensation". The response curve of a crystal to a Cs^{137} source placed at various points along its axis is called a "compensation curve".

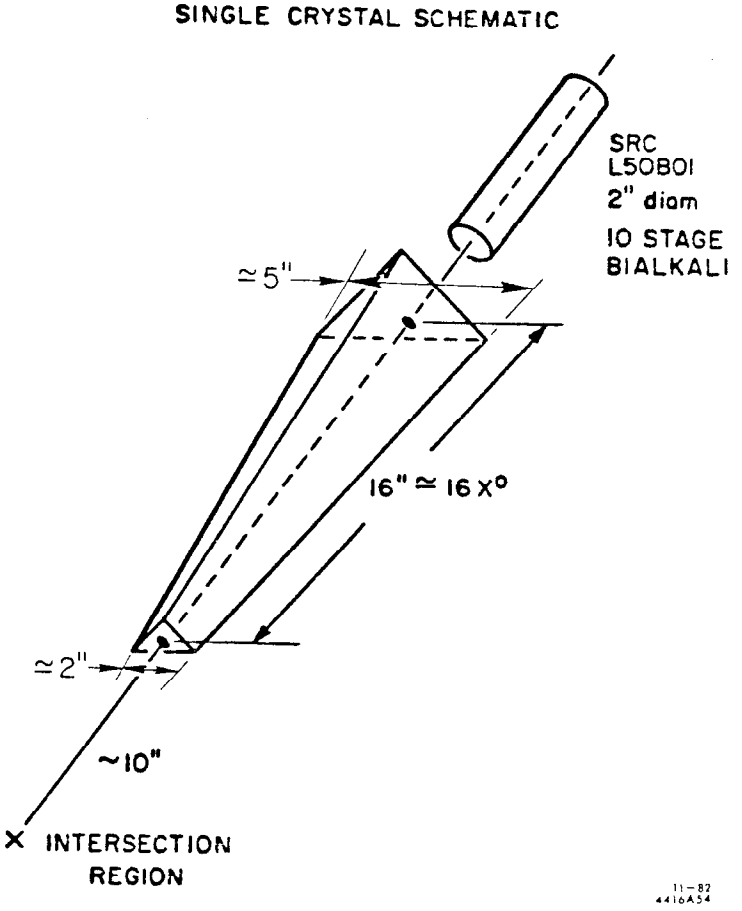

Fig. 2.4 Typical Crystal Ball crystal.

gaps "tunnel modules".

Figure 2.5 shows two schematic representations of the main detector. Figure 2.5(a) shows the main Ball in its actual shape with each crystal represented by a triangle. Figure 2.5(b) shows the inner surface of the Ball in a Mercator-like projection onto a plane. This representation is more convenient for event displays in which a number can be displayed in each crystal denoting the energy (in MeV) deposited in it. In both representations we have shown the directions of the same Cartesian coordinate system with the z axis parallel to the positron direction, the y axis pointing to the center of SPEAR, and the x-axis completing a right-handed sys-

tem. The center of this coordinate system coincides with the interaction point. Any reference to Cartesian coordinates refers to this coordinate system unless otherwise indicated.

Some aspects of the crystal stacking have implications for data analysis. Specifically, some fraction of the energy of a shower which begins in a tunnel module may propagate into the tunnel and so be lost. Also, some of the tunnel modules have a somewhat smaller volume than the rest of the Ball modules due to geometric constraints in the tunnel region. Thus, energies in these crystals will not in general be as well measured as those in other crystals. The same comments apply to the equator modules, although the effects are not as large.

The geometry of the individual crystals also determines to some extent how the data are analyzed. When calculating the energy in a shower, we can take as a first approximation the sum of the energy of the crystal with the largest energy and the energies of the crystals in some "neighborhood" of this crystal. Figure 2.6 shows schematically a small section of the Ball as viewed from the interaction point. As all crystals have a triangular cross-section, a given crystal (marked "*") shares an edge with three crystals (dark shading). In addition, it shares a vertex with 9 crystals (light shading). The shaded crystals make up the set of 12 "neighbors" of *, while the three darkly shaded crystals are the three "nearest neighbors" of *. Given the Molière radius of NaI(Tl) ($\approx$ 4 cm), a useful neighborhood for the calculation of energies is given by the twelve neighbor crystals. The energy so obtained is called the sum of 13 energy and is discussed further in the next chapter.

2.2.3 *Supplemental Detector Components*

In order to extend the solid angle coverage of the detector beyond 94%, four endcap arrays of NaI(Tl) crystals were added which brought the total solid angle coverage to 98%.[9] Each endcap array consisted of 15 crystals which were hexagonal in cross-section with a maximum diameter of six inches. The majority were 20 radiation lengths long and were used in a previous SPEAR experiment.[10] Three

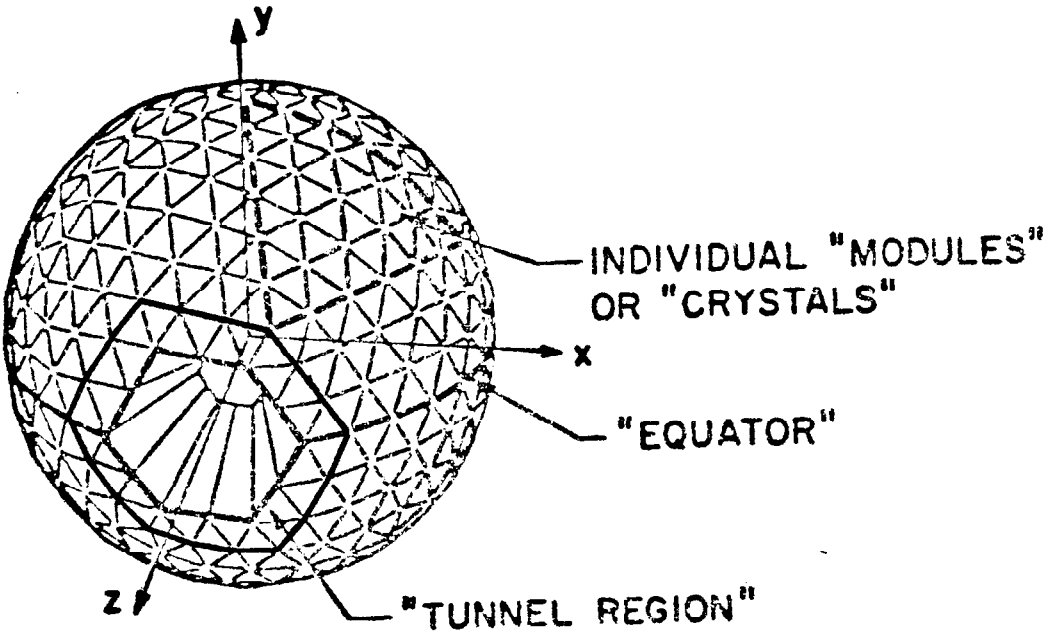

(a)

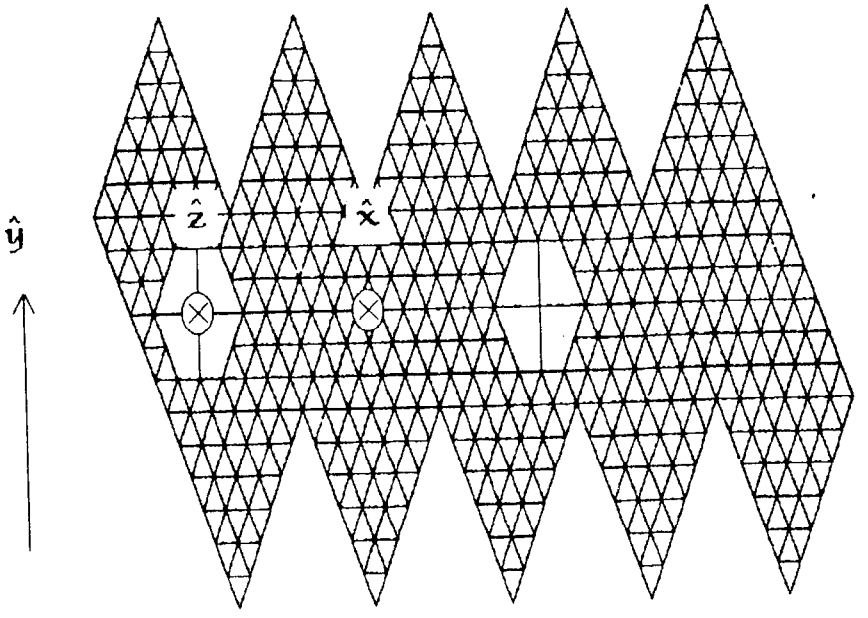

(b)

Fig. 2.5 Schematic representations of the main detector. (a) Actual shape. (b) Mercator-like projection.

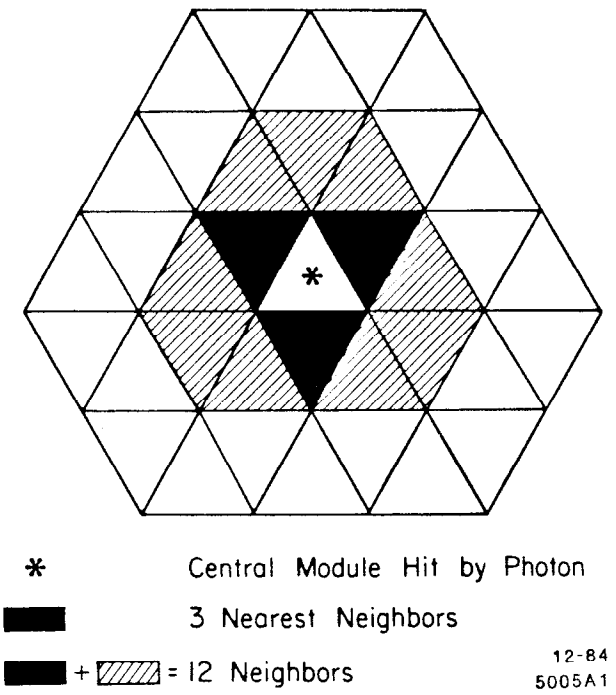

Fig. 2.6 Small section of inner surface of Ball.

crystals in each array were shorter (10 radiation lengths long). Each endcap array was preceded by two double-gap spark chambers for charged particle tagging and tracking. The endcap arrays were not used in any of the analyses described here except to veto those events which had a track in the endcaps, indicating that one or more particles had escaped the main Ball.

The luminosity monitor consisted of four arms, each with an aperture-defining scintillation counter and a shower counter, placed symmetrically about the interaction point.[11] In such an arrangement the luminosity as measured by the sum of the rates in the four counters is insensitive to displacements in the interac-

tion point to first order. The luminosity is determined by dividing the measured rate by the calculated Bhabha cross-section (integrated over the area of the scintillation counters). The accuracy of the luminosity measurement is estimated to be $\pm 4\%$. A comparison of the luminosity measured by the luminosity monitor and the luminosity measured by the $e^+e^- \to e^+e^-$ and $e^+e^- \to \gamma\gamma$ rates in the main detector found agreement to within $\pm 3\%$.[12] Luminosity measurements affect the final results obtained in this work only through the determination of the number of hadronic continuum events which were subtracted from the observed number of continuum events to yield the number of resonance decays.[7]

2.3 Electronics and Data Acquisition

The signals from each of the phototubes in both the main Ball and the endcap arrays were sent individually to the control room, along with signals from the magnetostrictive wires in the spark chambers, the cathode strips and sense wires in the MWPC's, and the signals from the luminosity monitor. The phototube pulse was divided so that it could be simultaneously presented to both the trigger logic and the integration circuits (to be described below). The analog sums of the pulses from groups of nine crystals were formed for use by the trigger logic. Various triggers could be formed with these sums, but the only one needed for this study was the total energy trigger. This trigger fired when the sum of the signals from all groups of nine crystals passed a certain discriminator threshold. This discriminator was set to generate a trigger when a signal corresponding to roughly 1260 MeV of deposited energy was received. This is far below the software threshold of $\approx$ 3100 MeV and 2500 MeV for the ψ' and J/ψ data, respectively.

The other part of the phototube signal was presented to the input of two RC circuits. In order to increase the dynamic range of the system, one RC circuit was preceded by a resistive divider which reduced the pulse by a factor of 21. Thus, to each crystal there corresponded two electronics channels, designated low and high, which integrated the pulse with and without reduction, respectively. If no hold was

received from the trigger logic, the charge on the capacitors was allowed to leak away so that virtually none remained at the time of the next beam crossing. If the trigger logic detected a valid trigger, a hold pulse was generated at $\approx$ 380 ns, corresponding to the peak of the integrated signal.† Upon receipt of the hold pulse, an FET switch was opened, isolating the capacitor from the rest of the system. Under computer control, the voltage on these capacitors was presented one at a time to the input of a single ADC which digitized the signals and stored them for a later DMA transfer to the online computer.

Data taking and monitoring of the experiment were supervised by a PDP-11/55T.[13]The highest-priority task was servicing interrupts from the experiment and writing the received information onto magnetic tape. After September 1979, the data were "compressed" by writing only those crystal energies above a threshold of $\approx$ 100 keV to tape. One in every 128 events was written uncompressed. In addition, selected events were processed through a "pipeline" which allowed various quantities (total energy, position of hits in the spark chambers, angular distribution of Bhabha events, etc.) to be monitored in real time. Other functions could be selected at the experimenter's discretion.

2.4 Data Rates

SPEAR typically delivered luminosities of 0.5×10^{30} cm^{-2}sec^{-1} and 1.5×10^{30} cm^{-2}sec^{-1} at the J/ψ and ψ' energies, respectively. The trigger rate was typically 2-3 Hz, of which 1 Hz and 0.5 Hz, respectively, were due to resonance decays on the J/ψ and ψ'. (The remainder of the triggers were due to non-resonance physics and cosmic ray and beam gas background.) The deadtime at this rate was 10-15%, attributable mainly to the dead time of the spark chambers.

† The maximum of the signal was sufficiently flat that a variation of 45 ns in the time of the arrival of the hold pulse corresponded to a 1% variation in the level of the integrated signal.

2.5 Particle Signatures

Particle identification is performed primarily using the NaI(Tl). Low-mass particles which have electromagnetic but no nuclear interactions (γ's, e^+'s, and e^-'s) initiate electromagnetic showers upon entry into the crystals and deposit virtually their total energy into crystal lattice excitations which are eventually converted into light by the thallium trapping centers. Muons, on the other hand, are too massive to initiate a shower, and instead interact with the crystal via ionization only. They deposit roughly 200 MeV in one or two crystals. Interacting hadrons ($\pi^{\pm}$'s ,$K^{\pm}$'s) are intermediate between the two cases. They may pass through the entire crystal without interaction and deposit minimum ionizing energy much like a muon. Alternatively, they may undergo a nuclear interaction in the crystal and leave an irregular energy deposition whose distribution depends on the trajectories of the nuclear fragments. (Some remnants may even backscatter and leave showers in the opposite hemisphere.)

In this study we have chosen to concentrate on those decays in which all of the final state particles are γ's. In this case all of the energy of the final state particles is deposited in the NaI(Tl) so that we can demand conservation of energy and momentum. These constraints not only allow us to better determine the final state four-vector's, but also provide a powerful discriminator against background. As we shall see, we can exploit the ability to observe all of the energy in the final state to identify even those decays in which overlap of the γ's makes identification of the individual four-vectors impossible.

References

1) SPEAR Storage Ring Group, *Proceedings of the Ninth International Conference on High Energy Accelerators*, SLAC, 1974, p. 37.

2) SLAC Storage Ring Group, *Proceedings of the Eighth International Conference on High Energy Accelerators*, CERN, 1971, p. 145.

3) M. Sands, *The Physics of Electron Storage Rings – An Introduction*, SLAC Report 121.

4) I. M. Ternov, Y. M. Loskutov, and L. I. Korovina,, *Zh. Eksp. Teor. Fiz.* **41** (1961) 1924 [*Sov. Phys.–JETP* **14** (1962) 921].
Sokolov, A.A., and Ternov, I.M., *Dokl. Akad. Nauk. SSSR* **153** (1963) 1052 [*Sov.Phys.–Dokl.* **8** (1964) 1203].

5) I. Kirkbride, Crystal Ball Note 252.

6) M. Oreglia, Ph.D. thesis, Stanford University, 1980, and SLAC-Report 236 (unpublished).

7) J. Gaiser, Ph.D. thesis, Stanford University, 1982, and SLAC-Report 255 (unpublished).

8) J. Gaiser *et. al.*, *IEEE Trans. of Nucl. Sci.* **NS-26** (1979) 173.

9) H. Sadrozinski and J. O'Reilly, Crystal Ball Note 239.

10) C. J. Biddick *et. al.*, *Phys. Rev. Lett.* **38** (1977) 1324.

11) H. Kolanoski, Crystal Ball Note 244.

12) C. Edwards *et. al.*, to be published in *Phys. Rev. D*, and SLAC-PUB 3030.

13) R. Chestnut *et. al.*, *IEEE Trans. on Nucl. Sci.* **NS-26** (1979) 4395.

Chapter 3

Data Samples and Data Production

3.1 Data Samples

All data used in this study were taken with the Crystal Ball detector during its residency at SPEAR (1978-1981). The detector remained in the same configuration during this time except for the minor changes to the inner detector noted in Chapter 2. The beam conditions were also substantially unchanged during this time except for the 1981 ψ' run during which a wiggler magnet was used to store more current. All three datasets were produced with the same offline code (described below), although the cuts used in the production program varied. (These variations had no effect on the efficiency for detection of the events considered in this study.) Table 3.1 compares the three datasets.

3.2 Offline Production

The standard offline production consists of five steps, described briefly below. More information can be found in the references.[1,2]

The first step calculates the energy deposited in each crystal from the ADC

Number of Events	ψ'	J/ψ	ψ''
Accumulated During	Fall '78 Spring '79 Fall '81	Fall '78 Spring '79 Fall '80	Winter '79
Luminosity (nb^{-1})	3351	771	1776
Produced Resonances	1.8×10^6	2.2×10^6	

Table 3.1 Datasets used in this analysis.

counts according to the simple formula

$$E_{xtal} = \left(C_{high\ channel} - P_{high\ channel}\right) * Ratio * Slope \quad \text{if } C_{high\ channel} \geq 350 \text{ or } C_{low\ channel} \geq 7000$$
$$= \left(C_{low\ channel} - P_{low\ channel}\right) * Slope \quad \text{otherwise} \qquad [3.1]$$

where $C_{high\ channel}$ and $C_{low\ channel}$ denote the number of counts in the digitized signal of the high and low channels corresponding to the crystal in question. The other parameters are calibration constants as defined in Appendix E. The low channel - high channel breakpoint corresponds roughly to an energy of 140 MeV.

In order to facilitate identification of energy depositions, the second step groups crystals into "connected regions". A connected region is defined as a contiguous set of crystals each containing more than 10 MeV. Two crystals are contiguous if one is contained in the set of twelve neighbors of the other. Figures 3.1 and 3.2 show a typical J/ψ event with three connected regions in the Mercator-like projection of the main detector described in Chapter 2. The sum of the energies of the crystals in each connected region is shown in the column headed "ECR". (Connected region

2 is listed twice.)

Two or more showers may of course overlap and form one connected region. The third step assigns the crystals in a connected region to one or more shower maxima (called "bumps") according to the following algorithm:

1. Initially mark all crystals as unflagged.
2. Find the unflagged crystal with the largest energy deposition in the connected region and label it the "bump module".
3. Get the three nearest neighbors and flag them as associated with this bump.
4. Sum the energies in the central crystal and its three neighbor crystals to form a preliminary bump energy.
5. Flag other crystals which are associated with this bump by the bump discriminator function: If

$$E_{xtal} < E_{bump}\, 0.72 e^{-9.4(1-\cos\theta)} \quad \text{and} \quad 15^\circ < \theta < 45^\circ$$
$$\text{or} \qquad [3.2]$$
$$\theta < 15^\circ$$

   (where θ is the angle between the bump module and the crystal being tested), then the crystal is assigned to this bump.
6. If any unflagged crystals are left in the connected region, go to 2.

The bumps algorithm was derived empirically by examining the distribution of bumps in a sample of ψ' events. It is used in the production of all Crystal Ball data, most of which contain interacting hadrons (unlike the clean events considered here). In the event shown in Figures 3.1 and 3.2, the bumps algorithm found four bumps. In this work, we use "track" interchangeably with "bump".

The fourth step processes data from the chambers. The first phase of the algorithm attempts to construct tracks from the chambers alone. Starting from the collision point, the spark chambers are searched for lines of sparks emanating

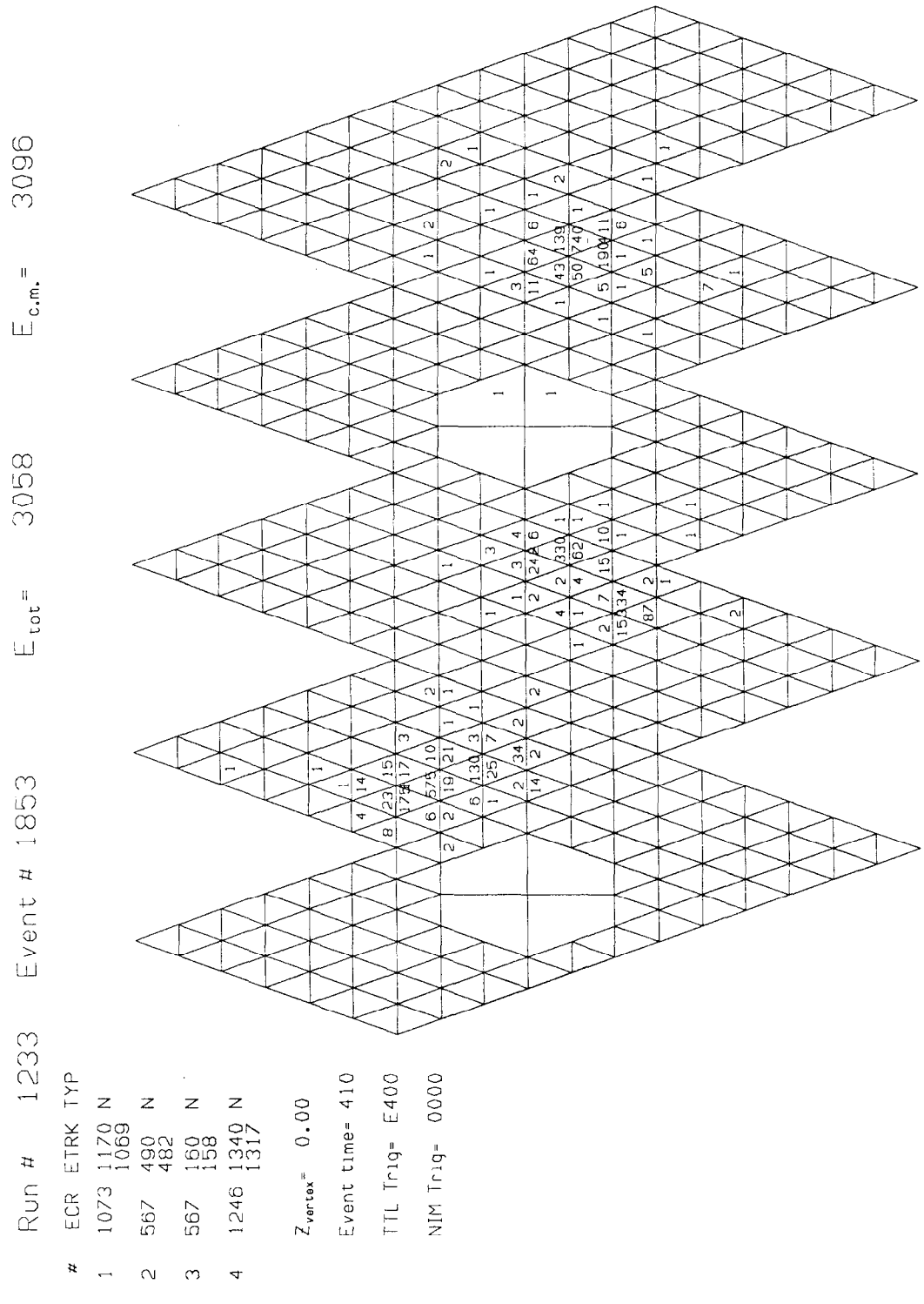

Fig. 3.1 Event display from J/ψ dataset.

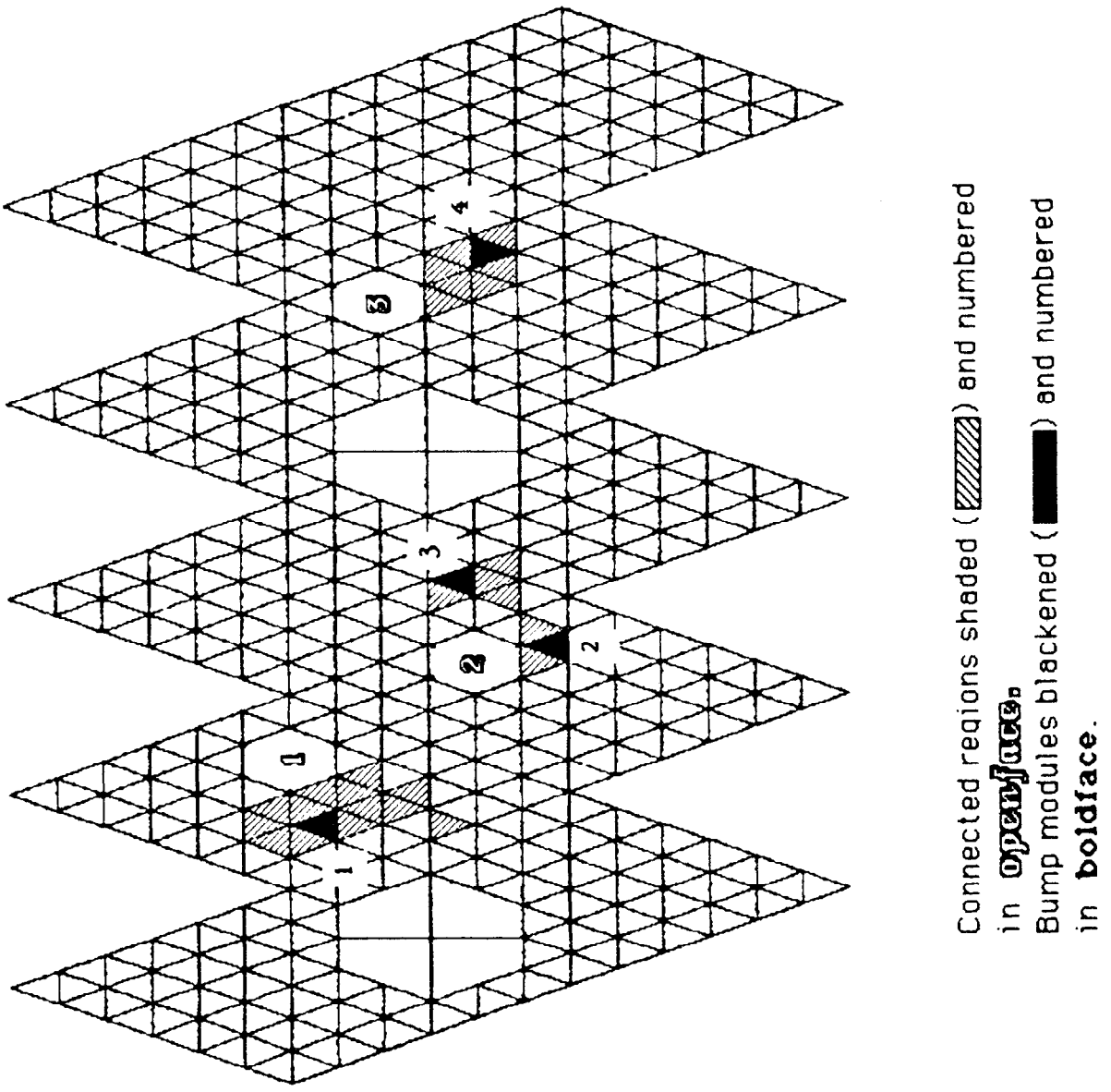

Fig. 3.2 Event displayed in Fig. 3.1 showing connected regions and bump modules.

from roughly z=0. The minimal criterion for defining a trajectory is a hit in each chamber in one of the planes parallel to the beam and a hit in each chamber in one of the planes at an angle to the beam. Tracks defined in this way are termed "IR" tracks and are assigned directions derived from the tracking chambers. If the track points to a bump in the Ball, the track is assigned the energy of the bump. If, as occasionally happens, the track points to a region of the Ball which contains no energy, it is termed a "zero-energy IR" track.

In the second phase, the algorithm uses any remaining unassigned hits in the chambers to tag remaining bumps. A line is drawn from any bump which has not been flagged as charged to the event vertex. Both the spark chambers and the MWPC's are searched for hits which lie in a small angular interval about this line. If two or more hits are found within this cone, the bump is tagged as charged. The direction of the resulting charged track is determined by the bump direction cosines.

The final step calculates an energy and a direction for each bump. Two estimates are made of a bump's energy. The first, the "sum of 13 energy", or E_{13}, is the unweighted sum of the energies of the bump module and its twelve neighbors. Two corrections are made to this sum. First, a shower may not be contained in the volume of 13 crystals. The fraction of energy of a shower which leaks outside the 13 crystals has been estimated from Bhabha studies to be 2.25%. Second, it is to be expected that the measured energy of a shower depends on where the incident particle enters a crystal. Specifically, some of the energy of a shower which is initiated close to the edge of a crystal will more likely be lost in the interstitial spaces and wrappings between the crystals than a shower initiated at the center. A crude measure of how close to the center of the central module the incident particle entered is given by the ratio of the energy in the central module divided by the sum of 13 energy, or $E_{max}/\sum_{i=1}^{13} E_i$. Figure 3.3 shows the variation of the (uncorrected) energy of a track (normalized to the beam energy) as a function of $E_{max}/\sum_{i=1}^{13} E_i$ for a sample of $e^+e^- \rightarrow e^+e^-$ (QED and resonance decays) and $e^+e^- \rightarrow (\gamma)\gamma\gamma$ events from the ψ' dataset. Overlaid on this graph is a plot of the

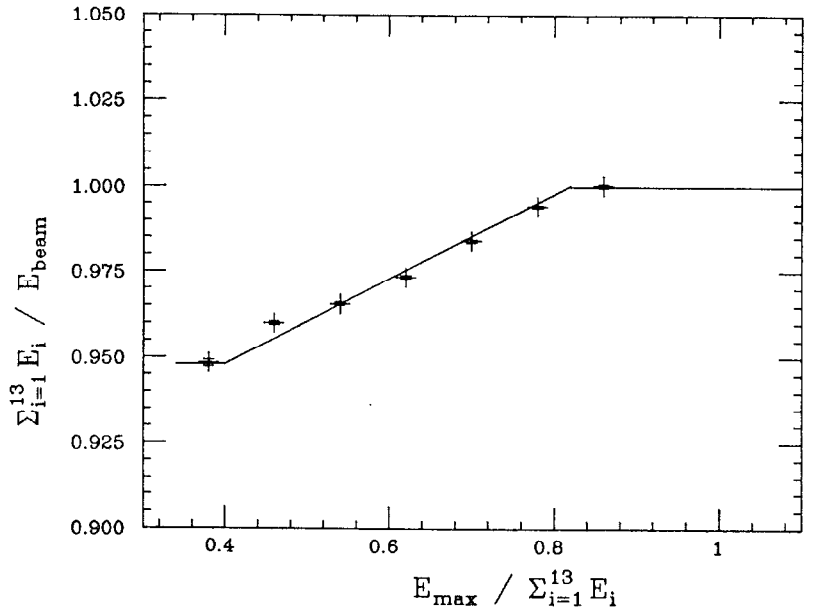

Fig. 3.3 $E_{max}/\sum_{i=1}^{13} E_i$ *vs.* $\sum_{i=1}^{13} E_i/E_{beam}$ for $e^+e^- \rightarrow e^+e^-$ (QED and resonance decays) and $e^+e^- \rightarrow \gamma\gamma$ events in ψ' dataset.

position correction function (PCORR) which is used to correct for this effect. (The position correction is actually the inverse of this function and so is always greater than or equal to unity.) The corrected sum of 13 energy is then

$$E_{13} \equiv \left(\sum_{i=1}^{13} E_i\right) * 1.0225 * \mathrm{PCORR}(E_{max}/\sum_{i=1}^{13} E_i) \qquad [3.3]$$

It should be borne in mind that the sum of 13 algorithm does not attempt to separate overlapping showers. If the neighbors of two bump modules overlap, the energy in the common crystals will be double counted with the consequence that the energy of each of the two bumps will be overestimated.

The estimates of the direction cosines and the second estimate of the shower energy (the "ESORT" energy) use the expected shape of a shower derived from Monte Carlo studies. The bump module is conceptually divided into 16 submodules. (See Fig. 3.4.) Under the assumption that the particle entered a given submodule, one can predict the expected fraction of the total energy of the shower which would be observed in each module in the connected region. The direction of the shower is taken to be the center of the submodule which minimizes the squared differences between the observed and predicted energies in the modules in the three nearest neighbors of the bump module (if there is more than one bump in the connected region) or in the entire connected region (if there is only one bump in the connected region). Directions obtained in this way will of course be quantized. If there is only one bump in a connected region, the ESORT energy for that bump is taken to be the sum of the energies of all the crystals in the connected region. If there is more than one bump, each bump in the connected region is assigned its preliminary energy as calculated in the bumps step. The energy in the remaining crystals is divided between the bumps in accordance with the energy predicted to be in each crystal by the Monte Carlo shower functions. Corrections similar to those used in the sum of 13 estimates are applied to obtain the final energies. The column labeled "ETRK" in Figure 3.1 shows the ESORT (upper entry) and E13 (lower entry) energies calculated for the four tracks in the event.

3.3 All-γ Production

All events which pass the production cuts are processed by the preliminary neutral analysis program. The first section of this program performs cuts; the second performs several CPU-intensive calculations of shower parameters and stores them for later use.

3.3.1 *Preliminary Cuts*

Events from all data samples are subjected to the following cuts:

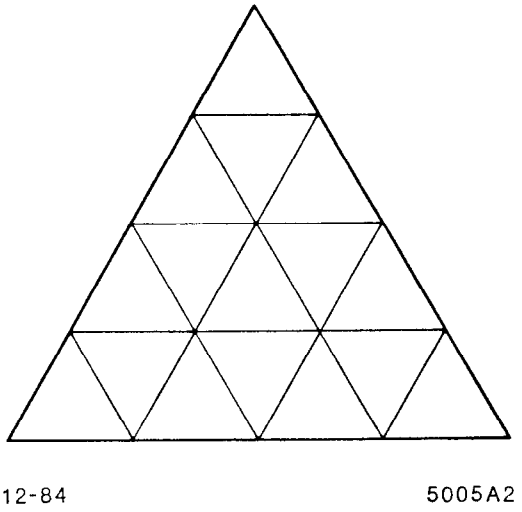

Fig. 3.4 Crystal Ball module divided into submodules.

1. The center-of-mass energy (E_{CM}) of the event is calculated from the beam energy recorded on tape. If twice the beam energy is not within 5 MeV of the mass of the J/ψ, ψ', or ψ'', it is assumed that the beam conditions were unstable or that the data in the event are unreliable, and the event is rejected.

2. It is required that $|E_{CM}-E_{vis}| < 600$ MeV, where E_{vis} is the sum of all energy in the Ball and endcaps. Figure 3.5 shows the visible energy distribution for a portion of the J/ψ data sample. Monte Carlo studies indicate that any all-γ event which fails this cut contains one or more γ's which lie outside the fiducial volume of the detector.

3. The number of tracks (defined as the number of bumps) is required to be between 3 and 15.

4. The number of tracks tagged as charged emanating from the primary vertex is required to be zero. (At this point we retain events with secondary vertices, and these vertices may have charged tracks. Such events are eliminated by a later cut.)

5. Finally, approximate momentum balance is required. Using x=y=z=0 as the

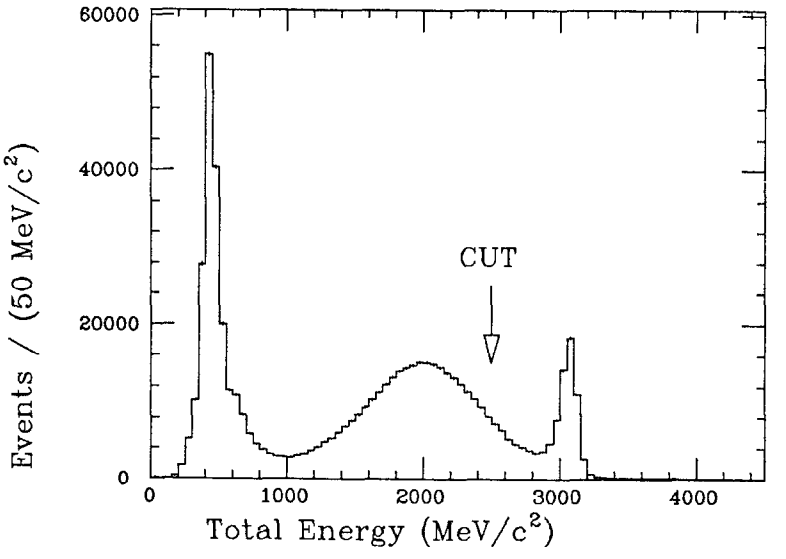

Fig. 3.5 Visible energy in J/ψ data.

origin, a momentum vector is calculated for each crystal where the direction is specified by the direction cosines of the center of the module and the magnitude is specified by the deposited energy. The sum of these vectors is required to satisfy $|P_X| < 400$ MeV/c, $|P_Y| < 400$ MeV/c, and $|P_Z| < 800$ MeV/c. This cut is designed to eliminate events at this stage before the CPU-intensive processing of the succeeding routines. Monte Carlo studies indicate that virtually no good events are thrown out by this cut; studies of the data indicate that events eliminated at this point have a confidence level in a kinematic fit to energy and momentum constraints of less than 0.001 and so would be eliminated by later cuts. Figure 3.6 shows a plot of P_Z *vs.* P_X for a small part of the J/ψ dataset. The box indicates the region of the cut. Figure 3.7 shows the same plot for a Monte Carlo sample of $J/\psi \rightarrow \gamma$ f, f $\rightarrow \pi^0\pi^0$ events.

Table 3.2 shows the effect of these cuts on the three datasets.

Number of Events	ψ'	J/ψ	ψ''
Input	4,002,706	4,593,147	1,887,023
After ECM check	3,978,868	4,591,559	1,867,903
After E_{vis} cut	1,316,995	785,298	570,542
With $\geq$3 tracks	546,668	391,318	225,689
With $\leq$15 tracks	542,107	386,814	224,926
With no charged tracks	38,912	39,620	13,990
After momentum balance cut	30,722	24,756	9,988

Table 3.2 Preliminary cuts.

3.3.2 *Secondary Cuts*

Data samples for the exclusive analyses are at this point subjected to further cuts. (The secondary cuts for the global shower analyses are somewhat different and are described in the section on $\psi' \rightarrow \gamma\eta$ and $\psi' \rightarrow \gamma\eta'$ decays.) The cuts just described select a sample of events which contain only γ's in the final state with little background. We next apply cuts to discard events in which the measurement of the parameters of one or more tracks is questionable. Specifically,

1. Events with more than ten tracks are rejected as we deal in this investigation with topologies which have no more than five γ's. (We allow for more than five tracks as some may be subsequently identified as spurious.)
2. Data from November 1978 are rejected. These were some of the first data taken with the detector while it was still in the process of being tested.
3. Events with endcap tracks are rejected, since the energies and directions of

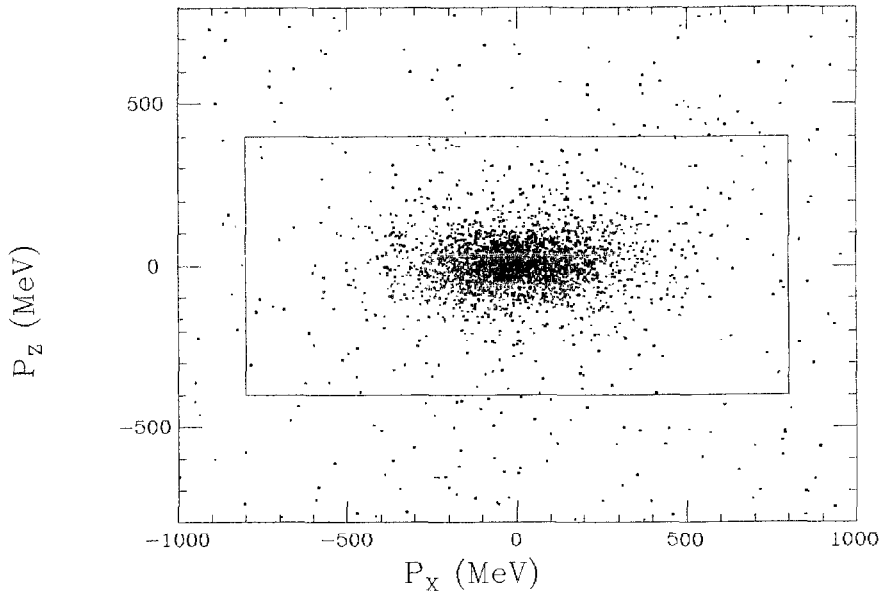

Fig. 3.6 P_z *vs.* P_x for sample of J/ψ Data.

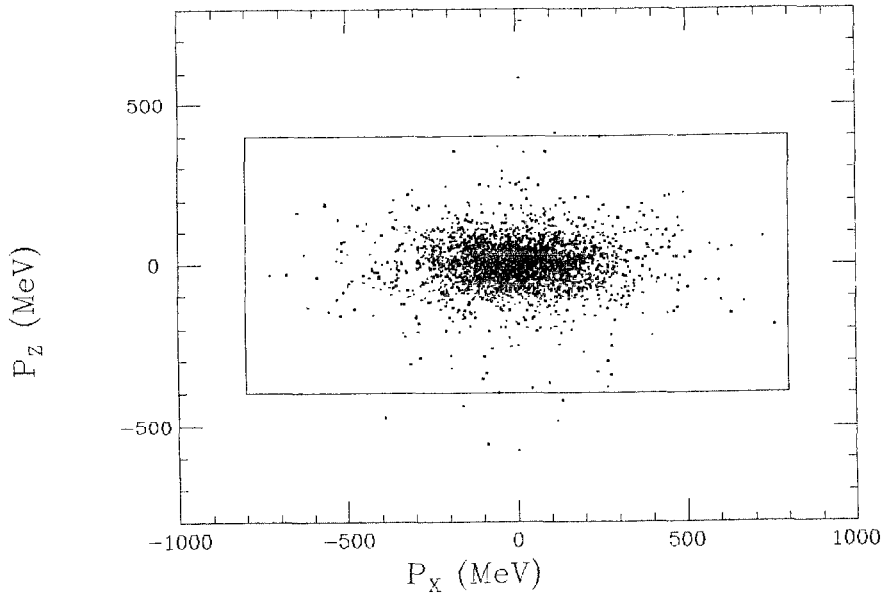

Fig. 3.7 P_z *vs.* P_x for $J/\psi \rightarrow \gamma \mathrm{f}, \mathrm{f} \rightarrow \pi^0\pi^0$ Monte Carlo.

these tracks are not as well measured as those in the main Ball.

4. Events with more than one vertex are rejected. Although we have removed events in the previous cut which deposited sufficient energy in the endcaps to generate a track, there remain events in which a part of a shower leaking from the tunnel modules enter the endcap spark chambers, giving rise to spurious hits and one or more phantom vertices.

These cuts combined with those described in the preceding section select a sample of events which contain only γ's in the final state with little contamination. However, there are typically correlations which favor small opening angles between two or more γ's. (For instance, they may come from the decay of a high energy π^0.) Routines have been developed which can separate showers due to single γ's from those due to the overlap of two γ's so that the number of photons in the final state can be correctly determined. (See Appendix C.) The more accurate of these routines, PIFIT, fits the observed energy distribution to two overlapping shower distributions and identifies π^0's by the large invariant mass of the sum of the calculated four-vectors. Another routine, SMOMT, does not extract the four-vectors of the γ's but rather determines the invariant mass of their sum from the second moment of their (overlapping) showers in the Ball. Thus, it can be used to calculate the invariant mass of two or more photons whose showers overlap, although it is less accurate in separating γ's from π^0's than PIFIT. In the exclusive analyses described in the following two chapters, we attempt to identify energy depositions corresponding to at most two overlapping γ showers. In order to eliminate events which do not meet this criterion, we make the following cuts:

5. Events containing a connected region with more than two bumps are rejected.

6. Any event containing a connected region with an SMOMT mass greater than 200 MeV/c^2 is rejected. As shown in Appendix C, the SMOMT mass of a connected region is seldom above 200 MeV/c^2 even for high energy π^0's. Any connected region with an SMOMT mass above this value most likely contains

more than two γ's and is unsuitable for this analysis.

Table 3.3 shows the effect of these additional cuts on the three data sets.

Number of Events	ψ'	J/ψ	ψ''
Input	30,722	24,756	9,988
With $\leq$ 10 Tracks	29,294	23,204	9,969
After Nov. '78 cut	28,953	23,204	9,969
After Endcap Track Cut	12,265	11,823	3,982
After Vertex cut	9,122	11,070	2,869
After 3 Bump Cut	9,006	10,785	2,868
After 200 MeV/c^2 SMOMT cut	8,218	9,719	2,837

Table 3.3 Secondary cuts.

3.3.3 π^0- γ *Separation*

As mentioned previously, the showers from the two γ's of an energetic π^0 often overlap, causing the two photons to be flagged as one track by the offline software. All events passing the secondary cuts are next processed through shower-fitting routines to flag those showers which appear to be due to merged π^0's. All tracks are classified as either

1. A good γ,
2. A good merged π^0, or
3. A bad track.

Good γ's and good merged π^0's are together referred to as good neutrals. Bad tracks are typically a π^0 which has been flagged as merged. The classification proceeds by the following steps.

1. All tracks are initially flagged as good γ's.
2. The routine PIFIT is called for each connected region. If the PIFIT mass is less than 90 MeV/c^2, track assignments are not altered. If the PIFIT mass is greater than 90 MeV/c^2, the highest energy track in the connected region is flagged as a π^0. (This γ-π^0 separation criterion is consistent with both Monte Carlo and data studies. See Appendix C.) If there are any other tracks in the connected region, they are flagged as bad tracks and ignored by subsequent routines.
3. Next, an attempt is made to identify showers coming from 2 γ's which come from a π^0 which overlap but which are not in the same connected region (and so not flagged by the previous step). If the 13 crystals associated with a good gamma overlap with the 13 crystals associated with another good gamma, PIFIT is called with starting values at the centers of the two central crystals. If the PIFIT mass if greater than 90 MeV/c^2 and less than 200 MeV/c^2, the higher energy track is flagged as a $\pi^0$and the lower energy track is marked as a bad track. Otherwise, the track assignments are unmodified. Figure 3.8 shows the distribution of PIFIT masses for these overlapping γ's for the J/ψ dataset.
4. Finally, a search is made for shower fluctuations which are identified as separate tracks by the offline software. These satellite showers, or split-offs, are expected to be of low energy and close in angle to a high energy shower. To determine criteria for identifying split-offs, we first examine a set of single-photon Monte Carlos (See Appendix B.) For those events in which the offline software detected more than one track, we plot in Figure 3.9 the energy of the second (and possibly third) highest energy track *vs.* the cosine of the angle between this track and the highest energy track. (We consider only those

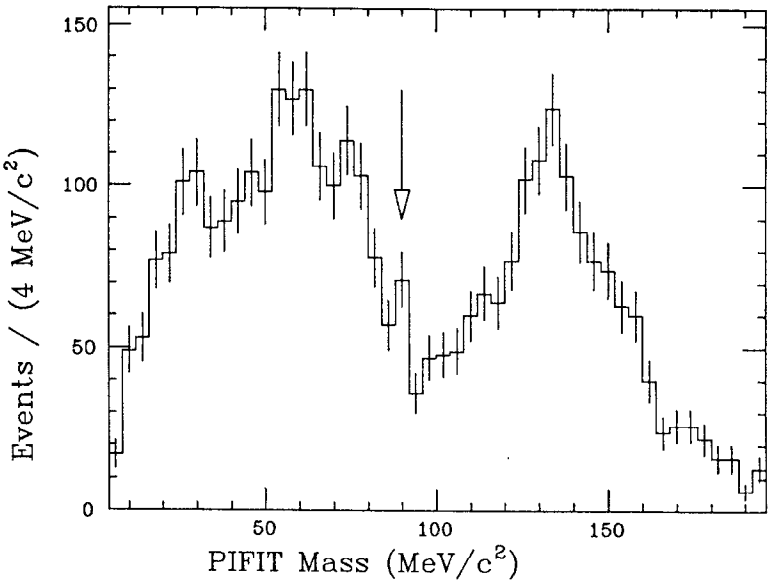

Fig. 3.8 Distribution of PIFIT masses for overlapping showers – J/ψ Data.

events in which the highest energy track is greater than 500 MeV and has not been flagged as a π^0.) We see the expected concentration of tracks in the upper left corner of the plot and display the boundary of a cut designed to identify these events. Figure 3.10 shows the effect of this cut on the J/ψ data. Any track which satisfies the criteria for a split-off is flagged as a bad track. The energy of the split-off is not added to the energy of the parent.

In the event shown in Figures 3.1 and 3.2, track 1 is flagged as a merged π^0 by step 2. In step 3, tracks 2 and 3 are identified as having come from the same π^0, so track 2 is flagged as a merged π^0 and track 3 is flagged a bad track. Track 4 is flagged a good γ.

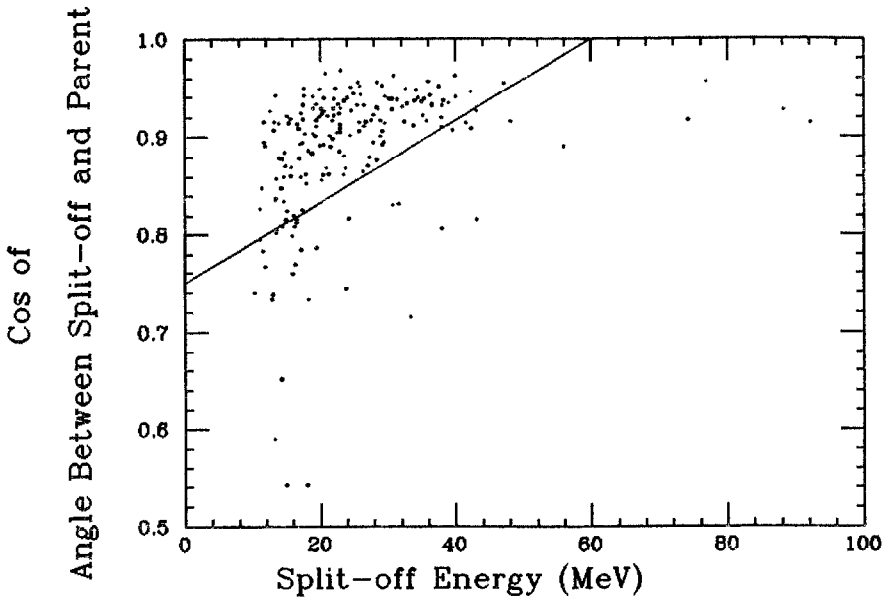

Fig. 3.9 Split-offs – single Monte Carlo γ's.

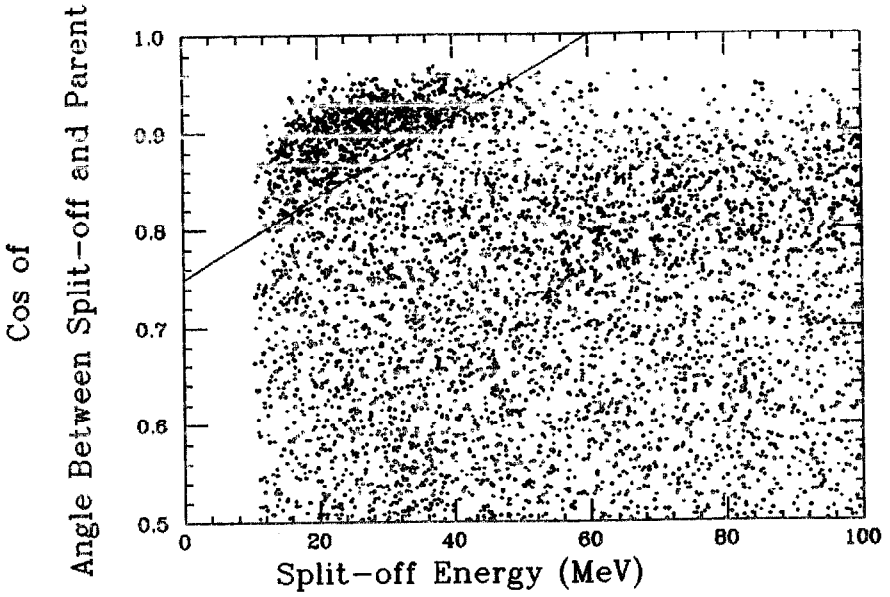

Fig. 3.10 Split-offs – J/ψ data.

3.3.4 *Final Cuts*

We make a final set of cuts to clean up the data samples and enhance the definition of the neutral tracks.

1. Events from individual bad runs are rejected. These runs have been flagged as bad by studies of parameters such as crystal occupancy.
2. Any event containing a track beyond $|\cos\theta| > 0.90$ is rejected, where θ is the angle the track makes with the beam axis. The cut eliminates events with tracks beyond the fiducial volume of the inner chambers.
3. Any event containing two tracks with an opening angle α such that $\cos\alpha > 0.90$ is rejected. This cut eliminates events in which the energy measurement of a shower is questionable due to the close proximity of another shower.

Table 3.4 shows the effects of these cuts on the three datasets.

Number of Events	ψ'	J/ψ	ψ''
Input	8218	9719	2837
After Bad Run Cut	7925	9538	2837
Solid Angle Cut	6516	8188	2378
Overlap Cut	6004	6868	2304

Table 3.4 Final cuts.

The directions of the neutral showers used in the last two cuts are obtained from ESORT. Subsequent stages of the analysis use directions determined by the more accurate shower fitting routines PIFIT (if the track has been flagged as a π^0) or GAMFIT (if the track has been flagged as a γ). (See Appendix C.)

References

1) Crystal Ball Offline Workshop, SLAC, August 29 - September 2, 1983.

2) M. Oreglia, Ph.D. thesis, Stanford University, 1980, and SLAC-Report 236 (unpublished).

Chapter 4

Charmonium Decays

4.1 Introduction

We discuss in this chapter the decays of charmonium states which are accessible to an all-photon analysis. We shall thus be primarily concerned with decays of the form $\psi' \rightarrow \gamma X, X \rightarrow \pi^0\pi^0, \eta\eta$, and $\gamma\gamma$. Note that by searching for only these decays we restrict the allowed quantum numbers of the states X that we can observe. For instance, a state of odd parity is forbidden to decay to $\pi^0\pi^0$ or $\eta\eta$ via a parity conserving (i.e., strong or electromagnetic) interaction. Also, a state with odd spin is forbidden to decay to $\pi^0\pi^0$ or $\eta\eta$ regardless of its parity, although in general it is allowed to decay to $\pi^+\pi^-$ (as demonstrated by the decay of the ρ^0).This is due to the fact that the wavefunction of two identical spinless mesons transforms like $(-1)^l$ (where l is the total angular momentum) under interchange of the two particles, whereas such a state must be even under interchange if the particles obey Bose statistics. Similarly, an argument involving conservation of parity and angular momentum can be made which shows that a spin-one particle cannot decay into two photons (Yang's theorem).[1] Thus, observation of the decay of a particle via one of these modes restricts its quantum numbers (typically 0^{++} or 2^{++}) whereas non-observation of these decays favors other assignments. Although an all-photon analysis restricts the decay channels we can observe, we shall see that in some cases

the channels which are accessible are exceptionally clean. In particular, the decay $\psi' \rightarrow \gamma\chi_0$, $\chi_0 \rightarrow \pi^0\pi^0$ is sufficiently free of background that we are able to use it to make a width measurement of the χ_0.

4.2 Theoretical Background

4.2.1 *Charmonium*

The discoveries of the J/ψ[3,4] and ψ'[5] were followed immediately by the interpretation[6] of these resonances as bound states of the charmed quark and charmed antiquark predicted several years earlier.[7] Collectively, such bound states were referred to as charmonium states (in analogy with positronium) with the J/ψ and ψ' corresponding to the 1S and 2S states. In addition to these states, it was predicted that there should be an entire family of particles corresponding not only to higher excited singlet S states but triplet S states and P and D states as well.[8] The lowest lying triplet P states, dubbed the χ_0, χ_1, and χ_2, were found shortly afterwards in radiative decays of the ψ',[9] and subsequent experiments have discovered other predicted states.[10] Figure 4.1 shows the current status of charmonium and indicates the reactions which are discussed in this chapter.

In addition to predicting the gross features of the particle spectrum, the charmonium model can be used to calculate the dynamics of the system by assuming that the binding of the quarks can be modeled by a nonrelativistic potential. Decay rates can then be calculated in a given theory by computing the annihilation amplitudes for a quark and antiquark bound by this potential. We study here the rates predicted by the candidate theory of strong interactions, QCD.

4.2.2 *Potential Models*

The analogy between positronium and charmonium extends beyond the similarity of their mass spectra. Just as the simplest atomic systems provide some of the most precise tests of QED, charmonium can be used to devise tests of QCD which

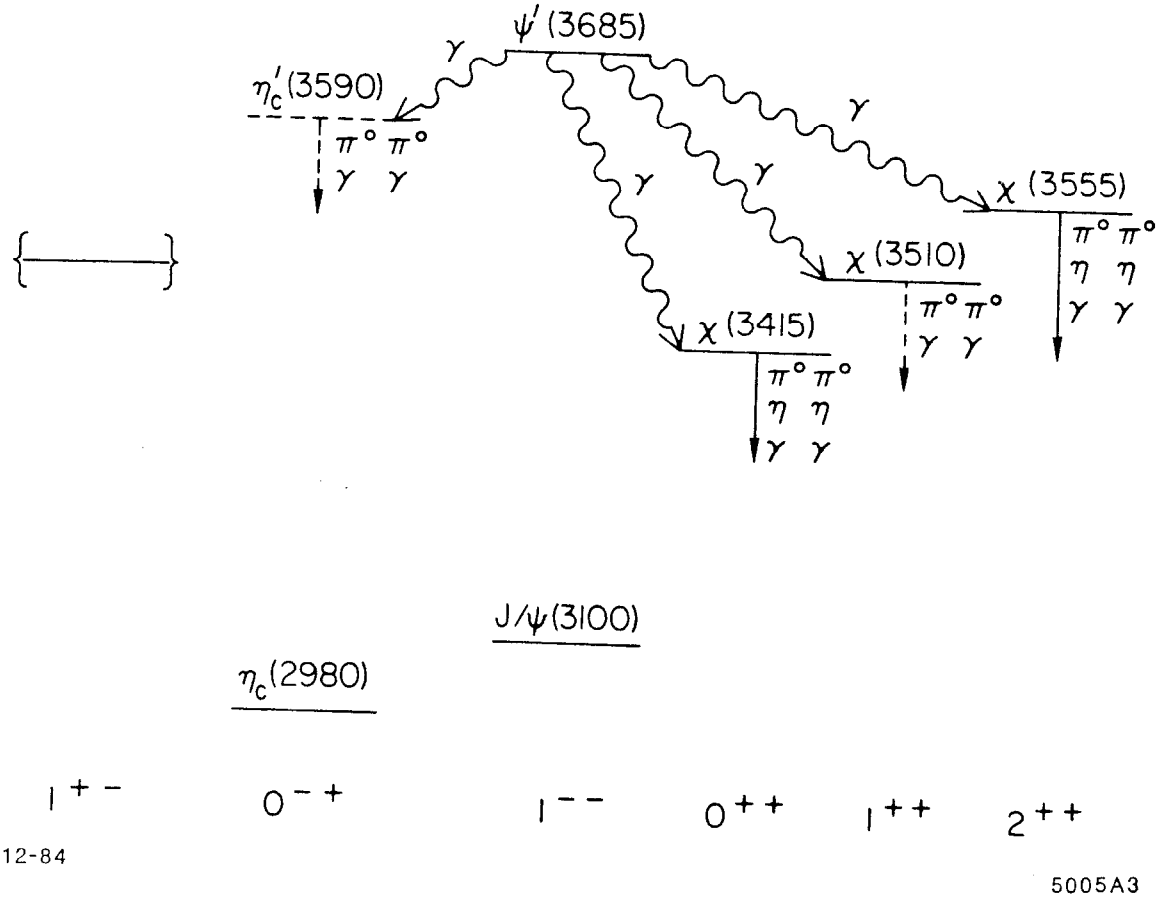

Fig. 4.1 Charmonium levels below open charm threshold. Solid lines show confirmed states; dotted line shows state in need of confirmation; bracketed line shows predicted but unobserved $^1P_1$ state. Solid and dotted arrows show branching ratios and upper limits, respectively, reported in this chapter.

are relatively free of complications. In the context of the charmonium model, we can calculate the decay rate of a state of charmonium to a final state of gluons. In the nonrelativistic reduction of the Bethe-Salpeter equation, the binding potential contributes a multiplicative factor which can be interpreted as the probability that the quark and antiquark meet to annihilate. As an example, we consider the decay of the J/ψ. We assume that gluons are spin-1 particles that transform as an SU(3) color octet and that any observable state must be a color singlet. An odd C-parity spin-1 particle such as the J/ψ is then forbidden to decay to two gluons.[2] Thus, the lowest order decay of the J/ψ is into three gluons which can be calculated from the diagram in Fig. 4.2 to be[11]

$$\Gamma(J/\psi \rightarrow ggg) = \frac{40}{81\pi}(\pi^2 - 9)\frac{\alpha_s^3}{M_{J/\psi}^2}|\psi(0)|^2 \qquad [4.1]$$

where α_s is the strong coupling constant of QCD. The annihilation probability (here the wave function at the origin squared) must be supplied by phenomenology and is typically obtained from the annihilation rate of the J/ψ to leptons,

$$\Gamma(J/\psi \rightarrow l^+l^-) = \frac{4\alpha^2(2/3)^2}{M_{J/\psi}^2}|\psi(0)|^2 \qquad [4.2]$$

where α is the coupling constant of QED. Alternately, these expressions can be combined with measurements of the full and leptonic widths of the J/ψ and solved for α_s:

$$\alpha_s \approx 0.19^{[11]} \qquad [4.3]$$

The calculation of the decay rates of the χ states is similar. However, the wave function vanishes at the origin for a P state, so the first nonzero contribution involves the derivative of the wave function at the origin. Unlike the J/ψ, the two gluon decays of the χ_0 and χ_2 are not forbidden. The lowest order diagram is shown in

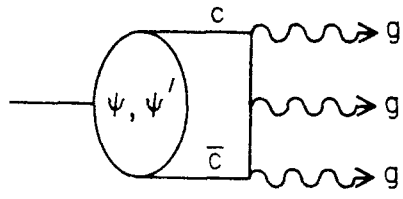

Fig. 4.2 Feynman diagram of the annihilation of the J/ψ or ψ' into three gluons.

Fig. 4.3, and the two gluon widths are[12]

$$\Gamma(\chi_0 \to gg) = \frac{96\alpha_s^2}{M^4}|\psi'(0)|^2$$
$$\Gamma(\chi_2 \to gg) = \frac{128\alpha_s^2}{5M^4}|\psi'(0)|^2 \qquad [4.4]$$

These rates again involve a wavefunction factor which must be supplied from phenomenology. We can take the ratio of these two rates so that the dependence on the wave function cancels:[12]

$$\frac{\Gamma(\chi_0 \to gg)}{\Gamma(\chi_2 \to gg)} = \frac{15}{4} \qquad [4.5]$$

Up to this point we have considered only first-order annihilation diagrams. Higher order contributions should also be included, and these have been calculated to the next order in α_s. Unlike the lowest order calculations, these rates depend on the particular renormalization scheme in which the calculation is performed. However, to order α_s these renormalization dependent terms cancel when taking the ratio of the χ_0 and χ_2 widths[13,14]

$$\frac{\Gamma(\chi_0 \to gg)}{\Gamma(\chi_2 \to gg)} = \frac{15}{4}(1 + 12\alpha_s/\pi) \qquad [4.6]$$

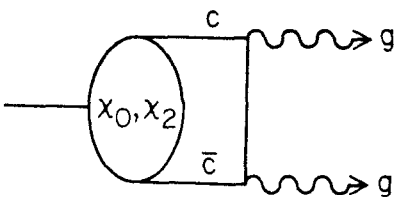

Fig. 4.3 Feynman diagram of the annihilation of the χ_0 or χ_2 into two gluons.

independent of both renormalization scheme and potential. Using a value of α_s = 0.19, the second term gives a correction of 73%, which, as noted by the authors of reference 13, is sufficiently large to cast some doubt on the validity of the perturbation expansion.

We can carry the analogy to positronium a step further and calculate the decay rate of charmonium to two photons. The first-order diagrams are identical to the two gluon decay diagrams above with the gluons replaced by photons (Fig. 4.4). The evaluation of these diagrams also proceeds in a parallel fashion except for the replacement of factors of α_s with α and the absence of color factors. We obtain

$$\begin{aligned} \Gamma(\chi_0 \to \gamma\gamma) &= \frac{9}{2} Q^4 \alpha^2 \frac{96}{M^4} |\psi'(0)|^2 \\ \Gamma(\chi_2 \to \gamma\gamma) &= \frac{9}{2} Q^4 \alpha^2 \frac{128}{5M^4} |\psi'(0)|^2 \end{aligned} \qquad [4.7]$$

where Q is the charge of the quark (2/3 for the charmed quark). Since the potential enters the expressions for both the two gluon and two photon widths as a multiplicative factor, we may take the ratio and obtain a potential-independent prediction of the ratio

$$R(2\gamma/2g)_{\chi_{0,2}} \equiv \frac{\Gamma(\chi_{0,2} \to \gamma\gamma)}{\Gamma(\chi_{0,2} \to gg)} = \frac{9}{2} Q^4 \left(\frac{\alpha}{\alpha_s}\right)^2 \qquad [4.8]$$

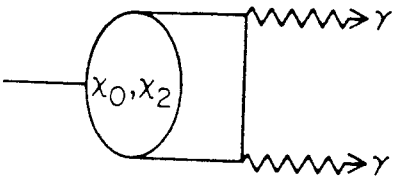

Fig. 4.4 Feynman diagram of the annihilation of the χ_0 or χ_2 into two photons.

for both the χ_0 and χ_2. Note that $R(2\gamma/2g)$ is not the same as the two photon branching ratio. In order to obtain the predicted branching ratios for the two photon decays of the $\chi_{0,2}$, we must add to the two gluon widths the widths for other decays such as $\chi_2 \rightarrow \gamma J/\psi$. As in the two gluon case, the two photon decay widths have been calculated to the next order in α_s,* and we can obtain a renormalization independent prediction by taking the ratio of the ratios:[12,13]

$$\frac{R(2\gamma/2g)_{\chi 2}}{R(2\gamma/2g)_{\chi 0}} = 1 + 1.65\frac{\alpha_s}{\pi} \qquad [4.9]$$

The two photon widths of the η_c and η_c' are derived in a similar fashion, but Equation [4.7] is replaced by an expression involving the wave function at the origin:

$$\Gamma(\eta_c, \eta_c' \rightarrow \gamma\gamma) = \frac{12Q^4\alpha^2|\psi_{1,2}(0)|^2}{M_{1,2}^2} \qquad [4.10]$$

where the subscripts 1 and 2 refer to the 1S and 2S wavefunctions and masses, respectively. The ratios of the two photon widths to the two gluon widths are

* Even though we are calculating the rate for a QED process, there are QCD corrections to the initial state.

identical to that of the P states:

$$\mathrm{BR}(\eta_c, \eta_c' \to \gamma\gamma) = \frac{\Gamma(\eta_c, \eta_c' \to \gamma\gamma)}{\Gamma(\eta_c, \eta_c' \to gg)} = \frac{9}{2} Q^4 \left(\frac{\alpha}{\alpha_s}\right)^2 . \qquad [4.11]$$

4.2.3 *QCD Sum Rules*

Alternatively, one can estimate these decay rates using QCD sum rules.[15] Essentially, this technique uses asymptotic freedom to equate an integral over s (where $s \equiv {E_{CM}}^2$) of the imaginary part of a vacuum polarization graph to the same integral of R, where $R \equiv \sigma(e^+e^- \to \text{hadrons})/\sigma(e^+e^- \to \mu^+\mu^-)$. The former integral is calculable, and it is found that in many cases the contribution of a single resonance is a sufficient approximation to the latter. As a specific example, the two photon width of the χ_2 can be calculated by evaluating the integral of the graph shown in Fig. 4.5 where the current J is assumed to have a tensor character.

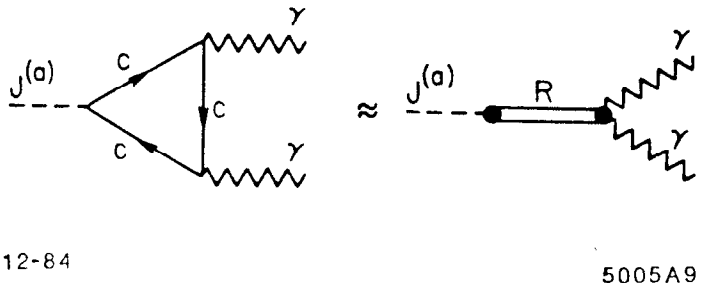

Fig. 4.5 Feynman diagrams of the annihilation of the χ_2 into two photons using QCD sum rules.

Numerical predictions of these theories will be given in the summary of this chapter where they are compared with the data. We turn now to brief descriptions of the data analyses used to search for all-photon charmonium decays.

4.3 $\chi_{0,2} \rightarrow \pi^0\pi^0$

We begin with the decay $\psi' \rightarrow \gamma\pi^0\pi^0$ and look for high invariant mass combinations of the $\pi^0\pi^0$ system. We do not need to use a kinematic fit to constrain the four-vectors to energy and momentum conservation, since in these decays the observed mass of the $\pi^0\pi^0$ system is determined almost completely by the energy of the low energy γ. Also, we do not want to use any cut which would bias the energy distribution of the low energy photon since the detector line shape has been determined from an independent channel (see Appendix A), and we will use this function to separate the natural width of a photon transition from the detector resolution. Monte Carlo studies show that the $\chi_{0,2} \rightarrow \pi^0\pi^0$ decays almost always yield three or four observed tracks, so we study only these cases. Table 4.1 shows the cuts used in this analysis and their effect on the ψ' and ψ'' datasets and the $\psi' \rightarrow \gamma\chi_0$, $\chi_0 \rightarrow \pi^0\pi^0$ and $\psi' \rightarrow \gamma\chi_0$, $\chi_0 \rightarrow \gamma\gamma$ Monte Carlos. The two major entries show the number of events which pass the cuts described in Chapter 3 with three and four tracks, respectively. The entries for the data show the number of events surviving each cut; the entries for the Monte Carlo show the fraction of the simulated events which survive.

4.3.1 *Three observed tracks*

We start with a preliminary look at the spectrum of the lowest energy track in all three-track events before any cuts (other than those outlined in Chapter 3) have been applied. Figures 4.6, 4.7, and 4.8 show this plot for the ψ' data, the ψ'' data, and a Monte Carlo of the process $e^+e^- \rightarrow (\gamma)\gamma\gamma$ [16] with $E_{CM} = M_{\psi'}$ and a luminosity roughly twice that taken at the ψ'. (Note that the natural log of the energy is plotted. Given the $E^{3/4}$ dependence of the energy resolution, such a scale keeps the plotted width of a monochromatic photon roughly constant independent of its energy.) The arrows in the first plot show the expected positions of the radiative photons in the transitions $\psi' \rightarrow \gamma\chi_{0,1,2}$ as calculated from the masses of the participant particles quoted by the Particle Data Group.[17] The existence of

Cut	ψ'	ψ''	$\psi' \to \gamma\chi_0$, $\chi_0 \to \pi^0\pi^0$ M.C.	$\psi' \to \gamma\chi_0$, $\chi_0 \to \gamma\gamma$ M.C.
3 Tracks	3159	1392	47%	56%
3rd Track PIFIT Cut	3136	1392	47	56
3rd Track not Eq. or Tun.	2344	998	36	45
$\lvert\cos\theta_3\rvert < 0.85$	2306	980	36	44
E_{CM} Cut	2044	859	34	42
Track 1 & 2 PIFIT Cut	222	4	29	0.2
Overlap Cut	213	3	28	0.2
4 Tracks	244	48	5.0%	1.2%
One Merged π^0	107	9	3.5	0.1
≥ 1 Open π^0	85	3	3.4	0.1
γ not Eq. or Tun.	69	2	2.8	0.1
$\lvert\cos\theta_3\rvert < 0.85$ Cut	68	2	2.7	0.1

Table 4.1 Cuts for $\psi' \to \gamma\pi^0\pi^0$ analysis.

transitions to the χ_0 and χ_2 states is obvious, although we have not yet clarified the nature of the decay products of the χ states. We can also inquire as to the source of the background. Note that it is flat when plotted on a log scale, indicating that it has the shape of $dN/dk \approx 1/k$. This is characteristic of a bremsstrahlung spectrum,

and we are led to suspect that the background is due to the process $e^+e^- \rightarrow (\gamma)\gamma\gamma$. This suspicion is given some measure of confirmation by Fig. 4.8 which indicates that the spectrum from $e^+e^- \rightarrow (\gamma)\gamma\gamma$ agrees in shape with the background seen on the ψ' with the exception of the excess of events in the ψ' and ψ'' plots below 50 MeV. These events are due to the process $e^+e^- \rightarrow (\gamma)\gamma\gamma$ + split-off in which the split-off was not flagged as a bad track by the algorithm described in Chapter 3.† This is demonstrated by Fig. 4.9 which shows the spectrum of the lowest energy track from three-track events from a Monte Carlo of the process $e^+e^- \rightarrow \gamma\gamma$ with an equivalent luminosity $\approx 17\%$ that of the ψ' dataset. It is clear that we will not be able to extract any signal on top of such a large background. For convenience, the energy spectra which follow begin at 50 MeV.

In order to analyze these events further, we select events in which the lowest energy track is a well-defined photon. First, we reject those events in which the lowest energy track has a PIFIT mass which is inconsistent with a photon. We also reject those events in which the lowest energy track is expected to have a poor energy resolution, i.e., events in which the bump module corresponding to the lowest energy track is an equator or tunnel module. Since we use no kinematic fit in this analysis, we require $|E_{vis} - E_{CM}| < 300$ MeV in order to reject backgrounds. The effect of these cuts on the $\psi'$and ψ'' data and the $\psi' \rightarrow \gamma\chi_0$, $\chi_0 \rightarrow \pi^0\pi^0$ and $\chi_0 \rightarrow \gamma\gamma$ Monte Carlos is shown in Table 4.1.

We next investigate the two high energy tracks. Any all-photon three-track event which is the result of a strong or electromagnetic decay of the ψ' must consist of $\gamma\gamma\gamma$ or $\gamma\pi^0\pi^0$ in order to conserve C-parity. Figure 4.10 shows a plot of the PIFIT mass of the highest energy track *vs.* the PIFIT mass of the second highest energy track for the ψ' data; Fig. 4.11 shows the same plot for the ψ'' data. We observe a cluster of events at low PIFIT masses in both plots and an additional cluster

† The border between the events we classify as $e^+e^- \rightarrow \gamma\gamma$ and $e^+e^- \rightarrow (\gamma)\gamma\gamma$ is arbitrary. We assign any event in which the radiative photon has less than 10 MeV to $e^+e^- \rightarrow \gamma\gamma$.

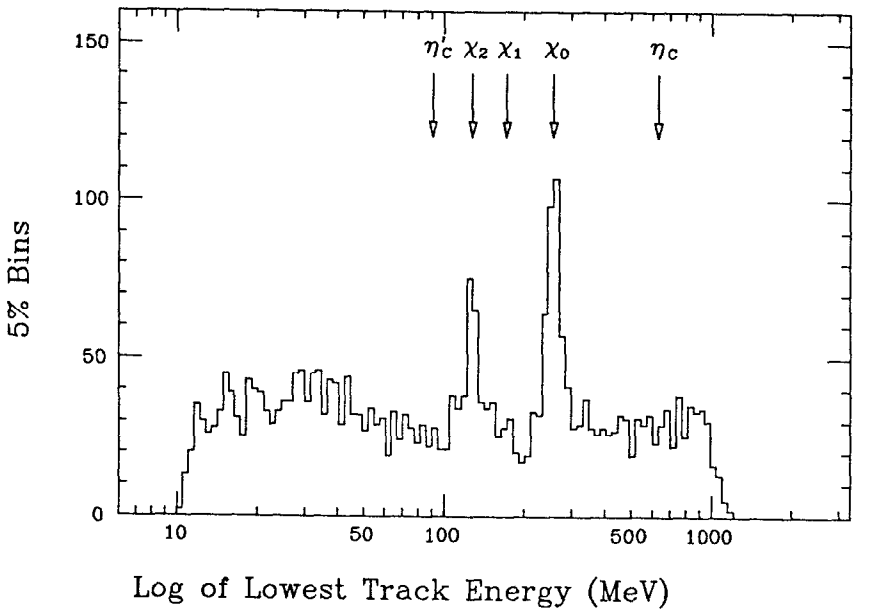

Fig. 4.6 Energy of lowest energy track: neutral three track events in ψ' data.

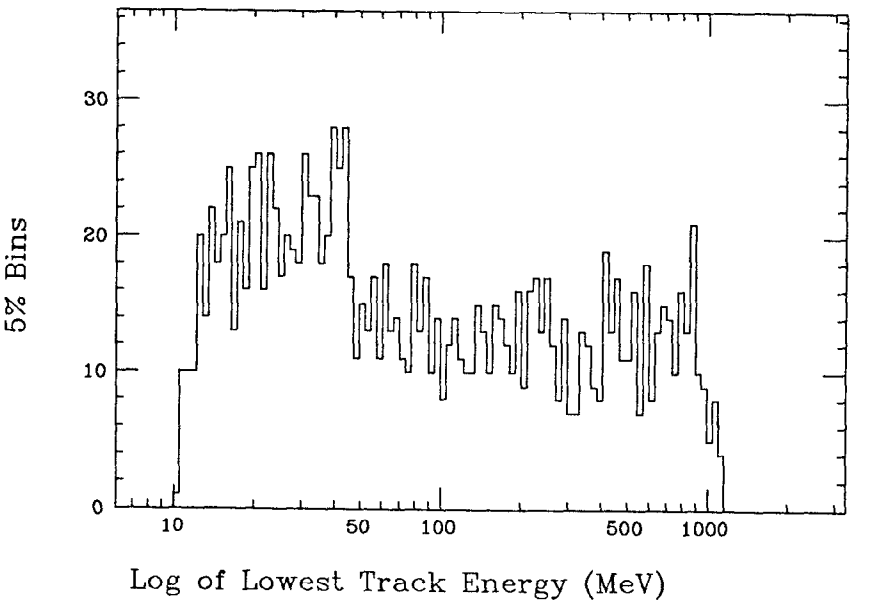

Fig. 4.7 Energy of lowest energy track: neutral three track events in ψ'' data.

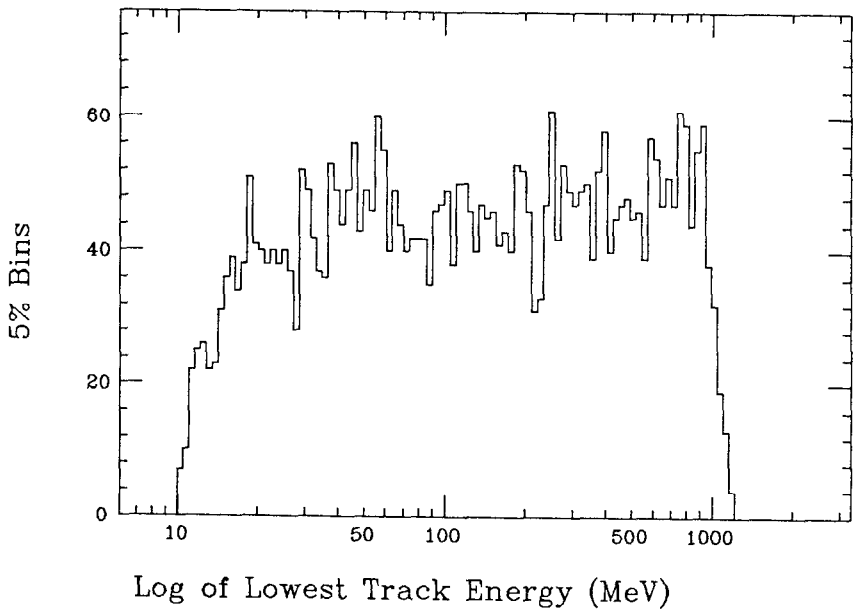

Fig. 4.8 Energy of lowest energy track: neutral three track events from $e^+e^- \rightarrow (\gamma)\gamma\gamma$ Monte Carlo.

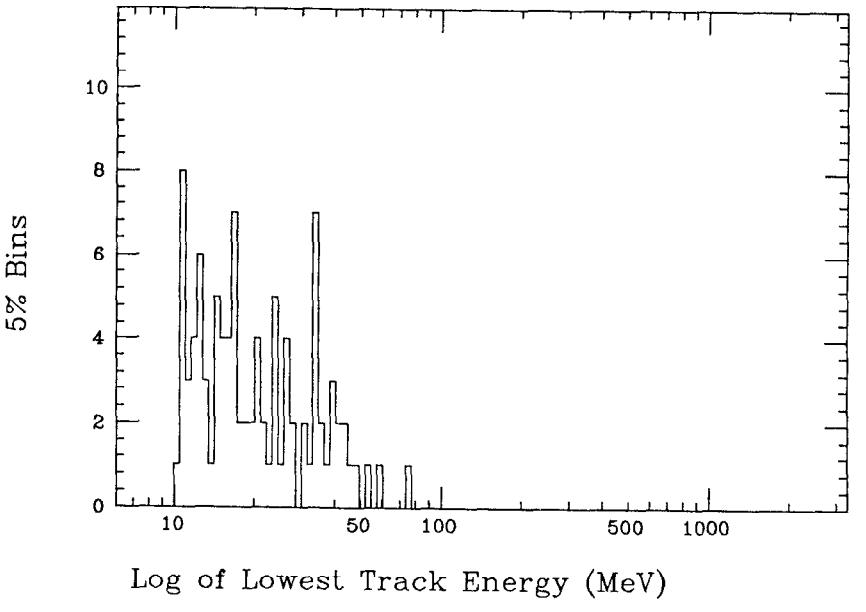

Fig. 4.9 Energy of lowest energy track: neutral three track events from $e^+e^- \rightarrow \gamma\gamma$ Monte Carlo.

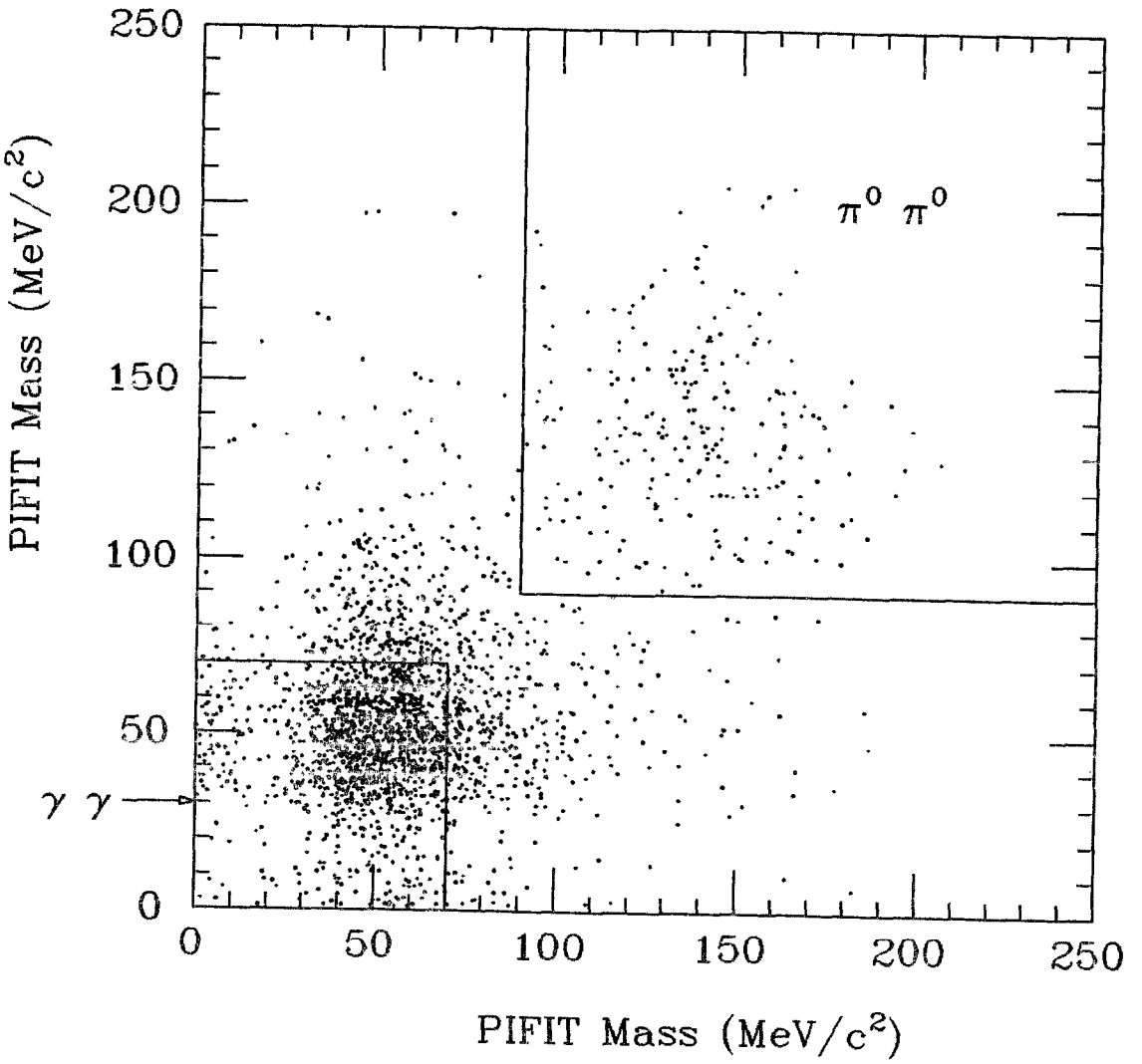

Fig. 4.10 PIFIT mass of highest energy track *vs.* PIFIT mass of second highest energy track - ψ' data.

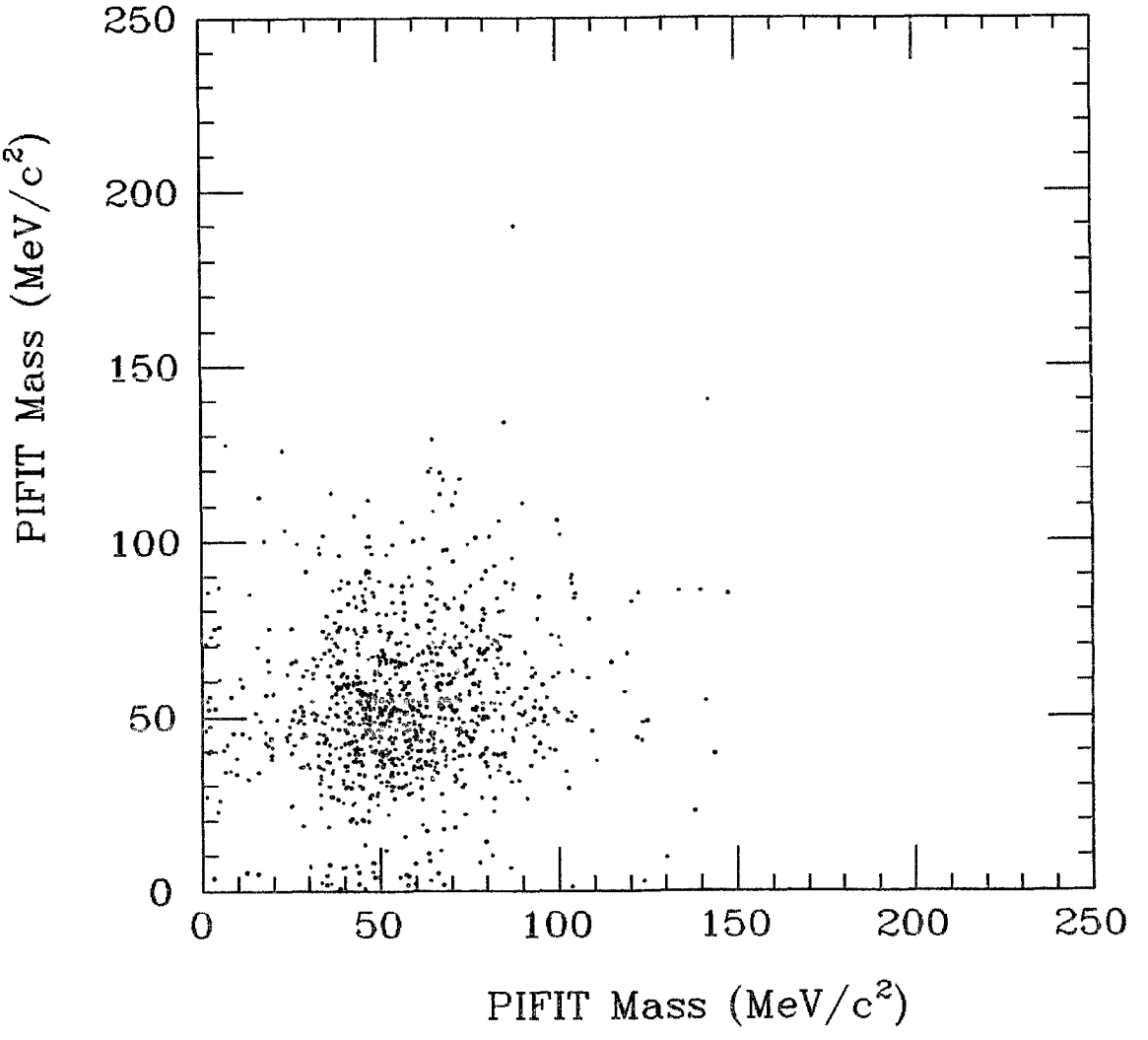

Fig. 4.11 PIFIT mass of highest energy track *vs.* PIFIT mass of second highest energy track: ψ'' data.

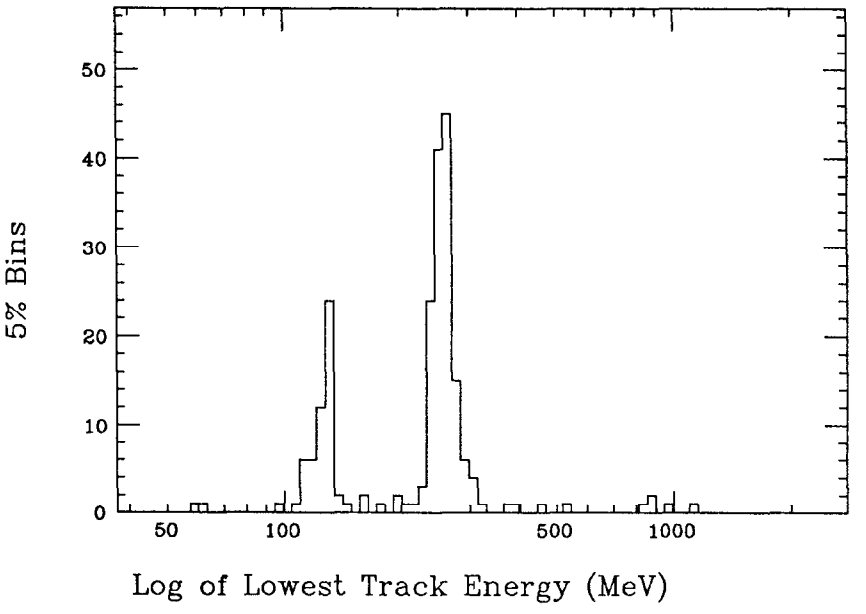

Fig. 4.12 Energy of γ in $\psi' \rightarrow \gamma\pi^0\pi^0$: three track events.

at high PIFIT masses in the ψ' plot; we take these two clusters to correspond to the two final states $\gamma\gamma\gamma$ and $\gamma\pi^0\pi^0$ where the former is due primarily to the QED process $e^+e^- \rightarrow (\gamma)\gamma\gamma$. We place a cut on the PIFIT masses to select the $\gamma\pi^0\pi^0$ candidates as shown by the box in the upper right in Fig. 4.10. We finally place an overlap cut requiring the cosine of the opening angle between any two tracks be no greater than 0.85. Figure 4.12 shows the final spectrum of the radiative photon in $\gamma\pi^0\pi^0$ after these cuts. The photon lines corresponding to the decays $\psi' \rightarrow \gamma\chi_{0,2}$, $\chi_{0,2} \rightarrow \pi^0\pi^0$ are now seen on top of essentially no background.

4.3.2 *Four Observed Tracks*

In this topology we search for those events which contain a radiative photon, a merged π^0, and a separated π^0. From the set of all four-track events, we select those which contain one and only one merged π^0 candidate (as determined by its PIFIT mass). We next calculate the invariant masses of the three pairs which can

be formed from the remaining tracks and accept only those events with at least one invariant mass combination in the π^0 mass window shown in Fig. 4.13. (If more than one pair of tracks forms an invariant mass between these limits we use that pair with an invariant mass closest to the π^0 mass. This occurs in 20% of the events.) We require that the remaining track point to a crystal which is not an equator or tunnel module and that it lie within $|\cos\theta| < 0.85$, where θ is the angle the track makes with the beam direction. The energy spectrum of this track is shown in Fig. 4.14. This spectrum is added to Fig. 4.12 to obtain the final $\psi' \rightarrow \gamma\pi^0\pi^0$ spectrum, yielding Fig. 4.15. In the next section we will describe fits to the two peaks at low photon energies corresponding to decays of the χ_0 and χ_2. The cluster of events at high photon energies corresponds to radiative decays to states at ≈ 1200 MeV/c^2 and will be discussed in the following chapter.

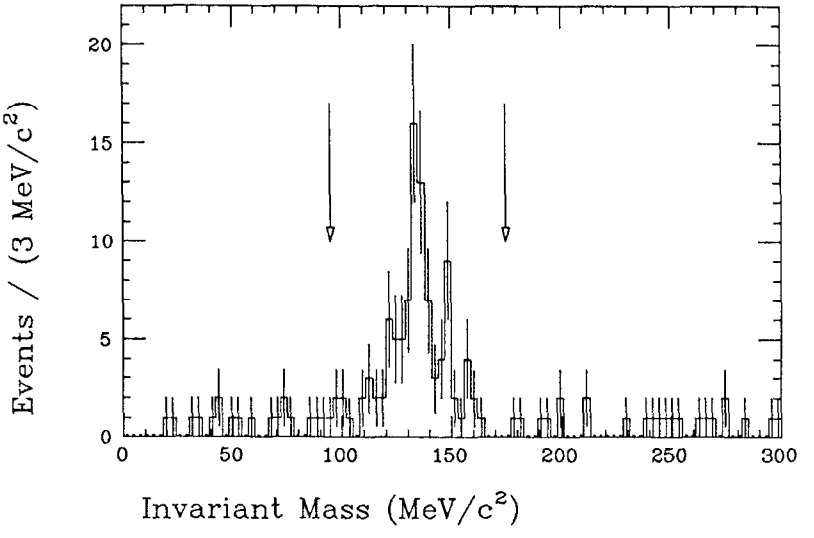

Fig. 4.13 Invariant masses of γ pairs: four track events (ψ' data).

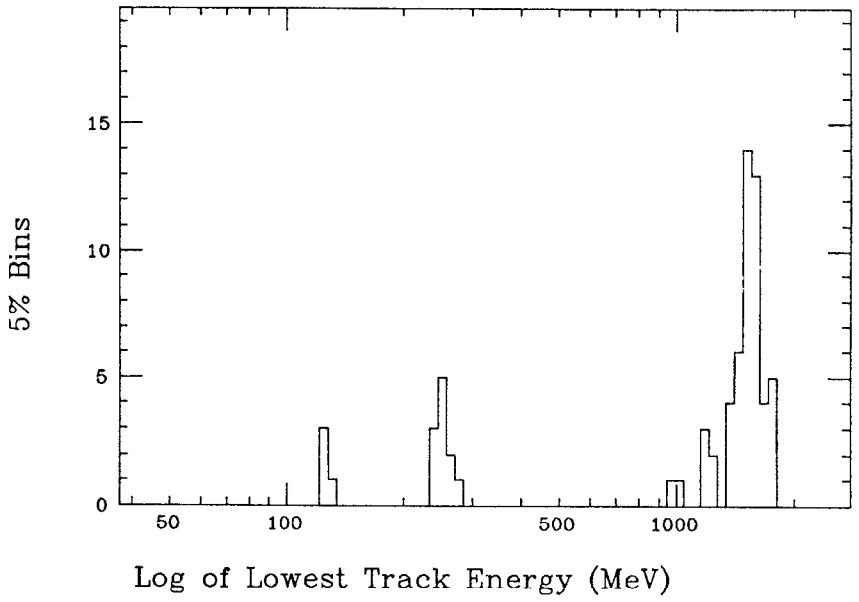

Fig. 4.14 Energy of radiative γ in $\psi' \to \gamma\pi^0\pi^0$: four track events.

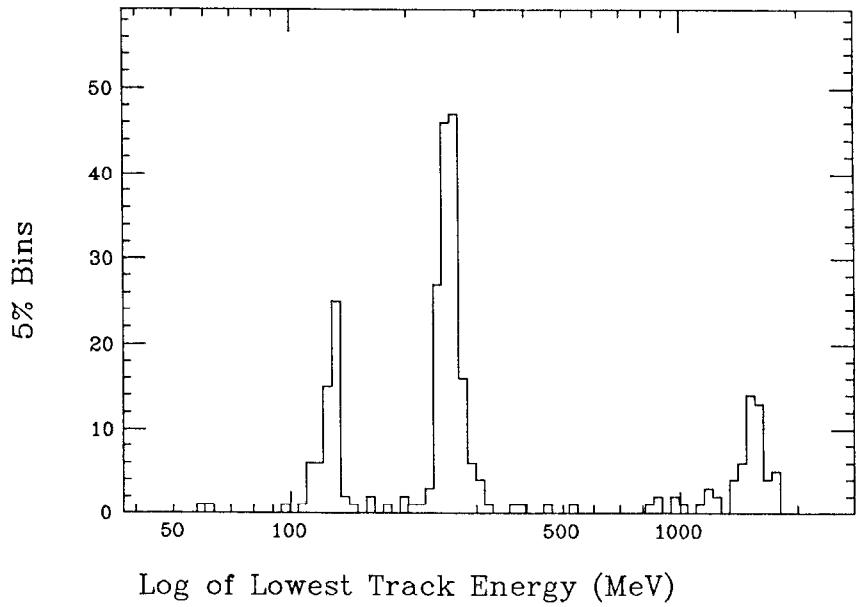

Fig. 4.15 Energy of radiative γ in $\psi' \to \gamma\pi^0\pi^0$: three and four track events.

4.3.3 χ_0 *Width and* $\chi_{0,2} \to \pi^0\pi^0$ *Branching Ratios*

The χ_0 peak in Fig. 4.15 has a width that is significantly larger than that expected from detector resolution which is presumably due to the natural line width of the χ_0 state. We can attempt to measure this width by unfolding the detector response function from the observed signal. This requires an accurate knowledge of the detector response function. The widths of all the particles in $\psi' \to \eta J/\psi, \eta \to \gamma\gamma, J/\psi \to l^+l^-$‡ are sufficiently small that the observed width of the energy distribution of the η is due solely to detector resolution. Additionally, the γ's in this reaction are uniformly distributed in energy between 193 and 390 MeV. The center of this Doppler box is (coincidentally) close to the energy of the transition photon in $\psi' \to \gamma\chi_0$ ($\approx$ 260 MeV). Thus, we can use this reaction to measure accurately the detector response function for photons in this energy range (as described in Appendix A). We find that the data are well fit by a Gaussian with a low energy tail where the width of the Gaussian has a slow energy dependence ($E^{3/4}$). We fit the observed χ_0 spectrum to a convolution of this function with a nonrelativistic Breit-Wigner function of variable mean, width, and amplitude. Assuming that the reaction $\psi' \to \gamma\chi_0$ is predominantly an E1 transition, we include a multiplicative factor of E_γ^3 to account for the variation of the dipole transition rate. Figure 4.16 shows the best fit to this function. We obtain

$$\Gamma_{\chi_0} = 8.8 \pm 1.3 \pm 1.5 \text{ MeV}/c^2$$

where the first error is statistical and the second systematic. The systematic error is due primarily to the variation in the width observed when the response function parameters are varied.

Additionally, the masses of all the particles in the reaction $\psi' \to \eta J/\psi, \eta \to \gamma\gamma, J/\psi \to l^+l^-$ are known with sufficient accuracy that the energy of the η in

‡ $l = e$ or μ.

this reaction can be calculated to ±0.15 MeV. As discussed in Appendix A, we can compare the observed energy of the η to the calculated value to determine the value of the offset of the energy scale which is found to be -3.3 ±0.6 MeV. Adding this offset to the observed mean of the Breit-Wigner, we measure the mass of the χ_0 to be

$$M_{\chi_0} = 3415.5 \pm 1.3 \pm 0.6 \ \ \mathrm{MeV}/c^2$$

The amplitude of the Breit-Wigner is found to be 148 ±13 events.

We can attempt to fit the χ_2 line with the same response function parameters, although this requires the extrapolation of these parameters from the region of their measurement (193 to 390 MeV) to the energy of the χ_2 line ($\approx$ 127 MeV). Also, the full width (Γ) of the χ_2 line has been measured in other experiments to be in the range 2-4 MeV/c^2.[18,19,20] Given the lower statistics of this peak, this width cannot be unfolded from the width of the response function at this energy ($\sigma \approx 5$ MeV). Studies of fits with the Breit-Wigner width set to a range of values show that the results are independent of this parameter within the range 0-4 MeV/c^2. Figure 4.17 shows the result of a fit with $\Gamma = 3$ MeV/c^2. From this fit we find the number of events in the peak to be 54 ±8.

In order to extract branching ratios we need to divide by an efficiency which in turn depends on an angular distribution. We need three angles to completely specify the angular distribution of the $\gamma\pi^0\pi^0$ system. We take them to be

θ_1 : The angle between the photon and the e^+ beam direction in the frame of the Ball

θ_2, ϕ_2 : The polar and azimuthal angles of the $\pi^0\pi^0$ axis in the rest frame of the $\pi^0\pi^0$ system (in the present case, the rest frame of the χ). The z axis coincides with the χ direction, and the x axis is defined such that the e^+ axis has $\phi = 0$.

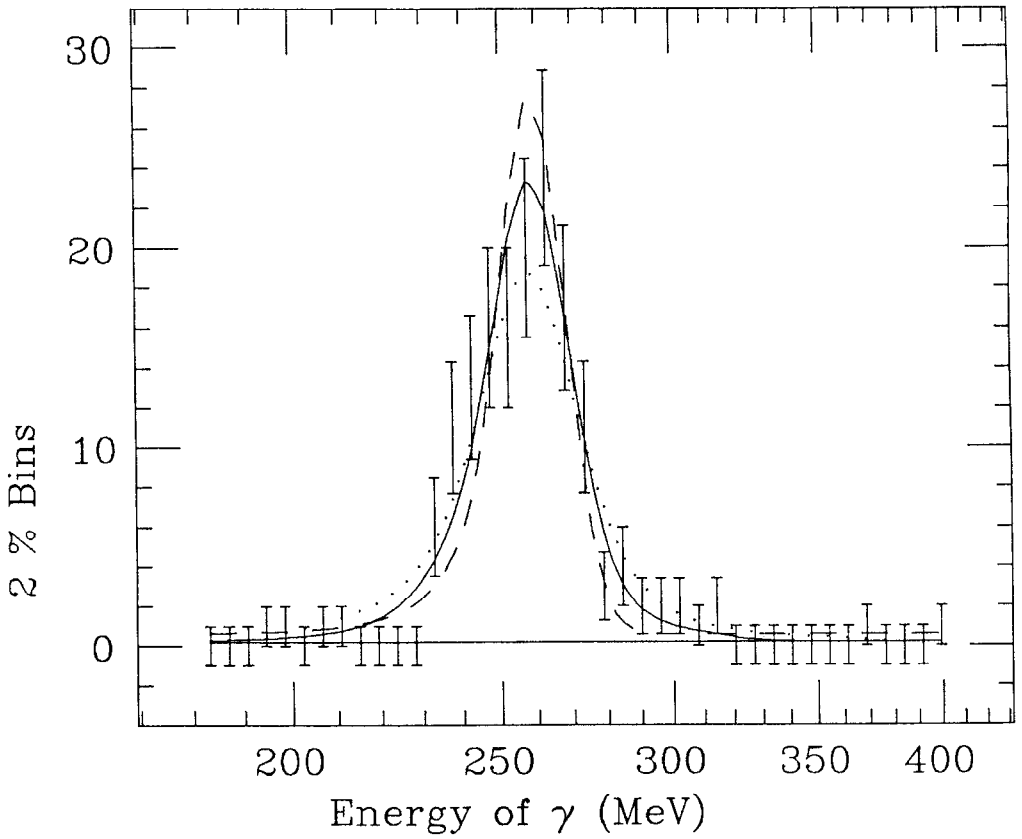

Fig. 4.16 Fit to γ spectrum in $\psi' \rightarrow \gamma\chi_0$, $\chi_0 \rightarrow \pi^0\pi^0$. Dashed line: $\Gamma = 0$ MeV/c^2. Dotted line: $\Gamma = 17$ MeV/c^2. Solid line: Best fit. Best fitted values: $E_0 = 257.3 \pm 1.3$ MeV/c^2, $\Gamma = 8.8 \pm 1.3$ MeV/c^2, Amp = 148 $\pm$13 Events.

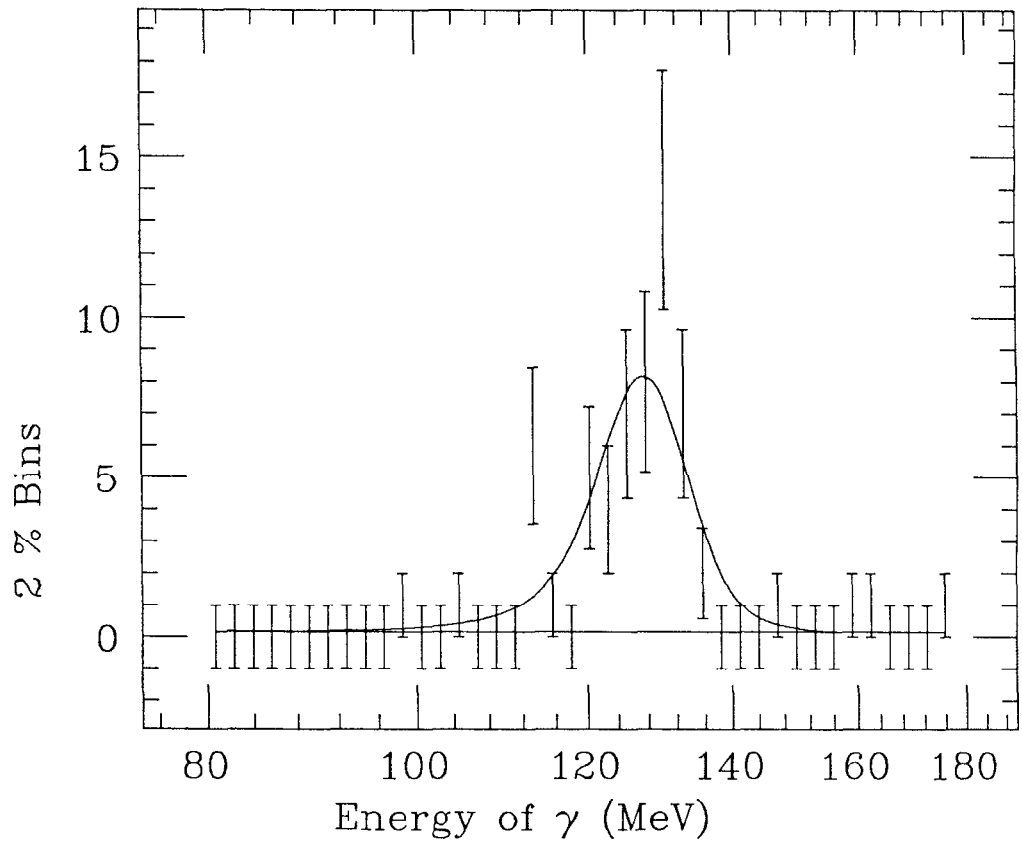

Fig. 4.17 Fit to γ spectrum in $\psi' \to \gamma\chi_2$, $\chi_2 \to \pi^0\pi^0$. Γ fixed at 3 MeV/c^2. Solid line: Best fit. Best fitted value: Amp = 54 $\pm$8 events.

The spin of the χ_0 is favored to be zero[21] and in this case the angular distribution is given simply by

$$\frac{d^3N}{d\cos\theta_1 d\cos\theta_2 d\phi_2} = 1 + \cos^2\theta_1 \qquad [4.12]$$

Studies of the process $\psi' \to \gamma\chi_2, \chi_2 \to \gamma J/\psi$[19] have measured the spin of the χ_2 to be two, and the angular distribution of its decay products is given by the somewhat more complicated formula[22]

$$\begin{aligned}\frac{d^3N}{d\cos\theta_1 d\cos\theta_2 d\phi_2} &= 3x^2\sin^2\theta_1\sin^2\theta_2 \\ &+ (1+\cos^2\theta_1)\left[(3\cos^2\theta_2 - 1)^2 + \frac{3}{2}y^2\sin^4\theta_2\right] \\ &+ \sqrt{3}x\sin 2\theta_1 \sin 2\theta_2 \left[3\cos^2\theta_2 - 1 - \frac{1}{2}\sqrt{6}y\sin^2\theta_2\right]\cos\phi_2 \\ &+ \sqrt{6}y\sin^2\theta_1\sin^2\theta_2(3\cos^2\theta_2 - 1)\cos 2\phi_2.\end{aligned} \qquad [4.13]$$

Due to the higher spin of the χ_2, this distribution depends on two unknown helicity amplitudes denoted by x and y. Previous studies[19] indicate that the transition $\psi' \to \gamma\chi_2$ is purely dipole, and we set x and y to values corresponding to a pure dipole transition ($\sqrt{3}$ and $\sqrt{6}$, respectively).

Using these angular distributions, we generate Monte Carlos to determine the detection efficiency. We obtain efficiencies of 30% and 37% for the decays $\psi' \to \gamma\chi_{0,2}$, $\chi_{0,2} \to \pi^0\pi^0$, respectively, and so obtain

$$\begin{aligned}\mathrm{BR}(\psi' \to \gamma\chi_0, \chi_0 \to \pi^0\pi^0) &= (2.9 \pm 0.3 \pm 0.5) \times 10^{-4} \\ \mathrm{BR}(\psi' \to \gamma\chi_2, \chi_2 \to \pi^0\pi^0) &= (8.8 \pm 1.3 \pm 1.6) \times 10^{-5}\end{aligned} \qquad [4.14]$$

where the first errors are statistical and the second are systematic. We can use the Particle Data Group averages[17] from inclusive measurements of the branching ratios of the decays $\psi' \to \gamma\chi_0$ and $\psi' \to \gamma\chi_2$ (= 8.2 ±1.4% and 7.4 ±1.3%, respectively) to deduce

$$\begin{aligned}\mathrm{BR}(\chi_0 \to \pi^0\pi^0) &= (3.5 \pm 0.3 \pm 1.2) \times 10^{-3} \\ \mathrm{BR}(\chi_2 \to \pi^0\pi^0) &= (1.2 \pm 0.2 \pm 0.4) \times 10^{-3}\end{aligned} \qquad [4.15]$$

where we have included the uncertainties in the ψ' radiative branching ratios in the systematic errors. These measurements will be compared to other experiments and theory in the summary at the end of this chapter.

We can in addition search for photon lines corresponding to the decays $\psi' \rightarrow \gamma X, X \rightarrow \pi^0\pi^0$, where X= η_c', χ_1, or η_c. We set 90% upper confidence limits of 3.1, 4.8, and 2.4 events, respectively, for these decays. We cannot use the accepted quantum number assignments for the intermediate states to calculate angular distributions since they are forbidden to decay to two π^0's. We instead estimate the efficiency using a Monte Carlo with flat distributions in $\cos\theta_1, \phi_2$, and $\cos\theta_2$. We obtain $\epsilon(\psi' \rightarrow \gamma(\eta_c', \chi_1, \eta_c), (\eta_c', \chi_1, \eta_c) \rightarrow \pi^0\pi^0) = 27\%$, 33% , and 36%, respectively, and deduce

$$\begin{aligned} \mathrm{BR}(\psi' \rightarrow \gamma\eta_c', \eta_c' \rightarrow \pi^0\pi^0) &< 8 \times 10^{-6} \\ \mathrm{BR}(\psi' \rightarrow \gamma\chi_1, \chi_1 \rightarrow \pi^0\pi^0) &< 1 \times 10^{-5} \\ \mathrm{BR}(\psi' \rightarrow \gamma\eta_c, \eta_c \rightarrow \pi^0\pi^0) &< 5 \times 10^{-6} \end{aligned} \qquad [4.16]$$

Again, using inclusive measurements of $\mathrm{BR}(\psi' \rightarrow \gamma\eta_c')$, $\mathrm{BR}(\psi' \rightarrow \gamma\chi_1)$, and $\mathrm{BR}(\psi' \rightarrow \gamma\eta_c)$, = 0.5 - 1.2 % , 8 $\pm$1.3 % , and 0.28 $\pm$0.06 % , respectively, we conclude

$$\begin{aligned} \mathrm{BR}(\eta_c' \rightarrow \pi^0\pi^0) &< 2 \times 10^{-3} \\ \mathrm{BR}(\chi_1 \rightarrow \pi^0\pi^0) &< 2 \times 10^{-4} \\ \mathrm{BR}(\eta_c \rightarrow \pi^0\pi^0) &< 2 \times 10^{-3} \end{aligned} \qquad [4.17]$$

at 90% confidence level.

4.4 $\chi_{0,2} \rightarrow \gamma\gamma$

We can use essentially the same analysis to search for the decays $\psi' \rightarrow \gamma\chi_{0,2}$, $\chi_{0,2} \rightarrow \gamma\gamma$ with the cuts modified to select events with two high energy γ's instead of two high energy π^0's. Table 4.2 enumerates the cuts and shows their effect for the ψ' and ψ'' datasets and the $\psi' \rightarrow \gamma\chi_0$, $\chi_0 \rightarrow \pi^0\pi^0$ and $\psi' \rightarrow \gamma\chi_0$, $\chi_0 \rightarrow \gamma\gamma$ Monte Carlos.

Cut	ψ'	ψ''	$\psi' \rightarrow \gamma\chi_0$, $\chi_0 \rightarrow \pi^0\pi^0$ M.C.	$\psi' \rightarrow \gamma\chi_0$, $\chi_0 \rightarrow \gamma\gamma$ M.C.
3 Tracks	3159	1392	47%	56%
3rd Track PIFIT Cut	3136	1392	47	56
3rd Track not Eq. or Tun.	2344	998	36	45
$\lvert\cos\theta_{1,2}\rvert < 0.65$	1137	452	26	31
$\lvert\cos\theta_3\rvert < 0.85$	1119	446	26	31
E_{CM}Cut	1012	576	25	30
Track 1 & 2 PIFIT Cut	522	247	0.03	19
Overlap Cut	462	222	0	18

Table 4.2 Cuts for $\psi' \rightarrow \gamma\gamma\gamma$ analysis.

As noted previously, there is substantial background in this channel from $e^+e^- \rightarrow (\gamma)\gamma\gamma$. However, the background differs from the signal in that the angular distribution of the two high energy γ's in $e^+e^- \rightarrow (\gamma)\gamma\gamma$ is peaked towards the beam direction, whereas the γ's in the decays $\psi' \rightarrow \gamma\chi_{0,2}$, $\chi_{0,2} \rightarrow \gamma\gamma$ are relatively isotropically distributed. For definiteness, we call the lowest energy track number

three. Of the two high energy tracks, track two lies closest to track three, and track number one is the remaining track. Figure 4.18 shows the distribution of $|\cos\theta_1|$, where θ_1 is the angle track 1 makes with the beam direction, for a Monte Carlo of $\psi' \rightarrow \gamma\chi_0$, $\chi_0 \rightarrow \gamma\gamma$. Figure 4.19 shows the same plot for an $e^+e^- \rightarrow (\gamma)\gamma\gamma$ Monte Carlo. We see the tendency for the QED events to peak at large $|\cos\theta_1|$ as mentioned above. We wish to place a cut on this variable which maximizes the statistical significance of any $\psi' \rightarrow \gamma\chi_0$, $\chi_0 \rightarrow \gamma\gamma$ signal which may be present in the data. The statistical significance of a signal goes as $S/\sqrt{B}$, where S is the number of events in the signal peak and B is the number of background events underneath it. Thus, we want to place our cut on $|\cos\theta_1|$ in such a way that the fraction of signal events over the square root of the fraction of background events which survive is maximized. Figure 4.20 shows the survival rates for the Monte Carlos; Fig. 4.21 shows the ratio. We see that the statistical significance of the signal is enhanced (albeit slightly) by a cut at $|\cos\theta_1| = 0.65$ as shown by the arrow in Fig. 4.21.

We must also place a cut on the PIFIT masses which selects events consistent with $\psi' \rightarrow \gamma\gamma\gamma$. We have seen in the previous section that there is a potentially large background from the $\pi^0\pi^0$ decay of the χ_0 and χ_2 if both of the π^0's are misidentified as γ's, and we must estimate this feeddown. We could in principle estimate the leakage from the Monte Carlo. However, since this number is crucial to separating the large $\psi' \rightarrow \gamma\pi^0\pi^0$ background from the $\psi' \rightarrow \gamma\gamma\gamma$ signal, it is preferable to determine it from the data. Consider the decay $\psi' \rightarrow \gamma\chi_0$, $\chi_0 \rightarrow \pi^0\pi^0$. If we select events from the three neutral track sample in which the energy of the lowest energy γ is consistent with the radiative photon in this decay, we will obtain a sample of events in which the two high energy tracks are likely to be π^0's with some contamination from $e^+e^- \rightarrow (\gamma)\gamma\gamma$ events. We now require that one of the high energy tracks have a PIFIT mass greater than 90 MeV/c^2 and plot the PIFIT mass of the other high energy track (Fig. 4.22). (Figure 4.23 shows the same plot for a $\psi' \rightarrow \gamma\chi_0$, $\chi_0 \rightarrow \pi^0\pi^0$ Monte Carlo for comparison.) The tail of the distribution is due to π^0's which have low PIFIT masses and a small residual contamination of

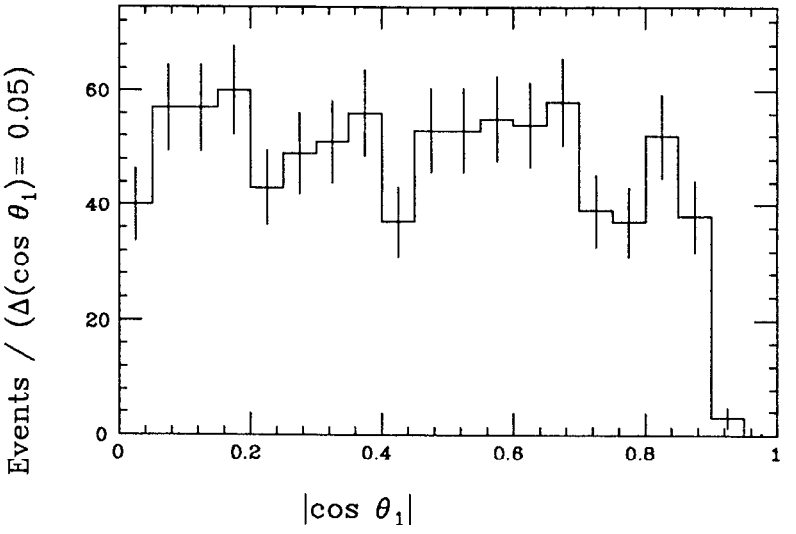

Fig. 4.18 Distribution of $|\cos\theta_1|$ for $\psi' \rightarrow \gamma\chi_0$, $\chi_0 \rightarrow \gamma\gamma$ Monte Carlo.

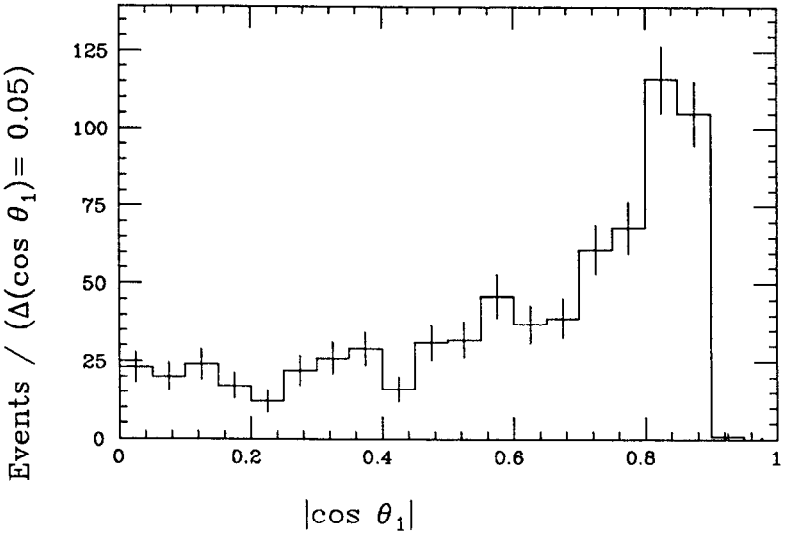

Fig. 4.19 Distribution of $|\cos\theta_1|$ for $e^+e^- \rightarrow (\gamma)\gamma\gamma$ Monte Carlo.

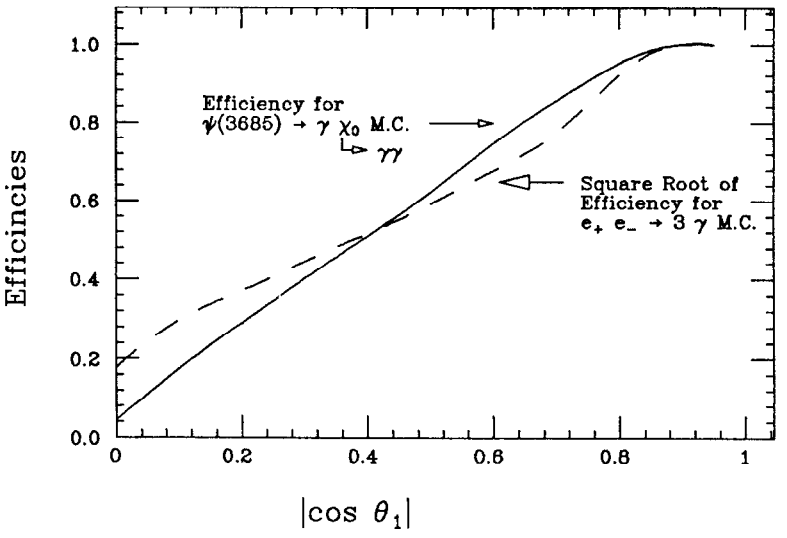

Fig. 4.20 Efficiencies of $|\cos\theta_1|$ cut for $\psi' \to \gamma\chi_0$, $\chi_0 \to \gamma\gamma$ and $e^+e^- \to (\gamma)\gamma\gamma$ Monte Carlos.

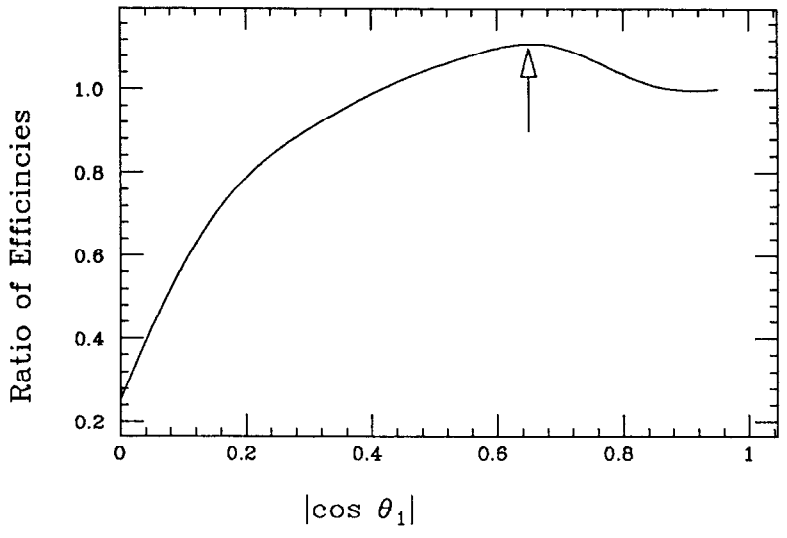

Fig. 4.21 Ratio of efficiencies of $|\cos\theta_1|$ cut for $\psi' \to \gamma\chi_0$, $\chi_0 \to \gamma\gamma$ and $e^+e^- \to (\gamma)\gamma\gamma$ Monte Carlos.

$e^+e^- \rightarrow (\gamma)\gamma\gamma$ events in which one of the high energy γ's has a PIFIT mass greater than 90 MeV/c^2 so that the other high energy γ is included in this distribution. Thus, the fraction of tracks below a certain PIFIT mass gives an upper limit for the probability that a π^0 with an energy $\approx$ 1700 MeV will be misidentified as a γ. For a cut at 70 MeV/c^2, we calculate from Fig. 4.22 (the ψ' data) that this probability is 8 $\pm$2 %. (From Fig. 4.23 (the $\psi' \rightarrow \gamma\chi_0$, $\chi_0 \rightarrow \pi^0\pi^0$ Monte Carlo), the probability is 5$\pm$0.5%.) Similarly, we calculate from the data that the probability that a 1.7 GeV π^0 is flagged a π^0 by a PIFIT cut at 90 MeV/c^2 is 88 $\pm$2%. We use a PIFIT cut of 70 MeV/c^2 on each high energy track (corresponding to the lower left box in Fig. 4.10) so that the probability that a $\psi' \rightarrow \gamma\chi_0$, $\chi_0 \rightarrow \pi^0\pi^0$ event is misidentified as a $\psi' \rightarrow \gamma\gamma\gamma$ event is less than $(0.08)^2$, or 0.6 $\pm$0.2%.

We wish to estimate the leakage from the channels $\psi' \rightarrow \gamma(\chi_0,\chi_2),(\chi_0,\chi_2) \rightarrow \pi^0\pi^0$ into the channels $\psi' \rightarrow \gamma(\chi_0,\chi_2),(\chi_0,\chi_2) \rightarrow \gamma\gamma$ with these cuts. (In what follows, where two quantities are indicated in parentheses, the first refers to the χ_0 channel and the second to the χ_2 channel.) Of the (137,48) events which were identified as $\psi' \rightarrow \gamma(\chi_0,\chi_2),(\chi_0,\chi_2) \rightarrow \pi^0\pi^0$ in the last section in the three-track topology, (113,41) pass the more restrictive angular cut described above. Using the 88% π^0 detection efficiency noted above, we estimate that the total number of events before the PIFIT cuts is (127,46). We expect 0.6% of these events to be misidentified by the PIFIT cut, so we predict a contamination of (0.8,0.3) events for the $\psi' \rightarrow (\chi_0,\chi_2),(\chi_0,\chi_2) \rightarrow \gamma\gamma$ decays. As noted above, this calculation gives an upper limit for the contamination. (A similar calculation from Monte Carlo yields (0.3,0.1) events.) We choose to subtract (0.8 $\pm$0.8, 0.3 $\pm$0.3) events and include the errors in the overall systematic error.

Figures 4.24 and 4.25 show the distribution of the energy of the lowest energy photon after the $|\cos\theta_1|$ and PIFIT cuts for the $e^+e^- \rightarrow (\gamma)\gamma\gamma$ Monte Carlo and the ψ'' data, respectively. Figure 4.26 shows the same distribution for the ψ' data. The arrows indicate the energies of photons corresponding to transitions to states which are expected to decay to two photons. We first examine the background by

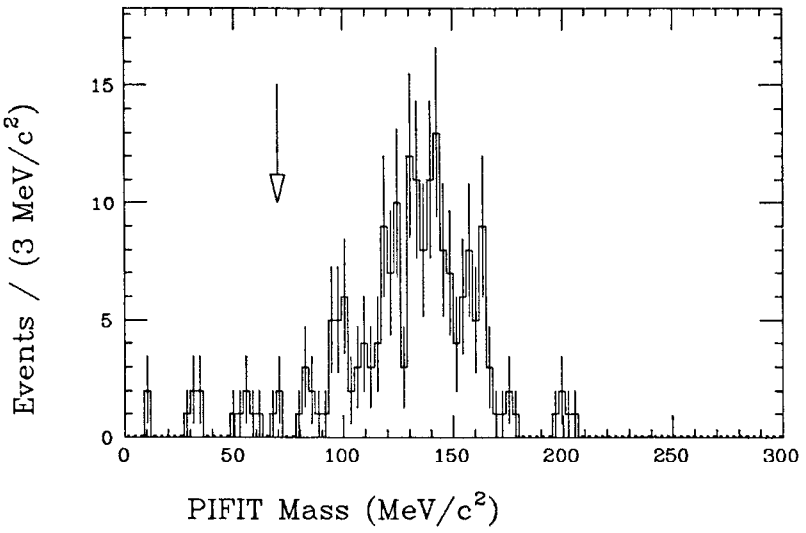

Fig. 4.22 PIFIT invariant mass distribution for high energy π^0's: $\psi' \rightarrow \gamma\chi_0$, $\chi_0 \rightarrow \pi^0\pi^0$ data.

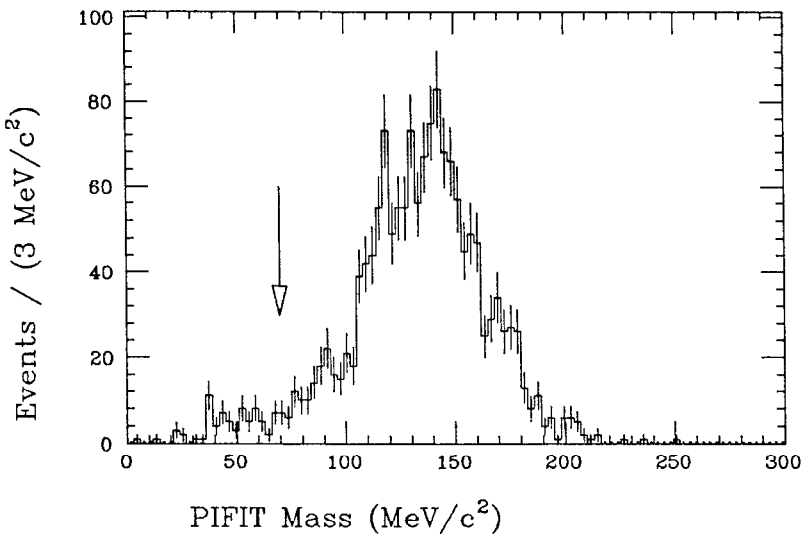

Fig. 4.23 PIFIT invariant mass distribution for high energy π^0's: $\psi' \rightarrow \gamma\chi_0$, $\chi_0 \rightarrow \pi^0\pi^0$ Monte Carlo.

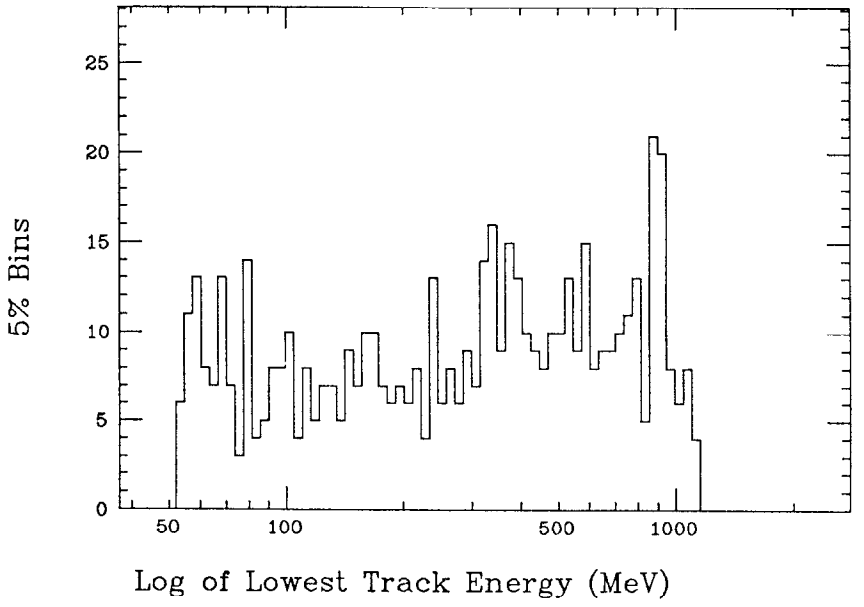

Fig. 4.24 Distribution of energy of lowest energy γ: $e^+e^- \to (\gamma)\gamma\gamma$ Monte Carlo.

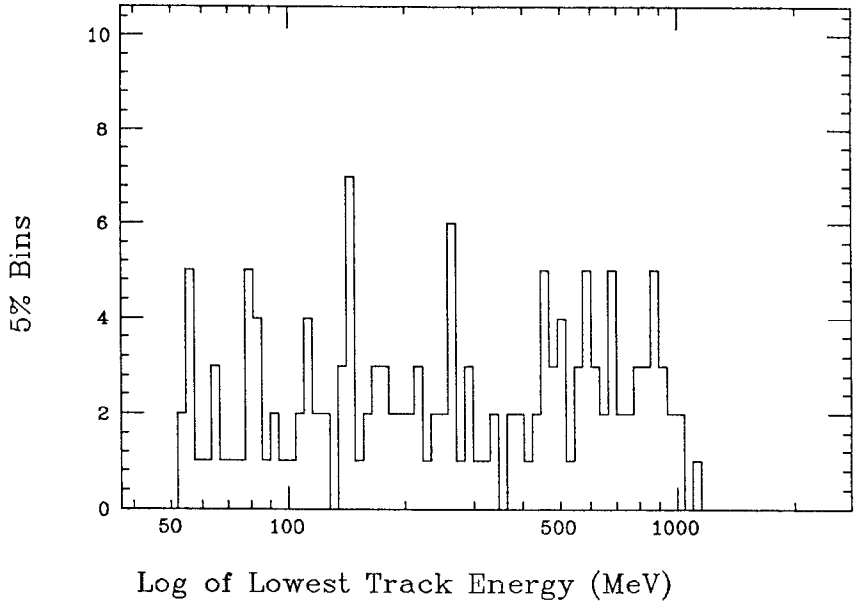

Fig. 4.25 Distribution of energy of lowest energy γ: $\psi'' \to 3\gamma$.

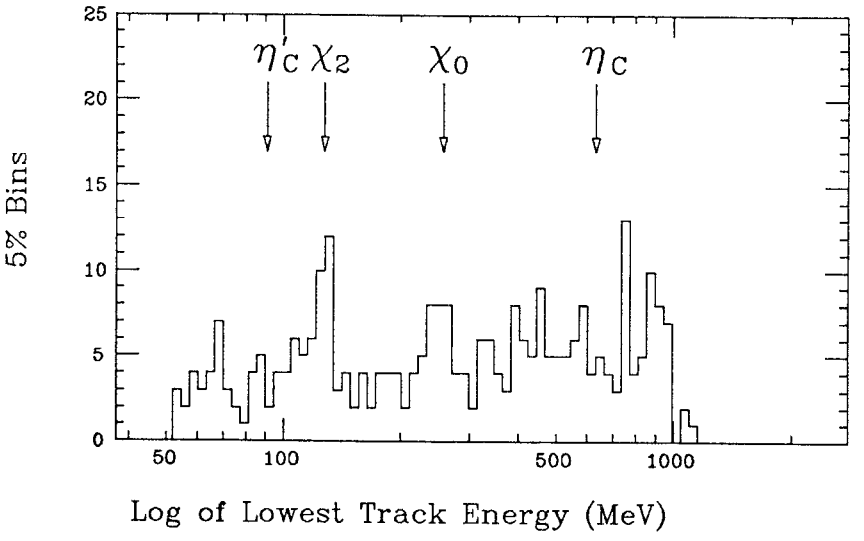

Fig. 4.26 Distribution of energy of lowest energy γ: $\psi' \rightarrow 3\gamma$.

fitting the energy distribution from the $e^+e^- \rightarrow (\gamma)\gamma\gamma$ Monte Carlo (Fig. 4.27). We see that a second order Legendre polynomial fits the data well. Figures 4.28 and 4.29 show the ψ'' and ψ' data fit to the same functional form. Both fits are acceptable, although the background shape on the ψ' is inconsistent with that in the ψ'' and Monte Carlo fits. In order to improve the fit to the ψ' spectrum , we add two signal amplitudes corresponding to the decays $\psi' \rightarrow \gamma\chi_{0,2}$, $\chi_{0,2} \rightarrow \gamma\gamma$ *with the means and widths of the radiative photons fixed to those found in the* $\gamma\pi^0\pi^0$ *study above* (Fig. 4.30). We see that the fit improves and observe 22 $\pm$7 and 12 $\pm$6 events corresponding to the decays $\psi' \rightarrow \gamma\chi_{0,2}$, $\chi_{0,2} \rightarrow \gamma\gamma$, respectively. For comparison, Figs. 4.31 and 4.32 show the same spectrum fit to constant and linear backgrounds, respectively. Also, given the factor of 1.8 in luminosity between the ψ' and ψ'' datasets (see Chapter 3), we see that the background in the ψ' plot agrees both in shape and normalization with that in the ψ''.

There is clear evidence for the transition $\psi' \rightarrow \gamma\chi_2$, $\chi_2 \rightarrow \gamma\gamma$, but the structure corresponding to the decay $\psi' \rightarrow \gamma\chi_0$, $\chi_0 \rightarrow \gamma\gamma$ appears to be of questionable significance. We can estimate the probability that a fluctuation of the background

would make a peak with this mean and width by using the fitted background to predict a number of counts for each bin, using Poisson statistics to generate several hundred Monte Carlo spectra, and fitting the resulting spectra using the identical procedure as was used to fit the ψ' spectrum. Such a study indicates that the probability that a peak of the observed amplitude or larger could be generated by a statistical fluctuation is 1 out of 300. Inasmuch as this confidence level is below the generally accepted 3σ criterion for a statistically significant structure at a fixed mass (1 out of 740), we quote below both a branching ratio and an upper limit for this decay. On the other hand, we see no structures which would correspond to transitions to the η_c and η_c'. We can set upper limits by fitting two additional line shape amplitudes with means and widths fixed to the values determined from a previous analysis of the inclusive photon spectrum of the ψ'. (The width of the η_c' was indistinguishable from zero in this analysis, and an upper limit of 7 MeV/c^2 was reported at 90% confidence level. We set the width of the η_c' to zero for these fits.) For the processes $\psi' \to \gamma\eta_c', \eta_c' \to \gamma\gamma$ and $\psi' \to \gamma\eta_c, \eta_c \to \gamma\gamma$ we obtain upper limits of 8.1 and 6.7 events, respectively, at 90% confidence level.

We again use Monte Carlo simulations to determine the detection efficiencies. The angular distribution of the decay $\psi' \to \gamma X, X \to \gamma\gamma$ where X has no spin is given by

$$\frac{d^3N}{d\cos\theta_1 d\cos\theta_2 d\phi_2} = 1 + \cos^2\theta_1 \qquad [4.18]$$

where θ_1, θ_2, and ϕ_2 are as defined in the analagous decay to $\gamma\pi^0\pi^0$. We obtain efficiencies of 15%, 18%, and 20%, respectively, for $X = \eta_c'$, χ_0, and η_c. The angular distribution for the same decay in which X is assumed to have spin 2 is given by

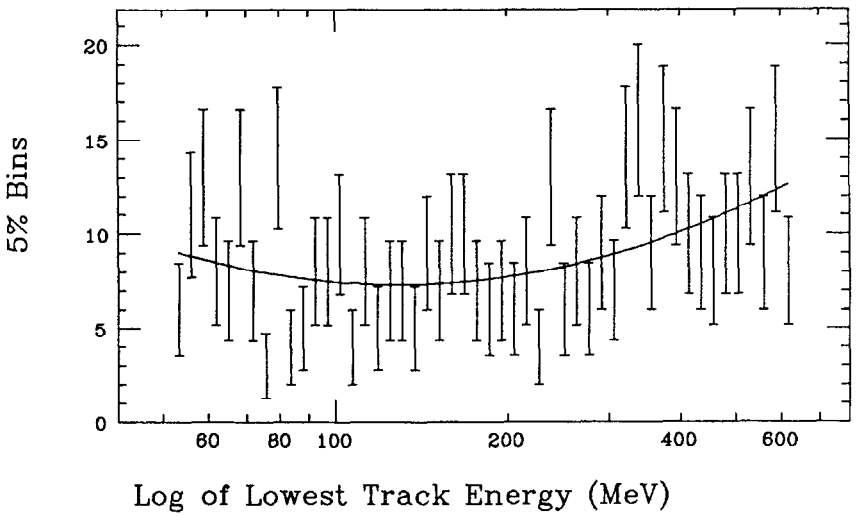

Fig. 4.27 Distribution of energy of lowest energy γ : $e^+e^- \rightarrow (\gamma)\gamma\gamma$ Monte Carlo (fit to second order polynomial). Best fitted values: $\mathcal{L}_0 = 217 \pm 10$, $\mathcal{L}_1 = 0.21 \pm 0.08$, $\mathcal{L}_2 = 0.2 \pm 0.1$, C.L. $= 0.48$.

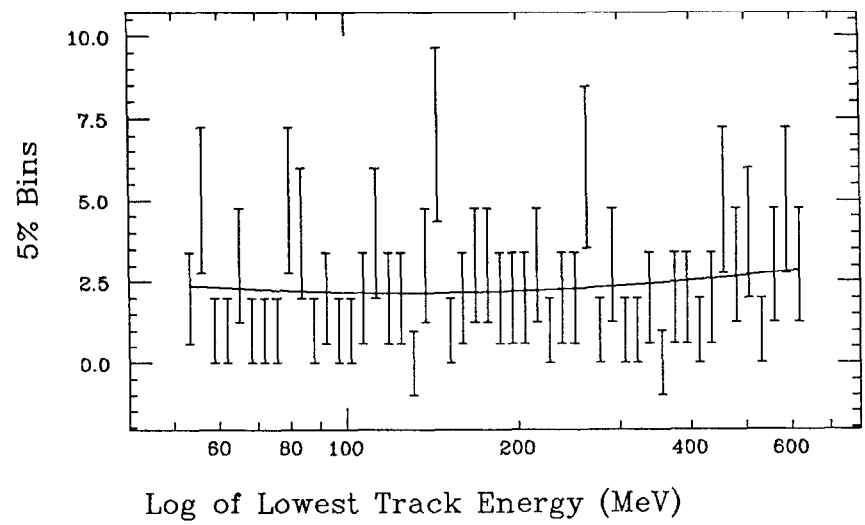

Fig. 4.28 Distribution of energy of lowest energy γ : $\psi'' \rightarrow 3\gamma$ (fit to second order polynomial). Best fitted values: $\mathcal{L}_0 = 58 \pm 5$, $\mathcal{L}_1 = 0.11 \pm 0.17$, $\mathcal{L}_2 = 0.13 \pm 0.20$, C.L. $= 0.40$

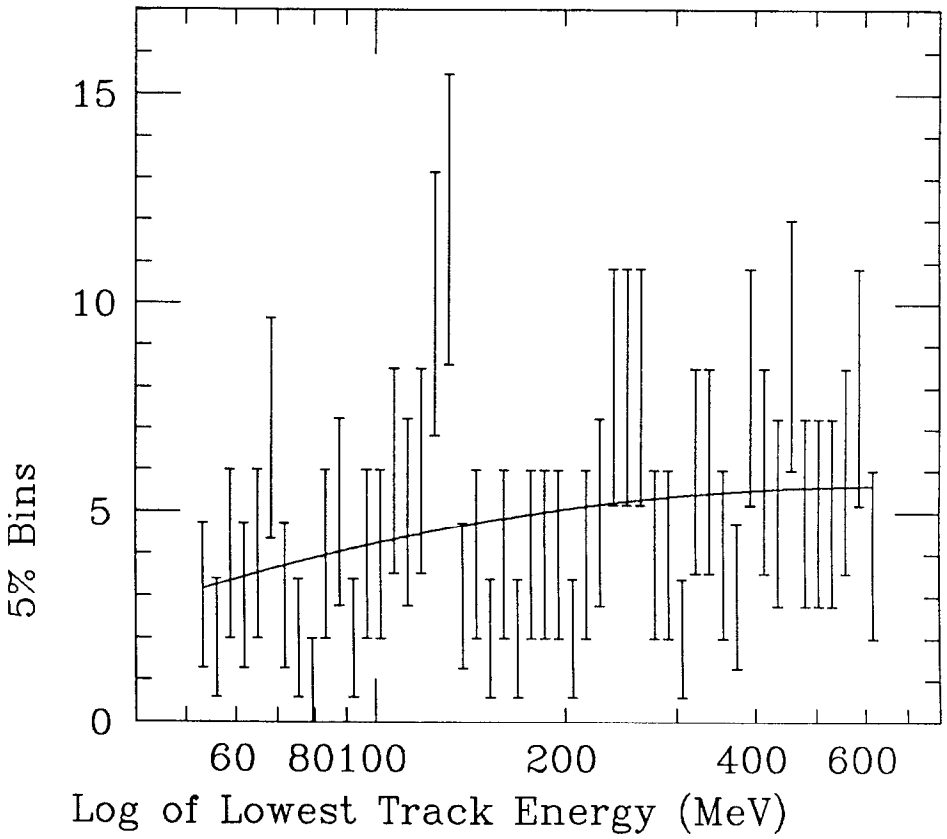

Fig. 4.29 Distribution of energy of lowest energy γ : $\psi' \rightarrow 3\gamma$ (Fit to second order polynomial) Best fitted values: $\mathcal{L}_0 = 120 \pm 8$, $\mathcal{L}_1 = 0.26 \pm 0.11$, $\mathcal{L}_2 = -0.82 \pm 0.14$, C.L. = 0.41.

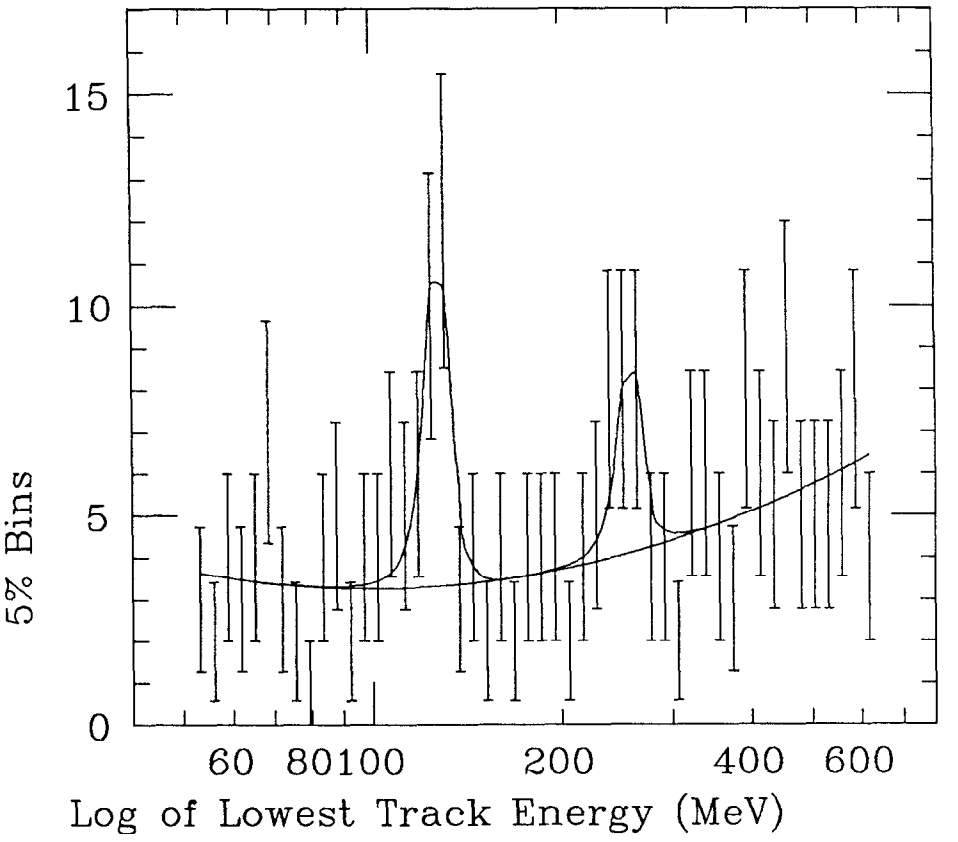

Fig. 4.30 Distribution of energy of lowest energy γ : $\psi' \rightarrow 3\gamma$ (fit to second order polynomial plus χ_0 and χ_2 line shapes). Best fitted values: $\mathcal{L}_0 = 102 \pm 8$, $\mathcal{L}_1 = 0.35 \pm 0.13$, $\mathcal{L}_2 = 0.24 \pm 0.18$, $\text{Amp}_{\chi_2} = 21.8 \pm 6.7$, $\text{Amp}_{\chi_0} = 12.4 \pm 6.0$, C.L. = 0.993.

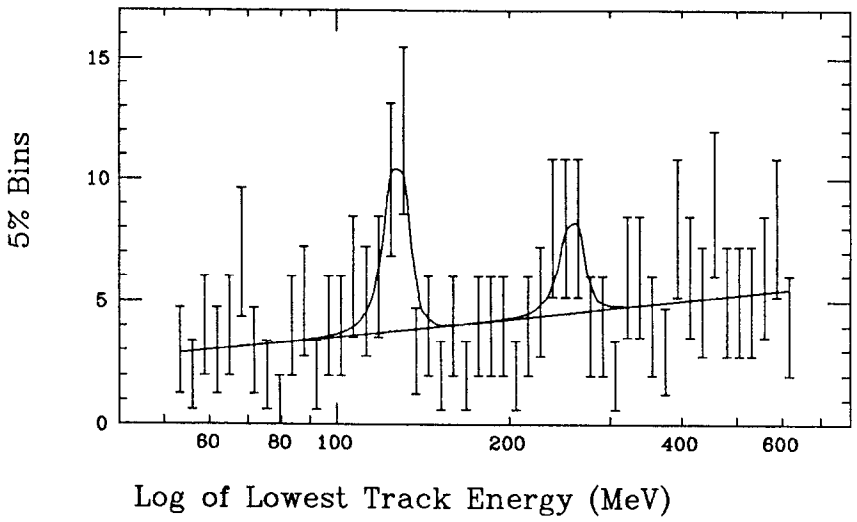

Fig. 4.31 Distribution of energy of lowest energy γ: $\psi' \rightarrow 3\gamma$ (fit to linear background plus χ_0 and χ_2 line shapes). Best fitted values: $\mathcal{L}_0 = 104 \pm 8$, $\mathcal{L}_1 = 0.32 \pm 0.11$, $\text{Amp}_{\chi_2} = 19.5 \pm 5.9$, $\text{Amp}_{\chi_0} = 10.4 \pm 5.7$, C.L. $= 0.988$.

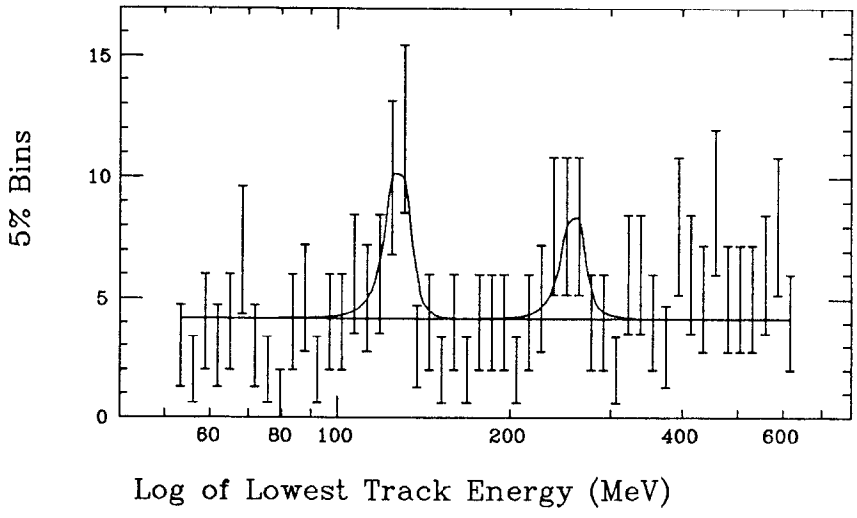

Fig. 4.32 Distribution of energy of lowest energy γ: $\psi' \rightarrow 3\gamma$ (fit to constant background plus χ_0 and χ_2 line shapes). Best fitted values: $\mathcal{L}_0 = 105 \pm 8$, $\text{Amp}_{\chi_2} = 17.8 \pm 6.3$, $\text{Amp}_{\chi_0} = 11.9 \pm 5.7$, C.L. $= 0.914$.

$$\begin{aligned}\frac{d^3N}{d\cos\theta_1 d\cos\theta_2 d\phi_2} &= 3x^2\sin^2\theta_1\sin^2\theta_2 \\ &+ (1+\cos^2\theta_1)\left[(3\cos^2\theta_2-1)^2+\frac{3}{2}y^2\sin^4\theta_2\right] \\ &+ \sqrt{3}x\sin 2\theta_1\sin 2\theta_2\left[3\cos^2\theta_2-1-\frac{1}{2}\sqrt{6}y\sin^2\theta_2\right]\cos\phi_2 \\ &+ \sqrt{6}y\sin^2\theta_1\sin^2\theta_2(3\cos^2\theta_2-1)\cos 2\phi_2 \\ &+ z^2\cos^2 2\phi_2\Big\{2x^2\sin^2\theta_1(1-\cos^4\theta_2) \\ &+ (1+\cos^2\theta_1)\left[\frac{3}{2}\sin^4\theta_2+\frac{1}{4}y^2(1+6\cos^2\theta_2+\cos^4\theta_2)\right] \\ &+ \sqrt{3}x\sin 2\theta_1\sin 2\theta_2\left[\sin^2\theta_2+\frac{1}{2\sqrt{6}}y(3+\cos^2\theta_2)\right]\cos\phi_2 \\ &+ \sqrt{6}y\sin^2\theta_1(1+\cos^4\theta_2)\cos 2\phi_2\Big\}.\end{aligned} \qquad [4.19]$$

x and y are ratios of helicity amplitudes defined previously. Unlike the $\pi^0\pi^0$ case, the decay products of the X here have non-zero spin, and there are two additional helicity amplitudes corresponding to the same and opposite photon helicities. We have factored the "same" helicity amplitude out of the above expression into the overall normalization, and denoted the ratio of helicity amplitudes by z. This ratio has not been calculated in any model. Thus, in order to determine the detection efficiency for the decay $\psi' \to \gamma\chi_2$, $\chi_2 \to \gamma\gamma$, we have run two separate Monte Carlos corresponding to the cases in which the helicities of the photons from the decay of the χ_2 are the same and opposite. The difference in efficiencies so obtained is slight (16.7% *vs.* 18.1%), and we include this difference in the systematic error.

Using the Monte Carlo efficiencies quoted above, we derive

$$\begin{aligned}&\mathrm{BR}(\psi' \to \gamma\chi_2, \chi_2 \to \gamma\gamma) = (7.0 \pm 2.1 \pm 2.0)\times 10^{-5} \\ &\left\{\begin{array}{l}\mathrm{BR}(\psi' \to \gamma\chi_0, \chi_0 \to \gamma\gamma) = (3.7 \pm 1.8 \pm 1.0)\times 10^{-5} \\ \mathrm{BR}(\psi' \to \gamma\chi_0, \chi_0 \to \gamma\gamma) \le 7.0\times 10^{-5}\end{array}\right\}\end{aligned} \qquad [4.20]$$

where the first errors are statistical and the second systematic. (We quote both a branching ratio and an upper limit for the χ_0 transition as noted above.) As in the $\gamma\pi^0\pi^0$ decays, we use the Particle Data Group averages[17] for the branching ratios of the ψ' to the χ states to derive

$$\begin{aligned} &\mathrm{BR}(\chi_2 \to \gamma\gamma) = (9.5 \pm 2.9 \pm 3.5) \times 10^{-4} \\ &\left.\begin{aligned} &\mathrm{BR}(\chi_0 \to \gamma\gamma) = (4.5 \pm 2.2 \pm 2.0) \times 10^{-4} \\ &\mathrm{BR}(\chi_0 \to \gamma\gamma) \leq 1.0 \times 10^{-3} \end{aligned}\right\} \end{aligned} \qquad [4.21]$$

The systematic errors for these two decays are shown in the following list. We add systematic errors linearly but add the statistical and systematic errors in quadrature when we quote a combined error. (This convention is followed throughout this study.)

Source	$\chi_0 \to \gamma\gamma$	$\chi_2 \to \gamma\gamma$
No. of ψ' decays	5%	5%
Error in $\psi' \to \gamma\chi_{0,2}$ branching ratios	17	18
Monte Carlo	5	7
Different helicity hypotheses	0	4
Fitting error (Different Backgrounds)	10	10
γ conversion	1.5	1.5
$\chi \to \pi^0\pi^0$ contamination	6.5	1.4
Total	45%	47%

Table 4.3 Systematic errors for $\chi_{0,2} \to \gamma\gamma$.

From the absence of any signals near the γ energies corresponding to the masses of the η_c and η_c', we can also set upper limits on the branching ratios of these states

to two photons. We set upper limits of 6.7 and 11.1 on the number of observed events at 90% confidence level corresponding to

$$\begin{aligned} \mathrm{BR}(\psi' \to \gamma\eta_c, \eta_c \to \gamma\gamma) &< 2.1 \times 10^{-5} \\ \mathrm{BR}(\psi' \to \gamma\eta_c', \eta_c' \to \gamma\gamma) &< 4.7 \times 10^{-5} \end{aligned} \qquad [4.22]$$

Using the measured values of the branching ratios BR $(\psi' \to \gamma\eta_c, \eta_c')$,[20] we deduce

$$\begin{aligned} \mathrm{BR}(\eta_c \to \gamma\gamma) &< 1 \times 10^{-2} \\ \mathrm{BR}(\eta_c' \to \gamma\gamma) &< 1 \times 10^{-2} \end{aligned} \qquad [4.23]$$

As our upper limit for the η_c branching ratio is substantially above both an earlier upper limit ($\mathrm{BR}(\eta_c \to \gamma\gamma) < 1.3 \times 10^{-3}$[23]) and a recently reported measurement ($\mathrm{BR}(\eta_c \to \gamma\gamma) = 2.4 \pm 2.0 \times 10^{-4}$[18]), we do not discuss it in the remainder of this chapter.

4.5 $\chi_{0,2} \to \eta\eta$

To search for these decays we use an analysis identical to that used to search for the decay $\psi' \to \gamma\theta$, $\theta \to \eta\eta$ which will be described in more detail in the next chapter. Briefly, we restrict our analysis to events with five tracks and fit the events to energy and momentum conservation, constraining two pairs of γ's to have the mass of the η. If more than one combination of γ's fits these constraints, we use the one with the highest confidence level.§ Figure 4.33 shows the fitted energy of the one γ which does not contribute to an η in each event on a log scale. The plot is sufficiently free of background that we simply count the events in the χ_0 and χ_2 peaks. We obtain 5 and 13 events consistent with $\psi' \to \gamma\chi_{0,2}$, $\chi_{0,2} \to \eta\eta$, $\eta \to \gamma\gamma$,

§ This analysis differs from that described in Chapter 5 only in that there is no cut on the mass opposite any two photons in the event. This cut is not necessary here because the photon lines are sufficiently narrow that there is no need to attempt to eliminate backgrounds.

respectively. Using Monte Carlo efficiencies of 22% and 29% and dividing by the square of the η branching ratio to two γ's, we obtain

$$\begin{aligned} \mathrm{BR}(\psi' \to \gamma\chi_0, \chi_0 \to \eta\eta) &= (2.3 \pm 0.7 \pm 0.7) \times 10^{-4} \\ \mathrm{BR}(\psi' \to \gamma\chi_2, \chi_2 \to \eta\eta) &= (6.2 \pm 3.1 \pm 1.9) \times 10^{-5} \end{aligned} \qquad [4.24]$$

where the first error is statistical and the second systematic. As with the $\pi^0\pi^0$ decays, we use the Particle Data Group averages[17] for the branching ratios of $\psi' \to \gamma\chi_{0,2}$ to obtain

$$\begin{aligned} \mathrm{BR}(\chi_0 \to \eta\eta) &= (2.8 \pm 0.9 \pm 1.3) \times 10^{-3} \\ \mathrm{BR}(\chi_2 \to \eta\eta) &= (8.4 \pm 4.2 \pm 4.0) \times 10^{-4} \end{aligned} \qquad [4.25]$$

where we have added the error in the branching ratios of $\psi' \to \gamma\chi_{0,2}$ in the systematic errors quoted above.

4.6 Comparisons With Previous Experiments

The decays $\psi' \to \gamma\chi_{0,2}$, $\chi_{0,2} \to \pi^0\pi^0$ have not been accessible to previous experiments. However, the analagous decays to charged π's have been measured. Assuming isospin invariance, these can be compared with the results of the current analysis (Table 4.4). It is seen that the product branching ratios measured in this study agree well with those measured in previous studies. Table 4.5 shows a comparison of other measured parameters of the χ_0. The most accurate measurement of the χ_0 mass comes from Mark II exclusive studies of the charged decays of the χ states.[26] The only previous χ_0 width measurement comes from a Crystal Ball study of the inclusive photon spectrum at the ψ'. The discrepancy between the current study and the previous result may be due to the more complicated background subtraction necessary in an inclusive analysis. Also, recent work[27] indicates that the photon energy resolution of the Crystal Ball may be larger in an inclusive study than in an exclusive analysis due to contamination of the photon shower with hadronic debris from the remainder of the event.

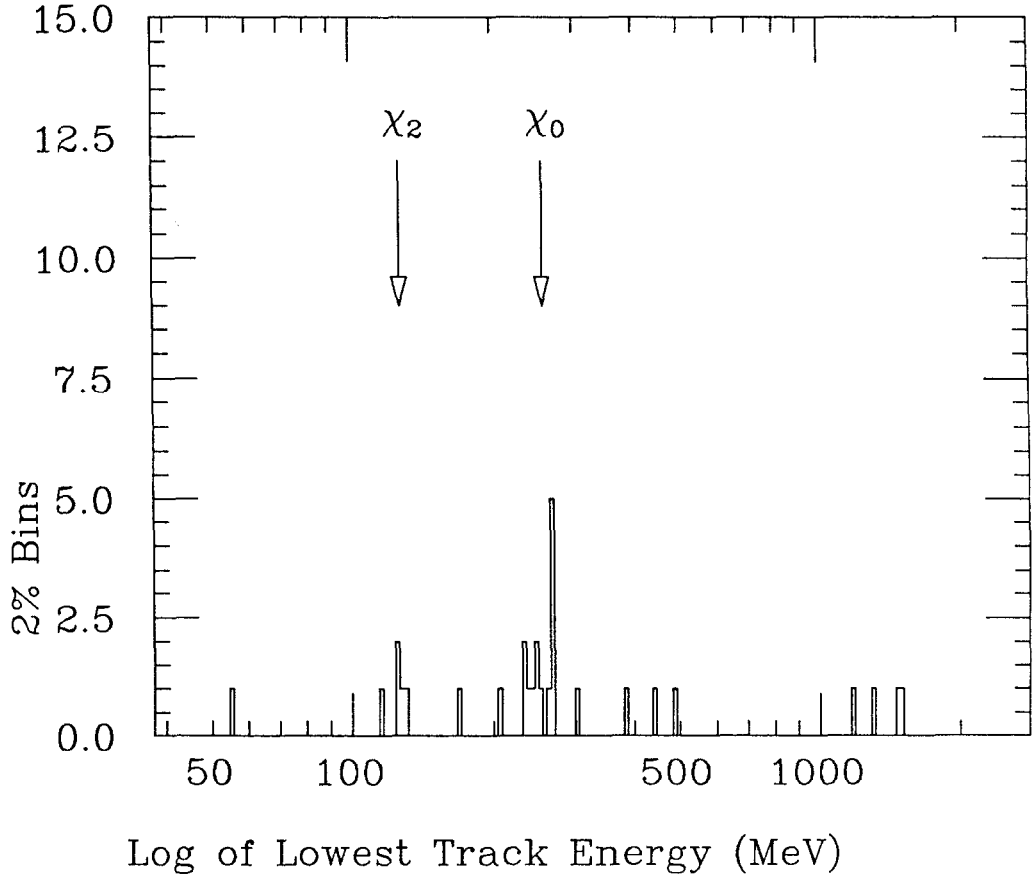

Fig. 4.33 Energy of direct photon in $\psi' \to \gamma\eta\eta$.

Decay	Branching Ratio $\times 10^{-4}$	
	This Exp.	Other Exp.
$\psi' \rightarrow \gamma\chi_0$, $\chi_0 \rightarrow \pi\pi$	8.7 $\pm$0.9 $\pm$1.5	9.0 $\pm$6.0[24]
		11.3 $\pm$3.2[25]
		7.8 $\pm$2.2[26]
$\psi' \rightarrow \gamma\chi_2$, $\chi_2 \rightarrow \pi\pi$	2.6 $\pm$0.4 $\pm$0.5	2.3 $\pm$1.2[24]
		4.5 $\pm$1.5[26]

Table 4.4 Branching ratios for $\chi_{0,2} \rightarrow \pi\pi$

Parameter	This Exp.	Other Exp.
$\Gamma(\chi_0)$(MeV/c^2)	8.8 $\pm$1.3 $\pm$1.5	17.0 $\pm$3.5[20]
Mass (χ_0) (MeV/c^2)	3415.6 $\pm$1.3 $\pm$0.6	3414.8 $\pm$1.1[26]

Table 4.5 χ_0 parameters.

The only previous measurements of the two photon decays of the χ_0 and χ_2 are unpublished upper limits from DASP (Table 4.6). There are no previous measurements of the two photon decay of the η_c' or the $\eta\eta$ decays of the χ_0 and χ_2.

4.7 Comparison With Theory

The comparison of the χ_0 width to theory is complicated by the dependence of the prediction on the derivative of the wavefunction (see Equation [4.4]). The first line in Table 4.7 shows the range of predictions for several different potential models. As noted in the introduction, the ratio $\Gamma(\chi_0 \rightarrow gg)/\Gamma(\chi_2 \rightarrow gg)$ is inde-

Decay	Branching Ratio ($\times 10^{-5}$)	
	This Exp.	Other Exp.
$\psi' \rightarrow \gamma\chi_0$, $\chi_0 \rightarrow \gamma\gamma$	$3.7 \pm 1.8 \pm 1.0$ or ≤ 7.0	≤ 14[28]
$\psi' \rightarrow \gamma\chi_2$, $\chi_2 \rightarrow \gamma\gamma$	$7.0 \pm 2.1 \pm 2.0$	≤ 4[28]

Table 4.6 Branching ratios and upper limit for $\chi_{0,2} \rightarrow \gamma\gamma$.

pendent of potential model and hence more easily compared with theory. In order to compute the experimental value of this ratio, we use a preliminary measurement of the width of the χ_2 ($2.92^{+1.76}_{-1.12}$ MeV/c^2) as recently measured in direct formation of charmonium states in proton antiproton annihilation[18] and correct by the measured branching ratio of $\chi_2 \rightarrow \gamma J/\psi$.[17] We present the results of calculations to zeroth and first order in α_s (Equations [4.5] and [4.6], respectively). As noted above, QCD sum rules predict partial widths of the χ states to $\gamma\gamma$. The authors of reference 15 have used these widths and the lowest-order prediction of the ratio two photon to two gluon widths from potential models (equation [4.8]) to predict the widths of the χ_0 and χ_2 to two gluons. This factor of course cancels in the ratio of two-gluon widths.

We note that although the potential model predictions for the χ_0 width are inconsistent with the data, the lowest-order predictions for the ratio of the widths is in better agreement with experiment. Ironically, the first-order correction is outside of the experimental error bars. The QCD sum rule prediction for the χ_0 width is also inconsistent with the data, but as noted above this prediction requires as input the value of the ratio of two photon to two gluon widths of the χ states from potential model calculations. The sum rule prediction for the ratio of the widths depends on the weaker assumption that the ratio of the two photon to two

Parameter	Measurement	Predicted by	Prediction
$\Gamma_{gg}(\chi_0)$ (MeV/c^2)	8.8 ±2.0	L. O. QCD	1 - 3[12,30,31]
		QCD Sum Rule	4 - 5[15]
$\Gamma_{gg}(\chi_0)/\Gamma_{gg}(\chi_2)$	2.9 ±1.6	L. O. QCD	3.75[12]
		F. O. QCD	6.47[13]
		QCD Sum Rule	1.8 - 3.1[15]

Table 4.7 Comparison of χ_0 width to theoretical predictions.

(L. O. QCD = Lowest Order QCD Potential Models.

F. O. QCD = First Order QCD Potential Models)

gluon widths of the χ_0 and χ_2 are the same and is in good agreement with the data. It should perhaps be noted that a calculation of the ratio of the widths from a theory other than QCD (e.g., assuming scalar gluons) predicts a ratio (125/2) which is grossly inconsistent with the data.[29]

The comparison of the $\gamma\gamma$ partial widths is similar. Here we use the branching ratios and the χ_0 full width measured in this study, the χ_2 full width measured in the proton antiproton formation experiment referenced earlier,[18] and the upper limit on the η_c' full width measured in a Crystal Ball inclusive analysis.[20] Again, the lowest order predictions depend on the assumed potential and hence lead to a range of predictions as shown in the first line of the following table. However, a more recent result using these same potentials but including first-order relativistic corrections leads to the somewhat surprising result that the predictions converge to essentially the same value. Alternately, we can eliminate the dependence on

the potential entirely by taking the ratio of the two photon width to the two gluon width to obtain predictions for the branching ratios to zeroth and first order in α_s.¶ Finally, QCD sum rules can be used to predict these widths. Table 4.8 shows the comparison between experiment and theory for the χ states, and Table 4.9 gives a similar comparison for the η_c'. (For clarity, we show only the branching ratio measurement for the $\chi_0 \to \gamma\gamma$ decay and not the upper limit.)

The lowest-order QCD potential model prediction for the two photon widths are in rough agreement with the data, but the branching ratio prediction for the χ_0 is in substantial disagreement. (If we more conservatively use the 90% confidence level upper limit, there is still a discrepancy between theory and experiment.) This is consistent with our previous observation that the measured width of the χ_0 is $\approx$4 times larger than the lowest order QCD prediction. The QCD sum rule predictions are in good agreement with the data.

The calculation of the branching ratio for the decay of a charmonium state to a given hadronic final state is not possible in potential models since no predictions are made beyond the formation of the gluonic state. QCD sum rules, on the other hand, can make certain predictions about the branching ratios to simple final states. In Table 4.10 we compare two of these predictions with our measurements. The agreement with experiment (at least in the case of the χ_2) is probably fortuitous given the large theoretical uncertainties.

Finally, the branching ratios of the χ states to $\eta\eta$ cannot be calculated from first principles. However, we can calculate the expected branching ratios if we assume that SU(3) is a good symmetry. In this case, the branching ratios to $\eta\eta$ should be the same as the branching ratios to $\pi^0\pi^0$ times a phase space and barrier factor which goes as $p^{(2l+1)}$ where p is the momentum of the π^0 or η in the χ rest frame and l is the spin of the χ. Table 4.11 compares the measured ratios with this prediction.

¶ The prediction involving the branching ratio of the χ_2 to $\gamma\gamma$ have been corrected to take into account the 15.8% branching ratio of $\chi_2 \to \gamma J/\psi$.

Parameter	Measurement	Predicted by	Prediction
$\Gamma_{\gamma\gamma}(\chi_0)$ (keV/c^2)	4.0 ±2.8	L. O. QCD	2.96- 6.52[32]
		Relativ. Corr.	1.34 - 1.48[32]
		QCD Sum Rule	4.6 - 5.4[33]
$\Gamma_{\gamma\gamma}(\chi_2)$ (keV/c^2)	2.8 ±2.0	L. O. QCD	0.88- 1.7[32]
		Relativ. Corr.	0.40 - 0.53[32]
		QCD Sum Rule	1.2 - 1.4[33]
BR($\chi_0 \rightarrow \gamma\gamma$)	4.5 ±2.2 ±2.0	L. O. QCD	13.1
	$\times 10^{-4}$		$\times 10^{-4}$
BR($\chi_2 \rightarrow \gamma\gamma$)	9.5 ±2.9 ±4.5	L. O. QCD	11.1
	$\times 10^{-4}$		$\times 10^{-4}$
BR(χ_2) / BR(χ_0)	2.1 ±1.8	L. O. QCD	0.85
		F. O. QCD	0.93

Table 4.8 Comparison of $\chi_{0,2} \rightarrow \gamma\gamma$ partial widths to theoretical predictions.

(L. O. QCD = Lowest Order QCD Potential Models.

F. O. QCD = First Order QCD Potential Models)

Parameter	Measurement	Predicted by	Prediction
$\Gamma_{\gamma\gamma}(\eta_c')$ (keV/c^2)	< 70	Lowest Order QCD	4.5[11]
		QCD Sum Rule	$\ll \Gamma_{\eta_c}$[15]
BR($\eta_c' \to \gamma\gamma$)	$< 1 \times 10^{-2}$	Lowest Order QCD	1.3 $\times 10^{-3}$[11]

Table 4.9 Comparison of $\eta_c' \to \gamma\gamma$ upper limit to theoretical predictions.

Parameter	Measurement ($\times 10^{-3}$)	Predicted by	Prediction
BR($\chi_0 \to \pi\pi$)	(10.5 $\pm$0.9 $\pm$1.8)	QCD Sum Rules	$\approx$ 17 $\times 10^{-3}$[34]
BR($\chi_2 \to \pi\pi$)	(3.6 $\pm$0.6 $\pm$1.2)	QCD Sum Rules	$\approx$ 3.6 $\times 10^{-3}$[34]

Table 4.10 Comparison of branching ratios of $\chi_{0,2} \to \pi^0\pi^0$ to theoretical predictions.

	BR($\chi \to \eta\eta$) ($\times 10^{-3}$)	BR($\chi \to \pi^0\pi^0$) ($\times 10^{-3}$)	Ratio	Prediction
χ_0	2.8±1.6	3.5 ±1.2	0.8 ±0.5	0.95
χ_2	0.84±0.58	1.2 ±0.5	0.7 ±0.6	0.79

Table 4.11 Comparison of branching ratios of $\chi_{0,2} \to \eta\eta$ to SU(3) predictions.

References

1) C. N. Yang, *Phys. Rev.* **77** (1950) 242.

2) See, for example, F. E. Close, *An Introduction to Quarks and Partons* (Academic, New York, 1979), p. 362.

3) J. Aubert *et. al.*, *Phys. Rev. Lett.* **33** (1974) 1404.

4) J.-E. Augustin *et. al.*, *Phys Rev. Lett.* **33** (1974) 1406.

5) G. Abrams *et. al.*, *Phys. Rev. Lett.* **33** (1974) 1453.

6) T. Appelquist and H. D. Politzer, *Phys. Rev. Lett.* **34** (1975) 43; C. G. Callan *et. al.*, *ibid.* **34** (1975) 52; A. de Rújula and S. L. Glashow, *ibid.* **34** (1975) 46.

7) B. J. Bjorken and S. L. Glashow, *Phys. Lett.* **11** (1964) 255; S. L. Glashow, J. Iliopoulos, J. Maiaini, *Phys. Rev.* **D2** (1970) 1285.

8) T. Appelquist, A. de Rújula, H. D. Politzer, S. L. Glashow, *Phys. Rev. Lett.* **34** (1975) 365; E. Eichten *et. al.*, *ibid.* **34** (1975) 369.

9) W. Braunschweig *et. al.*, *Phys Lett.* **57B** (1975) 407; G. J. Feldman *et. al.*, *Phys. Rev. Lett* **35** (1975) 821; W. Tannenbaum *et. al.*, *Phys. Rev. Lett* **35** (1975) 1323.

10) T. Himel *et. al.*, *Phys. Rev. Lett* **45** (1980) 1146; R. Partridge *et. al.*, *ibid.* **45** (1980) 1150; C. Edwards *et. al.*, *ibid.* **48** (1982) 70.

11) T. Appelquist, R. M. Barnett, K. Lane, *Ann. Rev. of Nucl. and Part. Sci.* **28** (1978) 387.

12) R. Barbieri, R. Gatto, R. Kögerler, *Phys. Lett.* **60B** (1976) 183.

13) R. Barbieri, M. Caffo, R. Gatto, E. Remiddi, *Phys. Lett.* **95B** (1980) 93.

14) R. Barbieri, M. Caffo, R. Gatto, E. Remiddi, *Nucl. Phys.* **B192** (1981) 61.

15) V. A. Novikov *et. al.*, *Phys. Rep.* **41C** (1978) 1.

16) F. A. Berends and R. Kleiss, *Nucl. Phys.* **B186** (1981) 22.

17) Particle Data Group, *Rev. Mod. Phys.* **56** (1984) S1.

18) C. Baglin *et. al.Proceedings of the XXII International Conference on High Energy Physics, Leipzig, 1984*, edited by A. Meyer and E. Wieczorek (Akademie der Wissenschaften der DDR, Zeuthen, 1984), and R. Cester, private communication.

19) M. Oreglia, Ph.D. thesis, Stanford University, 1980, and SLAC-Report 236 (unpublished).

20) J. Gaiser, Ph.D. thesis, Stanford University, 1982, and SLAC-Report 255 (unpublished).

21) G. Feldman and M. Perl, *Phys. Rep.* **33C** (1977) 285.

22) P.K. Kabir and A.J.G. Hey, *Phys. Rev. D* **13** (1976) 3161.
Note that the first occurrence of $\sin^2\theta_m$ in Eq. (6) of this reference should be replaced by $\sin 2\theta_m$. Also note that this equation is not invariant under the transformation $\theta_1 \rightarrow -\theta_1$ as would be expected. This is due to the fact that the e^+ beam direction defines both the z axis in the Ball frame and the direction of the x' axis in the $\pi^0\pi^0$ rest frame. Accordingly, one can choose either the e^- or e^+ direction to define $\theta_1 = 0$, but care must be taken to maintain this convention throughout.

23) K. Königsmann, in *Quarks, Leptons, and Supersymmetry*, proceedings of the XVIIth Recontre de Moriond - First Session, 1982, edited by J. Tran Tranh Van (Gif-sur-Yvette, France, Editions Frontieres, 1982), and SLAC-PUB-2910.

24) R. Brandelik *et. al.*, *Z. Physik* **C1** (1979) 233.

25) W. Tannenbaum *et. al.*, *Phys. Rev.* **D17** (1978) 1731.

26) T. Himel, Ph.D. thesis, Stanford University, 1979, and SLAC-Report 223 (unpublished).
Note that the χ mass values obtained in this experiment were subsequently updated by the Particle Data Group to incorporate more accurate measurements of the ψ' mass.

27) R. Cowan and J. Irion, private communication.

28) S. Yamada, in *Proceedings 1977 International Symposium on Lepton and Photon Interactions at High Energies*, Hamburg, 1977, edited by F. Gutbrod (Deutsches Electronen-Synchrotron DESY, Hamburg, 1977).

29) J. D. Jackson, *Phys. Lett.* **87B** (1979) 106

30) Jackson, J. D., *Phys. Rev. Lett.* **37** (1976) 1107.

31) M. G. Olsson, A. D. Martin, A. W. Peacock, University of Wisconsin preprint MAD/PH/193

32) L. Bergström *et. al.*, *Z. Physik* **16C** (1983) 263.

33) V. A. Novikov *et. al.*, *Phys. Lett.* **67B** (1977) 409.

34) V. L. Chernyak and A. R. Zhitnitsky, *Nucl. Phys.* **201B** (1982) 492.

Chapter 5

Non-Charmonium Decays (Heavy Mesons)

5.1 Introduction

Recent work by the Mark II collaboration[1] has directed attention to the non-charmonium decays of the ψ'. The Mark II measured the branching ratios of the J/ψ and ψ' to several hadronic final states. The ψ' branching ratio to a given final state X was normalized to the J/ψ branching ratio to the same final state X so that the final results were presented in the form of ratios of branching ratios. The Mark II results are summarized in Table 1.

It will be noted that the first six ratios fall between 8% and 23% with an average of 10.7 $\pm$2.3%. There are two exceptional final states, $\rho\pi$ and $K^{*\pm}K^{\mp}$, which are unobservable at a levels five and sixteen below this rate at 90% confidence level.

The theoretical prediction for these ratios is simply derived if we assume the validity of perturbative QCD. To first order, the dominant decay of the J/ψ is via three gluons, and the branching ratio for this process is proportional to (see Section 5.1)

$$\mathrm{BR}(J/\psi \to ggg) \sim \frac{\alpha_s^3}{\mathrm{M}_{J/\psi}^2} \frac{|\psi(0)|^2}{\Gamma_{full}(J/\psi)} \qquad [5.1]$$

where α_s is the strong coupling constant, $\psi(0)$ is the non-relativistic wavefunction at the origin, and $\mathrm{M}_{J/\psi}$ is the mass of the J/ψ. We can eliminate the dependence

Final State X	Ratio (%)
$p\bar{p}$	8.6 ±2.4
$p\bar{p}\pi^+\pi^-$	15.1 ±4.1
$K^+K^-\pi^+\pi^-$	22.2 ±9.0
$p\bar{p}\pi^0$	14.0 ±6.3
$2\pi^+2\pi^-\pi^0$	9.5±2.7
$3\pi^+3\pi^-\pi^0$	13.0 ±7.0
$K^{*\pm}K^{\mp}$	< 2.07 (90% C.L.)
$\rho\pi$	< 0.63 (90% C.L.)

Table 5.1 Ratios of ψ' to J/ψ branching ratios for hadronic decays (Mark II).[1]

on the wavefunction by using the predicted partial width to leptons from Equation (4.2):

$$\begin{aligned} \mathrm{BR}(J/\psi \to ggg) &\sim \frac{\alpha_s^3}{\mathrm{M}^2_{J/\psi}} \frac{\Gamma(J/\psi \to l^+l^-)\mathrm{M}^2_{J/\psi}}{\Gamma_{full}(J/\psi)} \\ &\sim \alpha_s^3 \mathrm{BR}(J/\psi \to e^+e^-) \end{aligned} \qquad [5.2]$$

The derivation is identical for the ψ'. If we assume that α_s does not vary significantly from the J/ψ mass to the ψ' mass, we see that

$$\frac{\mathrm{BR}(\psi' \to ggg)}{\mathrm{BR}(J/\psi \to ggg)} = \frac{\mathrm{BR}(\psi' \to l^+l^-)}{\mathrm{BR}(J/\psi \to l^+l^-)} = 12.0 \pm 2.2\% \qquad [5.3]$$

where we have used the experimental leptonic branching ratios from the Particle Data Group[2] . There currently does not exist a complete description of the process by which the gluons are converted into observable hadrons. However, if we assume that this unknown process does not change substantially between the masses of the J/ψ and ψ', the ratio of branching ratios to any hadronic final state X should be

the same as the ratio of branching ratios to three gluons:

$$\frac{\mathrm{BR}(\psi' \to X)}{\mathrm{BR}(J/\psi \to X)} \approx 12\% \qquad [5.4]$$

in good agreement with the values found for the first six decay modes given before but in striking disagreement with the results for the $\rho\pi$ and $K^{*\pm}K^{\mp}$ final states.

Although we have derived this simple result in the context of two quarks annihilating to form three gluons, it is generally valid for any process involving the initial annihilation of the quarks. In particular, it has been noted by several authors[3] that the partial width of a quarkonium state to a photon plus two gluons (Fig. 5.1) is given by an expression similar to equation (4.1) with one factor of α_s replaced by α and a modification of the SU(3) color factor. Thus, equation [5.4] should hold for radiative decays as well as hadronic decays.

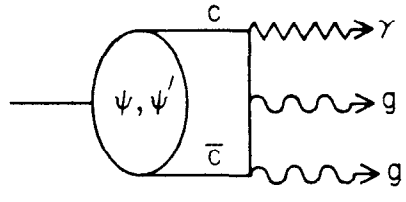

Fig. 5.1 Feynman diagram of the annihilation of the J/ψ or ψ' into two gluons and a photon.

As part of the current study, we have searched for radiative decays of the ψ' to attempt to find other channels which violate the "12% rule". We discuss in this chapter radiative decays of the ψ' which can be studied with an exclusive analysis, namely, $\psi' \to \gamma f$ and $\psi' \to \gamma\theta$. (The decays $\psi' \to \gamma\eta$ and $\psi' \to \gamma\eta'$ require a more specialized analysis and are discussed separately in Chapter 6.) These decays have

been thoroughly studied on the J/ψ, and we present a parallel study of the decays $J/\psi \to \gamma f$ and $J/\psi \to \gamma\theta$ which can be used to check the validity of the analysis techniques.

5.2 $J/\psi, \psi' \to \gamma\pi^0\pi^0$

The signatures of the decays $J/\psi, \psi' \to \gamma\pi^0\pi^0$ are in principle simple. If we were to demand that all final-state particles be observed in the detector, we would look for events with five γ's. Since the γ's deposit their total energy in the Ball, we would be able to impose energy and momentum constraints on the observed events. The addition of the two π^0 invariant mass constraints would allow us to make 5C fits. (One constraint is lost due to the unknown z-vertex.)

However, the decays $J/\psi, \psi' \to \gamma\pi^0\pi^0$ rarely leave five separated tracks. The two γ's from the decay of an energetic π^0 will have a small opening angle in the frame of the Ball. The inner radius of the Ball and the Moliére radius of NaI are such that the showers from these two γ's begin to overlap around $E_{\pi^0} = 600$ MeV and cannot be separated by the offline software starting around $E_{\pi^0} = 800$ MeV. To identify and measure the four-vectors of these π^0's requires the use of the more sophisticated shower identification routine PIFIT (described in Appendix C). Figure 5.2 shows the efficiency for detecting a single π^0 uniformly distributed in solid angle as a function of π^0 energy and the fraction flagged as separated and merged. Merged π^0's can be identified in a single connected region or two connected regions. (See Section 3.3.3.) Note that the efficiency shown in the plot is not applicable to a π^0 embedded in a real event due to overlaps with other particles. We see that although the efficiency for detecting a π^0 is roughly constant, the fractions of π^0's in the three categories vary dramatically.

Thus, the decays $J/\psi, \psi' \to \gamma\pi^0\pi^0$ may be observed to have three, four, or five tracks depending on whether the γ's from the π^0's are separated or merged with correspondingly different numbers of constraints in the kinematic fit. (As noted in Chapter 3, we treat π^0's which decay into γ's which are merged as one track.) We

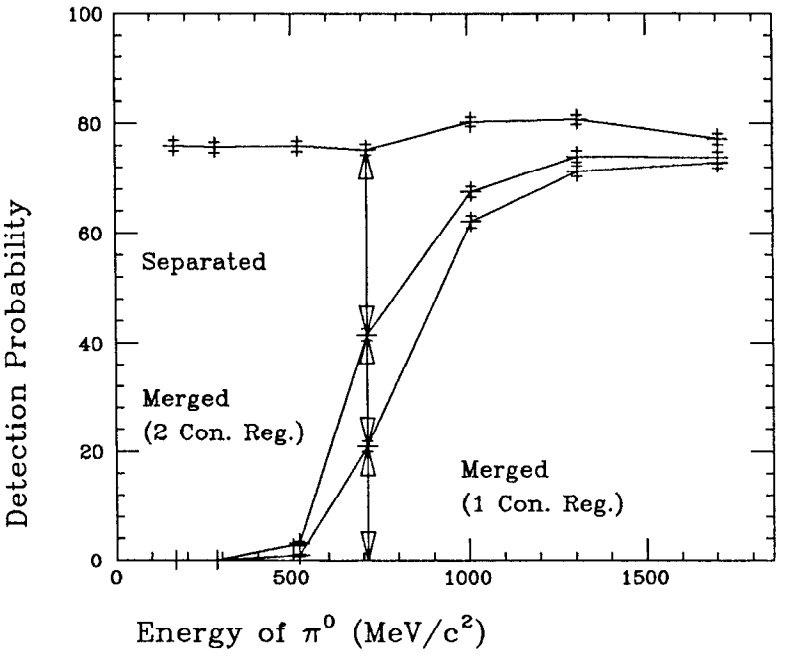

Fig. 5.2 Efficiency for detection of single Monte Carlo π^0's.

describe briefly below the cuts used to select events contributing to $J/\psi, \psi' \rightarrow \gamma\pi^0\pi^0$ in each of these topologies.

5.2.1 *3 Observed Tracks*

In order to search for this topology, we sort the three tracks by their PIFIT masses. Figures 5.3 and 5.4 show the largest PIFIT mass in the event plotted against the second largest PIFIT mass for the J/ψ and ψ' datasets, respectively. As discussed in Chapter 4, the two clusters correspond to the topologies $\gamma\gamma\gamma$ and $\gamma\pi^0\pi^0$. Requiring that the two highest PIFIT masses each be above 90 MeV/c^2 corresponds to the cut whose boundaries are shown in the plots. Additionally, we require that the PIFIT mass of the remaining track be below 90 MeV/c^2. We fit to energy and momentum constraints and place a confidence level cut at 10%.* The

* As noted in Appendix B, the fit errors for each track depend on whether it has been classified

small plots in Figs. 5.3 and 5.4 show the confidence level plots for these fits.

5.2.2 *4 Observed Tracks*

Here we search for events with one track having a large PIFIT mass and an open π^0 in the remaining three tracks. Figures 5.5 and 5.6 shows the PIFIT mass of all tracks which have been PIFITed *vs.* the three invariant mass combinations of the remaining tracks.† We see in both the J/ψ and ψ' data a concentration of events with a high PIFIT mass and an invariant mass combination near the π^0 mass. We fit the events to energy and momentum conservation and constrain two of the γ's to form a π^0 mass. The small plots in Figs. 5.5 and 5.6 show the confidence level distributions for all fits. Note that one event may have more than one combination of tracks which falls inside the box in Figs. 5.5 and 5.6. In such a case we use the fit to remove the ambiguity by accepting that assignment of tracks which has the highest confidence level. We require that an event have at least one good fit, where a good fit is defined to have a confidence level greater than 10%. The percentage of events in which the fit must be employed to resolve ambiguities is small as illustrated by the plots in the lower right corners of Figs. 5.5 and 5.6 which show the number of good fits per event.

5.2.3 *5 Observed Tracks*

Finally, we look for events with five tracks, none of which has a PIFIT mass consistent with a π^0 mass. In this topology, there is a background in the ψ' data, namely $\psi' \to \gamma\gamma J/\psi, J/\psi \to 3\gamma$, which can be confused with the processes in which

---

as a γ or a π^0.

† Simple counting would yield $4 \times 3 = 12$ entries in this plot per event. However, we plot the PIFIT mass only for those tracks we have been PIFITed, i.e., those tracks which have more than 500 MeV or are in a connected region with more than one track. Also, we form invariant mass combinations between pairs of tracks which have not been flagged as π^0's. Thus, there is actually a maximum of 12 entries per event in this plot.

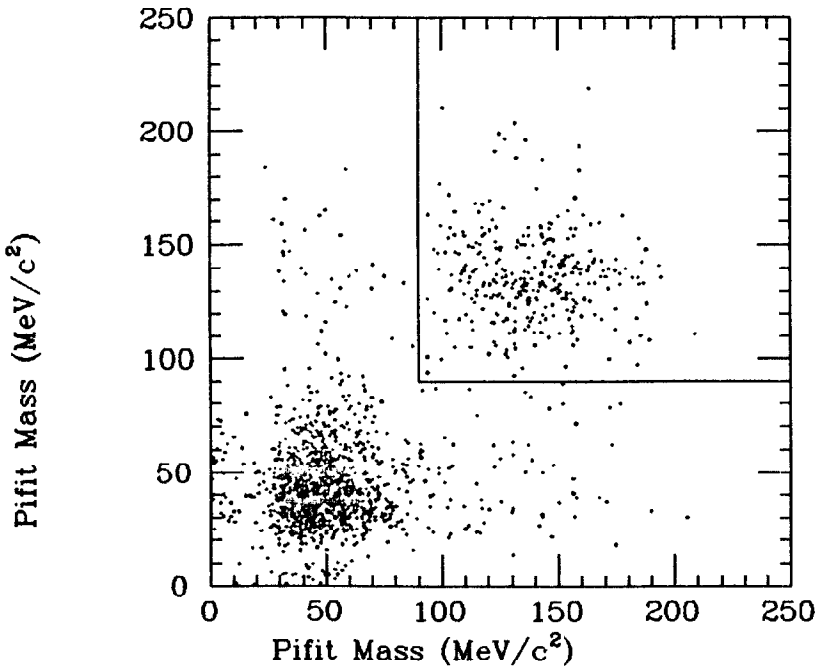

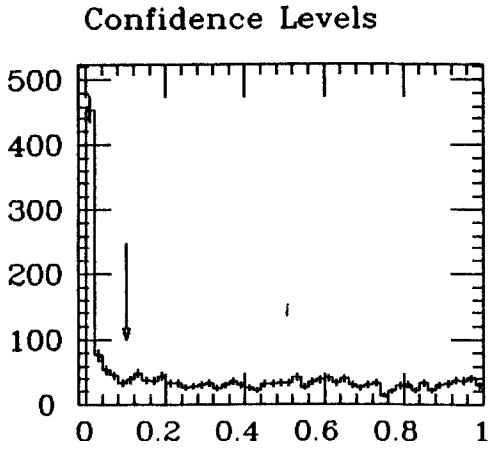

Fig. 5.3 PIFIT mass *vs.* PIFIT mass for three track events : J/ψ data.
(Inset shows confidence levels of kinematic fits. Cuts shown by box and arrow.)

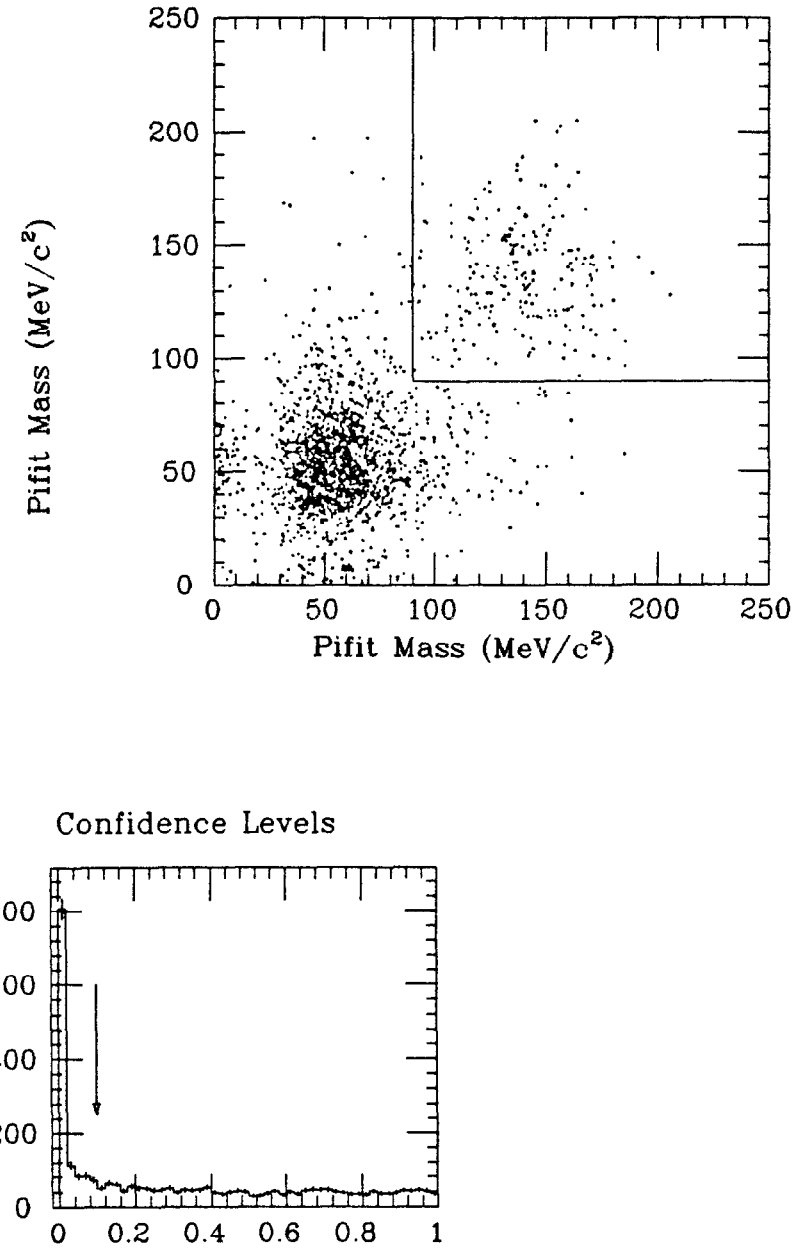

Fig. 5.4 PIFIT mass *vs.* PIFIT mass for three track events : ψ' data.
(Inset shows confidence levels of kinematic fits. Cuts shown by box and arrow.)

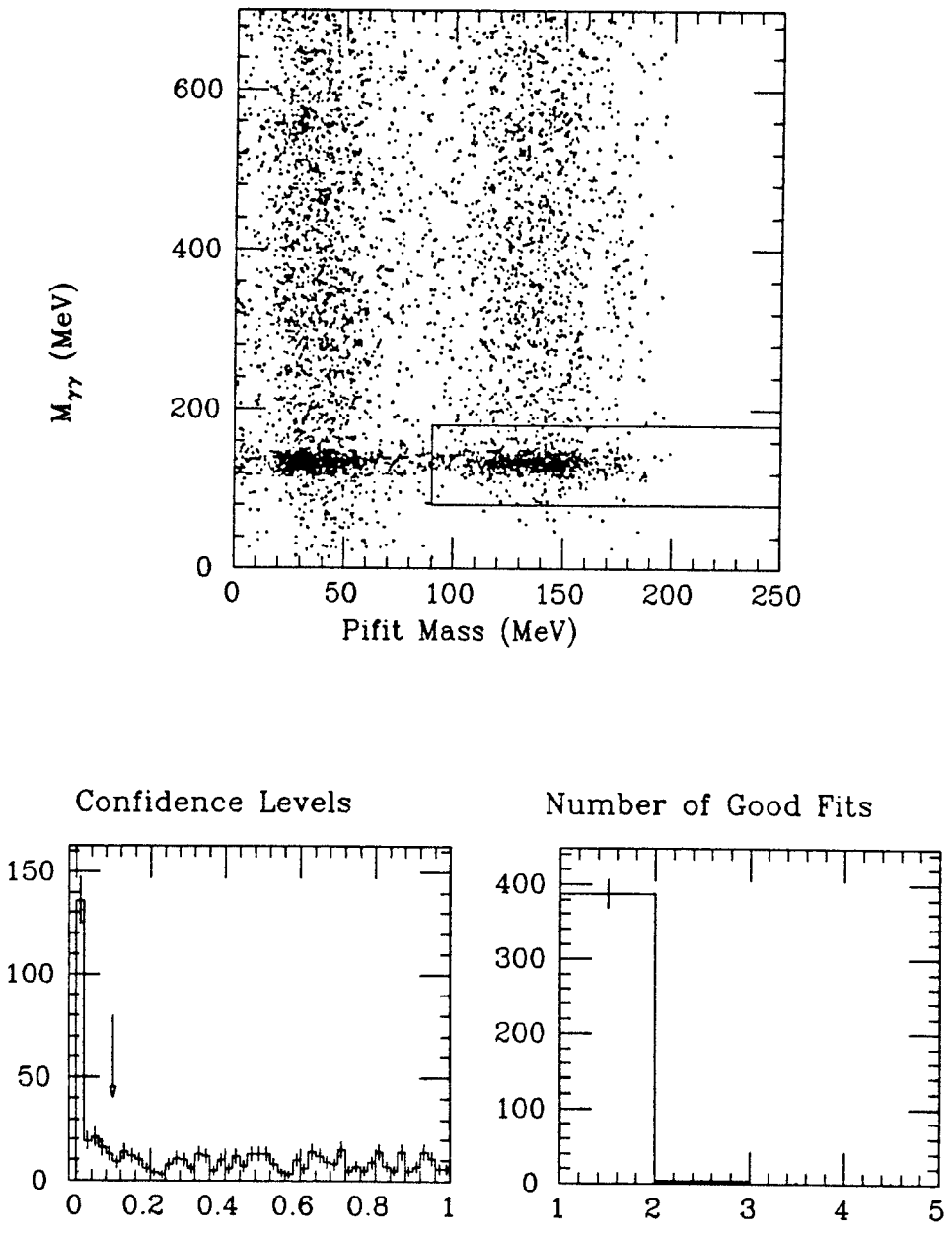

Fig. 5.5 PIFIT mass *vs.* 2γ invariant mass for four track events: J/ψ data.
(Insets show confidence levels of kinematic fits and number of good fits. Cuts shown by box and arrow.)

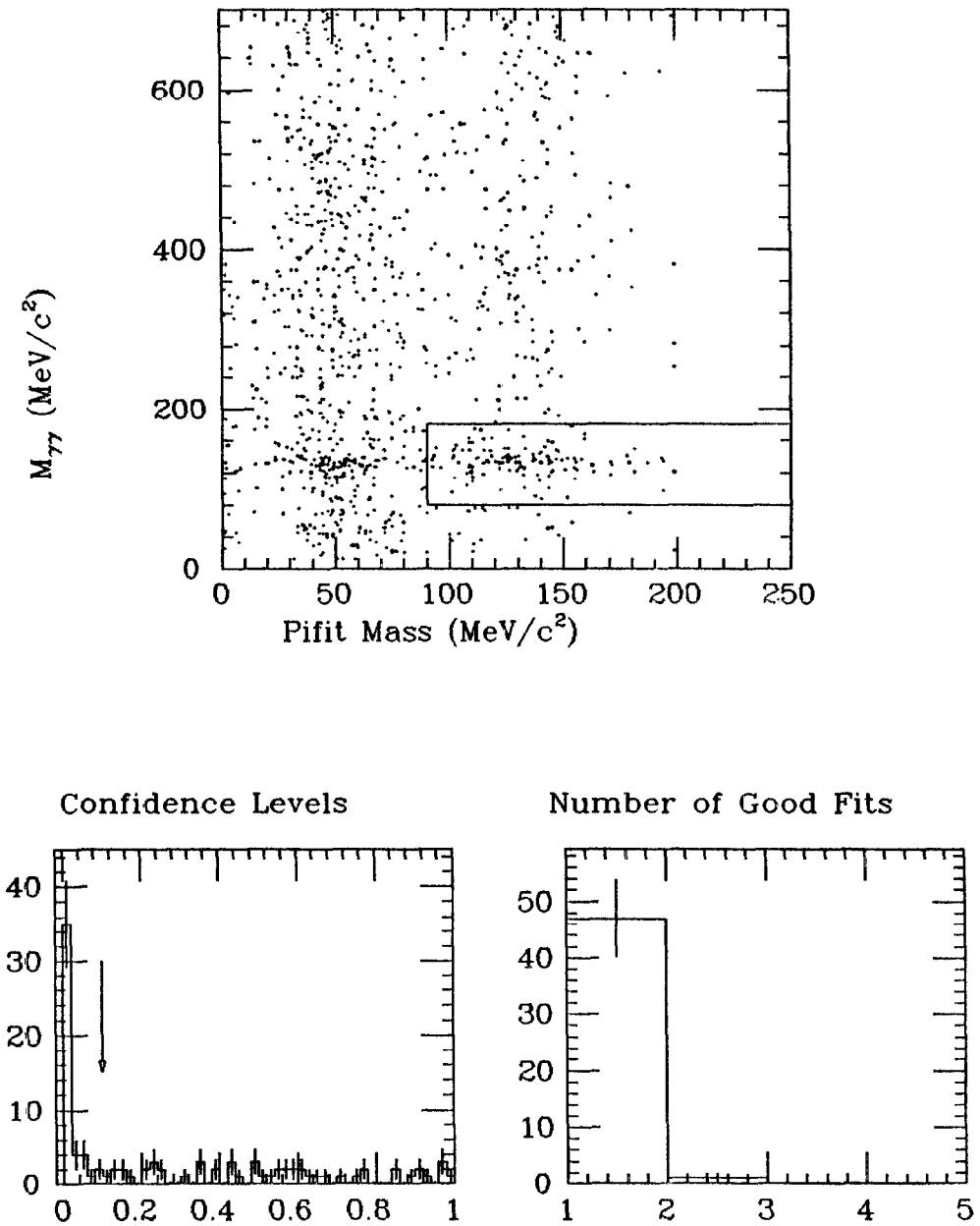

Fig. 5.6 PIFIT mass *vs.* 2γ invariant mass for four track events: ψ' data.
(Insets show confidence levels of kinematic fits and number of good fits. Cuts shown by box and arrow.)

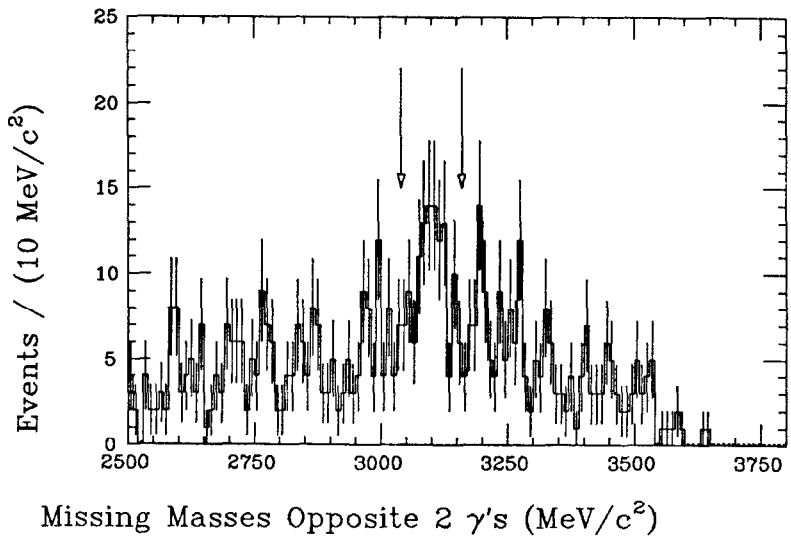

Fig. 5.7 Missing mass opposite 2 γ's: ψ' data.

we are interested. The first part of this decay chain includes cascade transitions through the χ states and $\psi' \rightarrow \eta J/\psi$, while the second part includes $J/\psi \rightarrow \gamma\eta$, $\eta \rightarrow \gamma\gamma$ and $J/\psi \rightarrow \gamma\eta'$, $\eta' \rightarrow \gamma\gamma$. In order to exclude these events, we examine the missing mass opposite all pairs of γ's in the 5-track ψ' dataset as shown in Fig. 5.7. We see a clear peak at the mass of the J/ψ, and we remove those events which have a missing mass which falls between the arrows.

Figure 5.8 shows the 2γ *vs.* 2γ mass for all pairs of γ's in the 5-track J/ψ dataset. Figure 5.9 shows the same plot for the ψ' events which pass the above cut. We see events consistent with $\gamma\pi^0\pi^0$ in both plots, and select those events which fall inside the boxes. These events are fitted to energy and momentum conservation plus the additional constraints that two pairs of γ's form π^0's. Once again, if an event has more than one assignment of tracks which falls inside the box, we accept the one with the highest confidence level. In any case, we require that an event

have at least one combination of tracks which gives a confidence level greater than or equal to 10% . The small plots in Figs. 5.8 and 5.9 show the distribution of confidence levels and the number of good fits per event.

5.2.4 *Combined Topologies*

We display the events which pass the confidence level cut in the form of pseudo-Dalitz plots in which the invariant mass squared of the two π^0's is plotted against the $\gamma\pi^0$ invariant mass squared (Figs. 5.10 and 5.11). Note that each event is plotted twice (once for each $\gamma\pi^0$ combination) with the same abscissa. The bands at large $\pi^0\pi^0$ invariant mass in the ψ' plot correspond to the decays $\psi' \rightarrow \gamma\chi_{0,2}$, $\chi_{0,2} \rightarrow \pi^0\pi^0$ as discussed in Chapter 4. Figures 5.12 - 5.15 show the distributions of the $\gamma\pi^0$ and $\pi^0\pi^0$ invariant masses corresponding to these Dalitz plots. (We show the $\pi^0\pi^0$ invariant mass plot only up to 3200 MeV/c^2 in the ψ' case since we have previously studied the $\chi_{0,2} \rightarrow \pi^0\pi^0$ decays. Also, there are twice as many counts in the $\gamma\pi^0$ plots as in the $\pi^0\pi^0$ plots.)

We are primarily interested in $\pi^0\pi^0$ resonances. However, the $\gamma\pi^0$ plot is of interest insofar as we are able to remove any background of the form $J/\psi,\psi' \rightarrow X\pi^0$, $X \rightarrow \gamma\pi^0$. The Mark III collaboration has announced preliminary results of studies of hadronic decays of the J/ψ.[4] They report BR($J/\psi \rightarrow \omega\pi^0$) = (6.7 $\pm$0.6 $\pm$1.1) $\times 10^{-4}$ where the first error is statistical and the second systematic. This decay is of interest here inasmuch as the ω decays to $\gamma\pi^0$ with a branching ratio of 8.7%.[2] We note that in the $\gamma\pi^0$ plot that there is some structure near the ω mass, although the signal appears on the peak of a rather uneven background. In order to determine the boundaries of an appropriate cut, we examine the decay $J/\psi \rightarrow \omega\pi^0\pi^0$, $\omega \rightarrow \gamma\pi^0$. Events consistent with this decay will be observed in the Ball with 4, 5, or 6 tracks depending on how many π^0's are merged. Figure 5.16 shows the $\gamma\pi^0$ invariant mass plot of events from these three topologies which pass a kinematic fit with a confidence level of 10% or greater. (Each event appears in this plot three times.) The ω peak can be fit with a Gaussian of mean = 785 $\pm$4 MeV/c^2 and σ = 27.6

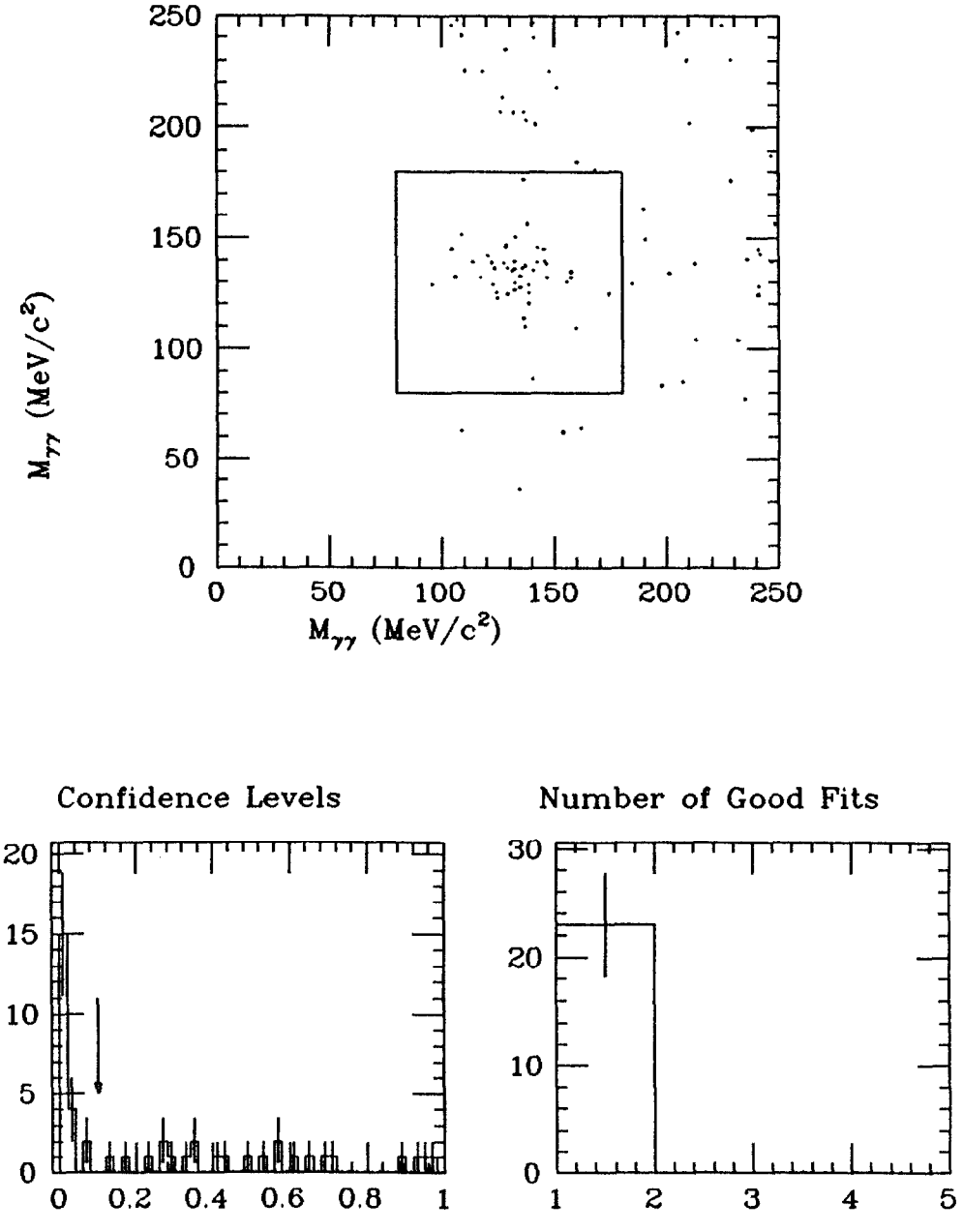

Fig. 5.8 2γ invariant mass *vs.* 2γ invariant mass for five track events: J/ψ data.
(Insets show confidence levels of kinematic fits and number of good fits. Cuts shown by box and arrow.)

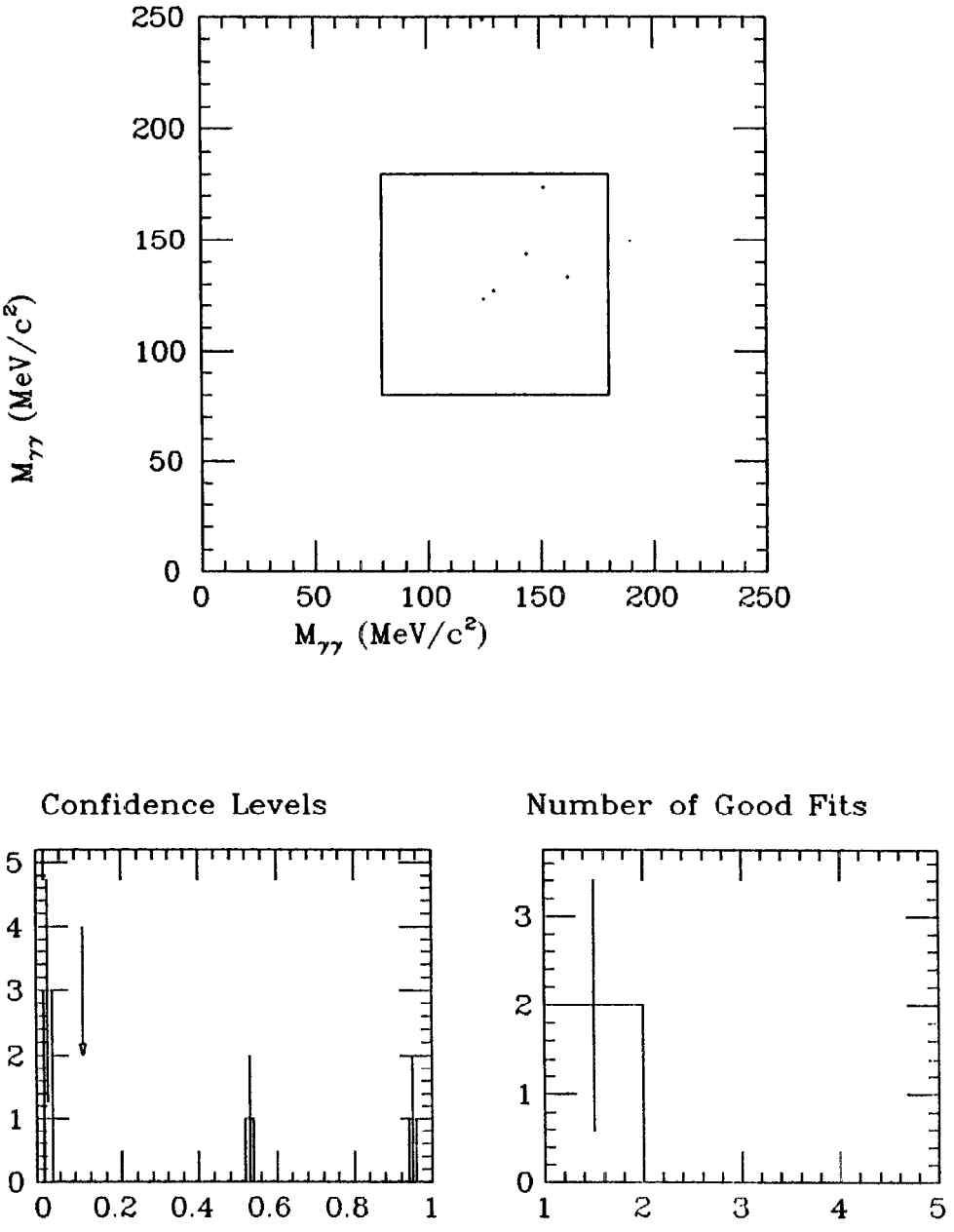

Fig. 5.9 2γ invariant mass *vs.* 2γ invariant mass for five track events: ψ' data.
(Insets show confidence levels of kinematic fits and number of good fits. Cuts shown by box and arrow.)

± 3.7 MeV/c^2. Returning to $J/\psi \rightarrow \gamma\pi^0\pi^0$, Fig. 5.17 shows the same plot as Fig. 5.14 with arrows indicating the boundaries of a window 55 MeV/c^2 (i.e., 2σ) wide centered at 785 MeV/c^2. We eliminate any event which has a $\gamma\pi^0$ combination inside of this window. The same decay is much more difficult to detect on the ψ' due to the $\pi^0\pi^0$ decays of the χ states which must peak at low $\gamma\pi^0$ mass due to the low energy of the direct γ in these decays. However, in order to maintain consistency between the J/ψ and ψ' analyses, we make the same $\gamma\pi^0$ cut for the ψ' data. Figures 5.18 and 5.19 show the final $\pi^0\pi^0$ distributions.‡

‡ It should again be noted that the distribution shown in Fig. 5.19 is dominated by the transitions $\psi' \rightarrow \gamma\chi_0$, $\chi_0 \rightarrow \pi^0\pi^0$ and $\psi' \rightarrow \gamma\chi_2$, $\chi_2 \rightarrow \pi^0\pi^0$ which have been previously discussed in chapter 4. The plot in Fig. 5.19 extends only up to 3 GeV as we now wish to focus attention on the non-charmonium decays.

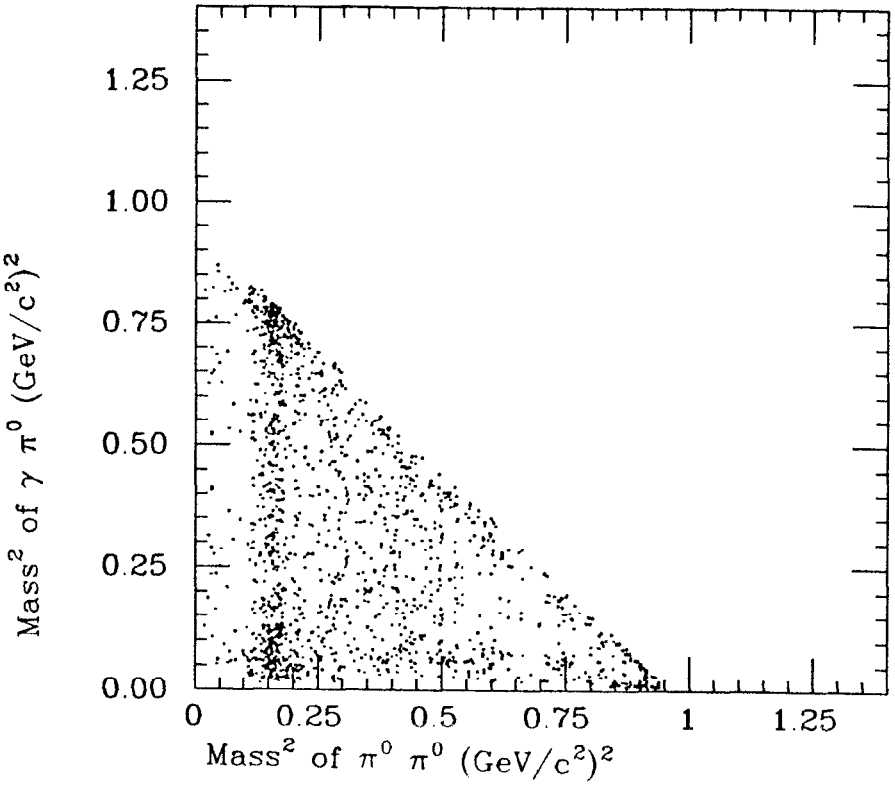

Fig. 5.10 $\pi^0\pi^0$ mass *vs.* $\gamma\pi^0$ mass for all events: J/ψ data.

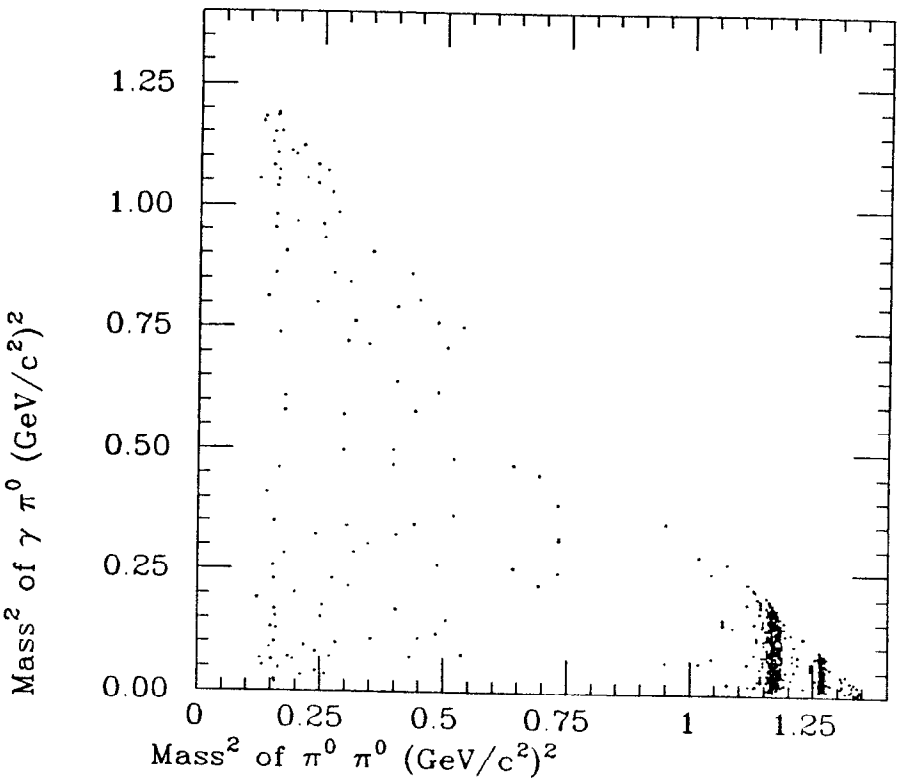

Fig. 5.11 $\pi^0\pi^0$ mass *vs.* $\gamma\pi^0$ mass for all events: ψ' data.

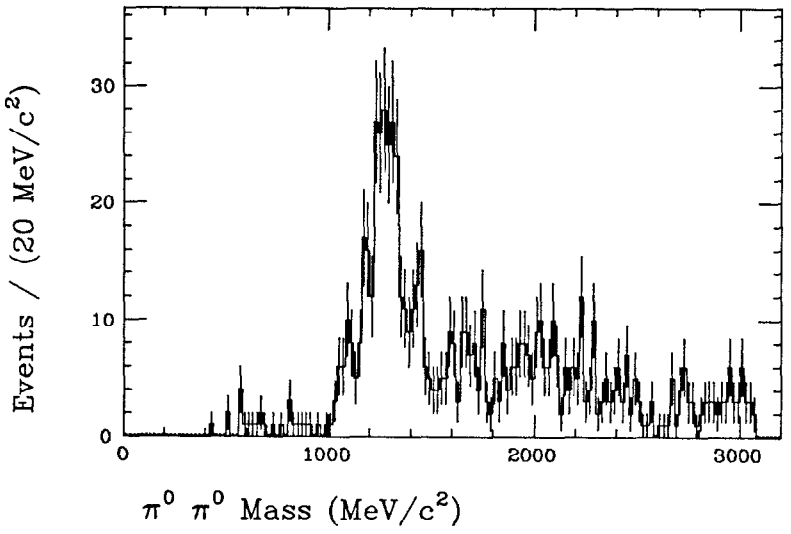

Fig. 5.12 $\pi^0\pi^0$ invariant mass distribution in $J/\psi \rightarrow \gamma\pi^0\pi^0$: J/ψ data.

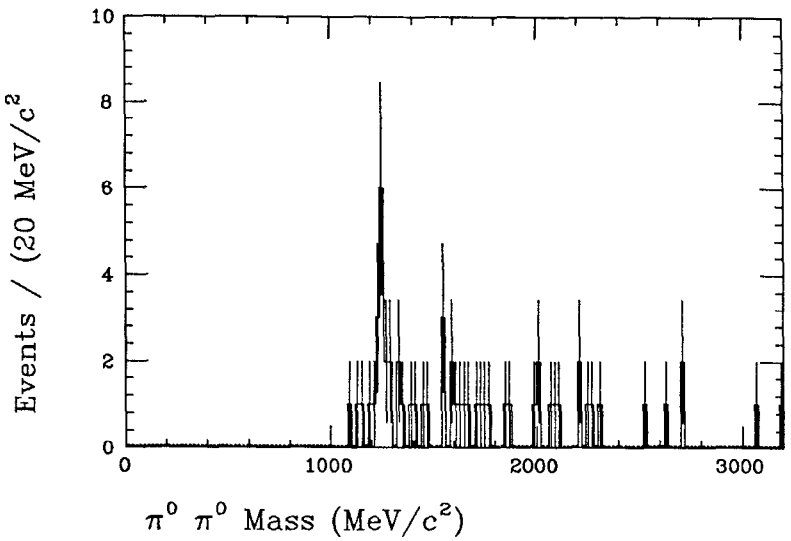

Fig. 5.13 $\pi^0\pi^0$ invariant mass distribution in $\psi' \rightarrow \gamma\pi^0\pi^0$: ψ' data.

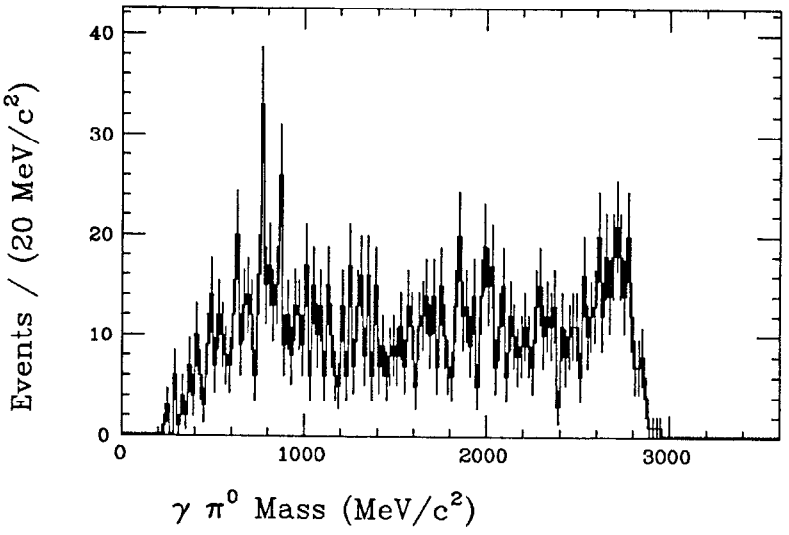

Fig. 5.14 $\gamma\pi^0$ invariant mass distribution in $J\psi \rightarrow \gamma\pi^0\pi^0$: J/ψ data

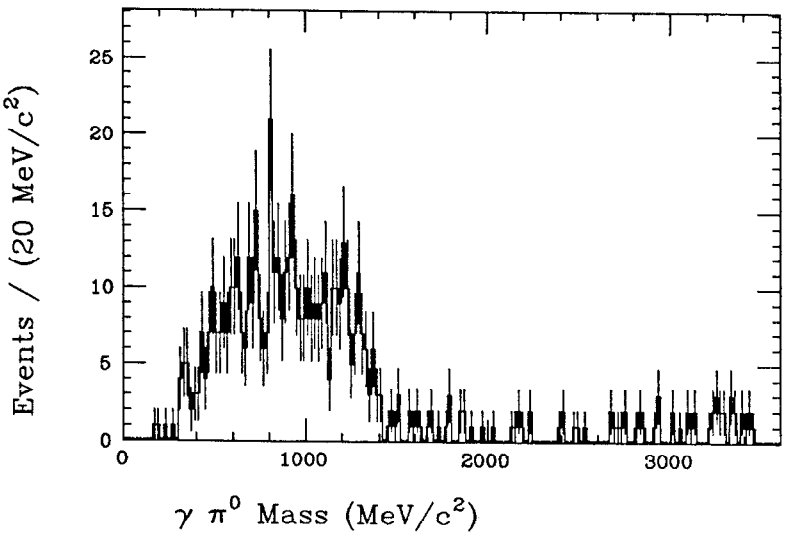

Fig. 5.15 $\gamma\pi^0$ invariant mass distribution in $\psi' \rightarrow \gamma\pi^0\pi^0$: ψ' data.

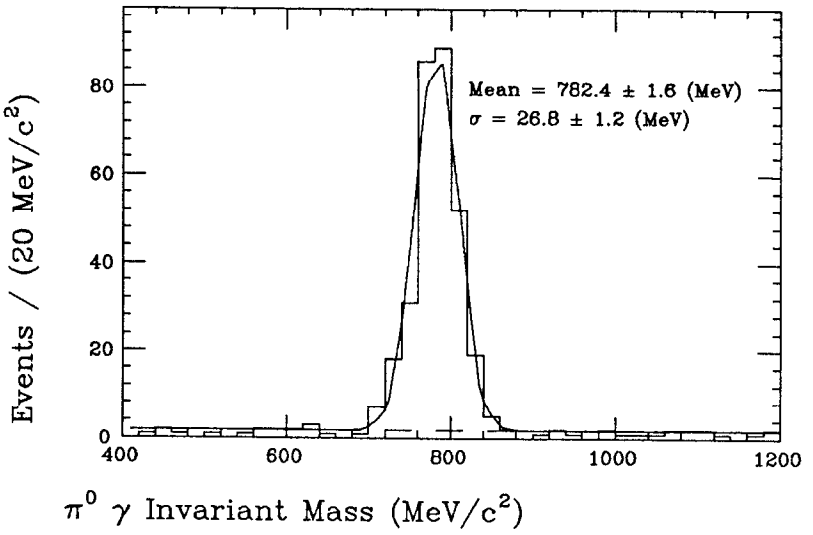

Fig. 5.16 $\gamma\pi^0$ invariant mass distribution from $J/\psi \rightarrow \gamma\pi^0\pi^0\pi^0$

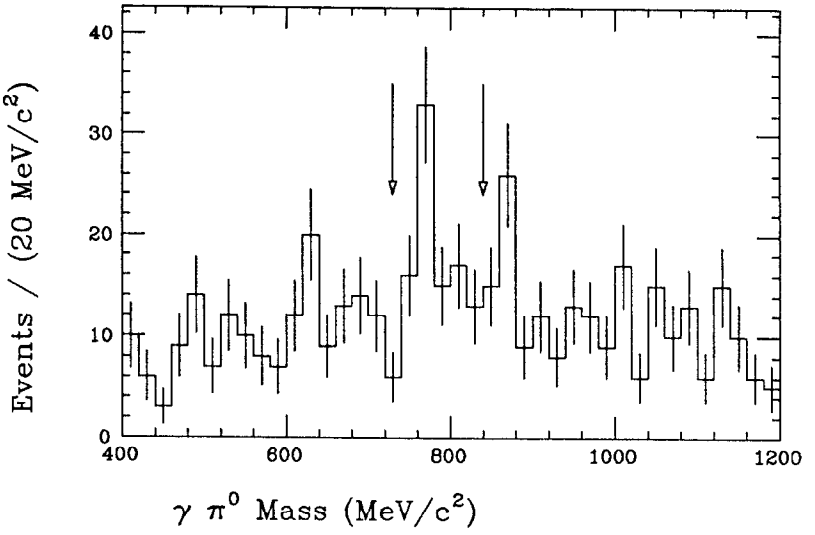

Fig. 5.17 $\gamma\pi^0$ invariant mass distribution in $J/\psi \rightarrow \gamma\pi^0\pi^0$.

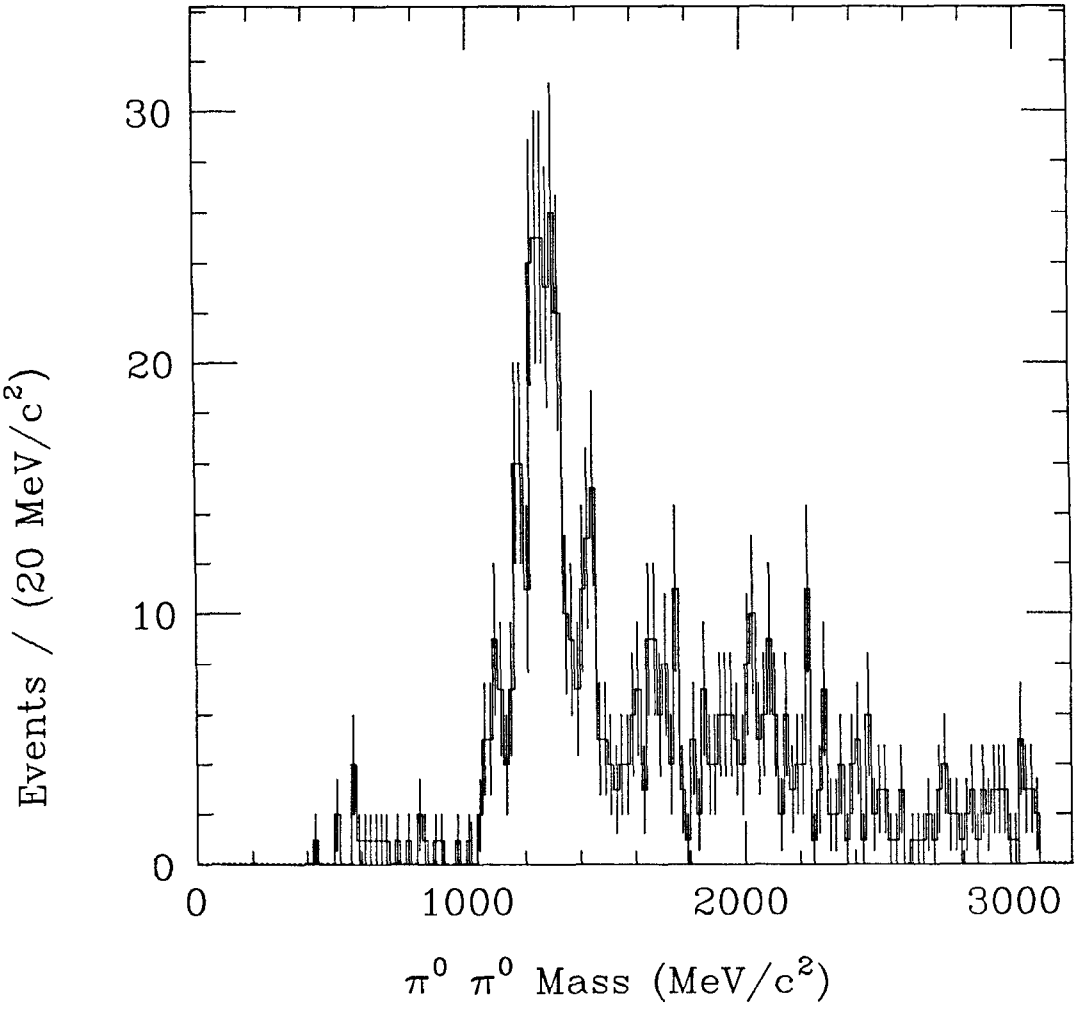

Fig. 5.18 $\pi^0\pi^0$ invariant mass distribution in $J/\psi \rightarrow \gamma\pi^0\pi^0$ after ω cut: J/ψ data.

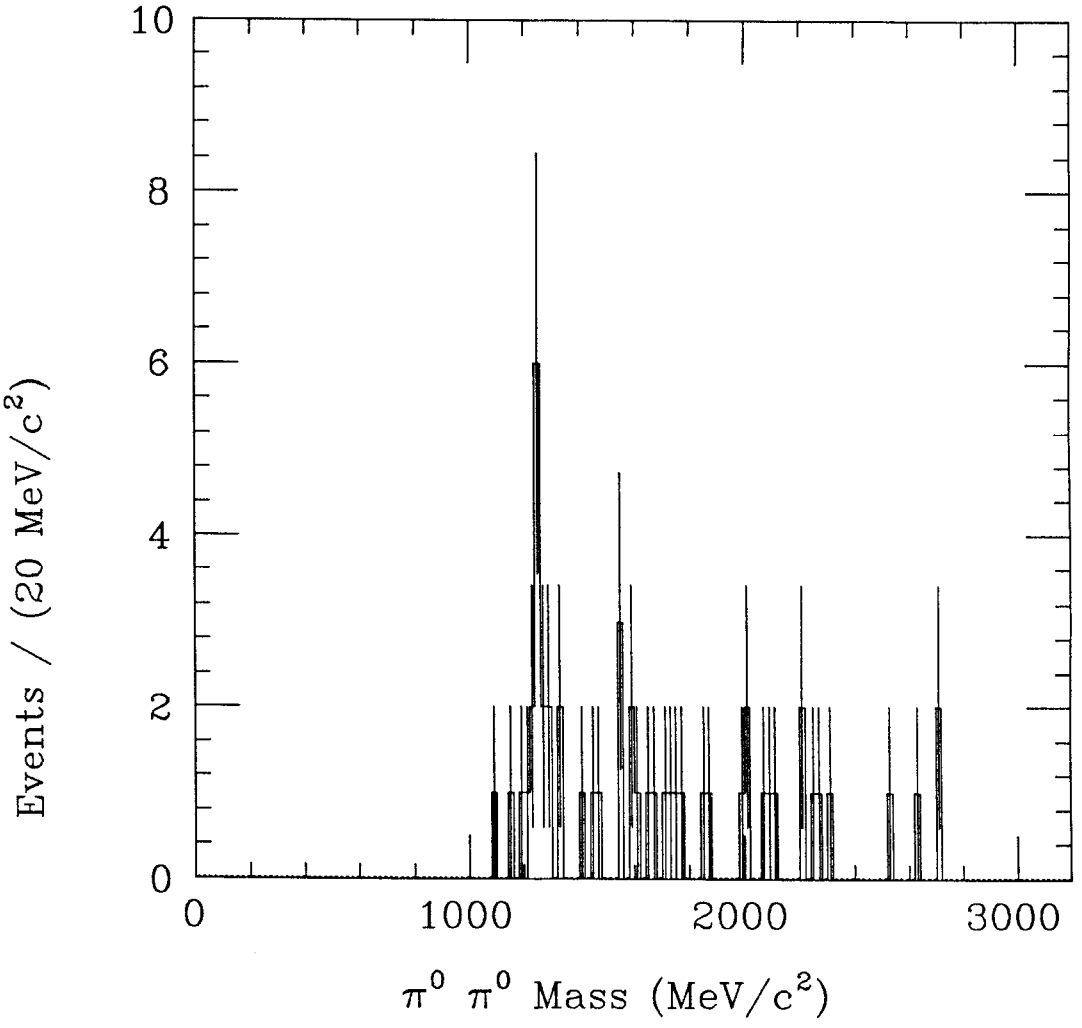

Fig. 5.19 $\gamma\pi^0$ and $\pi^0\pi^0$ invariant mass distribution in $\psi' \rightarrow \gamma\pi^0\pi^0$ after ω cut: ψ' data.

5.2.5 *Analysis of the $\pi^0\pi^0$ Spectrum*

We investigate first the energy dependence of our analysis procedure. We generate several Monte Carlo datasets of the decays $J/\psi, \psi' \rightarrow \gamma X, X \rightarrow \pi^0\pi^0$ (with the width of X set to zero and all angular distributions flat) for different values of the mass of X and subject them to the same analysis as the data. Figures 5.20 and 5.21 show the fractions of the Monte Carlo events which survive plotted against the mass of X. The efficiency drops rapidly below $M_X = 500$ MeV/c^2 due to the merging of the showers from the two π^0's. However, in the range 900 MeV/$c^2 \leq M_X \leq M_{J/\psi}$ or $M_{\psi'}$, the efficiency is flat within errors. We shall be concerned with a signal at the mass of the f(1270) which is comfortably above the efficiency threshold.

We next attempt to fit the J/ψ spectrum. The Mark III collaboration has studied this decay via the charged mode: $J/\psi \rightarrow \gamma\pi^+\pi^-$.[5] Since the C and G parities of the $\pi\pi$ system in $J/\psi \rightarrow \gamma\pi\pi$ are even, the total isotopic spin of the two π's must be either zero or two. Thus, structures seen in $J/\psi \rightarrow \gamma\pi^+\pi^-$ should also been present in $J/\psi \rightarrow \gamma\pi^0\pi^0$. If the isotopic spin of such a structure is zero, it should be produced in $J/\psi \rightarrow \gamma\pi^0\pi^0$ with a product branching ratio half that observed in $J/\psi \rightarrow \gamma\pi^+\pi^-$; if the isotopic spin is two, the ratio is reversed. The Mark III collaboration reports evidence for structures in the $\pi^+\pi^-$ spectrum near 1.7 and 2.1 GeV in addition to the f at 1.27 GeV (Fig. 5.22). They identify the 1.7 GeV structure with the θ, and terms the 2.1 GeV structure "X". In order to parametrize the background in our $\pi^0\pi^0$ invariant mass plot, we fit the distribution to two non-interfering relativistic Breit-Wigner line shapes with means and widths fixed to the values found for the high mass structures in the Mark III study plus a relativistic Breit-Wigner of variable mean and width corresponding to the f.§ Figure 5.23 shows

§ As in the Mark III study, we do not include an energy-dependent width. The variations in the fitted parameters when this effect and the small contribution from the fitted mass resolution ($\sigma \approx$ 20 MeV/c^2 at the mass of the f) are taken into account are included in the systematic errors.

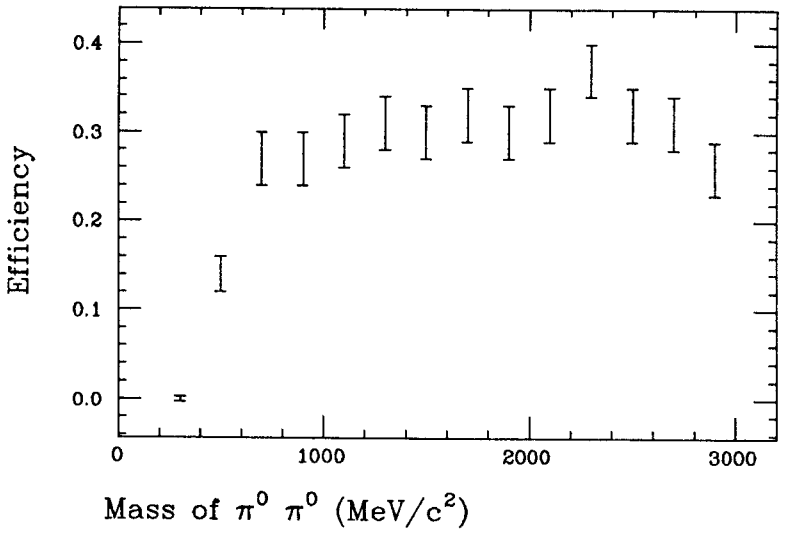

Fig. 5.20 Monte Carlo detection efficiency for $J/\psi \rightarrow \gamma X, X \rightarrow \pi^0\pi^0$ as a function of M_X .

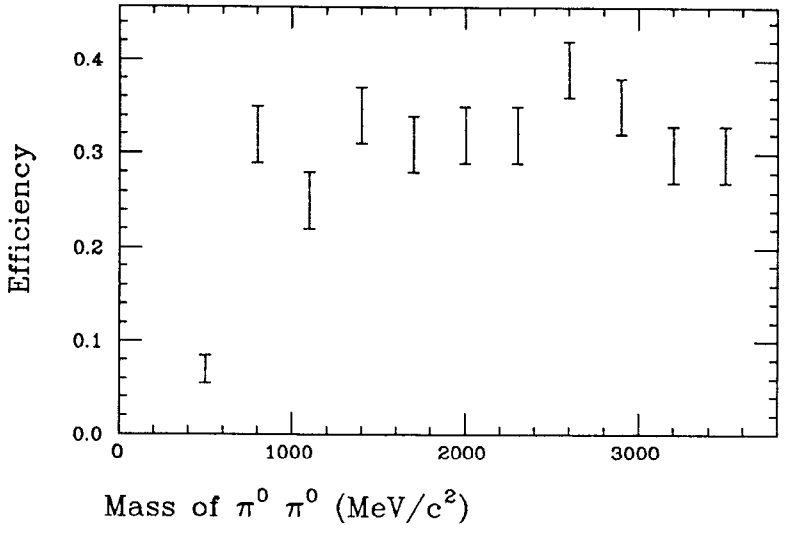

Fig. 5.21 Monte Carlo detection efficiency for $\psi' \rightarrow \gamma X, X \rightarrow \pi^0\pi^0$ as a function of M_X .

a fit to the $\pi^0\pi^0$ invariant mass distribution on the J/ψ with these structures plus a third-order Legendre polynomial. Figure 5.24 shows the same plot with a fit to the same structures but with the width of the f fixed to the Particle Data Group value of 178 MeV/c^2.[2] In both fits the mass of the f (1278 $\pm$7 $\pm$5 MeV/c^2 and 1288 $\pm$7 $\pm$5 MeV/c^2) agrees within errors with the Particle Data Group value of 1274 $\pm$5 MeV/c^2.[2] The best fitted width of the f (137 $\pm$15 $\pm$20 MeV/c^2) is just within the error bars of the Particle Data Group value of 178 $\pm$20 MeV/c^2[2] and is consistent with the best value found in the Mark III study (139^{+55}_{-39} MeV/c^2).[5] As is noted in reference 5, the confidence level that all reported measurements of the width of the f come from a common source is only 0.1%. The discrepancy might be related to the possible structure on the high mass side of the f in both the current analysis and the Mark III study. (It is intriguing to note that a hint of a $\pi\pi$ near 1400 MeV/c^2 resonance has been seen in studies of hadronic collisions.[7]) We also note that the confidence level of the fit is reduced if the structures corresponding to the Mark III θ and X signals are removed (Fig. 5.25). As a consistency check of our analysis with that of the Mark III, we measure

$$\begin{aligned} \mathrm{BR}(J/\psi \rightarrow \gamma\theta)\mathrm{BR}(\theta \rightarrow \pi^0\pi^0) &= (7.8 \pm 2.2 \pm 2.7) \times 10^{-5} \\ \mathrm{BR}(J/\psi \rightarrow \gamma X)\mathrm{BR}(X \rightarrow \pi^0\pi^0) &= (9.4 \pm 2.4 \pm 3.2) \times 10^{-5} \end{aligned} \qquad [5.5]$$

to be compared the Mark III measurements of

$$\begin{aligned} \mathrm{BR}(J/\psi \rightarrow \gamma\theta)\mathrm{BR}(\theta \rightarrow \pi^+\pi^-) &= (1.6 \pm 0.4 \pm 0.3) \times 10^{-4} \\ \mathrm{BR}(J/\psi \rightarrow \gamma X)\mathrm{BR}(X \rightarrow \pi^+\pi^-) &= (3.0 \pm 0.5 \pm 0.6) \times 10^{-4} \end{aligned} \qquad [5.6]$$

where an enhancement of a factor of two over the $\pi^0\pi^0$ decays is expected if the isospins of the resonances are zero. Thus, the measured branching ratios for these structures are consistent within errors. However, it should be emphasized that the values in this study are obtained from a highly constrained fit since we have fixed the means and widths of the two resonances. One would not ordinarily include two resonant structures in a fit of the high-mass region of Fig. 5.18, and we have done so only due to the results of the Mark III study.

In order to perform a Monte Carlo simulation of $J/\psi \rightarrow \gamma f$, we need to specify the spins and helicity amplitudes of the particles involved. For this purpose we use a previous Crystal Ball study (using this same dataset) in which the helicity amplitudes x and y (defined in Chapter 4) were found to be 0.88 $\pm$0.13 and 0.04 $\pm$ 0.19, respectively. A Monte Carlo simulation of $J/\psi \rightarrow \gamma f$ with these helicity amplitudes indicates that the detection efficiency of this decay is 6.9 %.¶ Using this detection efficiency with the observed amplitude of 263 $\pm$20 events yields a branching ratio of

$$\mathrm{BR}(J/\psi \rightarrow \gamma f) = (1.7 \pm 0.1 \pm 0.5) \times 10^{-3} \qquad [5.7]$$

where we have included in the systematic error the variation of the fitted amplitude under different background assumptions. This is consistent with the average of all measurements used by the Particle Data Group[2] (excepting the previous Crystal Ball result) of $\mathrm{BR}(J/\psi \rightarrow \gamma f) = (1.6 \pm 0.4) \times 10^{-3}$, and the previous Crystal Ball result of $\mathrm{BR}(J/\psi \rightarrow \gamma f) = (1.48 \pm 0.25 \pm 0.30) \times 10^{-3}$[6]

Having checked our technique on the J/ψ data, we examine the ψ' data. In this case the background is adequately fit by a constant. In addition, we fit a Breit-Wigner line shape of mean and width fixed to the values found in the J/ψ fit to account for the structure seen near the mass of the f (Fig. 5.26). Using the fitted amplitude of 18 $\pm$ 5 events and a Monte Carlo efficiency of 6.6%, we derive

$$\mathrm{BR}(\psi' \rightarrow \gamma f) = (1.5 \pm 0.4 \pm 0.5) \times 10^{-4} \qquad [5.8]$$

where the first error is statistical and the second is systematic. We can take the ratio of this measurement to our previous measurement of $\mathrm{BR}(J/\psi \rightarrow \gamma f)$. A part of the systematic errors in these two measurements is identical and so cancels out.

¶ This efficiency includes the branching ratio of $f \rightarrow \pi^0\pi^0$ of 28%, i.e., the detection efficiency for the decay $J/\psi \rightarrow \gamma f$, $f \rightarrow \pi^0\pi^0$ is 25%.

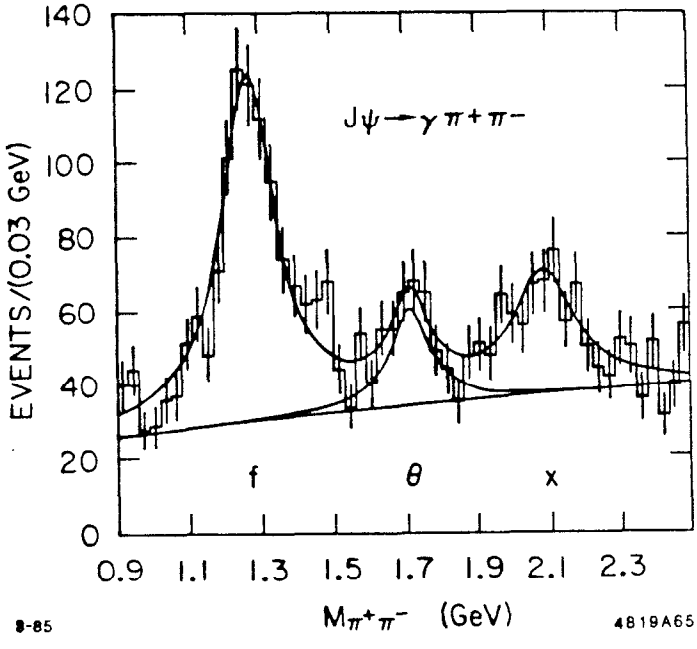

Fig. 5.22 $\pi^+\pi^-$ invariant mass distribution in $J/\psi \to \gamma\pi^+\pi^-$ from Mark III. [5]

We obtain

$$\frac{\mathrm{BR}(\psi' \to \gamma\,\mathrm{f})}{\mathrm{BR}(J/\psi \to \gamma\,\mathrm{f})} = 9 \pm 3\%. \qquad [5.9]$$

Several checks can be performed to determine if this signal is due to a background. There is the (somewhat unlikely) possibility that the $\gamma\pi^0\pi^0$ events are not associated with the ψ' resonance but rather result from an underlying continuum process. Figure 5.27 shows the $\pi^0\pi^0$ spectrum which results when the same analysis applied to the J/ψ and ψ' data is applied to the ψ'' dataset. There are only three events, all of which have $\pi^0\pi^0$ masses above 3 GeV which are probably due to the background $e^+e^- \to (\gamma)\gamma\gamma$ in which the two high energy γ's are misidentified as merged π^0's. Next, it is conceivable that the events are due to the process $\psi' \to XJ/\psi$, $J/\psi \to \gamma\,\mathrm{f}$ where the decay products of the X system are not detected

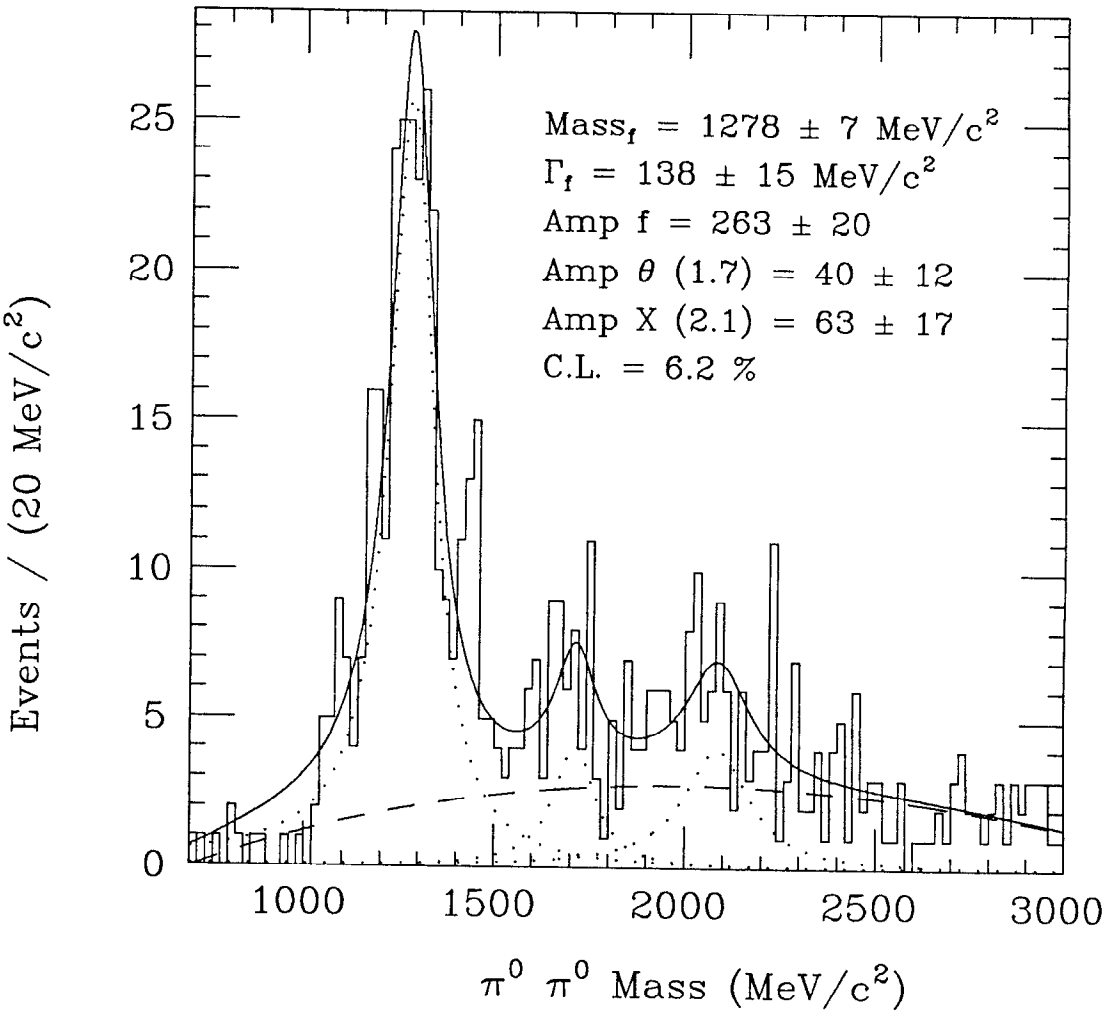

Fig. 5.23 Fit of $\pi^0\pi^0$ invariant mass distribution in $J/\psi \to \gamma\,\pi^0\pi^0$ fitted to three Breit-Wigner line shapes and polynomial background.

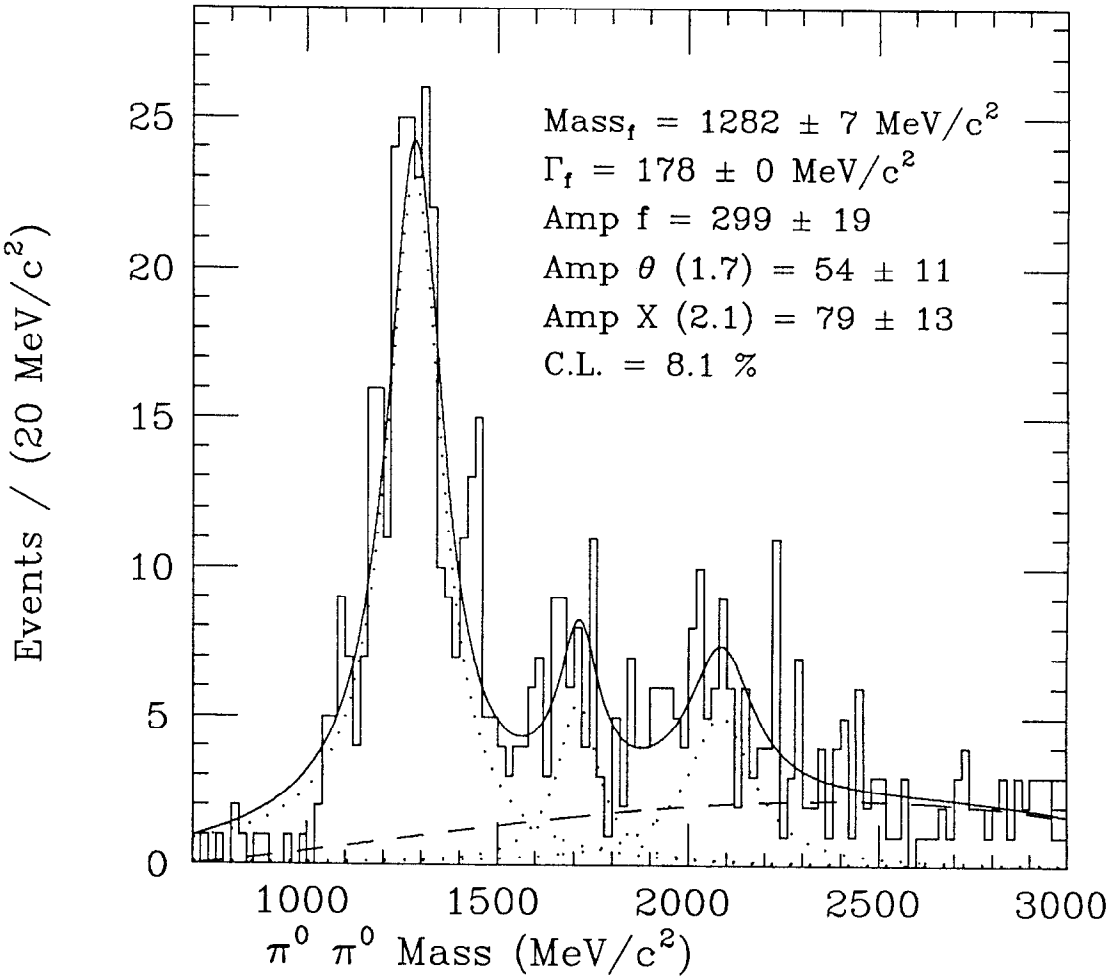

Fig. 5.24 Fit of $\pi^0\pi^0$ invariant mass distribution in $J/\psi \rightarrow \gamma\pi^0\pi^0$ fitted to three Breit-Wigner line shapes and phase space background. (Width of the f fixed at 178 MeV/c^2.)

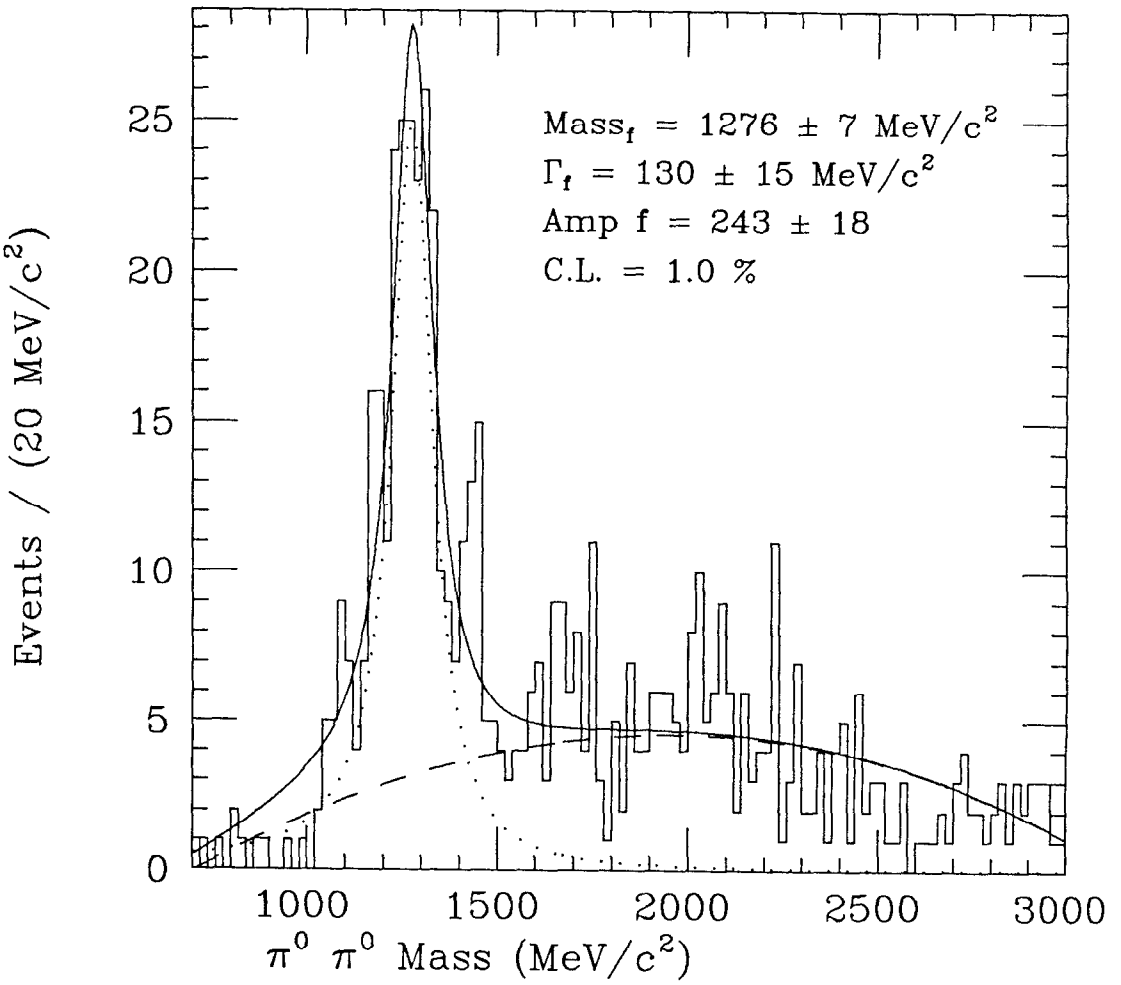

Fig. 5.25 Fit of $\pi^0\pi^0$ invariant mass distribution in $J/\psi \rightarrow \gamma\,\pi^0\pi^0$ fitted to one Breit-Wigner line shape and polynomial background.

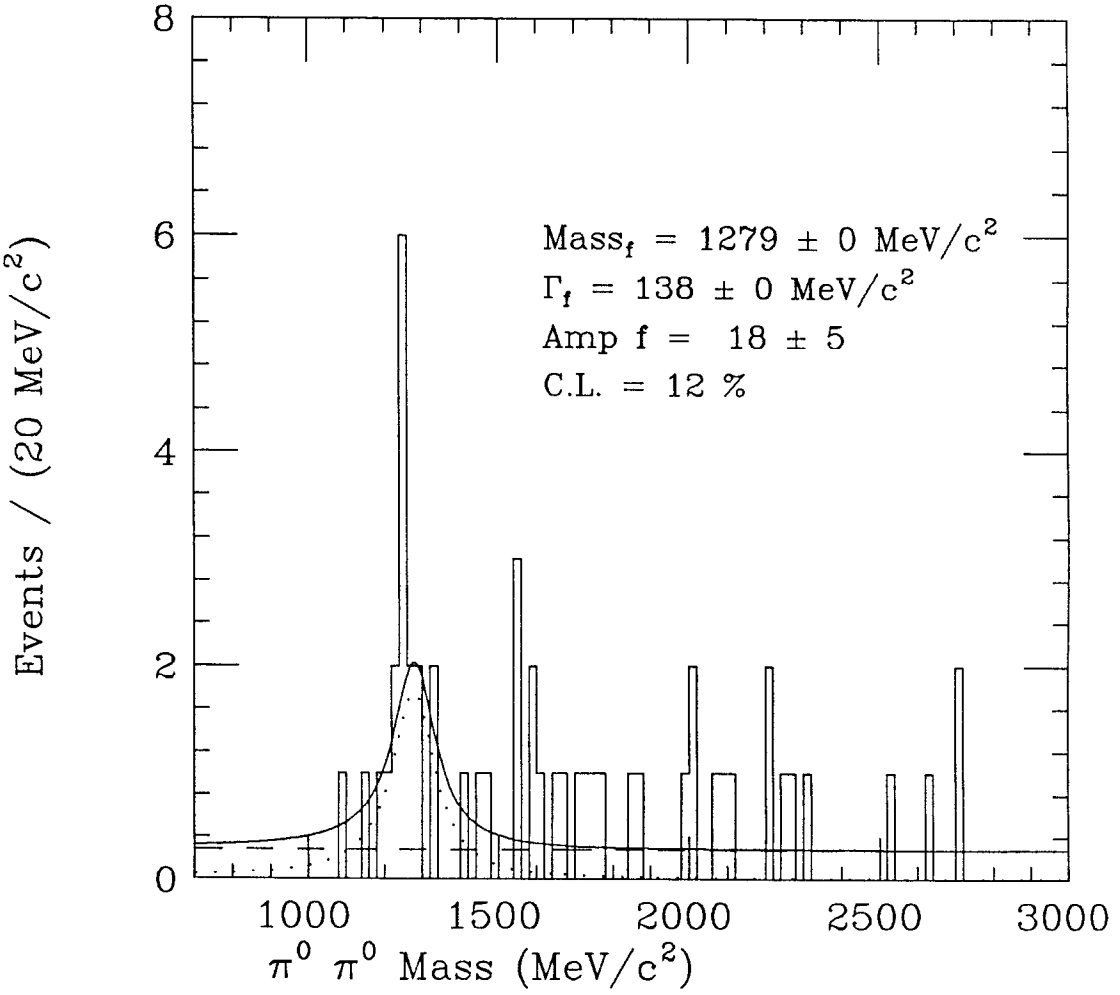

Fig. 5.26 Fit of $\pi^0\pi^0$ invariant mass distribution in $\psi' \rightarrow \gamma\,\pi^0\pi^0$ fitted to one Breit-Wigner and constant background.

(perhaps going down the beampipe). We have investigated this background for the case with the largest branching ratio, namely, $X = \pi\pi$ (both charged and neutral modes). In a Monte Carlo of this process with twice as many events as would be expected from known branching ratios, no events pass the analysis cuts. (Events which can pass the initial topology cuts due to the loss of some final state particles cannot pass the kinematic fit to energy and momentum conservation.) Finally, there is a possibility that the decay $\psi' \rightarrow \gamma\chi_0$, $\chi_0 \rightarrow \pi^0\pi^0$ could be a background for this decay if one of the π^0's were separated. In this case there would be one merged π^0 and three identified γ's, and it is possible that one of the γ's from the decay of the π^0 could be incorrectly identified as the direct γ. Figure 5.28 shows the $\pi^0\pi^0$ invariant mass spectrum from a Monte Carlo of this process with a factor of eight more events than would be expected from measured branching ratios. (See Chapter 4.) We estimate a contamination of one-half of an event from this channel which we have included in the systematic error quoted above.

We can further check if the events have a topology consistent with the decay $\psi' \rightarrow \gamma\,\mathrm{f}$, $\mathrm{f} \rightarrow \pi^0\pi^0$. Figure 5.29 shows the distribution of $|\cos\theta_\pi|$ (where θ_π is the angle the $\pi^0\pi^0$ axis makes with the γ direction in the rest frame of the $\pi^0\pi^0$ system) for events with $\pi^0\pi^0$ masses between 1000 and 1550 MeV/c^2. The solid histogram shows the distribution from the J/ψ data; the dashed and dotted histograms show the distributions from Monte Carlos of $J/\psi \rightarrow \gamma\,\mathrm{f}$, $\mathrm{f} \rightarrow \pi^0\pi^0$where the f is assigned spin 0 and spin 2, respectively (normalized to the data).** We see that the data are peaked towards high $|\cos\theta_\pi|$. That this effect is not an artifact of the cuts is demonstrated by the distribution from the spin-0 f Monte Carlo, which is flat. Figure 5.30 shows the same plot for the ψ' dataset and two Monte Carlos of $\psi' \rightarrow \gamma\,\mathrm{f}$, $\mathrm{f} \rightarrow \pi^0\pi^0$ where the spin of the f is assigned spin 0 and spin 2. Again, there is a tendency for the points to cluster at large $|\cos\theta_\pi|$ consistent with the J/ψ data,

** We have once again used the helicity parameters from reference 6. The data and the spin-2 histograms do not overlap exactly since we use a different set of cuts than that used in reference 6.

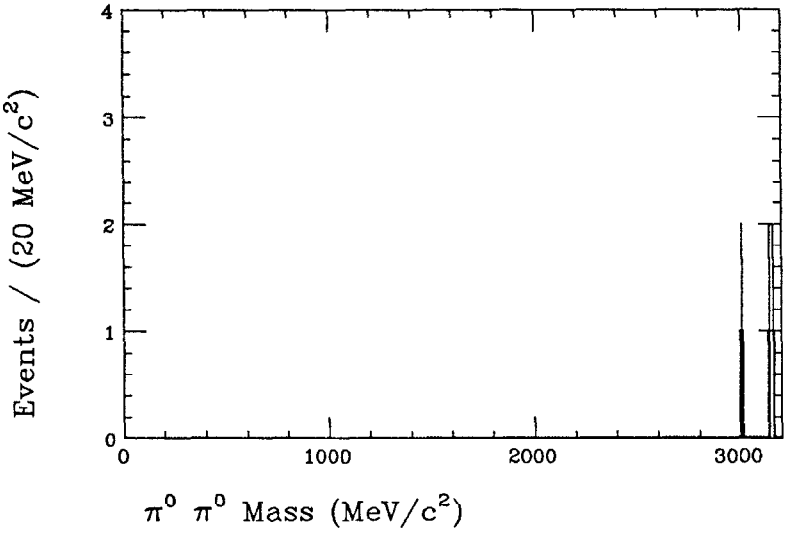

Fig. 5.27 $\pi^0\pi^0$ invariant mass distribution in $\psi'' \rightarrow \gamma\pi^0\pi^0$: ψ'' data.

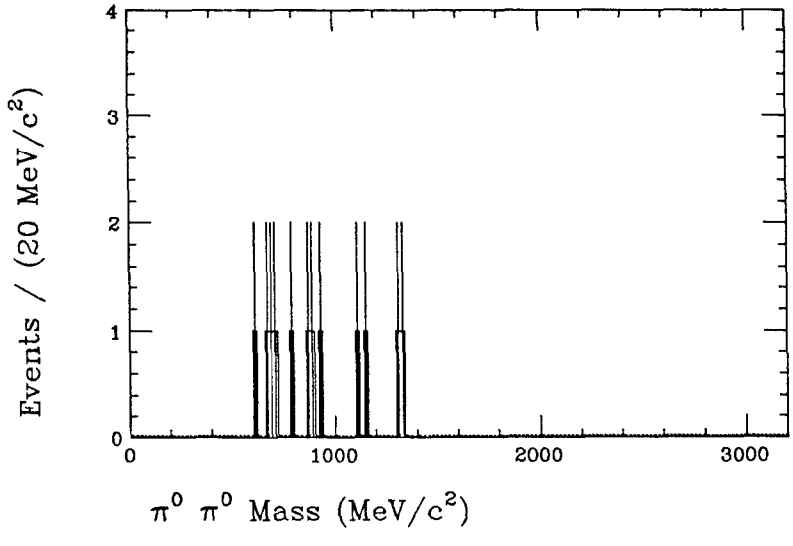

Fig. 5.28 $\pi^0\pi^0$ invariant mass distribution in $\psi' \rightarrow \gamma\chi_0$,$\chi_0 \rightarrow \pi^0\pi^0$: Monte Carlo.

but the statistics are too low to make a spin assignment.

5.3 J/ψ, $\psi' \rightarrow \gamma\eta\eta$

In contrast to the $\gamma\pi^0\pi^0$ channel, the signature of the $\gamma\eta\eta$ channel is relatively simple in that the γ's from the decay of a single η at SPEAR energies do not overlap. Thus, we use the same analysis that was used to search for $\gamma\pi^0\pi^0$, but we use only the five-track topology and fit to the η mass instead of the π^0 mass. Figures 5.31 and 5.32 show the same invariant mass plots as Figs. 5.8 and 5.9 but on expanded scales in order to show the clusters at the $\eta\eta$ mass. We select events shown in the boxes to be subjected to kinematic fits to energy and momentum conservation and the additional constraints that two pairs of γ's form η's. The small plots in Figs. 5.31 and 5.32 show the distributions of confidence levels and the number of good fits per event. Figures 5.33 and 5.34 show the $\eta\eta$ invariant mass distributions which result.

We again check the efficiency of our technique by generating series of Monte Carlos of the decays J/ψ, $\psi' \rightarrow \gamma X$, $X \rightarrow \eta\eta$ for different masses M_X . Figures 5.35 and 5.36 show the variation of detection efficiencies at the J/ψ and ψ' energies, respectively. We see that the efficiency for the J/ψ decays is reasonably flat, whereas the efficiency for the ψ' decays drops off at low values of M_X . This is due to the one cut that is different in the J/ψ and ψ' analyses, namely, the rejection of events in the ψ' data which have a missing mass opposite two γ's which is consistent with a J/ψ mass (see Section 5.2).

We fit the J/ψ invariant mass spectrum to a single Breit-Wigner plus a flat background and allow all parameters to vary (Fig. 5.39). We obtain a good fit to a resonance with a mass of 1655 ± 33 ± 5 MeV/c^2 and $\Gamma = 219^{+74}_{-54} \pm 20$ MeV/c^2, consistent with the original Crystal Ball observation of the $\theta(1640)$ (using the same dataset) of M = 1640 ± 50 MeV/c^2 and $\Gamma = 220^{+100}_{-70}$ MeV/c^2.[8] In order to obtain an efficiency for this decay, we use the values of the helicity parameters $x = 0.87$ and $y = -0.64$ obtained in the original Crystal Ball analysis and obtain a Monte

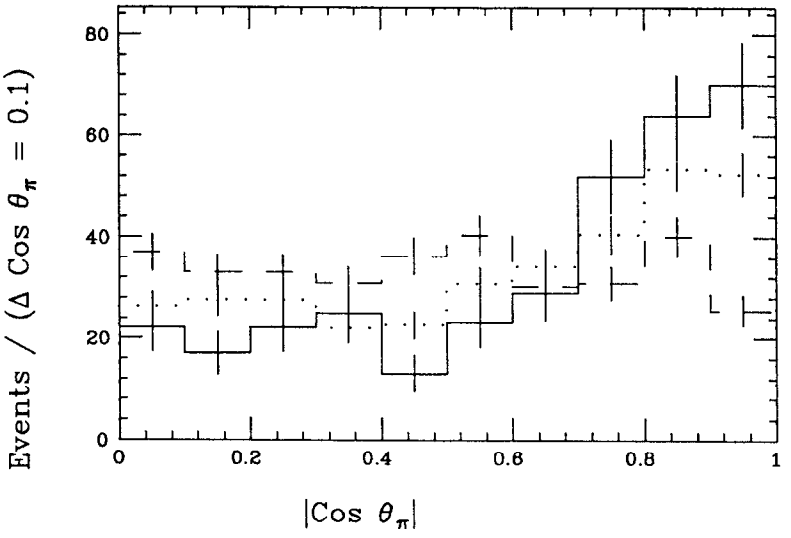

Fig. 5.29 Distribution of $|\cos\theta_\pi|$ in J/ψ data (solid histogram) , $J/\psi \to \gamma$ f (spin-0 f) Monte Carlo (dashed histogram), and $J/\psi \to \gamma$ f (spin-2 f) Monte Carlo (dotted histogram).

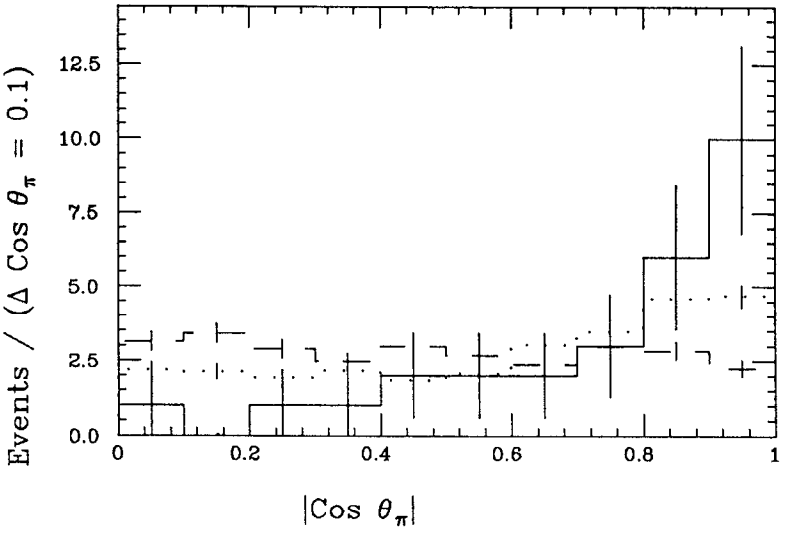

Fig. 5.30 Distribution of $|\cos\theta_\pi|$ in ψ' data (solid histogram) and $\psi' \to \gamma$ f (spin-0 f) Monte Carlo (dashed histogram), and $\psi' \to \gamma$ f (spin-2 f) Monte Carlo (dotted histogram).

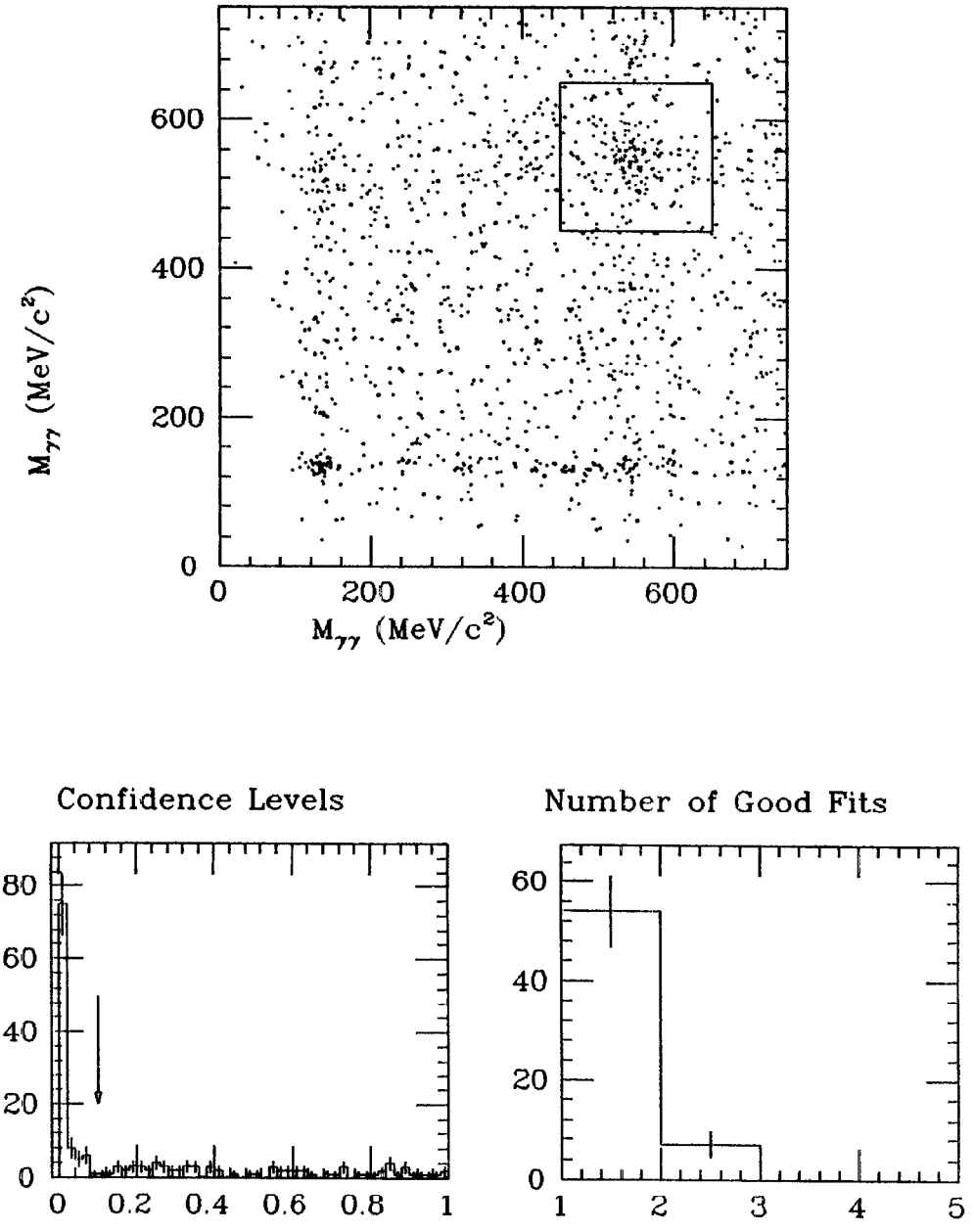

Fig. 5.31 2γ invariant mass *vs.* 2γ invariant mass for five track events: J/ψ data.
(Insets show confidence levels of kinematic fits and number of good fits. Cuts shown by box and arrow.)

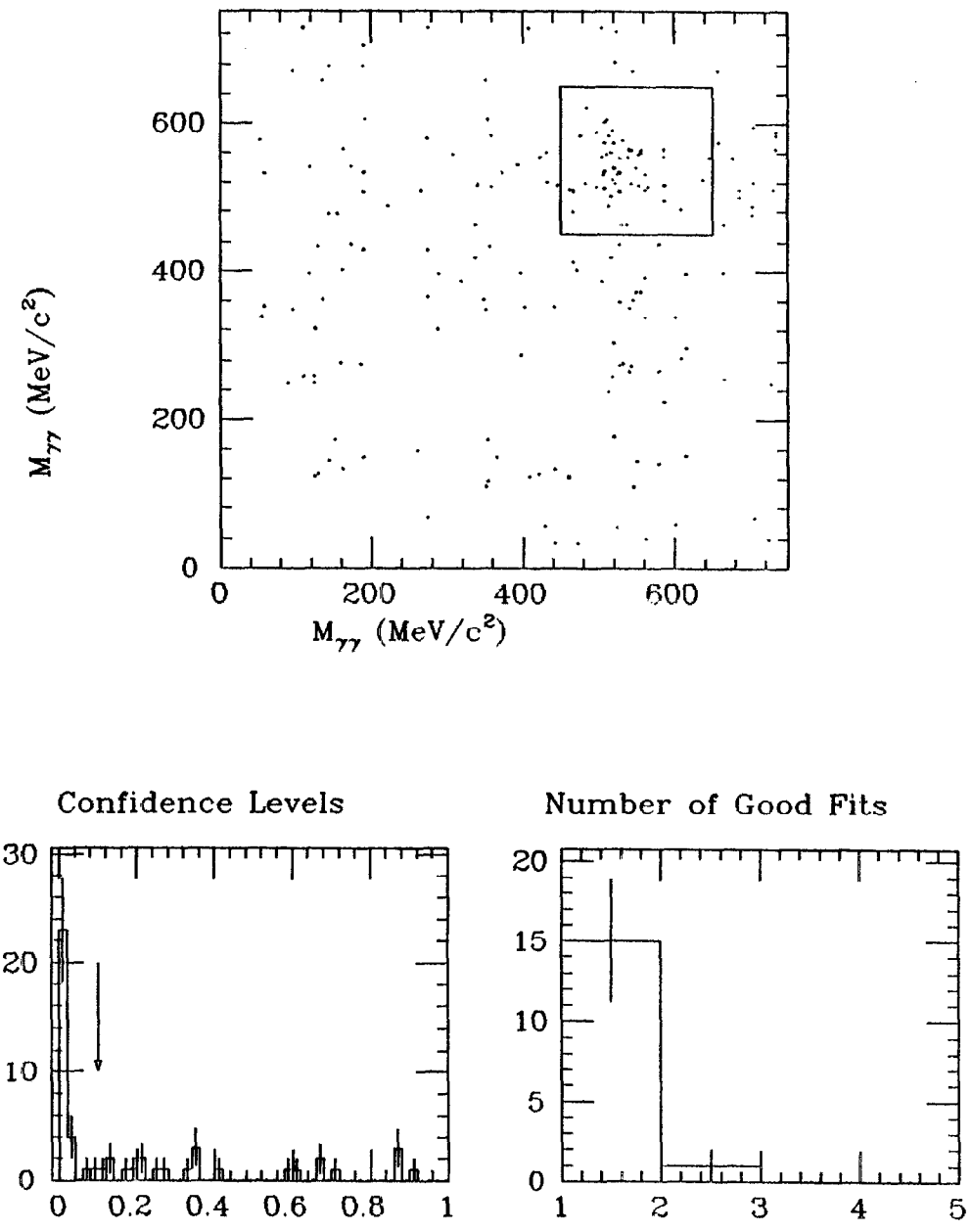

Fig. 5.32 2γ invariant mass *vs.* 2γ invariant mass for five track events: ψ' data.
(Insets show confidence levels of kinematic fits and number of good fits. Cuts shown by box and arrow.)

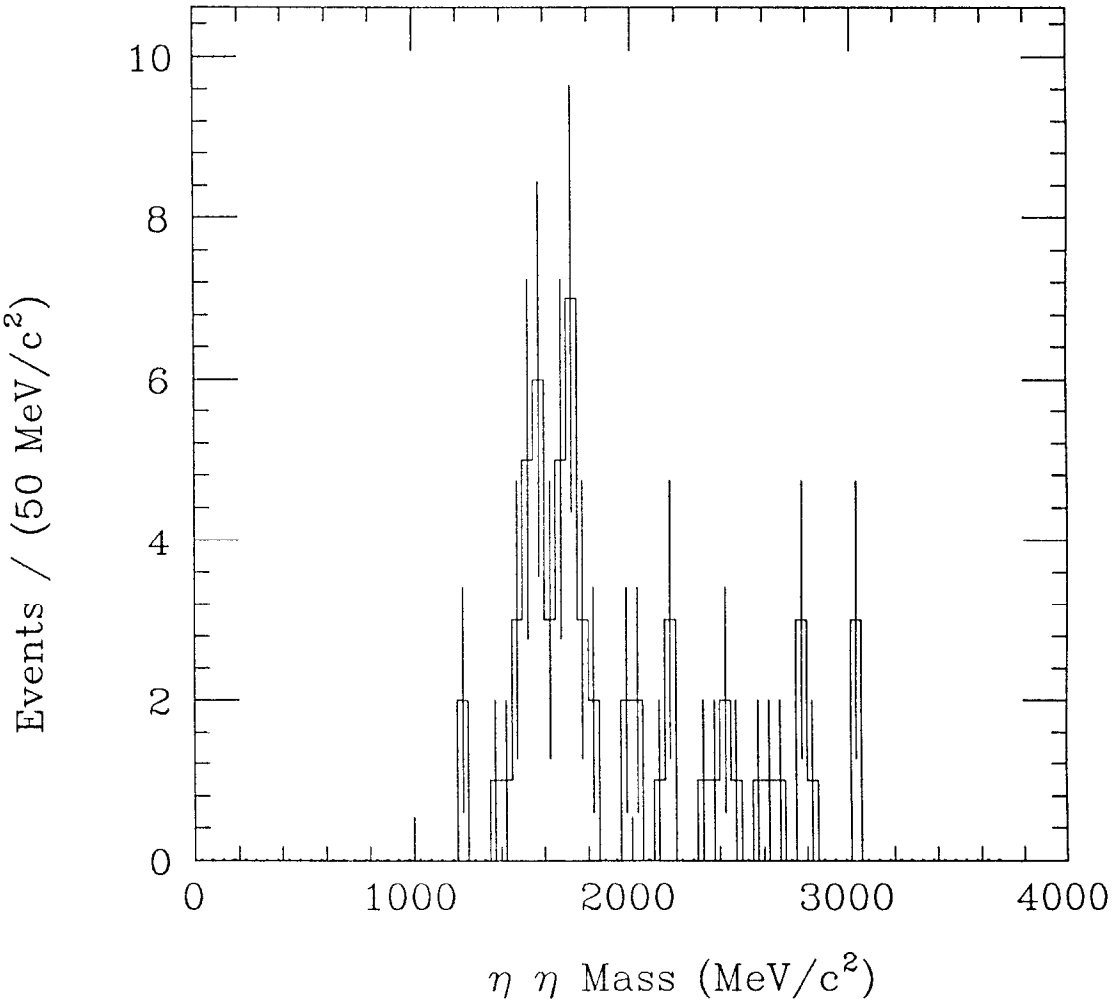

Fig. 5.33 $\eta\eta$ invariant mass distribution in $J/\psi \rightarrow \gamma\eta\eta$.

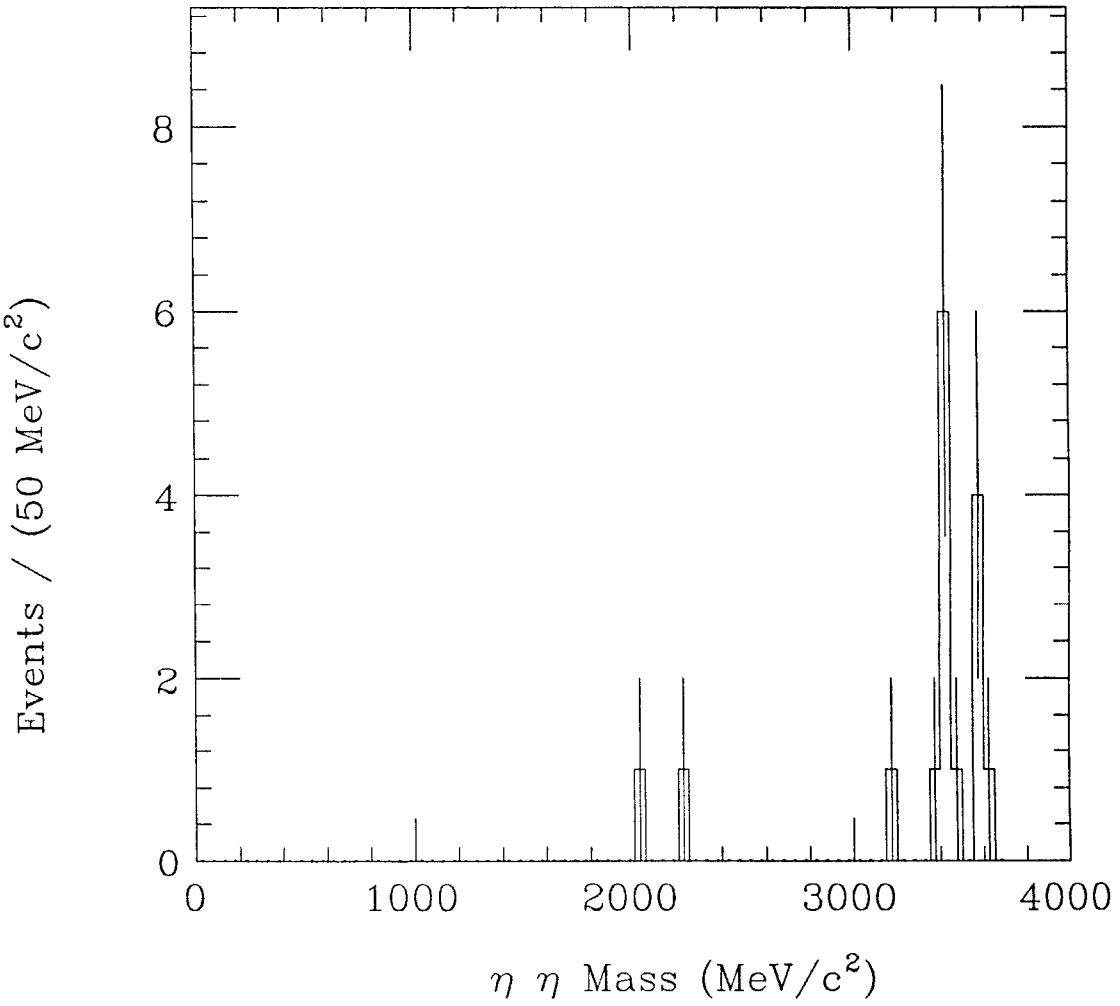

Fig. 5.34 $\eta\eta$ invariant mass distribution in $\psi' \to \gamma\eta\eta$.

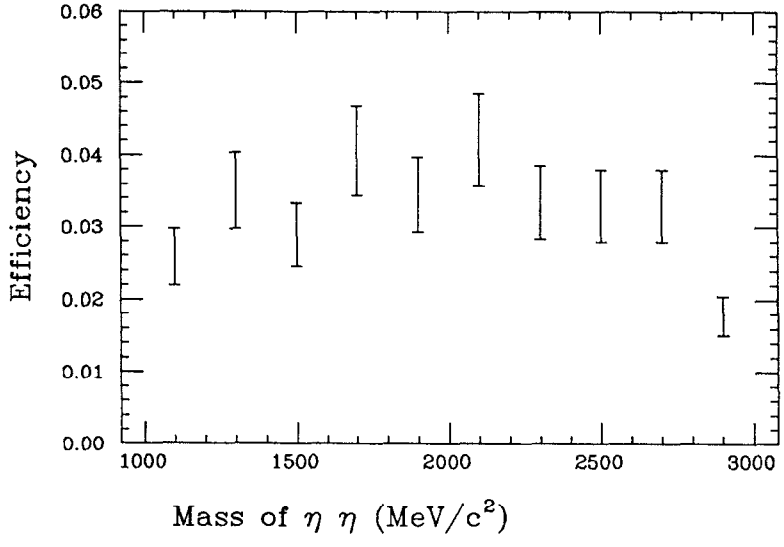

Fig. 5.35 Detection efficiency for $J/\psi \rightarrow \gamma X, X \rightarrow \eta\eta$ as a function of M_X .

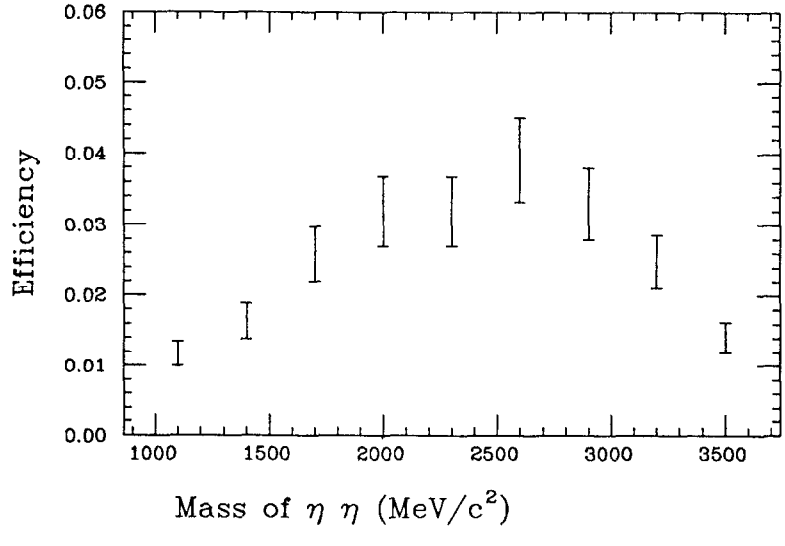

Fig. 5.36 Detection efficiency for $\psi' \rightarrow \gamma X, X \rightarrow \eta\eta$ as a function of M_X

.

Carlo efficiency of 2.5% (including the branching ratios of the η to $\gamma\gamma$) and so derive $\mathrm{BR}(J/\psi \rightarrow \gamma\theta(1640)) \times \mathrm{BR}(\theta(1640) \rightarrow \eta\eta) = (5.8 \pm 1.4 \pm 1.5) \times 10^{-4}$, consistent with the original Crystal Ball measurement of $(4.9 \pm 1.4 \pm 1.0) \times 10^{-4}$.

Shortly after the Crystal Ball observation of the $\theta(1640)$, the Mark II collaboration reported evidence of structure in the K^+K^- invariant mass spectrum in the decay $J/\psi \rightarrow \gamma K^+K^-$ near the same mass.[1] However, they were able to resolve two peaks which they associated with the f′ and θ (at 1700 $\pm$30 MeV/c^2). In order to avoid ambiguities, we refer to the single resonance reported in the original Crystal Ball analysis as $\theta(1640)$ and call the higher mass K^+K^- resonance $\theta(1720)$.*† The Mark III collaboration has recently repeated the Mark II study of $J/\psi \rightarrow \gamma K^+K^-$ and have reported masses, widths, and helicity amplitudes for the two states f′ and $\theta(1720)$(see Fig. 5.38). Motivated by these analyses, we attempt a fit of the $\eta\eta$ invariant mass spectrum in $J/\psi \rightarrow \gamma\eta\eta$ to two non-interfering Breit-Wigner line shapes with masses and widths fixed to Mark III values obtained from a similar fit to the K^+K^- invariant mass spectrum ($M_{f'} = 1525 \pm 10 \pm 10$ MeV/c^2, $\Gamma_{f'} = 85 \pm 35$ MeV/c^2, $M_{\theta(1720)} = 1720 \pm 10 \pm 10$ MeV/c^2, and $\Gamma_{\theta(1720)} = 130 \pm 20$ MeV/c^2). Using the helicity amplitudes for the f′(x = 0.63 and y = 0.17) and $\theta(1720)$ (x = -1.07 and y = -1.09) found in the Mark III study, we obtain Monte Carlo efficiencies of 2.8% and 3.2%, respectively, for $J/\psi \rightarrow \gamma f'$, $f' \rightarrow \eta\eta$ and $J/\psi \rightarrow \gamma\theta(1720), \theta(1720) \rightarrow \eta\eta$. Combining these efficiencies with the observed numbers of events in the peaks (12$\pm$5 and 20 $\pm$6), we obtain

$$\begin{aligned} \mathrm{BR}(J/\psi \rightarrow \gamma f')\mathrm{BR}(f' \rightarrow \eta\eta) &= (1.9 \pm 0.8 \pm 0.5) \times 10^{-4} \\ \mathrm{BR}(J/\psi \rightarrow \gamma\theta(1720))\mathrm{BR}(\theta(1720) \rightarrow \eta\eta) &= (2.6 \pm 0.8 \pm 0.7) \times 10^{-4} \end{aligned} \qquad [5.10]$$

In the corresponding ψ' spectrum there are events at high mass (from the decays $\chi_{0,2} \rightarrow \eta\eta$ discussed in chapter 4) but no events below 2 GeV. Using upper limits

*† We use the more accurate Mark III measurement of the mass to label this state.

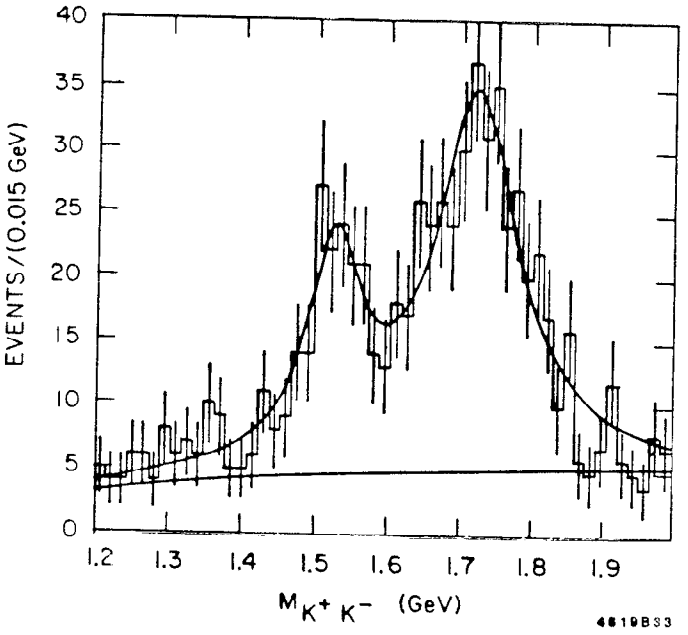

Fig. 5.38 K^+K^- Invariant mass distribution in $J/\psi \rightarrow \gamma K^+K^-$ from Mark III. [5]

of 2.3 events, we can set branching ratio upper limits for $\psi' \rightarrow \theta(1640)$, f', or $\theta(1720)$ of 1×10^{-4} at 90% upper confidence level. Using the measurements of these decays on the J/ψ, we can translate these into limits on the ratios of branching ratios:

$$\frac{\mathrm{BR}(\psi' \rightarrow \theta(1640))}{\mathrm{BR}(J/\psi \rightarrow \theta(1640))} < 10\%$$

or

$$\begin{aligned} \frac{\mathrm{BR}(\psi' \rightarrow \mathrm{f}')}{\mathrm{BR}(J/\psi \rightarrow \mathrm{f}')} &< 22\% \\ \frac{\mathrm{BR}(\psi' \rightarrow \theta(1720))}{\mathrm{BR}(J/\psi \rightarrow \theta(1720))} &< 15\% \end{aligned} \qquad [5.11]$$

The upper limits are larger than would be obtained by simply dividing 2.3 events by the number of events observed on the J/ψ due to the decreased efficiency in the ψ' analysis as noted above.

We cannot compare the ψ' results to previous experiments as these are the first measurements of these branching ratios. We postpone a comparison with theory until after the discussion of the radiative decays to low mass mesons in the next chapter.

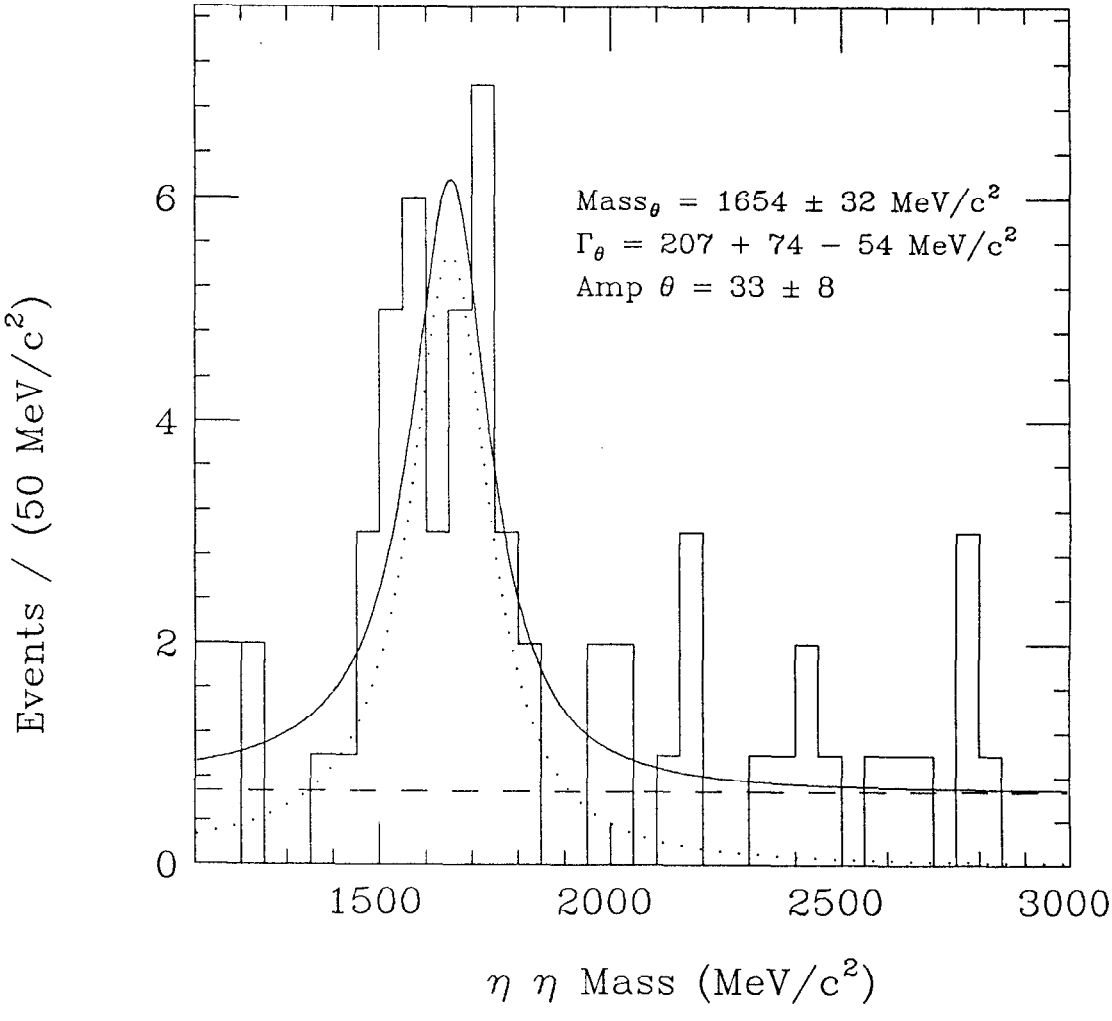

Fig. 5.39 $\eta\eta$ invariant mass distribution in $J/\psi \rightarrow \gamma\eta\eta$ fit to a single Breit-Wigner.

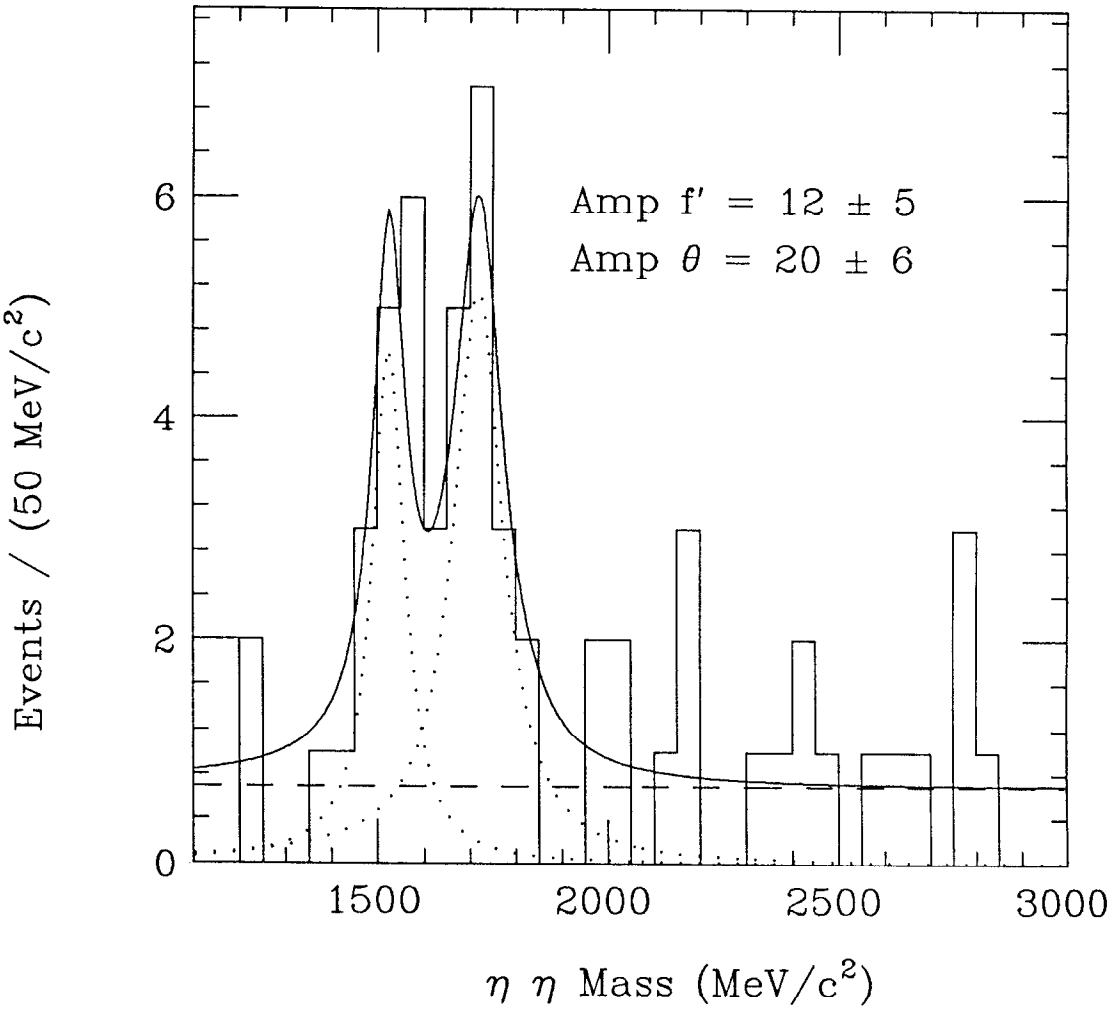

Fig. 5.40 $\eta\eta$ invariant mass distribution in $J/\psi \to \gamma\eta\eta$ fit to two Breit-Wigners.

References

1) M. Franklin, Stanford Ph.D. Thesis (unpublished);
M. Franklin *et. al.*, *Phys. Rev. Lett.* **51** (1983) 963.

2) Particle Data Group, *Rev. of Mod. Phys.* **56** (1984) S1.

3) T. Appelquist, A. De Rújula, H. D. Politzer, S. L. Glashow, *Phys. Rev. Lett.* **34** (1975) 363 ;
M. Chanowitz, *Phys. Rev D* **12** (1975) 918 ;
L. Okun and M. Voloshin, ITEP-95-1976 (unpublished);
S. J. Brodsky, T. A. DeGrand, R. R. Horgun, D. G. Coyne, *Phys. Lett.* **73B** (1978) 203 ;
K. Koller and T. Walsh, *Nucl. Phys.* **B140** (1978) 449.

4) J. Perrier, in *Physics in Collision*, proceedings of the International Conference, Santa Cruz, 1984, edited by A. Seiden (Editions Frontieres, in press), and SLAC-PUB 3436.

5) K. E. Einsweiler, Ph.D. thesis, Stanford University, 1984, and SLAC-Report 272 (unpublished).

6) C. Edwards *et. al.*, *Phys. Rev. D* **25** (1982) 3065.

7) N. Cason, in *Experimental Meson Spectroscopy – 1983*, proceedings of the Seventh International Conference, Upton, New York, edited by S. J. Lindenbaum (American Institute of Physics, New York, 1984).

8) C. Edwards *et. al.*, *Phys. Rev. Lett.* **48** (1982) 458.

Chapter 6

Non-Charmonium Decays (Light Mesons)

6.1 Introduction

In this chapter we continue the investigation of the radiative decays of the ψ'. Here we consider decays to mesons which are sufficiently light that the observed tracks of their decay products typically overlap, rendering an exclusive analysis worthless. We are interested in particular in the decays $\psi' \to \gamma\eta$ and $\psi' \to \gamma\eta'$. The 2γ decay mode of these mesons is an exception to the comment just made, and we first investigate these reactions in the 2γ channel using an exclusive analysis. This approach is ultimately limited by the background from the QED process $e^+e^- \to (\gamma)\gamma\gamma$. We next use the "global shower technique" to measure the branching ratios for the decays $\psi' \to \gamma\eta$, $\eta \to \pi^0\pi^0\pi^0$ and $\psi' \to \gamma\eta'$, $\eta' \to \eta\pi^0\pi^0$. The analyses have been optimized to extract signals from the ψ' data. As such, they do not yield the most accurate possible values when applied to the J/ψ data. Nevertheless, we demonstrate each of our analyses on the J/ψ where the signal to background ratio is substantially larger than on the ψ'.

6.2 $\psi' \to \gamma\eta$,$\psi' \to \gamma\eta'$, η, $\eta' \to \gamma\gamma$

From the datasets which have been processed through the algorithms described in Chapter 3 we select all events containing three tracks. We reject those events in which the PIFIT mass of any of the three tracks is greater than 90 MeV/c^2 and so inconsistent with a γ. We fit the events to energy and momentum constraints and require the confidence level of the fit be greater than 10%. Finally, we require that the angles of the two highest energy tracks with respect to the beam direction be such that $\cos\theta < 0.70$ so as to reduce background from the QED process $e^+e^- \to (\gamma)\gamma\gamma$. Figures 6.1 and 6.2 show the Dalitz plots for the J/ψ and ψ' datasets, where the highest invariant mass combination has been plotted against the lowest invariant mass combination. Both plots show an accumulation at high invariant mass corresponding to $e^+e^- \to (\gamma)\gamma\gamma$. In addition, Fig. 6.1 shows clear bands corresponding to the reaction $J/\psi \to \gamma\eta$, $\eta \to \gamma\gamma$ and $J/\psi \to \gamma\eta'$, $\eta' \to \gamma\gamma$ whereas Fig. 6.2 shows no such structure. We show Figs. 6.3 and 6.4 the lowest invariant mass combinations plotted on a linear scale.* We again see structures corresponding to the η and η' in the J/ψ data, but no such structures in the ψ' data. In order to suppress the QED background, we require that the lowest energy γ in the event have at least 400 MeV. This corresponds to eliminating those events lying to the right of the arrows in Figs. 6.1 and 6.2. Figures 6.5 and 6.6 show the distributions of the lowest invariant mass combinations after this cut. Figures 6.7 and 6.9 show fits to the η and η' peaks in the J/ψ plots to Gaussians plus a flat background. Using Monte Carlo efficiencies of 18.5% and 17% for the reactions $J/\psi \to \gamma\eta$, $\eta \to \gamma\gamma$ and $\psi' \to \gamma\eta'$, $\eta' \to \gamma\gamma$, respectively, we calculate the branching ratios $\mathrm{BR}(J/\psi \to \gamma\eta) = (9.9 \pm 1.0 \pm 2.0) \times 10^{-4}$ and $\mathrm{BR}(\psi' \to \gamma\eta') = (6.9 \pm 1.2 \pm 2.0) \times 10^{-3}$, where

---

* As can be seen from the Dalitz plots, there are decays of the form $J/\psi \to \gamma\eta$, $\eta \to \gamma\gamma$ in which the two γ's from the decay of the η do not form the lowest invariant mass combination in the event and hence fall outside the peak in Fig. 6.3. However, such events are eliminated by the QED cut which follows, so there is no gain in efficiency in considering other invariant mass combinations.

the first errors are statistical and the second systematic. In order to derive upper limits for the same reactions from the ψ', we attempt to fit the same regions in the ψ' plots to Gaussians with means and widths fixed to be those found in the fits to the J/ψ plots – only the amplitudes and background parameters are allowed to vary. Using linear backgrounds, we derive 90% confidence level upper limits of $\mathrm{BR}(\psi' \to \gamma\eta) < 5.1 \times 10^{-5}$ and $\mathrm{BR}(\psi' \to \gamma\eta') < 1.7 \times 10^{-3}$. (These upper limits are determined as described in the next section.) Figures 6.8 and 6.10 show signal amplitudes corresponding to the 90% confidence level limits superimposed on the data.

6.3 $\psi' \to \gamma\eta$, $\psi' \to \gamma\eta'$ Using Global Showers

We next employ the global shower technique (described in Appendix D) to search for the decays $\psi' \to \gamma\eta$, $\eta \to \pi^0\pi^0\pi^0$ and $\psi' \to \gamma\eta'$, $\eta' \to \eta\pi^0\pi^0$. These decays have the advantage over the $\gamma\gamma$ decays of the η and η' that they are not contaminated by the QED process $e^+e^- \to (\gamma)\gamma\gamma$. Also, the rates for these decays are substantial fractions of the total decay rates of the η and η', and the errors in these rates are small. ($\mathrm{BR}(\eta \to \pi^0\pi^0\pi^0) = 31.8 \pm 0.8$ % ; $\mathrm{BR}(\eta' \to \eta\pi^0\pi^0) = 21.8 \pm 0.5$ % .[1])

As mentioned in Chapter 3, the secondary cuts for this analysis are slightly different than those used in the exclusive analyses. We do not remove events with more than two bumps in a connected region or with large SMOMT masses since these features are characteristic of the decays we are studying. We discard an event if it has an endcap track or if any connected region has more than 10% of its energy in endcap crystals. We also demand that the sum of the energies in the crystals be within 300 MeV of the center of mass energy. This cut is designed to eliminate those events in which one or more γ's are missing. Finally, we do not cut on the confidence level from the kinematic fit; however, we do discard those events in which the fit does not converge. Table 6.1 shows the effects of these cuts and the cuts described in Appendix D on the J/ψ and ψ' datasets.

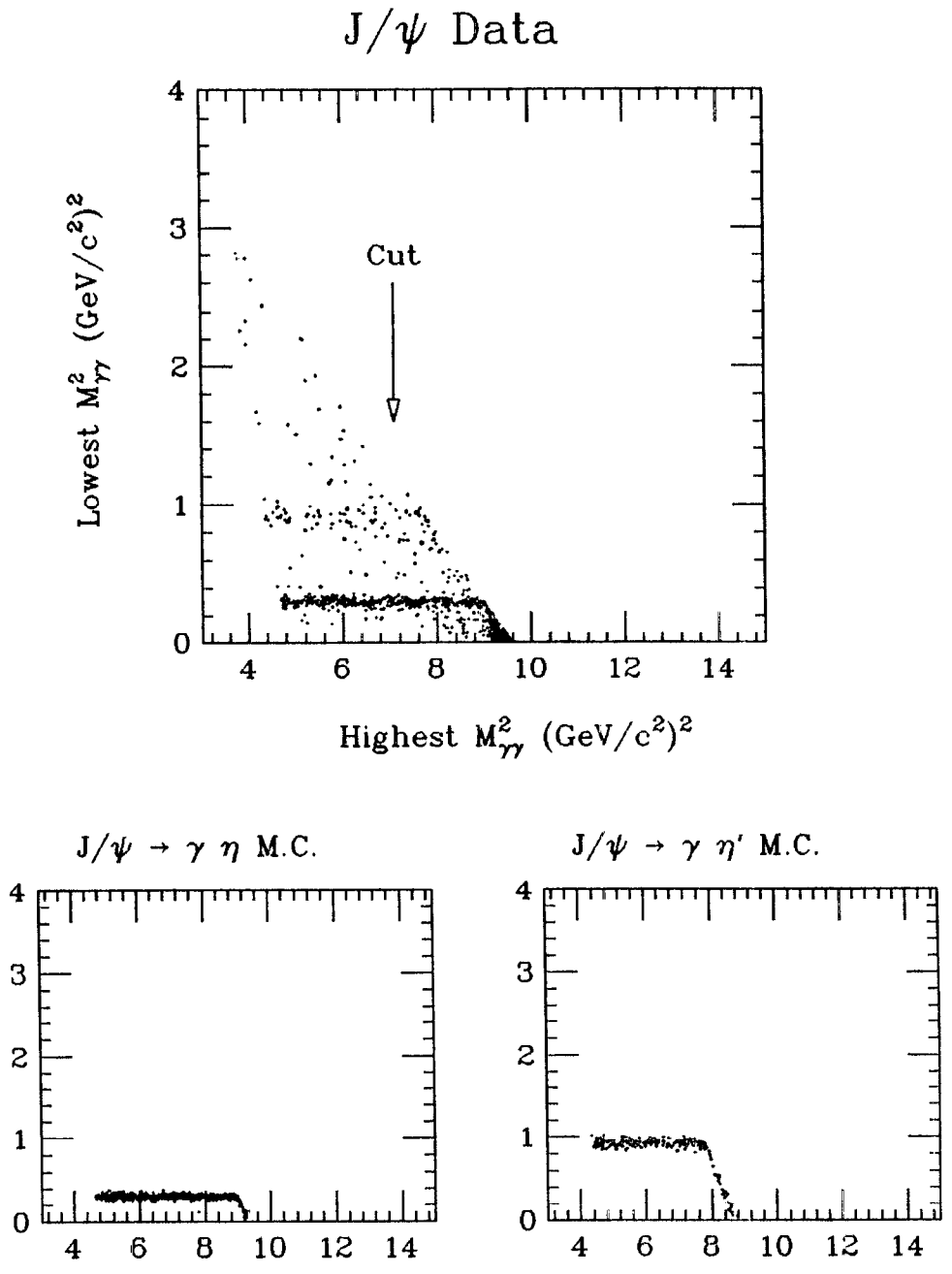

Fig. 6.1 3γ Dalitz plot: lowest 2γ invariant mass combination *vs.* highest 2γ invariant mass combination. Top plot shows J/ψ data; insets show $J/\psi \to \gamma\eta$ and $J/\psi \to \gamma\eta'$ Monte Carlos.

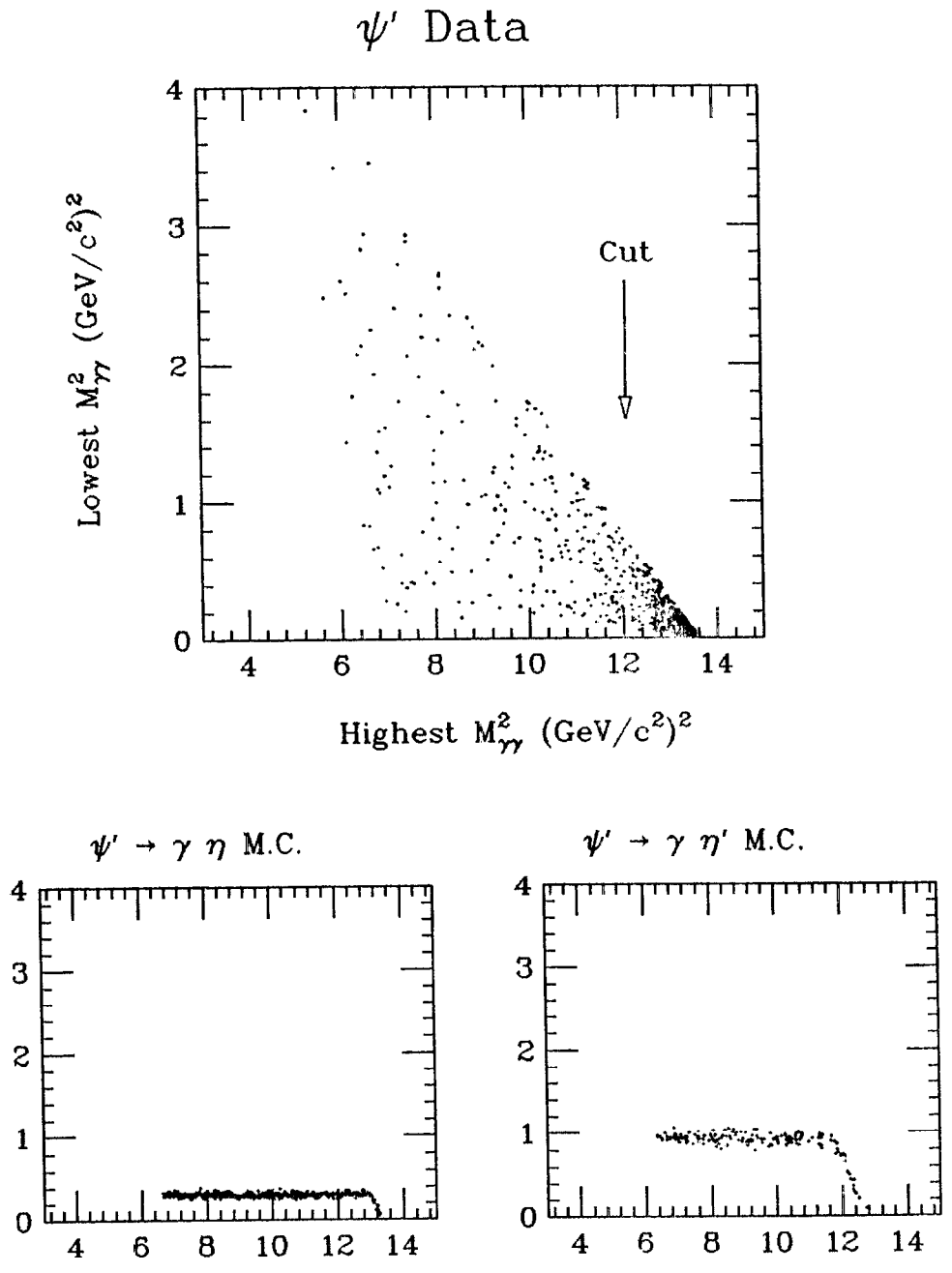

Fig. 6.2 3γ Dalitz plot: lowest 2γ invariant mass combination *vs.* highest 2γ invariant mass combination. Top plot shows ψ' data; insets show $\psi' \to \gamma\eta$ and $\psi' \to \gamma\eta'$ Monte Carlos.

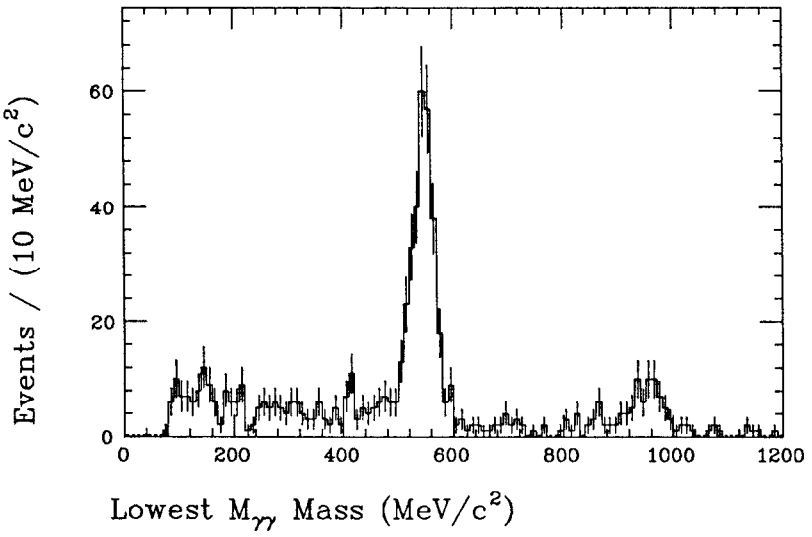

Fig. 6.3 Lowest 2γ invariant mass combination: J/ψ data.

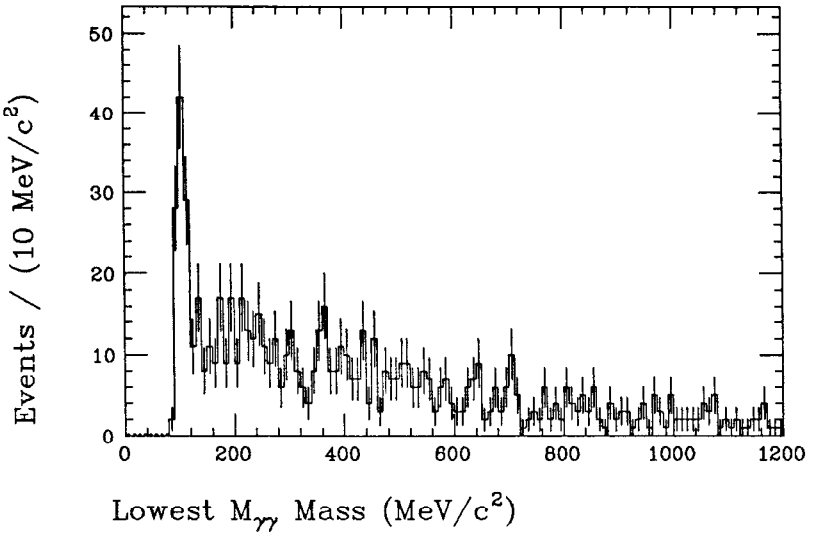

Fig. 6.4 Lowest 2γ invariant mass combination: ψ' data.

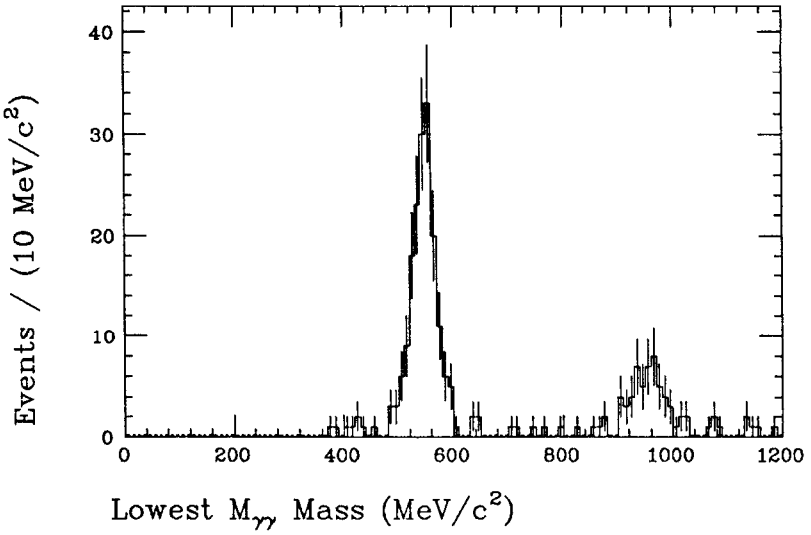

Fig. 6.5 Lowest 2γ invariant mass combination after 400 MeV cut on lowest γ energy: J/ψ data.

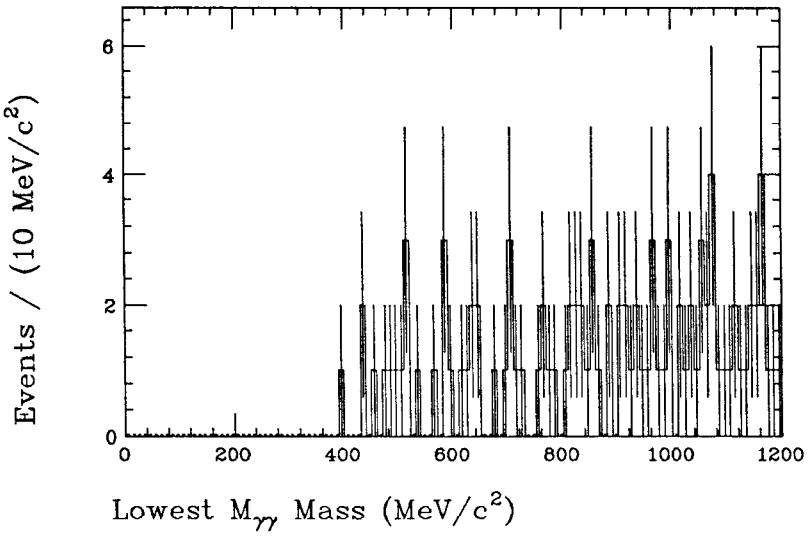

Fig. 6.6 Lowest 2γ invariant mass combination after 400 MeV cut on lowest γ energy: ψ' data.

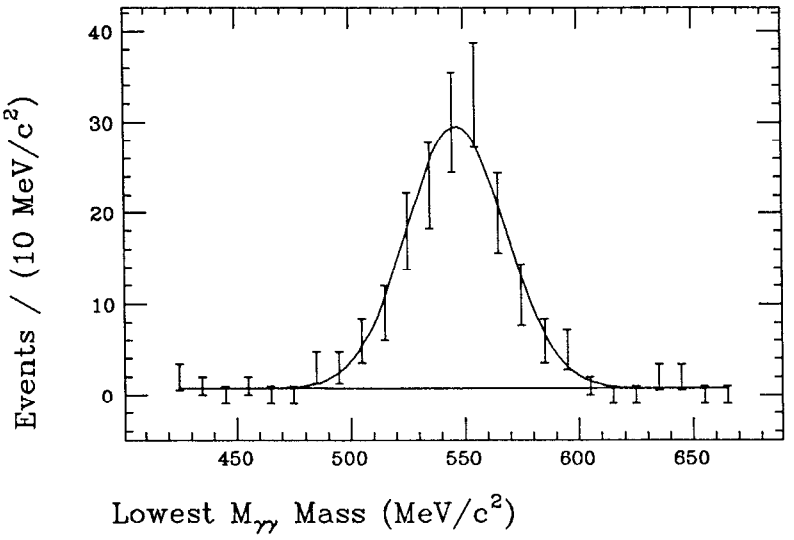

Fig. 6.7 Fit to η peak: J/ψ data. Fit parameters: mean = 546.6 $\pm$1.9 MeV/c^2, $\sigma = 21.7 \pm 1.6$ MeV, amplitude = 157 $\pm$14 events.

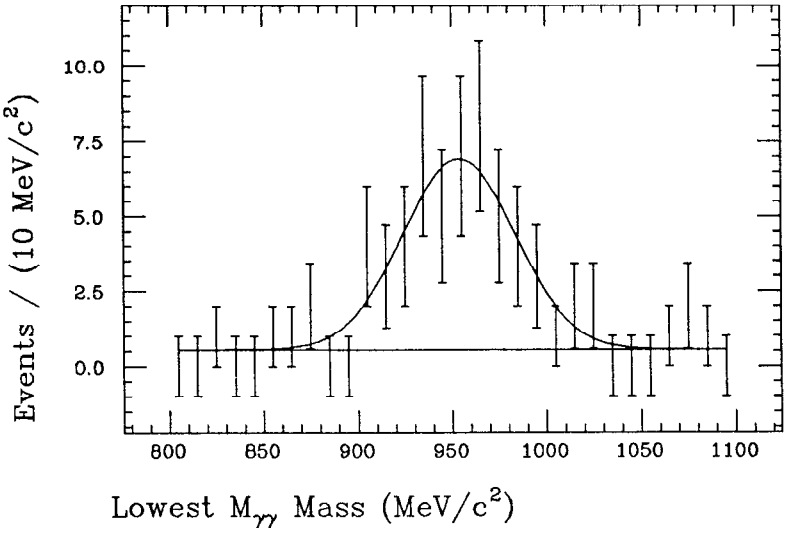

Fig. 6.8 Fit to η region: ψ' data.

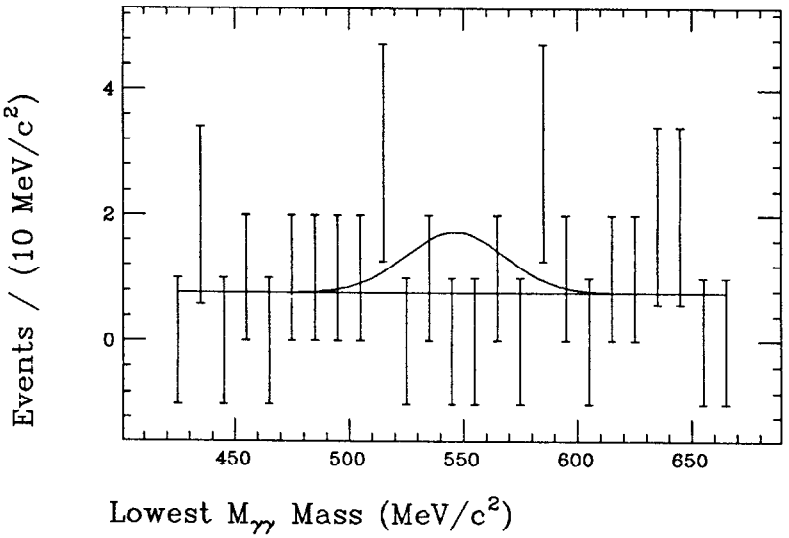

Fig. 6.9 Fit to η' peak: J/ψ data. Fit parameters: mean = 954 $\pm$5 MeV/c^2, $\sigma = 30 \pm 5$ MeV, amplitude = 48 $\pm$8 events.

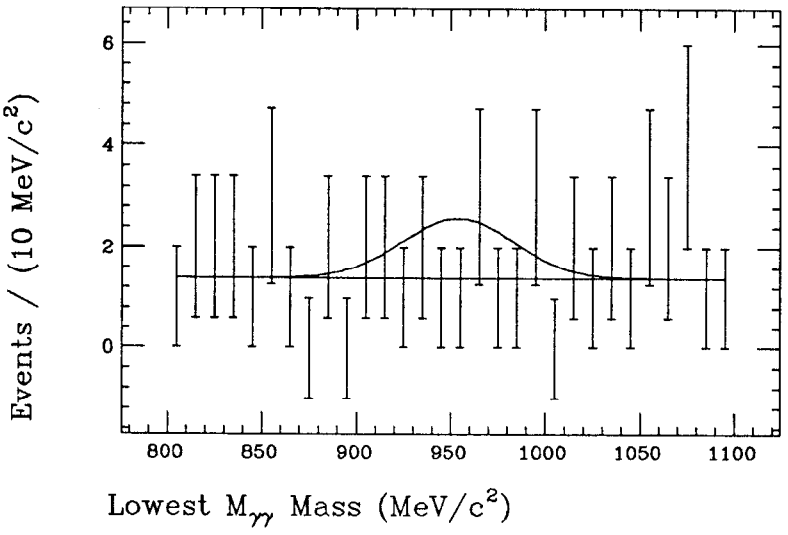

Fig. 6.10 Fit to η' region: ψ' data.

Number of Events	ψ'	J/ψ
Input	30,722	24,756
After Nov. '78 cut	30,328	24,756
After endcap track cut	12,997	12,626
After 1 vertex cut	9,794	11,826
After $\|E_{vis} - E_{CM}\| < 300$ MeV cut	8,213	9,833
After < 10 % Connected Region Energy in Endcaps Cut	8,196	9,805
With Direct γ Identified	7,749	8,897
With Convergent Fit	7,728	8,854
With Global Shower Mass > 0.	7,152	8,610
With Direct γ PIFIT Mass < 90.	5,607	6,652

Table 6.1 Preliminary cuts for global shower analysis.

Figure 6.11 shows the invariant mass spectrum opposite the direct photon for the J/ψ dataset. For completeness we have displayed the invariant mass spectrum from zero to the mass of the J/ψ. However, the detection efficiency of the global shower algorithm drops rapidly beyond 1500 MeV/c^2 (see Appendix D), accounting for the decrease in the population of the plot at high invariant mass. On the low end of the spectrum, the fact that we assign any connected region with an SMOMT mass less than 90 MeV/c^2 an invariant mass of zero (Appendix D) is responsible for the sharp turn-on. There are distinct peaks at the η and η' masses and hints of structure near the mass of the f. We apply the cuts described in Appendix D to select for the η decays. The result is shown in Fig. 6.12 for the J/ψ data and the $J/\psi \rightarrow \gamma\eta$ Monte Carlo (inset). Figures 6.13 and 6.14 show these plots fitted to Gaussians of variable mean, width, and amplitude plus flat backgrounds

(dashed lines). We see that neither the data nor the Monte Carlo is particularly well fit by this simple function. The solid lines show fits to Gaussians with low-energy tails plus flat backgrounds. (For convenience, we use the same function described in Appendix A to fit the gamma energy line shape.) We see that the fits are substantially improved for both the data and the Monte Carlo. Using the 320 $\pm$24 events in the peak and a Monte Carlo efficiency of 14%,† we obtain BR $(J/\psi \to \gamma\eta) = (1.01 \pm 0.06 \pm 0.16) \times 10^{-4}$ (first error statistical, second systematic) consistent with the Particle Data Group value of $(8.6 \pm 0.9) \times 10^{-4}$.

Figure 6.15 shows the plot which results from the application of the η' cuts described in Appendix D to the J/ψ data and a Monte Carlo of $J/\psi \to \gamma\eta'$ (inset). Again, we show these spectra fitted to line shape functions and Gaussians. (We use a linear background for the J/ψ data.) We again see that a low-energy tail is necessary to fit the signal shape. Using the 705 $\pm$66 events in the data peak with a Monte Carlo efficiency of 7.7 % , we derive BR $(J/\psi \to \gamma\eta') = (4.1 \pm 0.4 \pm 0.7) \times 10^{-3}$ to be compared with the Particle Data Group value of $(3.6 \pm 0.5) \times 10^{-3}$. These results are summarized in Table 6.2.

Figure 6.18 shows the plot analogous to Fig. 6.11 for the ψ' data. The structures corresponding to the resonances in the J/ψ data are now absent. Instead, the observed spectrum has a shape characteristic of the QED background. (See Appendix D.) Figure 6.19 shows the spectrum which results after application of the η cuts. Where previously we obtained a peak of over 300 events, there are now essentially no events near the η mass. In order to fit this plot, we fix the parameters of the line shape from the J/ψ fit . An upper limit analysis yields a 90% confidence upper limit of 4.2 events as shown by the curve in Fig. 6.20. Combining this with a Monte Carlo efficiency of 13% and folding in the estimated systematic errors, we

† This number refers to the efficiency for detecting the decay $J/\psi \to \gamma\eta$; the efficiency for detecting $J/\psi \to \gamma\eta$, $\eta \to \pi^0\pi^0\pi^0$ is $0.15/0.32 = 47$ % . (The efficiency quoted in the text is slightly higher than 15% due to leakage from the $\gamma\gamma$ mode.) Similar comments apply to the other efficiencies quoted in this section.

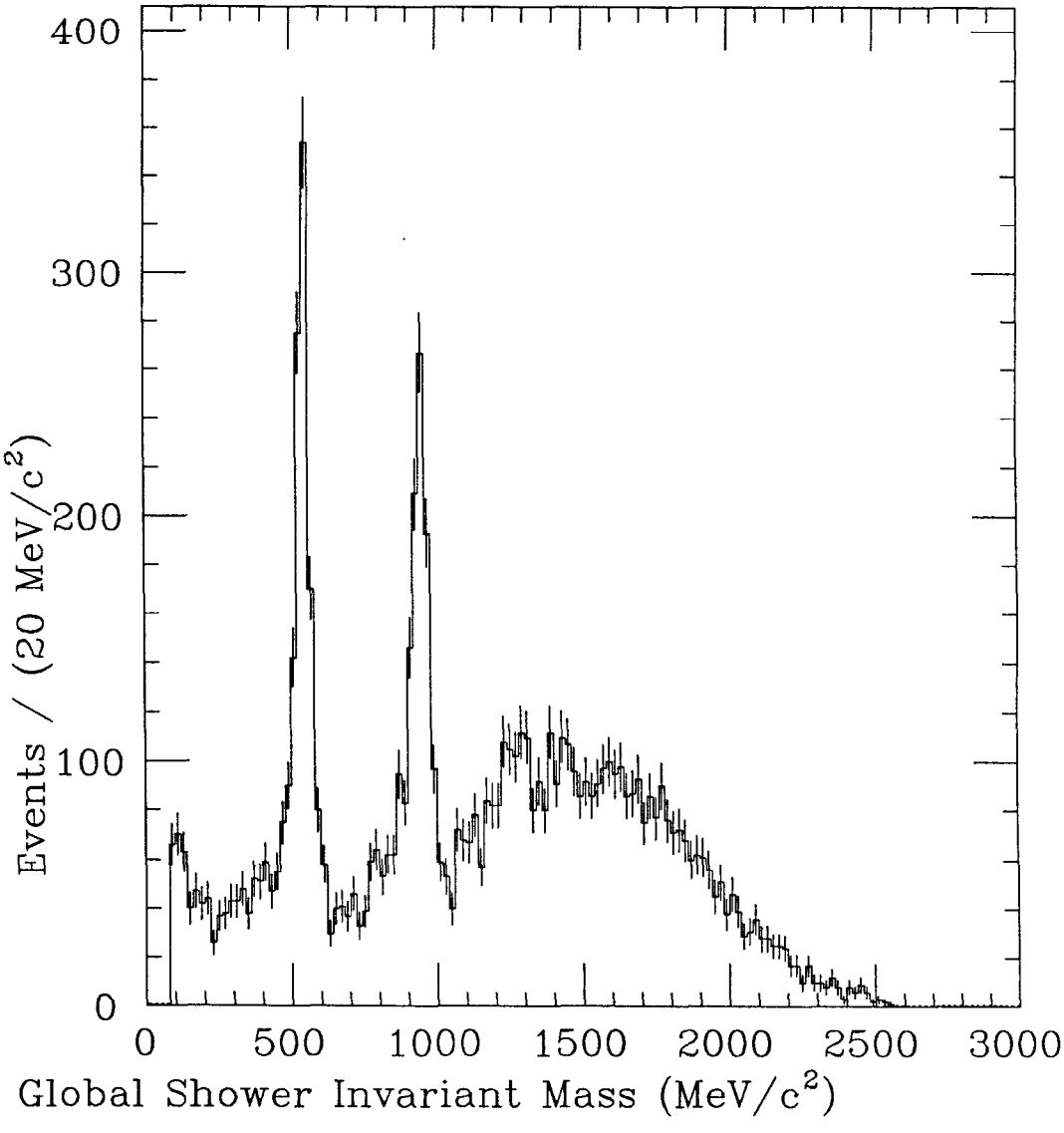

Fig. 6.11 Global shower invariant mass spectrum on J/ψ.

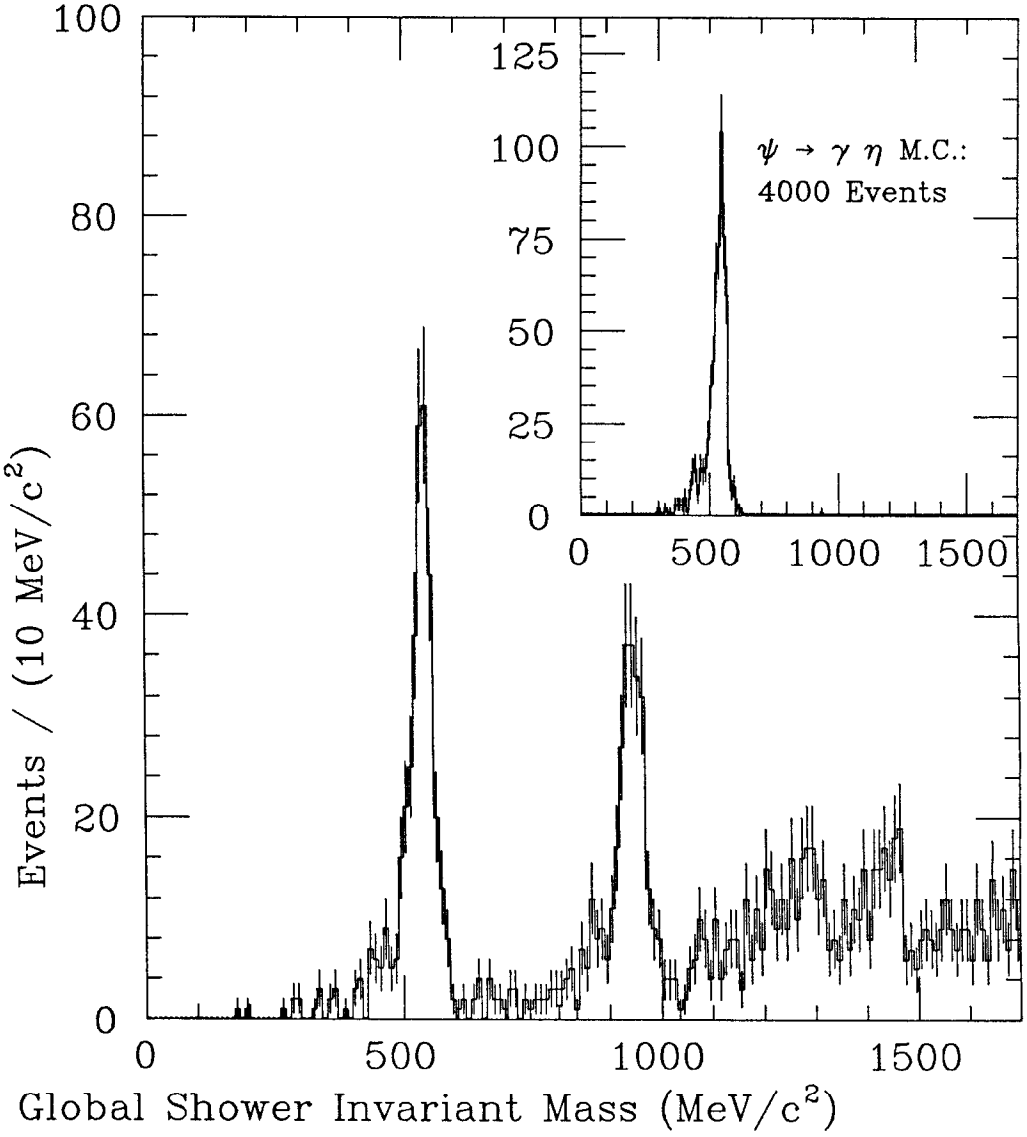

Fig. 6.12 Global shower invariant mass spectrum on J/ψ after η cuts. (Inset shows plot for 4000 generated $J/\psi \rightarrow \gamma\eta$ Monte Carlo events.)

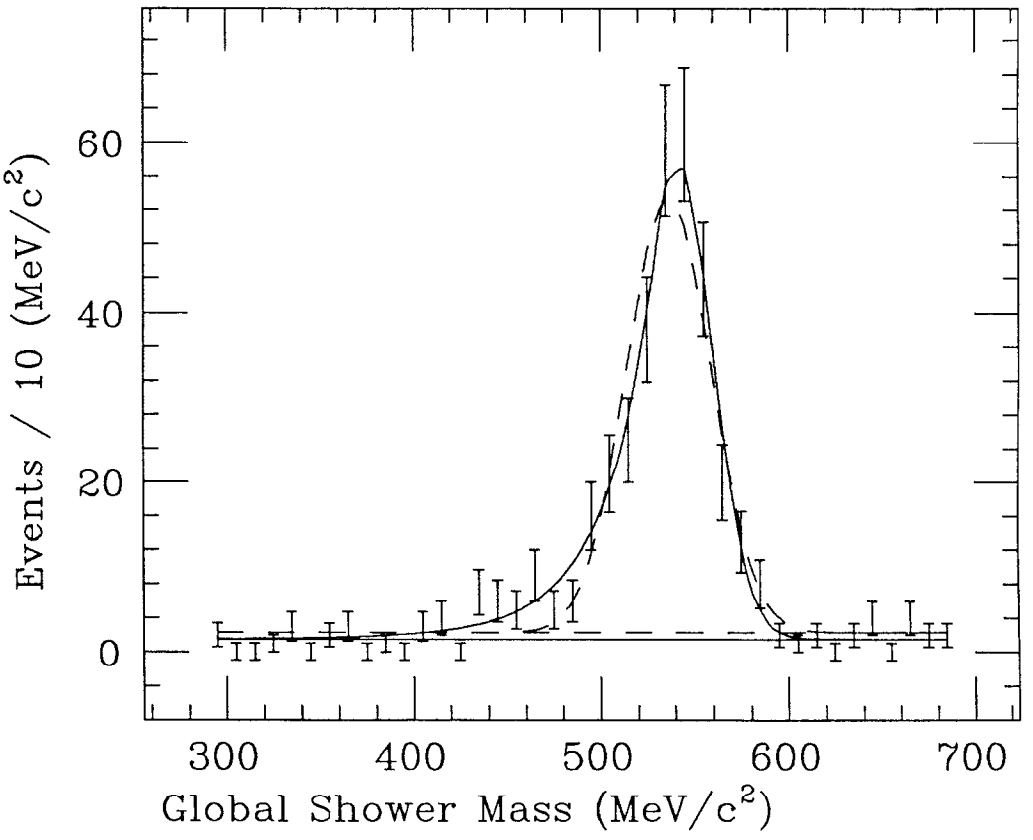

Fig. 6.13 Global shower invariant mass spectrum on J/ψ after η cuts fitted to line shape function (solid line) and Gaussian (dashed line) plus constant background. Best fitted values:

Parameter	Lineshape Fit	Gaussian Fit
M_0	541.2 $\pm$1.9 MeV/c^2	536.6 $\pm$1.6 MeV/c^2
σ	18.5 $\pm$1.5 MeV/c^2	22.5$\pm$1.5 MeV/c^2
r	11$\pm$12	
β	0.7 $\pm$0.2	
Conf. Lev.	0.160	0.0003

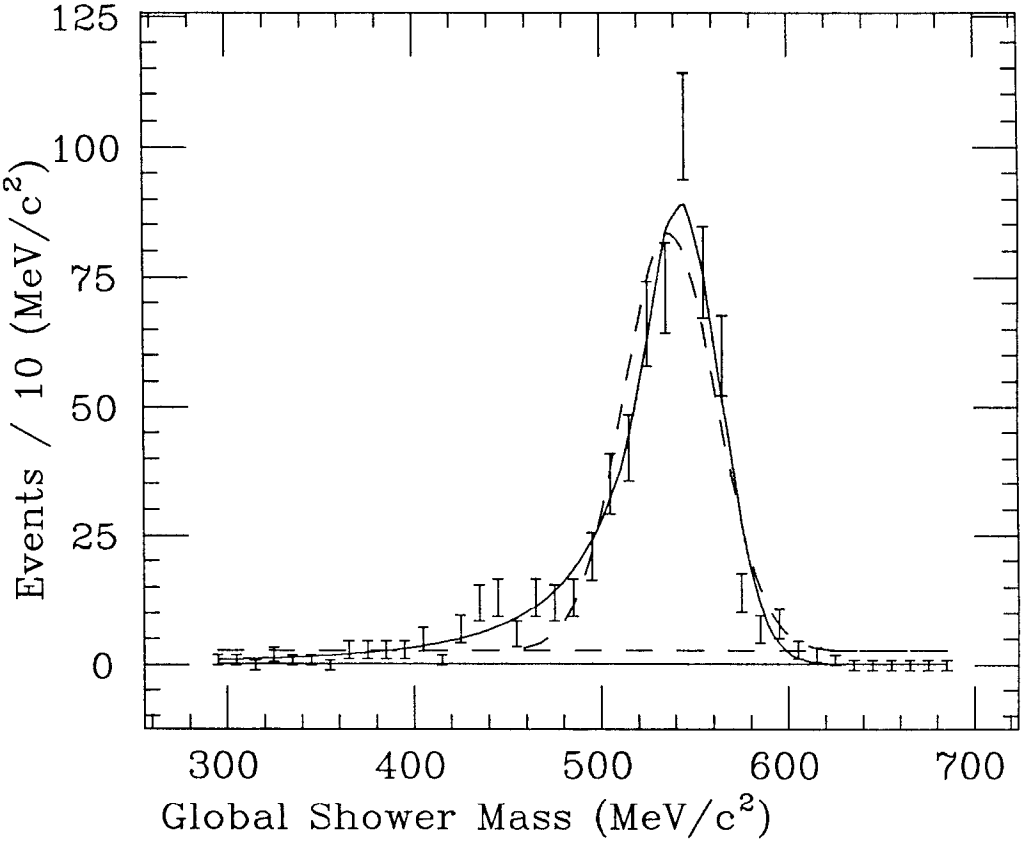

Fig. 6.14 Global shower invariant mass spectrum on $J/\psi \to \gamma\eta$ Monte Carlo after η cuts fitted to line shape function (solid line) and Gaussian (dashed line) plus constant background. Best fitted values:

Parameter	Lineshape Fit	Gaussian Fit
M_0	542.7 $\pm$2.0 MeV/c^2	536.9 $\pm$1.3 MeV/c^2
σ	21 $\pm$2 MeV/c^2	24.5$\pm$1.1 MeV/c^2
r	3.5$\pm$1.6	
β	0.7 $\pm$0.2	
Conf. Lev.	0. 4	8×10^{-3}

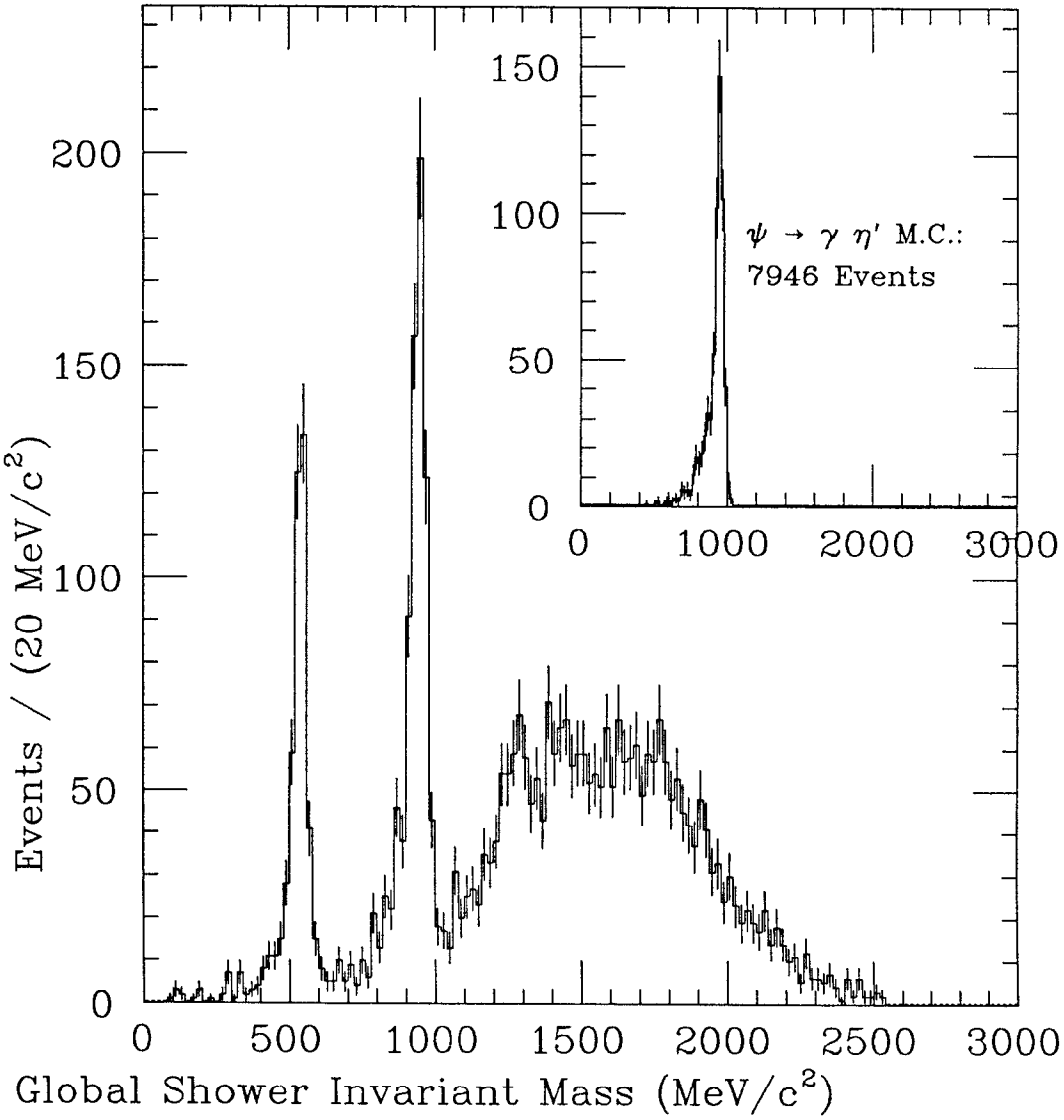

Fig. 6.15 Global shower invariant mass spectrum on J/ψ after η' cuts. (Inset shows plot for 7946 generated $J/\psi \rightarrow \gamma\eta'$ Monte Carlo events.)

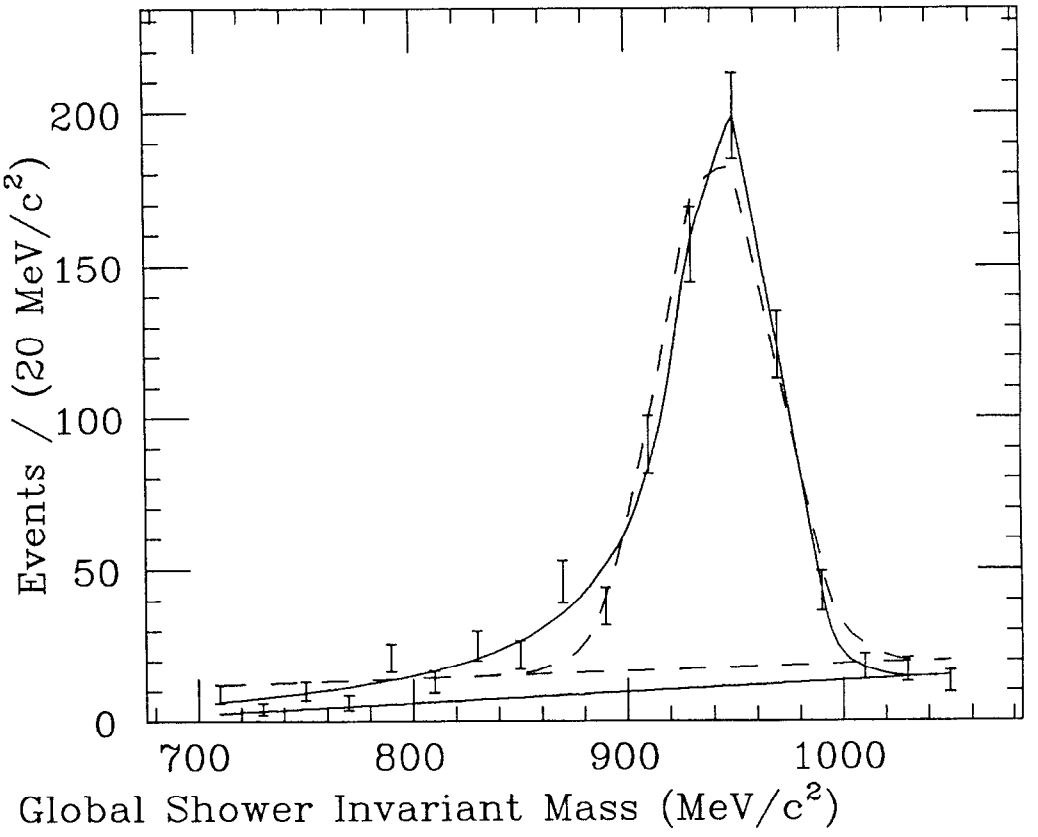

Fig. 6.16 Global shower invariant mass spectrum on J/ψ after η' cuts. fitted to line shape function (solid line) and Gaussian (dashed line) plus linear background. Best fitted values:

Parameter	Lineshape Fit	Gaussian Fit
M_0	946.2 $\pm$2.0 MeV/c^2	941.9 $\pm$1.5 MeV/c^2
σ	23.0 $\pm$2.0 MeV/c^2	26.5$\pm$1.8 MeV/c^2
r	2.2$\pm$1.7	
β	0.9 $\pm$0.2	
Conf. Lev.	0.05	1.2×10^{-9}

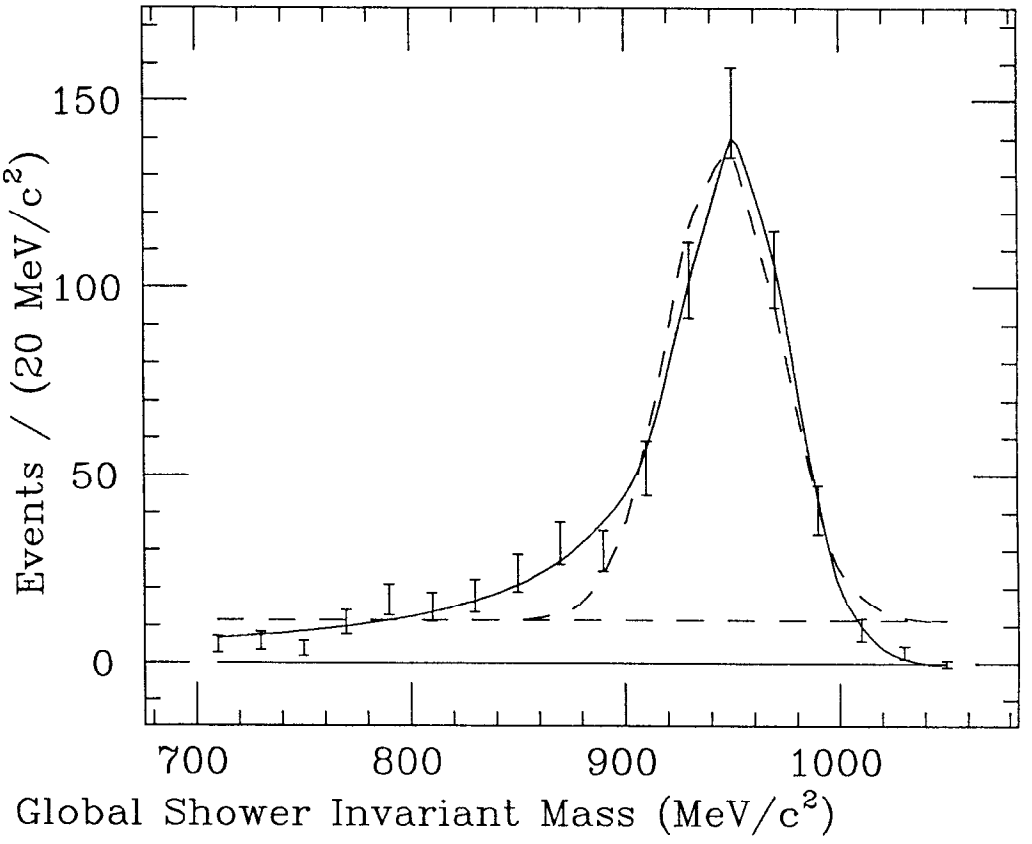

Fig. 6.17 Global shower mass spectrum on $J/\psi \rightarrow \gamma\eta'$ Monte Carlo after η' cuts fitted to line shape function (solid line) and Gaussian (dashed line) plus linear background. Best fitted values:

Parameter	Lineshape Fit	Gaussian Fit
M_0	950.8 $\pm$1.9 MeV/c^2	946.2 $\pm$1.8 MeV/c^2
σ	26 $\pm$2 MeV/c^2	25.9$\pm$1.7 MeV/c^2
r	1.5$\pm$0.5	
β	0.8 $\pm$0.2	
Conf. Lev.	0.40	1×10^{-12}

obtain an upper limit of BR($\psi' \rightarrow \gamma\eta$)<$2.0\times10^{-5}$.

Similarly, Fig. 6.21 shows the invariant mass spectrum after the η' cuts have been applied. Again, the large peak of the J/ψ plots is absent. Combining the 90% confidence level upper limits of 13 events (Fig. 6.22) with a Monte Carlo efficiency of 7.3%, we obtain BR($\psi' \rightarrow \gamma\eta'$)< 1.4×10^{-4} . The ψ' results are summarized in Table 6.3.

The upper limits from the 2γ and global shower analyses are derived as follows. The amplitude of the signal is fixed at zero. An integration is then performed over all parameters which are allowed to vary (here, the background parameters) to obtain the volume of the likelihood function corresponding to zero amplitude. The amplitude is then increased by a small amount (0.25) and another volume integration is performed. The process is repeated until the likelihood is virtually zero. The function so obtained gives the integrated likelihood as a function of the amplitude and so includes correlations between the signal amplitude and other parameters. The amplitude corresponding to 90% of the integral of this function is taken to be the 90% confidence level upper limit. It should be noted that the plots showing the upper limits are somewhat misleading. The amplitude corresponding to the 90% confidence level upper limit is plotted on top of the background corresponding to the maximum value of the likelihood, whereas in fact the upper limit does not correspond to any one set of background parameters.

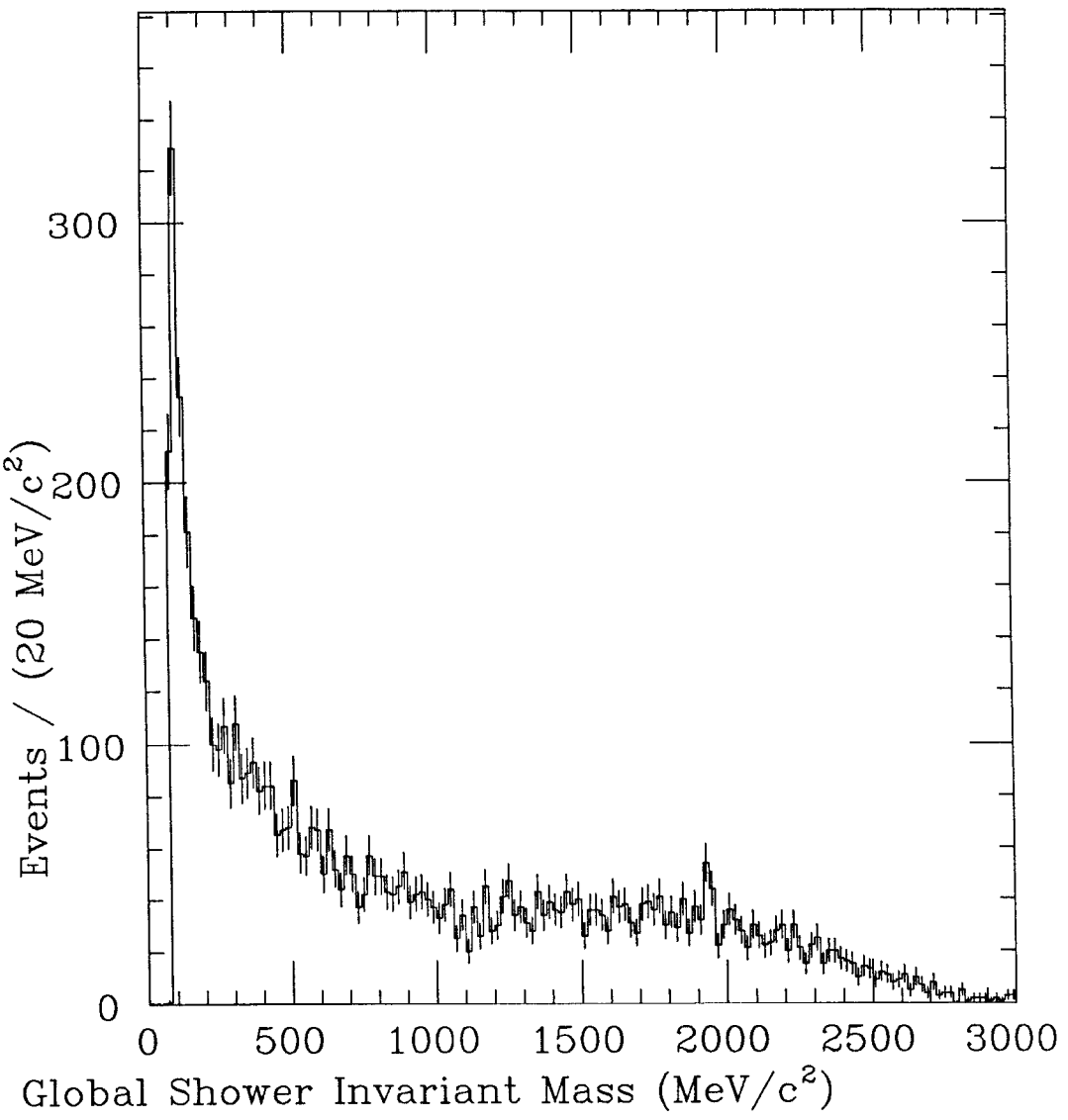

Fig. 6.18 Global shower invariant mass spectrum on ψ'.

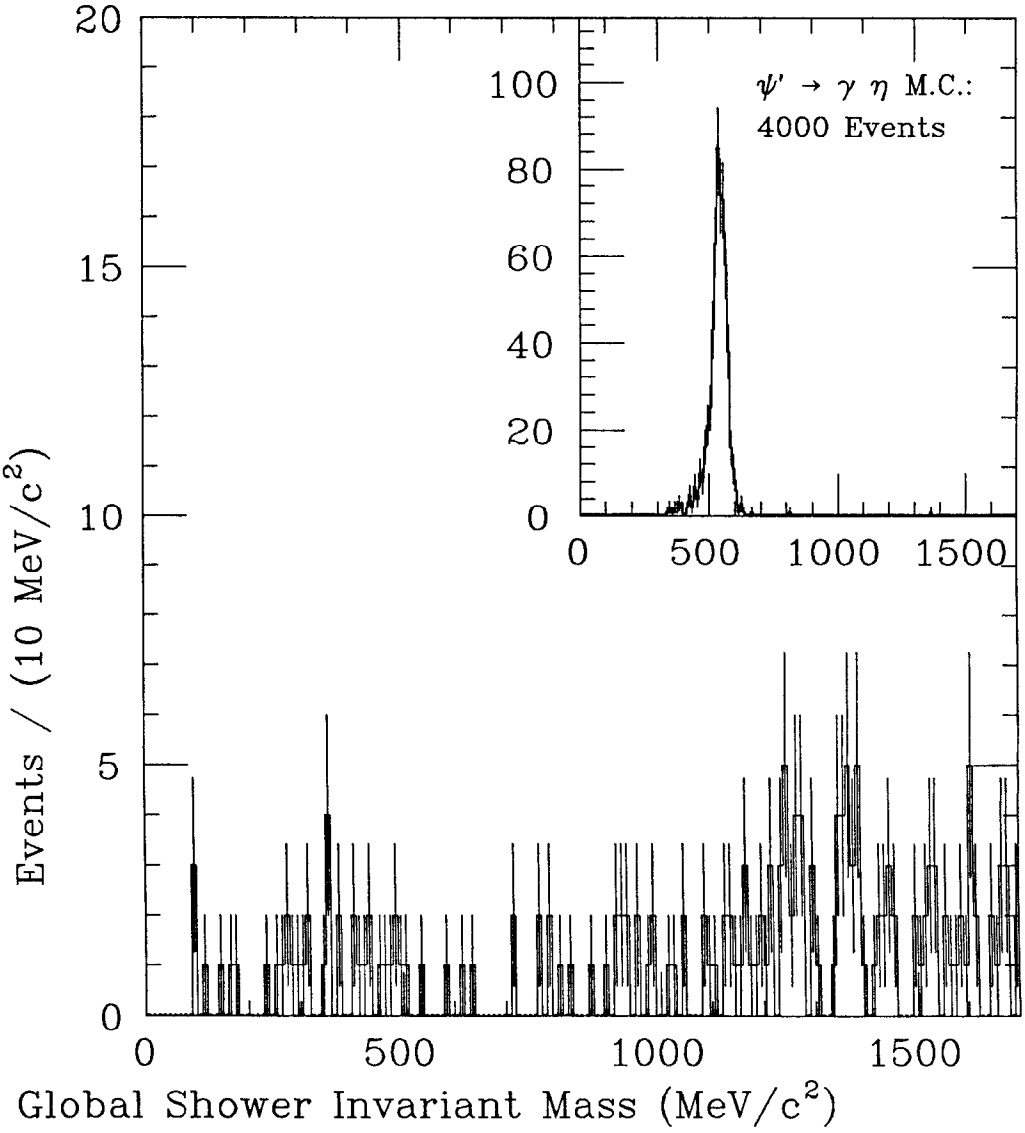

Fig. 6.19 Global shower invariant mass spectrum on ψ' after η cuts. (Inset shows plot for 4000 generated $\psi' \rightarrow \gamma\eta$ Monte Carlo events.)

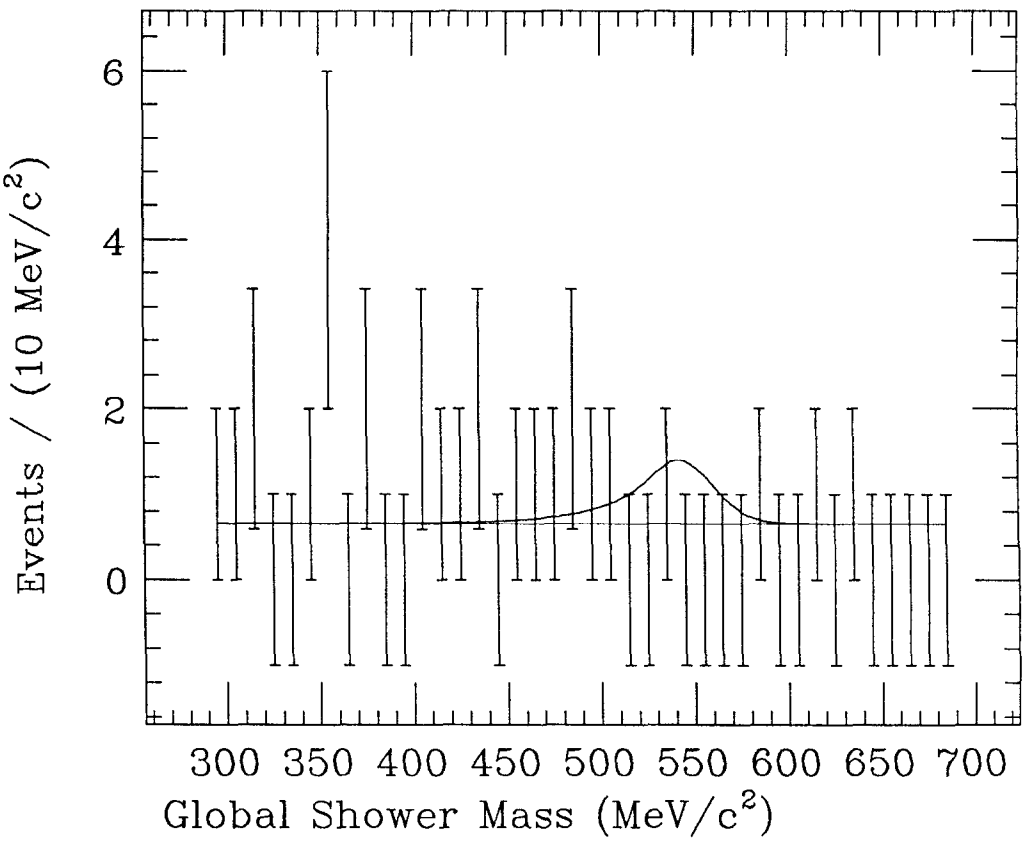

Fig. 6.20 Global shower mass spectrum on ψ' after η cuts fitted to line shape plus constant background. Signal shape fixed to that in J/ψ plot. Solid line shows signal amplitude corresponding to 90% confidence level upper limit.

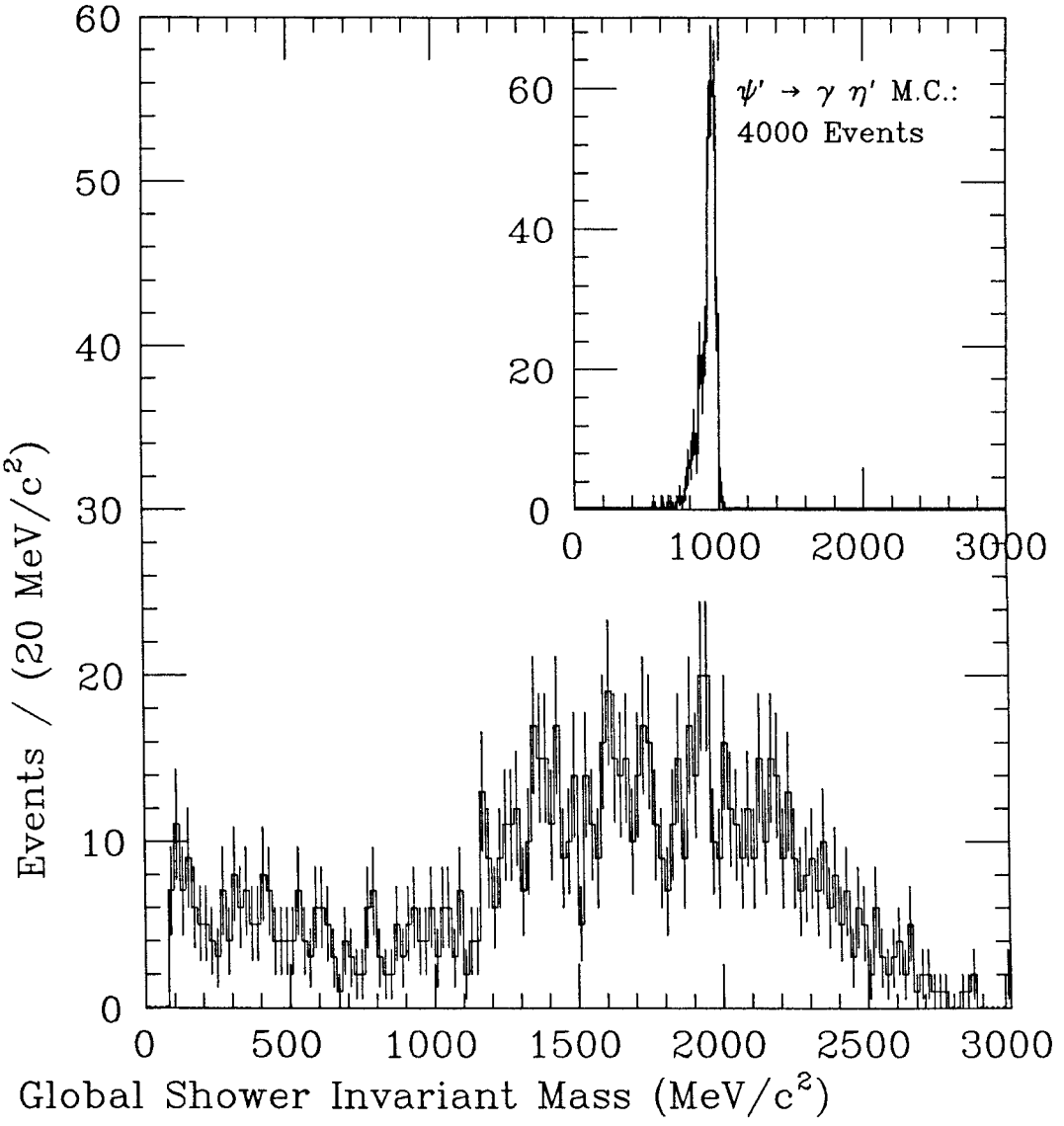

Fig. 6.21 Global shower invariant mass spectrum on ψ' after η' cuts. (Inset shows plot for 4000 generated $\psi' \rightarrow \gamma\eta'$ Monte Carlo events.)

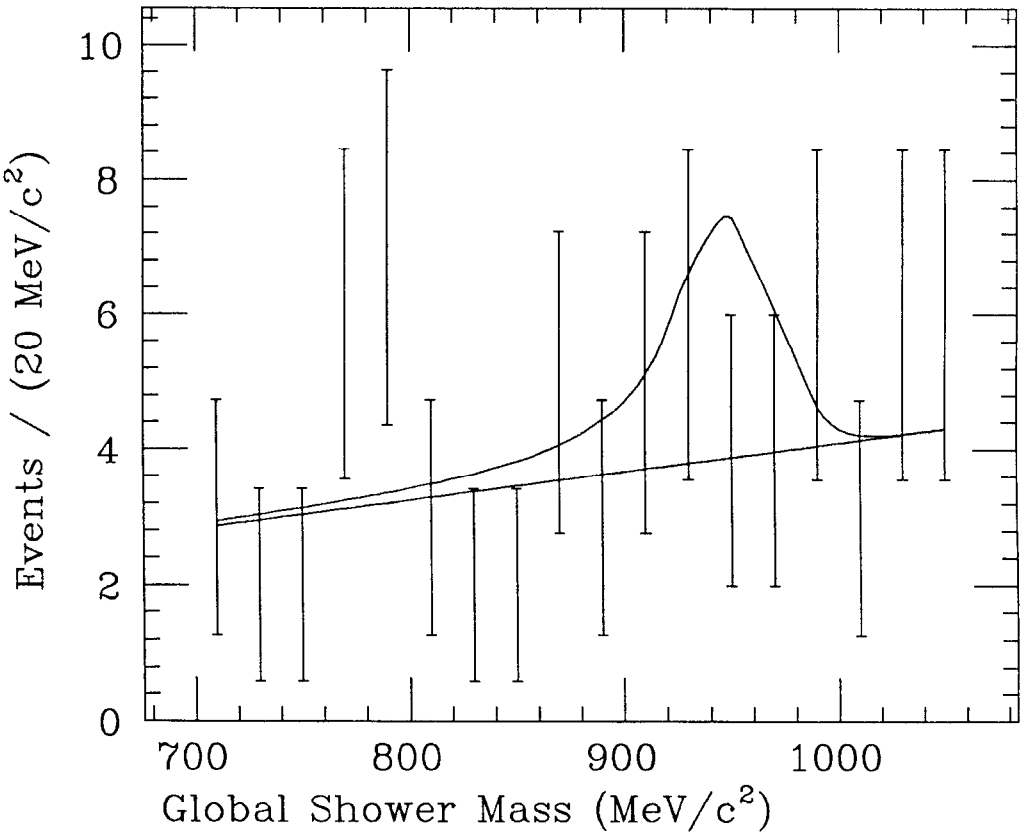

Fig. 6.22 Global shower mass spectrum on ψ' after η' cuts fitted to line shape plus linear background. Signal shape fixed to that in J/ψ plot. Solid line shows signal amplitude corresponding to 90% confidence level upper limit.

Decay	This Analysis	Previous Crystal Ball[2]	Other Experiments
$\eta \to \gamma\gamma$	99 ±10 ±20	88 ±19	82 ±10[3]
$\eta \to \pi^0\pi^0\pi^0$	101 ±6 ±16		
Average	100 ±14	88 ±19	86 ±9
$\eta' \to \gamma\gamma$	690 ±120 ±200	440 ±140	290 ±110[3]
$\eta' \to \gamma\rho$		410 ±100	470 ±20 ±70[6]
$\eta' \to \eta\pi^0\pi^0$	410 ±40 ±70	420 ±120	
Average	440 ±45	390 ±40	355 ±46

Table 6.2 $J/\psi \to \gamma\eta, \gamma\eta'$ branching ratios ($\times 10^5$).
("Average" for "Other Experiments" refers to Particle Data Group value.)

6.4 Summary

Tables 6.2 and 6.3 summarize the results of the analyses of this chapter and compare them with other experiments. The branching ratios obtained from the J/ψ data agree well with previous measurements. (The branching ratio of $J/\psi \to \gamma\eta'$ is somewhat confused. The reported values have ranged from (2 - 6) $\times 10^{-3}$. The Particle Data Group quotes a number in the low end of this range,[1] while the most recent measurement favors a higher value.[6]) The upper limits obtained from the ψ' analysis are below previously quoted upper limits but disagree with a measurement of $\psi' \to \gamma\eta'$ from the Mark II. In this regard it should be noted that the global shower technique is relatively free from background whereas an analysis of $\psi' \to \gamma\eta'$, $\eta' \to \gamma\rho$ can be contaminated by the continuum process $e^+e^- \to \gamma\rho$.

Decay	This Analysis	Other Experiments
$\eta \to \gamma\gamma$	< 5.1	< 20[4]
$\eta \to \pi^0\pi^0\pi^0$	< 2.0	
$\eta' \to \gamma\gamma$	< 170	< 630[5]
$\eta' \to \gamma\rho$		< 110[7]
		20 ± 10[8]
$\eta' \to \eta\pi^0\pi^0$	$< 14.$	

Table 6.3 $\psi' \to \gamma\eta, \gamma\eta'$ branching ratios and 90% confidence level upper limits $(\times 10^5)$.

The number of such events contained in the Crystal Ball ψ' sample corresponding to an integrated luminosity of 3300 nb^{-1} is estimated to be 550 events. If even a small fraction of these events is accompanied by a spurious low energy photon, the topology will mimic that of $\psi' \to \gamma\eta'$, $\eta' \to \gamma\rho$.

6.5 Comparison with Theory

Table 6.4 shows the ratios of branching ratios for the decays measured in this and the preceding chapter. The ψ' branching ratios have been normalized in each case to the J/ψ branching ratios measured in this study so that common systematic errors cancel. It is seen that in one case the data agree with the naive prediction of $12.0 \pm 2.2\%$, in one case the data are ambiguous, and in two cases there is substantial disagreement between the limits in the observed ratios and the theoretically expected value.

Final State γY	BR($\psi' \to \gamma Y$) ($\times 10^{-4}$)	BR($J/\psi \to \gamma Y$) ($\times 10^{-4}$)	Ratio (%) (%)
γf	1.5 $\pm$0.4 $\pm$0.5	17 $\pm$1 $\pm$5	9 $\pm$3
$\gamma\theta(1640)$,	< 1	5.8 $\pm$1.4 $\pm$1.5	< 10
$\gamma\theta(1720)$,	< 1	2.6 $\pm$0.8 $\pm$0.7	< 15
$\theta \to \eta\eta$			
$\gamma\eta$	< 0.2	10.1 $\pm$0.6 $\pm$1.6	< 1.8
$\gamma\eta'$	< 1.4	41 $\pm$5 $\pm$7	< 2.6

Table 6.4 Ratios of ψ' to J/ψ branching ratios for radiative decays (Crystal Ball).

Combining the Crystal Ball (Table 6.4) and Mark II (Table 5.1) results, we see that four decays ($\rho\pi$, K*K, $\gamma\eta$, and $\gamma\eta'$) are suppressed on the ψ' compared to the lowest-order QCD prediction and the branching ratios of the J/ψ to these final states. Some models have been put forth to explain the anomalous decays. G. Karl and W. Roberts[9] have suggested that there is an oscillation in the amplitude for three gluons to hadronize to the $\rho\pi$ and K*K final states which has a node at the mass of the ψ'. Brodsky and Lepage[10] have suggested that ψ' decays should be suppressed beyond the ratio of 12% by a factor of $(M_{J/\psi}/M_{\psi'})^n$ due to quark helicities where the power n depends on the decay mode in question. For the decay $\psi' \to \gamma\eta$, $n = 4$[11] yielding a suppression factor of roughly 1/2 which is insufficient to account for the suppression observed in the data. Also, for certain other decays the suppression is predicted to be even larger (n=8 for $p\bar{p}$ yielding a suppression factor of 1/4) even though the experimental value for the $\psi'/J/\psi$ ratio for these decays is in good agreement with 12.0% . (See Table 5.1.) Of course, rather than speaking of a suppression of ψ' decays, one can equally well describe the disagreement between

theory and experiment as an enhancement of J/ψ decays. Hou and Soni[12] have postulated that there is a vector glueball near 2.2 GeV with which the J/ψ mixes in order to enhance the decay rates of the J/ψ to $\rho\pi$ and K*K.

Finally, it is possible that the mechanism which we have assumed is responsible for radiative decays is not the dominant process in $\psi' \to \gamma\eta$ and $\psi' \to \gamma\eta'$ decays. Fritzsch and Jackson[13] have proposed a model of J/ψ decays in which the $c\bar{c}$ system radiates a photon to a virtual η_c. Assuming that SU(4) is broken, the η_c and η (or η') can mix so that the virtual η_c can become a real η(or η'). (See Fig. 6.23.) In a model such as this the fundamental assumption of the derivation in Chapter 4 that the two quarks annihilate is no longer valid. Rather than depending on the wavefunction at the origin, the decay rates depend on an overlap integral between initial and final states. Presumably the ψ' would decay in a similar fashion by a radiative transition to a virtual η_c' (and perhaps η_c). At the present time, no calculation has been made for the decay rates of $\psi' \to \gamma\eta$ and $\psi' \to \gamma\eta'$ in the context of this model.

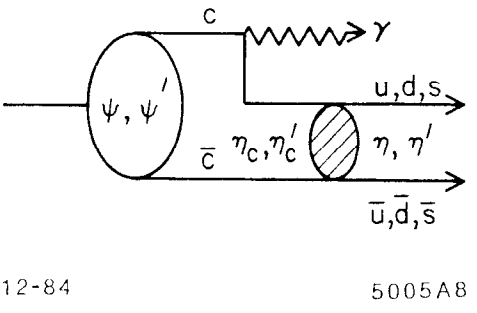

Fig. 6.23 Feynman diagram of the radiative decay of the J/ψ or ψ' to a virtual η_c or η_c' .

In summary, no theoretical model has been presented which convincingly explains the suppression of certain ψ' decays. The only pattern one sees in the suppressed channels ($\rho\pi$, K*K, $\gamma\eta$ and $\gamma\eta'$) is that they all consist of a vector and a

pseudoscalar. This pattern may perhaps be useful in elucidating the suppression mechanism.

References

1) Particle Data Group, *Rev. of Mod. Phys.* **56** (1984) S1.

2) K. Königsmann, in *Quarks, Leptons, and Supersymmetry*, proceedings of the XVIIth Recontre de Moriond - First Session, 1982, edited by J. Tran Tranh Van (Gif-sur-Yvette, France, Editions Frontieres, 1982), and SLAC-PUB-2910.

3) R. Brandelik, *Zeitschrift für Physik* **C1** (1979) 233.

4) S. Yamada, in *Proceedings 1977 International Symposium on Lepton and Photon Interactions at High Energies*, Hamburg, 1977, edited by F. Gutbrod (Deutsches Electronen-Synchrotron DESY, Hamburg, 1977).

5) W. Braunschweig, *Physics Letters* **67B** (1977) 249.

6) J. Richman, Ph.D. thesis, California Institute of Technology, 1985 (unpublished).

7) W. Bartel, *Physics Letters* **64B** (1976) 483.

8) D. Scharre, in *High Energy Physics - 1980*, Proceedings of the XX International Conference, Madison, Wisconsin, edited by L. Durand and L. G. Pondrum (American Institute of Physics, New York, 1981).

9) G. Karl and W. Roberts, *Phys. Lett.* **144B** (1984) 263.

10) S. J. Brodsky and G. L. Lepage, *Phys. Rev. D* **24** (1981) 2848.

11) S. J. Brodsky, private communication.

12) Wei-Shu Hou and A. Soni, *Phys. Rev. Lett.* **50** (1983) 569; *Phys. Rev. D* **29** (1984) 101.

13) H. Fritzsch and J. D. Jackson, *Phys. Lett.* **66B** (1977) 365.

Chapter 7

Summary and Conclusions

In the preceding chapters we have described a study of radiative ψ' decays using the Crystal Ball detector. Since this detector has excellent energy and position resolution for photons, we have concentrated on those final states which contain only γ's. We have measured the following branching ratios from radiative decays of the ψ' to charmonium states (first errors statistical, second systematic):

Decay	Branching Ratio
$\chi_0 \to \pi^0\pi^0$	$(3.5 \pm 0.3 \pm 1.2) \times 10^{-3}$
$\chi_2 \to \pi^0\pi^0$	$(1.2 \pm 0.2 \pm 0.4) \times 10^{-3}$
$\chi_0 \to \gamma\gamma$	$(4.5 \pm 2.2 \pm 2.0) \times 10^{-4}$ or $\leq 1.0 \times 10^{-3}$ (90% C.L.)
$\chi_2 \to \gamma\gamma$	$(9.5 \pm 2.9 \pm 4.5) \times 10^{-4}$
$\chi_0 \to \eta\eta$	$(2.8 \pm 0.9 \pm 1.3) \times 10^{-3}$
$\chi_2 \to \eta\eta$	$(8.4 \pm 4.2 \pm 4.0) \times 10^{-4}$
$\eta_c' \to \gamma\gamma$	$< 1 \times 10^{-2}$ (90% C.L.)

Table 7.1 Measured branching ratios of charmonium states.

We estimate the probability that the peak corresponding to the $\chi_0 \to \gamma\gamma$ decay

is due to a background fluctuation to be 1 in 300, and we quote both a branching ratio and an upper limit for this decay. Using the exceptionally clean signal of the decay chain $\psi' \rightarrow \gamma\chi_0$, $\chi_0 \rightarrow \pi^0\pi^0$, we have also measured the mass and width of the χ_0 to be 3415.5 $\pm$1.3 $\pm$0.6 MeV/c^2 and 8.8 $\pm$ 1.3 $\pm$ 1.5 MeV/c^2, respectively, where we have unfolded the natural line width from the observed line width using the known detector response function as determined by a study of $\psi' \rightarrow \eta J/\psi, J/\psi \rightarrow e^+e^-, \eta \rightarrow \gamma\gamma$.

In addition, we have measured the branching ratios of non-charmonium decays of the ψ'. We have performed a parallel analysis on the J/ψ, and we express our results in terms of the ratios of branching ratios of the ψ' and J/ψ to the same final state:

Final State γY	BR($\psi' \rightarrow \gamma Y$) ($\times 10^{-4}$)	BR($J/\psi \rightarrow \gamma Y$) ($\times 10^{-4}$)	Ratio (%)
γf	1.5 $\pm$0.4 $\pm$0.5	17 $\pm$1 $\pm$5	9 $\pm$3
$\gamma\theta(1640)$ or $\gamma\theta(1720)$, $\theta \rightarrow \eta\eta$	< 1 < 1	5.8 $\pm$1.4 $\pm$1.5 2.6 $\pm$0.8 $\pm$0.7	< 10 < 15
$\gamma\eta$	< 0.2	10.1 $\pm$0.6 $\pm$1.6	< 1.8
$\gamma\eta'$	< 1.4	41 $\pm$5 $\pm$7	< 2.6

Table 7.2 Ratios of ψ' to J/ψ branching ratios for radiative decays.

Upper limits are 90% confidence level. We quote two results for the θ depending on whether we fit one ($\theta(1640)$) or two (f' and $\theta(1720)$) Breit-Wigner line shapes to the $\eta\eta$ invariant mass plots for events consistent with $J/\psi \rightarrow \gamma\eta\eta$. (In the latter case, we obtain BR($J/\psi \rightarrow \gamma$f')BR(f' $\rightarrow \eta\eta$) = (1.9$\pm$0.8$\pm$0.5) $\times 10^{-4}$.) Similarly,

most of the systematic error in the value of BR($J/\psi \rightarrow \gamma$f) is due to the uncertainty of how many structures to fit in the $\pi^0\pi^0$ invariant mass plot for events consistent with $J/\psi \rightarrow \gamma\pi^0\pi^0$. The Mark III collaboration[1] has reported evidence for structures at 1.7 and 2.1 GeV/c^2 (referred to as θ and X) in the $\pi^+\pi^-$ invariant mass plot in $J/\psi \rightarrow \gamma\pi^+\pi^-$. If in addition to the signal seen in the $\pi^0\pi^0$ plot at the mass of the f, we include two additional non-interfering Breit-Wigner line shapes with means and widths fixed to the best fitted Mark III values of the θ and X, we obtain BR($J/\psi \rightarrow \gamma\theta$)BR($\theta \rightarrow \pi^0\pi^0$) = $(7.8 \pm 2.2 \pm 2.7) \times 10^{-5}$ and BR($J/\psi \rightarrow \gamma X$)BR($X \rightarrow \pi^0\pi^0$) = $(9.4 \pm 2.4 \pm 3.2) \times 10^{-5}$. These branching ratios are consistent with the Mark III results if it is the θ and X have isospin zero.

The theoretical predictions for the processes we have studied should be fairly reliable since unknown parameters can be determined from other measurements within the charmonium family. However, as detailed in Chapters 4-6, there are some notable discrepancies. The measured width of the χ_0 is a factor of 3 to 8 larger than that expected from lowest-order QCD potential models. Although the two photon partial widths of the χ_0 and χ_2 (calculated from the measured two photon branching ratios and full widths) agree with the theoretical predictions from both QCD potential models and sum rules, the branching ratio of the χ_0 to two photons is a factor of three smaller than that predicted by QCD potential models. (The disagreement exists even if we instead compare the theoretical expectation with the 90% confidence level upper limit.) This disagreement is disturbing inasmuch as the theoretical prediction does not depend on the assumed interquark potential and so is simply a ratio of coupling constants. Whether this disagreement can be attributed to higher order corrections is unclear.

The simplest model of non-charmonium decays of the J/ψ and ψ' predicts that the ratio of branching ratios of these two resonances to any non-charmonium final state should be roughly 12%. One of the channels we have studied, $J/\psi, \psi' \rightarrow \gamma$f, is consistent with this prediction, and the upper limit on another, $J/\psi, \psi' \rightarrow \gamma\theta(1640)$, is inconclusive. Two other channels ($J/\psi, \psi' \rightarrow \gamma\eta$, $J/\psi, \psi' \rightarrow \gamma\eta'$) are

unobserved on the ψ' at levels of 1.4% and 2.6%, respectively, of their branching ratios on the J/ψ at 90% confidence level. This result is puzzling since it is a basic assumption of the charmonium model that the ψ' is an excited state of the J/ψ and so presumably should behave similarly (when proper account is taken of the different wavefunctions). It is more so when combined with results from a Mark II study on hadronic decays of the ψ' which also observed that some decay modes were suppressed (one, $\rho\pi$, by more than an order of magnitude), while others obeyed the simple QCD prediction.

The data are as yet insufficient to determine if these discrepancies require the modification of some of our fundamental ideas about the nature of the charmonium family or whether they indicate that more precise theoretical calculations are required. What is certain is that we have no convincing explanations for these effects. The charmonium family has not yet been fully explored (experimentally or theoretically) and may still contain surprises.

References

1) K. E. Einsweiler, Ph.D. thesis, Stanford University, 1984, and SLAC-Report 272 (unpublished).

Appendix A

Energy Response Function

A.1 Introduction

The results of this study depend on a detailed knowledge of the response of the Crystal Ball detector to a photon. Many of the gross features of the interaction of an electromagnetic particle showering in a scintillator can be modeled with the Electron Gamma Shower Monte Carlo (EGS). Studies of this type are described in Appendix B. However, one aspect of the detector response, the energy resolution for photons, is particularly crucial for the investigations presented here, and it has been shown that Monte Carlo simulations are unable to describe adequately this function. (See Appendix B.)

In this Appendix we extract the energy response function for photons (or "line shape") from the data themselves. We use the reactions listed in Table A.2, each of which contains a photon (and/or a particle which decays into two photons) of well-defined energy. These reactions are relatively free from background and combined yield information on the line shape parameters over most of the range of photon energies of interest. We summarize the results of these studies at the end of this appendix.

Particle	Mass (MeV)	Width (keV)
J/ψ	3069.9 ±0.1	63 ±9
ψ'	3686.0 ±0.1	215±40
η	548.8 ±0.6	0.83±0.12
η'	957.57±0.25	280±10

Table A.1 Masses and widths of particles used in resolution studies.[1]

Reaction	Energy of Decay Product 1 (MeV)	Energy of Decay Product 2 (MeV)
$J/\psi \rightarrow \gamma\eta$	1499.8 ±0.1	1597.08 ±0.15
$J/\psi \rightarrow \gamma\eta'$	1400.4 ±0.1	-
$\psi' \rightarrow \eta J/\psi$	582.88 ±0.15	-

Table A.2 Energies of particles used in resolution studies.

A.2 Monoenergetic Photons

We begin with radiative decays to states of well-known masses. Two candidate reactions are $J/\psi \rightarrow \gamma\eta$ and $J/\psi \rightarrow \gamma\eta'$. We note from Table A.1 that the widths of the participant particles in these reactions are extremely small and that their masses have been measured with very high accuracy. Thus, we can calculate the energy of the monochromatic photon in these reactions with small errors as shown in Table A.2. (The widths of the lines are negligible in comparison with the detector resolution.) We discuss the two reactions separately.

A.2.1 $J/\psi \rightarrow \gamma\eta$

We identify the η via its two-photon decay so that the final state consists of three photons. Thus, we must contend with backgrounds from the reactions $e^+e^- \rightarrow (\gamma)\gamma\gamma$ and $J/\psi \rightarrow \gamma\eta'$, $\eta' \rightarrow \gamma\gamma$. Also, we wish to make our selection in such a way that we do not introduce a bias in the sample of high energy photons (such as would result from a kinematic fit). Finally, we require that the events in our sample are such that there is no possibility of ambiguity between the direct photon and one of the photons from the decay of the η.

We start with the all-neutral J/ψ sample which has been processed through the neutral analysis program as described in Chapter 3 and select those events which have three and only three tracks. Figure A.1 shows a plot of the energy of the lowest energy track *vs.* the opening angle of the two lowest energy tracks. Several distinct structures are visible. At small photon energies and very small and large opening angles are clusters due to $e^+e^- \rightarrow (\gamma)\gamma\gamma$. A band from the decay $J/\psi \rightarrow \gamma\eta$, $\eta \rightarrow \gamma\gamma$ is visible along with a fainter band from $J/\psi \rightarrow \gamma\eta'$, $\eta' \rightarrow \gamma\gamma$. The observed energy of the η should be reasonably close to its actual value of 1597 MeV from Table A.2. By requiring the low energy photon to have 400 MeV or more, we eliminate the possibility of confusion between the direct photon and the high energy photon from the η decay since they will be separated by 300 MeV. In addition, the QED background is suppressed by this cut. We also require that the opening angle between the two low energy photons be such that $\cos\theta_{23} > 0.5$ so as to reduce background from other channels. These cuts define the box shown in Fig. A.1. Note that the energy of the high energy photon is unconstrained by these cuts.

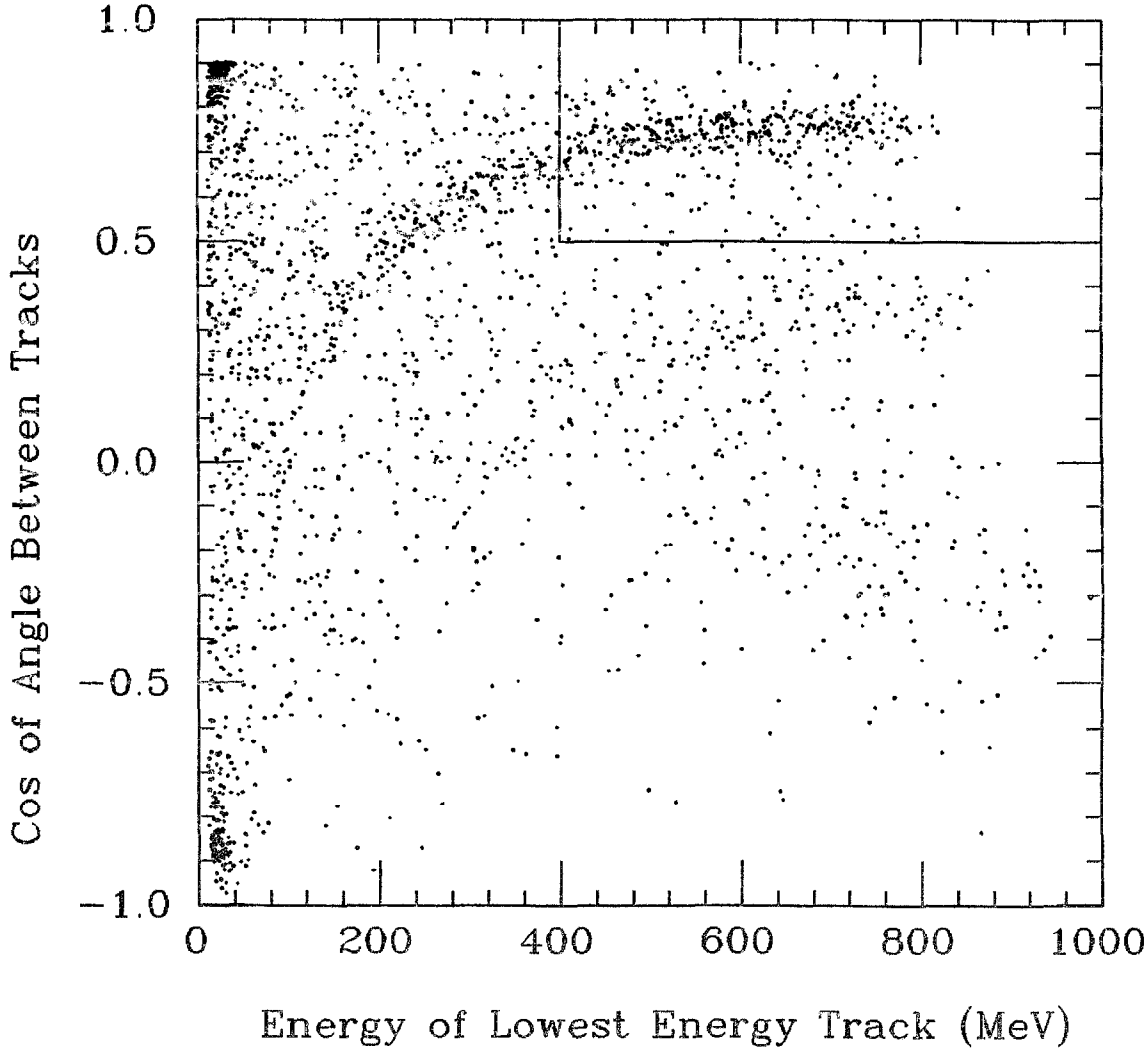

Fig. A.1 Three track events at J/ψ: energy of lowest energy track *vs.* cosine of opening angle of two lowest energy tracks. (Box shows cut.)

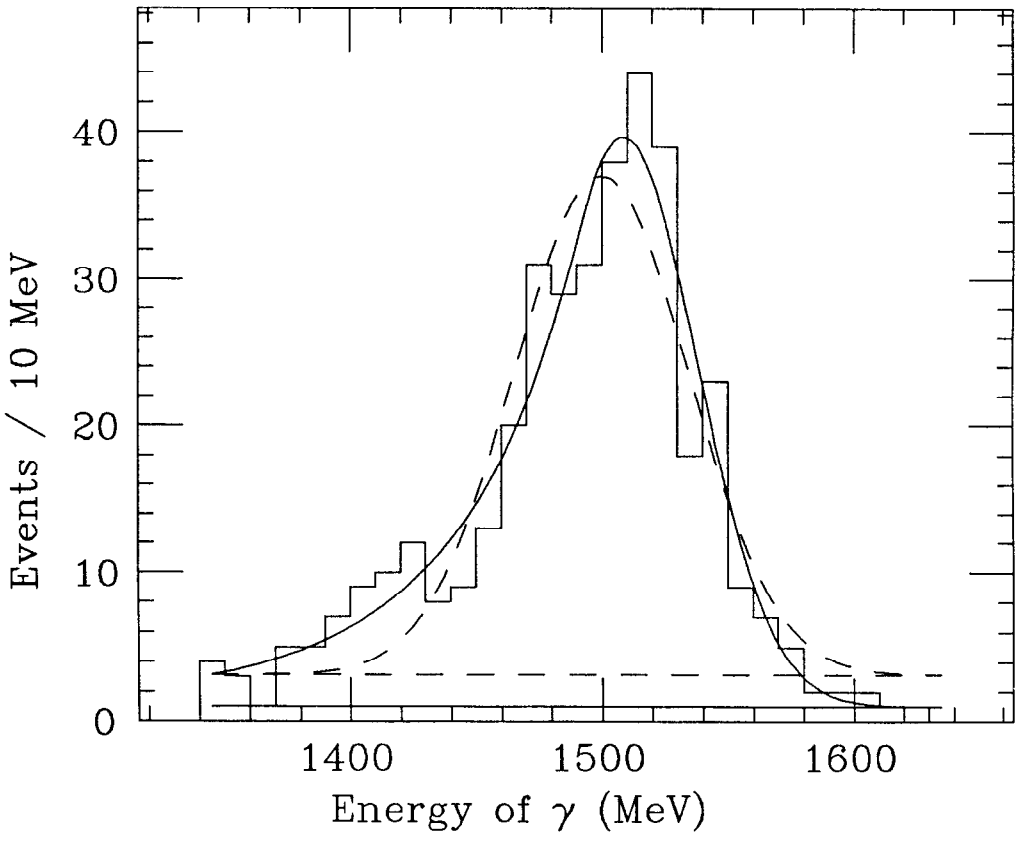

Fig. A.2 $J/\psi \rightarrow \gamma\eta$: Energy of direct gamma fitted to line shape function (solid line) and Gaussian (dotted line). Fitted parameters:

Parameter	Lineshape Fit	Gaussian Fit
α	8.7 $\pm$4.6 MeV	0.1 $\pm$3.2 MeV
σ_0	2.2 $\pm$0.3%	2.5 $\pm$0.3 %
r	8 $\pm$12	
β	0.65 $\pm$0.23	
Conf. Lev.	0.777	0.004

The dotted line in Figure A.2 shows the spectrum of the high energy photon from events selected as described above fit to a Gaussian line shape.* As can be seen, this simple function does not adequately fit the spectrum. We can improve the fit if we supplement the Gaussian with a low energy tail. We define the "line shape function" to be

$$\begin{aligned}\frac{dN}{dE} = g\left(E, E_0; \alpha\sigma_0\beta r\right) &= \exp\left(\left(E-\alpha-E_0\right)^2/2\sigma^2\right) \quad E \geq E_0 - \beta\sigma \\ &= A\left(\frac{E_1 - E_0 + \beta\sigma}{E_1 - E}\right)^r \quad E < E_0 - \beta\sigma\end{aligned} \qquad [A.1]$$

where

E = observed energy

E_0 = actual energy

α = energy offset. In general, $\alpha = \alpha(E_0)$

$\sigma = \sigma_0 E_0^{3/4}$(GeV)

β, r = parameters describing the power-law tail: β defines the joining point; r is the power.

A, E_1 = parameters determined from the requirement that the two pieces of the function join continuously and have a continuous first derivative.

This functional form has been found to work well in fits to inclusive photon spectra in the Crystal Ball. The functional form for σ is expected both from Monte Carlo studies and from test beam results with a Crystal Ball prototype. The solid

* The fit minimizes $-2ln\mathcal{L}$ where $\mathcal{L}$ is the product of likelihoods for all bins in the histogram; Poisson errors are assumed for each bin. A χ^2 is calculated at the end of the minimization in order to calculate the confidence level of the fit, but this quantity is not maximized. The errors shown on the parameters are the parabolic errors calculated from the curvature of the function $-2ln\mathcal{L}$ at its minimum.

line in Fig. A.2 shows a fit with this function which yields a significantly higher confidence level than the Gaussian fit. (As illustrated by this fit, the power parameter r typically has the largest relative error of the fit parameters.)

A.2.2 $J/\psi \rightarrow \gamma\eta'$

We identify the η' in this reaction by its decay to $\gamma\rho$. Thus, we look for J/ψ events which have two charged and two neutral tracks in the final state, where at least one of the neutral tracks must have more than 1000 MeV and neither neutral track is allowed to have a PIFIT mass greater than 80 MeV/c^2. We discard any event that has a track beyond $|\cos\theta| > 0.90$ (where θ is the angle between the track and the beam direction) or two tracks with an opening angle $\theta_{opening}$ such that $\cos\theta_{opening} > 0.90$. To reduce background from competing channels we eliminate any event in which the two gamma mass, $M_{\gamma\gamma}$, falls in the windows 100 MeV/c^2 $< M_{\gamma\gamma} <$ 170 MeV/c^2 or 510 MeV/c^2 $< M_{\gamma\gamma} <$ 570 MeV/c^2. Finally, we require that the missing mass opposite the two neutral tracks be less than 1000 MeV/c^2. 1000 events pass these cuts. The solid line in Fig. A.3 shows the spectrum of neutral tracks in these events fitted to a line shape function; the dotted line shows a fit to a simple Gaussian. In this case, both fits are acceptable, although both assign a large fraction of the events to background.

A.3 Monoenergetic Particles Decaying to Two Photons

The studies described above are sufficient to measure the energy response function for high-energy γ's. However, there are no corresponding decays of the J/ψ or ψ' involving low energy monochromatic photons. (The radiative photons in the decays $\psi' \rightarrow \gamma\chi_1$ and $\psi' \rightarrow \gamma\chi_2$ are potential candidates, but the masses and widths of these states are not known to sufficient accuracy.) Alternatively, we can measure the energy of a particle of small width and known energy which decays into two γ's such as the η in $\psi' \rightarrow \eta J/\psi$. Although simple in concept, this procedure is complicated by the fact that we must unfold the sum of two line shape functions,

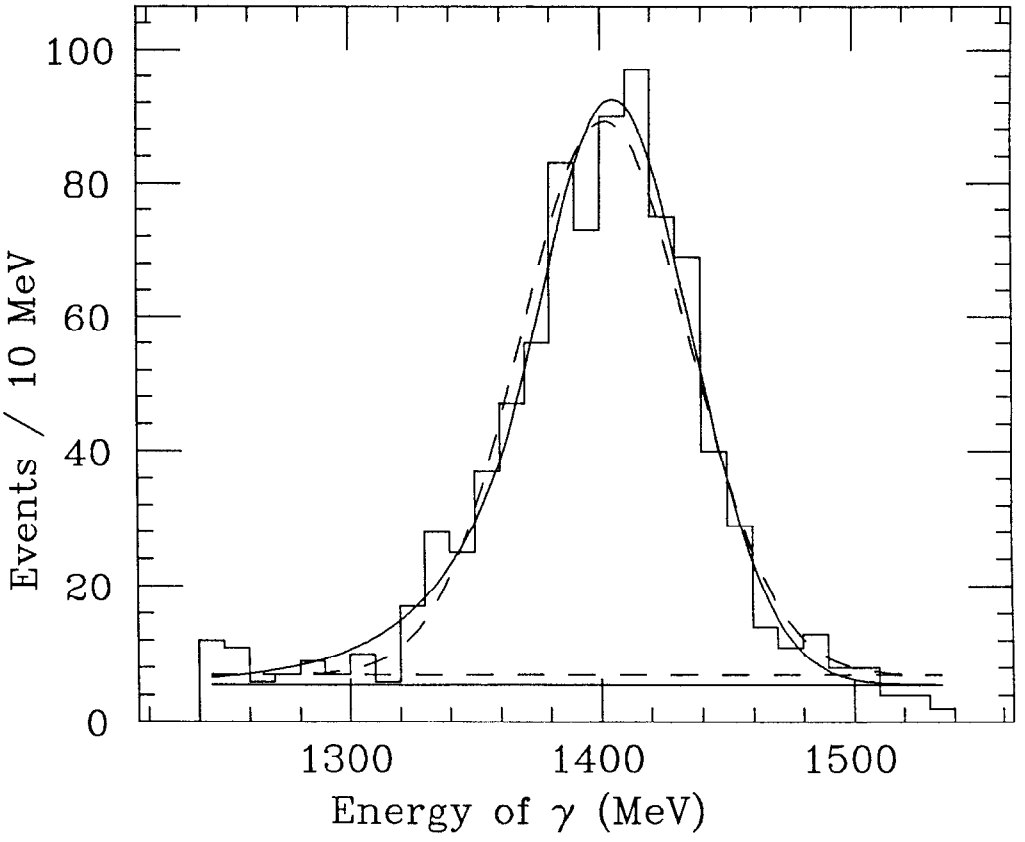

Fig. A.3 $J/\psi \rightarrow \gamma\eta'$: Energy of direct gamma fitted to line shape function (solid line) and Gaussian (dotted line).

Best fitted values:

Parameter	Lineshape Fit	Gaussian Fit
α	4.8 $\pm$2.0 MeV	1.6 $\pm$1.5 MeV
σ_0	2.5 $\pm$0.2%	2.6 $\pm$0.1 %
r	20 $\pm$15	
β	1.03 $\pm$0.12	
Conf. Lev.	0.203	0.110

and we discuss the treatment of this problem first. We consider the decay $X \rightarrow \gamma\gamma$ where we assume the energy of the X is known precisely so that any spread in the observed distribution of the energy of X can be attributed to the detector response function. It is important in the following to distinguish between actual and observed values of energies. We let k_1, k_2, and k_X denote the actual values of the energies of the two γ's and the X, and K_1, K_2, and K_X the corresponding observed energies. k_1 and k_2 are constrained to sum to k_X by conservation of energy; K_1 and K_2 sum to K_X by definition.

The probability distribution of K_1 and K_2 is related to that of k_1 and k_2 by

$$P(K_1, K_2) = \iint g\,(K_1, k_1;\ \alpha\sigma_0\beta r)\, g\,(K_2, k_2;\ \alpha\sigma_0\beta r)\, p(k_1 k_2)\ dk_1\, dk_2 \qquad [A.2]$$

where we have assumed that the response function is separable (see below). $p(k_1\, k_2)$ is the joint probability distribution of the two random variables k_1 and k_2. By assumption, the sum of these two variables is constrained:

$$p(k_1\, k_2) = \delta\,(k_X - k_1 - k_2)\ f(k_1) \qquad [A.3]$$

where $f(k_1)$ is the distribution of the single random variable k_1. [A.2] becomes

$$P(K_1, K_2) = \int g\,(K_1, k_1;\ \alpha\sigma_0\beta r)\, g\,(K_2, k_X - k_1;\ \alpha\sigma_0\beta r)\, f(k_1)\ dk_1. \qquad [A.4]$$

We will measure the sum $K_X \equiv K_1 + K_2$. The probability distribution of this variable is

$$P_X(K_L < K_X < K_H) = \iint_V P(K_1, K_2) dK_1\, dK_2 \qquad [A.5]$$

where V is the volume in which $K_L < K_X < K_H$. Substituting the expression for P from Equation [A.4], we obtain

$$P(K_L < K_X < K_H) = \iiint_V g\,(K_1, k_1;\ \alpha\sigma_0\beta r)\, g\,(K_2, k_X - k_1;\ \alpha\sigma_0\beta r)\, f(k_1)\ dk_1\, dK_1\, dK_2. \qquad [A.6]$$

The parameters of the model are varied to obtain the best maximum likelihood fit to the data under study. If we assume a set of values for α, σ_0, β and r and a functional form for $f(k_1)$, we can perform the integral in [A.6] and calculate the expected distribution of K_X . (We set K_L and K_H equal to the low and high edges of each bin in the data histogram so that the integral in [A.6] is evaluated once for every bin.) Given an experimental distribution for K_X, we can vary the parameters of the line shape function to find the best likelihood fit and hence the maximum likelihood estimates of the parameters.

A.3.1 *Example:* $e^+e^- \rightarrow e^+e^-$

We illustrate the procedure with the simplest case, $e^+e^- \rightarrow e^+e^-$.† Here, each particle is constrained to have the beam energy, so $f(k_1) = \delta(k_1 - E_{beam})$. Figure A.4 shows the distribution of K_1 and K_2 assuming $E_{beam} = 1843$ MeV, $\alpha = 0$, $\sigma_0 = 2.6\%$, $\beta = 0.8$, and $r = 7.0$. The distribution of K_X can be illustrated by taking the projection of this plot along the $K_1 + K_2 \equiv K_X$ axis, as shown in the lower right inset in Fig. A.4.

Figure A.5 shows the distribution of track energies for a sample of events selected to be consistent with the reaction $e^+e^- \rightarrow e^+e^-$ from the ψ' sample. Figure A.6 shows the distribution of the sum of the track energies from this same sample. The line in Fig. A.5 shows a fit to the line shape function of equation [A.1]. The line in Fig. A.6 shows the same function as illustrated in Fig. A.4 but with parameters determined from the likelihood fit described in the previous section. We emphasize that the fit function is the convolution of two line shapes. Although the fit function itself resembles a line shape, this is due to the fact that the convolution of two functions which are approximately Gaussian is again approximately Gaussian. The

† This analysis cannot be used to obtain estimates of the line shape parameters since this set of events contains both $e^+e^- \rightarrow e^+e^-$ and $e^+e^- \rightarrow \gamma e^+e^-$. However, the separability argument which follows doesn't depend on the values of the line shape parameters but only on the demonstration that they can be obtained consistently from two different techniques.

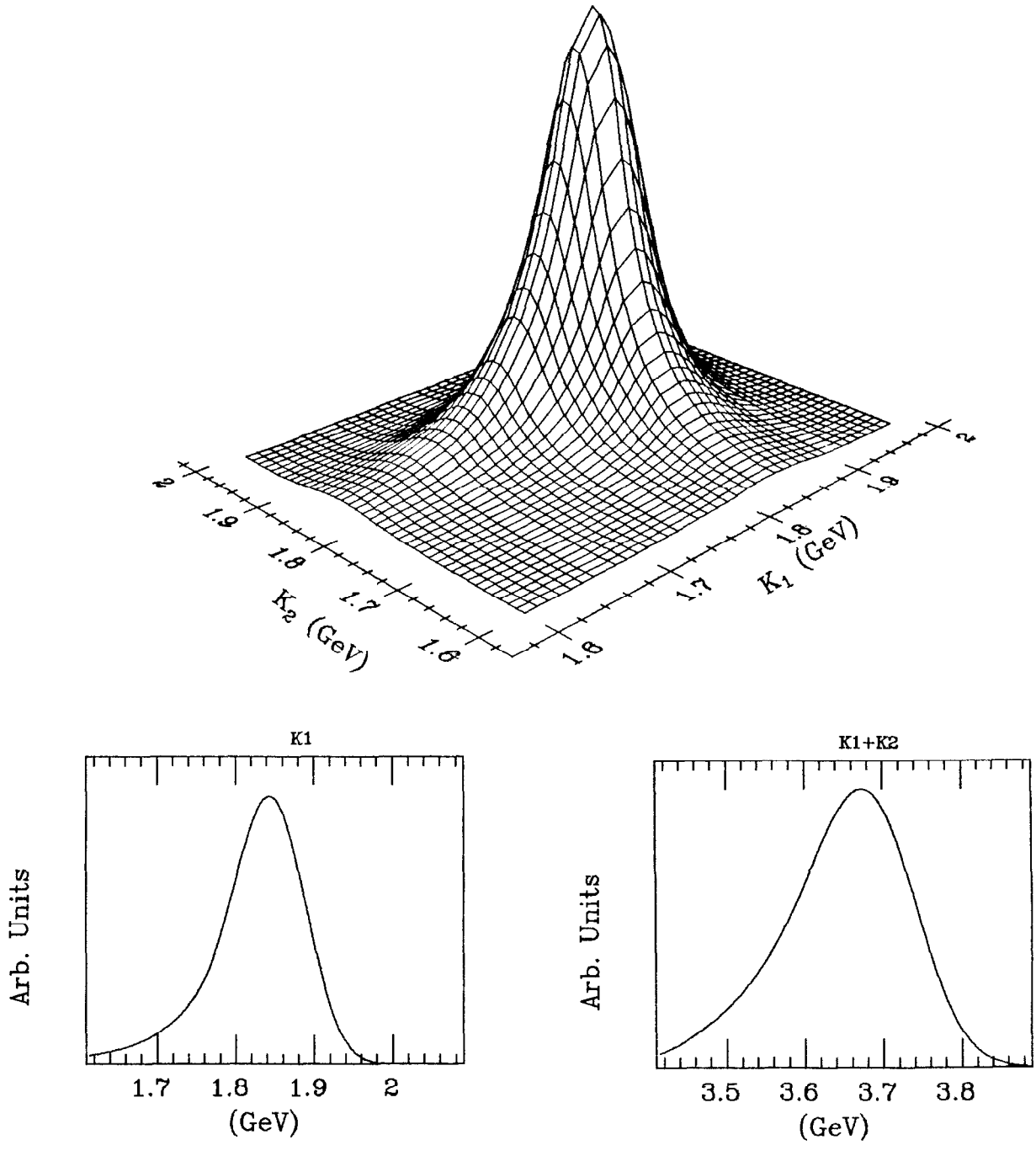

Fig. A.4 Expected energy distribution for Bhabha event at E_{beam} = 1843 MeV. ($\alpha = 0, \sigma_0 = 2.6\%, \mathrm{r} = 7, \beta = 0.8$.)

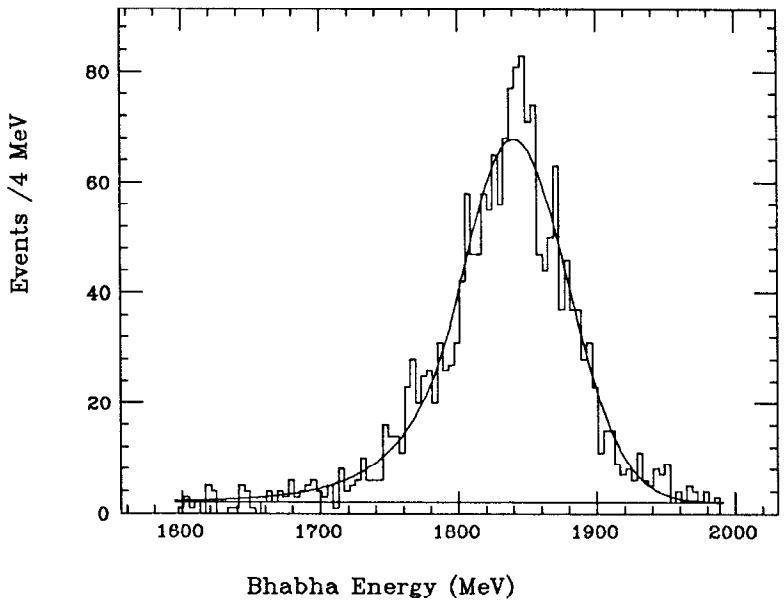

Fig. A.5 $e^+e^- \rightarrow e^+e^-$ at ψ' energy – energy of single track fit to line shape.

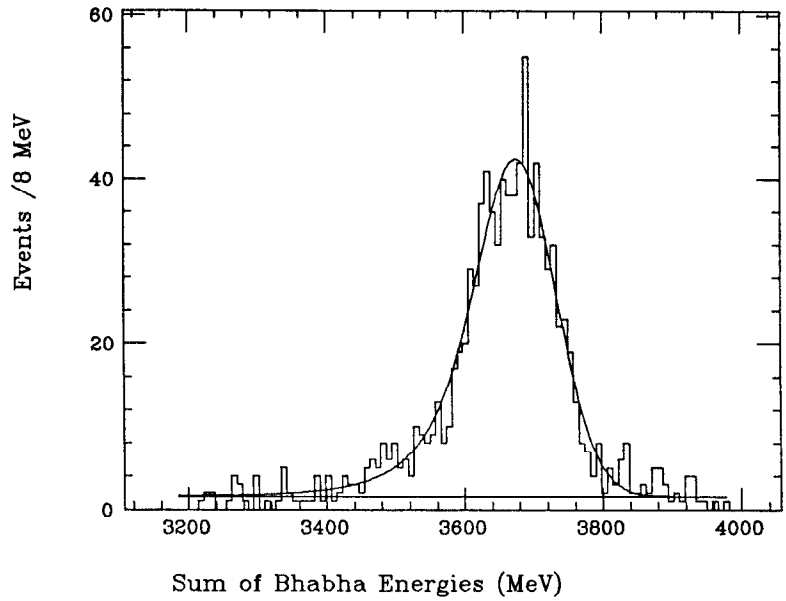

Fig. A.6 $e^+e^- \rightarrow e^+e^-$ at ψ' energy – sum of energies of two tracks.

two fits yield the following values for the line shape parameters:

Parameter	Single Track Energy	Sum of Track Energies
α	-2.3 $\pm$1.4 MeV	-2.4 $\pm$1.5 MeV
σ_0	2.5 $\pm$0.1 %	2.5 $\pm$0.1 %
β	1.1 $\pm$0.1	1.2 $\pm$0.1
r	20 $\pm$14	6 $\pm$2

Table A.3 Values of line shape parameters for $e^+e^- \rightarrow e^+e^-$ as determined from fit to single track spectrum and unfolding of sum of track spectra.

We take the agreement of these two methods for fitting the spectrum as an indication that our assumption of separability made in order to obtain Equation [A.2] was in fact justified and that the measurements of two γ energies are indeed independent.

A.3.2 $\psi' \rightarrow \eta J/\psi$

We note from Table A.2 that the energy of the η in the reaction $\psi' \rightarrow \eta J/\psi$ is very well determined. Thus, the sum of the energies of the γ's from the 2γ decay of the η in this decay is known with high accuracy so that Equation [A.3] holds. In this decay the individual photons have energies in the range 193 MeV to 390 MeV, and the variation of σ (7.6 to 12.8 MeV if σ_0= 2.6%) cannot be neglected. Thus, the probability distribution $f(k_1)$ cannot simply be taken to be a δ function. However, since the η has no spin, the angular distribution of the γ's is isotropic in the η rest frame. Since the η in this reaction has a fixed energy, the distribution of energies of the γ's is flat in the lab frame between the limits $(E_\eta/2)(1 \pm \beta)$ and zero outside. Thus, $f(k_1)$ can be taken to be unity if the limits of the k_1 integral in [A.6] are taken to be the boundaries of the Doppler box. Figure A.7 shows the calculated distribution of K_1 and K_2 for this case for a given set of line shape parameters.

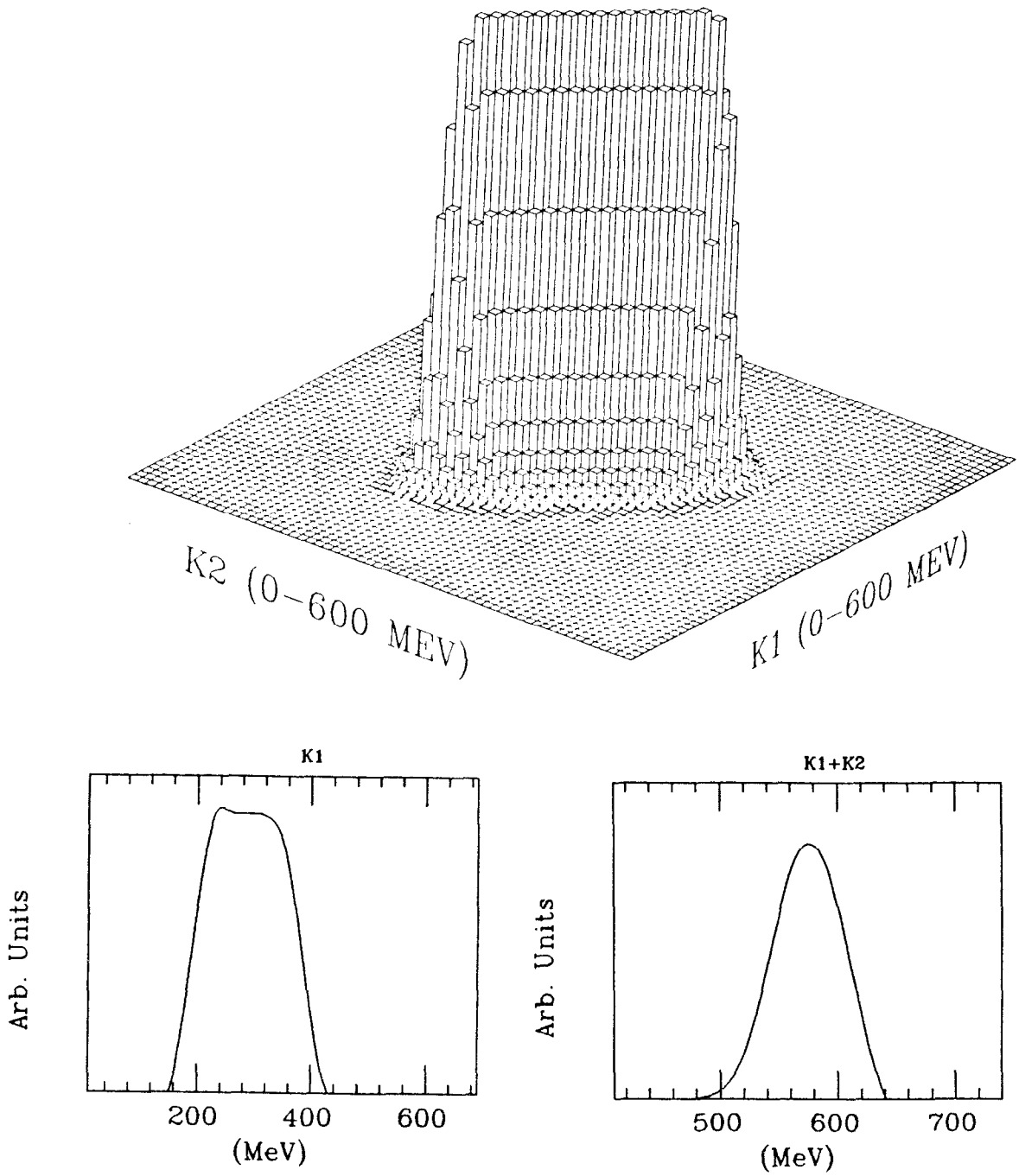

Fig. A.7 Expected energy distribution for $\psi' \rightarrow \eta J/\psi$.
($\alpha = 0, \sigma_0 = 2.6\%, \mathrm{r} = 7, \beta = 0.8$.)

We identify $\psi' \rightarrow \eta J/\psi$ decays by selecting events with two neutral tracks and two electrons or two muons corresponding to the leptonic decays of the J/ψ. Electrons are easy to identify in the Ball since they are tagged as charged by the chambers and deposit their total energy in the NaI(Tl) unlike any other charged particle. Muons are straightforward to detect since they are minimum ionizing and deposit roughly 210 MeV in the NaI(Tl). We do not use any cuts which would bias the gamma energies (such as a confidence level cut from a kinematic fit) in the event selection. The full set of cuts used to select these events are detailed in a footnote.‡

Since we accept any event of the topology $\psi' \rightarrow \gamma\gamma, J/\psi \rightarrow l^+l^-$,§ our sample will also include photon cascades through the χ states and events from $\psi' \rightarrow \pi^0 J/\psi$ in addition to the $\psi' \rightarrow \eta J/\psi$ decays in which we are interested. The simplest way to eliminate this background is to require the two photons to have an invariant mass consistent with an η mass. However, as Fig. A.8 shows, this approach is inadequate

---

‡ Only data after November 1978 are considered. The cuts are slightly different for the $\gamma\gamma e^+e^-$ and $\gamma\gamma\mu^+\mu^-$ topologies. Where a choice is indicated in parentheses, the first applies to the $\gamma\gamma e^+e^-$ case, and the second to the $\gamma\gamma\mu^+\mu^-$. An event is kept if it has

1. Four tracks total (two charged and two neutral),
2. (E_{vis}> 3000 MeV , 800 MeV < E_{vis}< 1400 MeV),
3. No endcap or zero-energy I.R. tracks,
4. No secondary vertices,
5. ($E_{charged}$ > 2500 MeV, 350 MeV < $E_{charged}$ < 1000 MeV), where $E_{charged}$ is the sum of the measured energies of the charged tracks,
6. $|\cos\theta| < 0.90$, for all tracks, where θ is the angle a given track makes with the beam direction,
7. $\cos\alpha < 0.90$ for all pairs of tracks, where α is the opening angle between any two tracks. Additionally, the $\gamma\gamma\mu^+\mu^-$ events are required to have two muon candidates, where a muon candidate is defined to be a track with 140 MeV < E_{13} < 350 MeV and $E_4/E_{13} > 0.96$, where E_4 is the sum of the energies in the central module of the track and its three nearest neighbors.

§ $l = e$ or μ.

inasmuch as there is no clean separation between the ηl^+l^- events and other $2\gamma l^+l^-$ events. However, the photons in the events in which we are interested have not only a unique invariant mass but also a unique energy. The existence of these two constraints on the three variables describing the two photons ($E_{\gamma\ low}$, $E_{\gamma\ high}$, and $\cos\theta_{opening}$) implies that there are functional relations between any two of these three variables. Figure A.9 shows the expected correlations between the two photons in the known decays $\psi' \rightarrow \pi^0 J/\psi$, $\psi' \rightarrow \eta J/\psi$, and $\psi' \rightarrow \gamma\chi_{0,1,2}$, $\chi_{0,1,2} \rightarrow \gamma J/\psi$ on a plot of the lower photon energy *vs.* the cosine of the opening angle between the two photons; Fig. A.10 shows this same plot for the data. The η band is now clearly separated from the bands corresponding to the χ_1 and χ_2 cascades and low-energy background. The region of the $\psi' \rightarrow \pi^0 J/\psi$ band is also well-separated from the $\psi' \rightarrow \eta J/\psi$ decays. The only possible source of contamination is the $\psi' \rightarrow \gamma\chi_0, \chi_0 \rightarrow \gamma J/\psi$ decay, but as can be seen from Fig. A.10, this contamination must be small. The box shows the limits of the region inside of which we accept events as $\psi' \rightarrow \eta J/\psi$.

Figure A.11 shows the sum of the energies of the photons in these events. Again it should be emphasized that the intrinsic width of this distribution is of the order of keV. The observed width is due solely to the energy resolution of the detector. The solid line shows the result of the likelihood fit described previously.

It is important for certain analyses to obtain the line shape function for those crystals in the Ball which are the "best" in terms of resolution (see Chapter 4). Figure A.12 shows the same distribution as Fig. A.11 but using only that subset of events in which the bump modules of the photon tracks are not equator or tunnel modules. The solid line shows the best fit to a line shape function.

A.3.3 $J/\psi \rightarrow \gamma\eta$

We have considered high and low energy showering particles, but we have as yet no information regarding photons of intermediate energies. However, the η in the decay $J/\psi \rightarrow \gamma\eta$ is sufficiently energetic that the two photons from its decay have

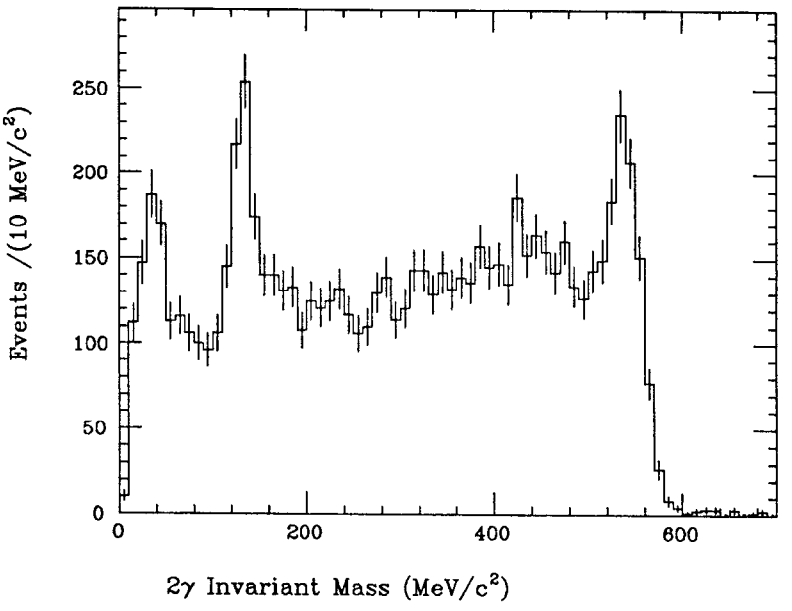

Fig. A.8 Invariant mass distribution of two γ's in $\psi' \rightarrow \gamma\gamma J/\psi$.

individual energies in the range from 49 to 1548 MeV. We use the same events that were selected for the study described in Section A.2.1. Because we require the low energy photon to have an energy of 400 MeV or more, the energies of the photons in our sample range from 400 to 1200 MeV. The solid and dotted lines in Figure A.13 show the energy distribution of the η in this reaction fit to a line shape and a Gaussian function, respectively.

A.4 Summary

Tables A.4 and A.5 below summarize the line shape parameters we have obtained in this study. We see that in all the reactions we have examined, good fits to the gamma line shape have been obtained using the function given by Equation [A.1]. However, this functional form suffers from the drawback that its parameters are correlated, as illustrated by Fig. A.14 which shows a contour plot of the like-

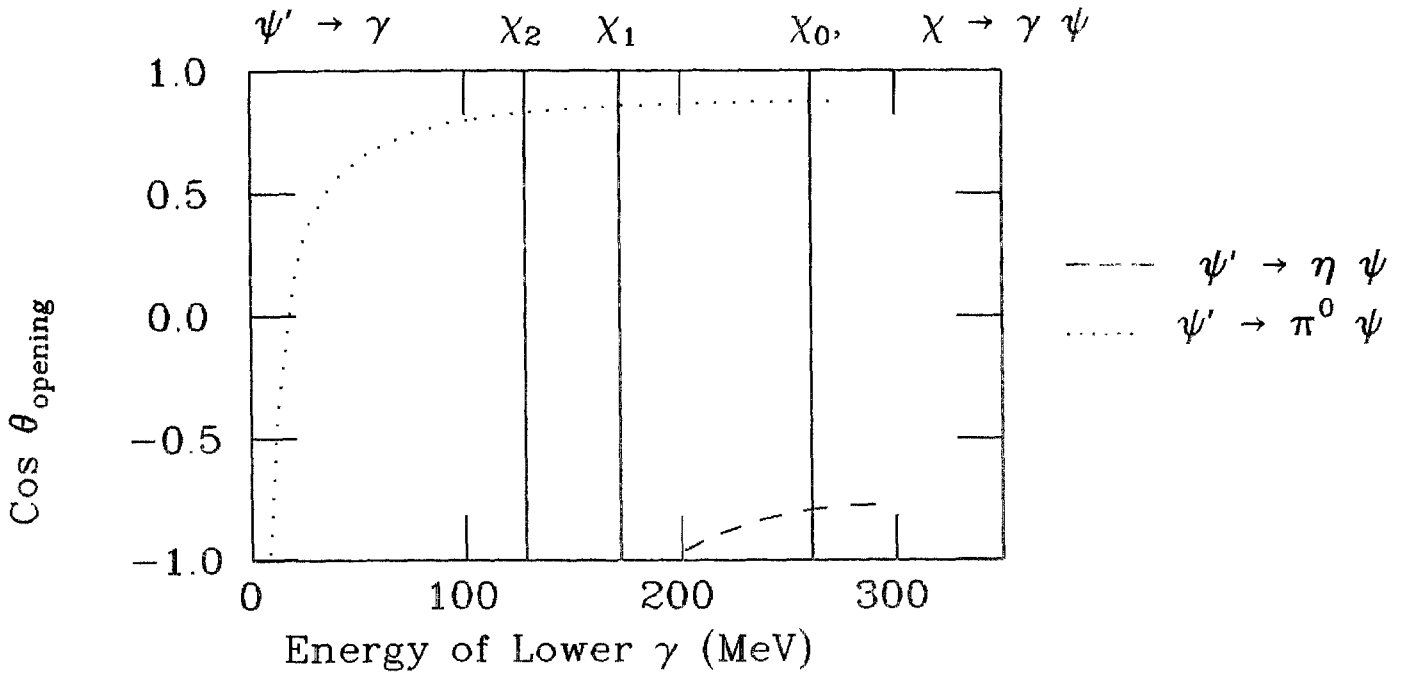

Fig. A.9 Expected correlations in $\psi' \to \gamma\gamma J/\psi$.

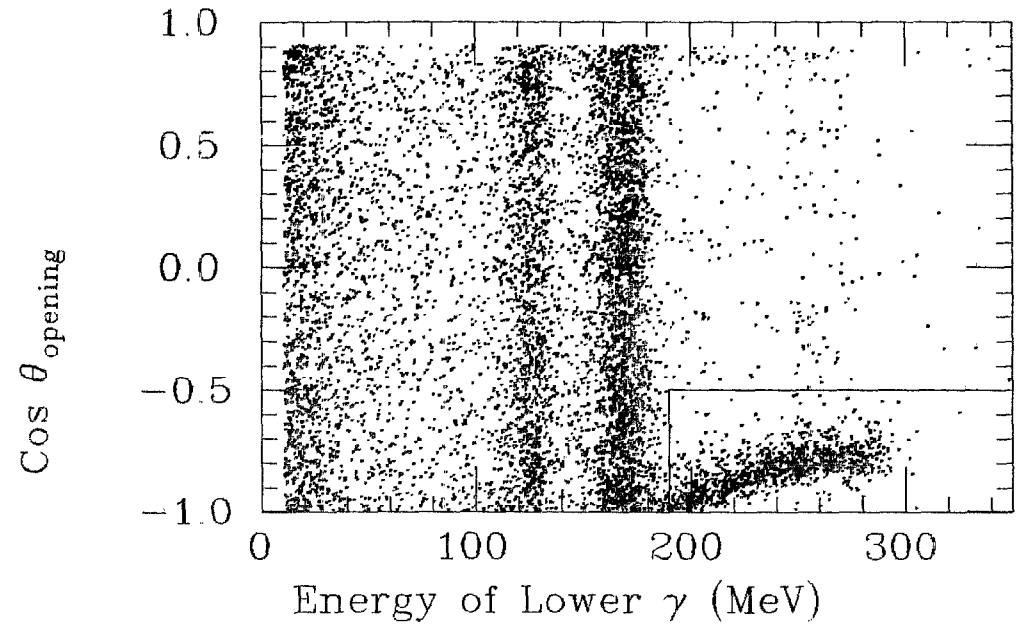

Fig. A.10 Observed correlations in $\psi' \to \gamma\gamma J/\psi$. (Box shows cut.)

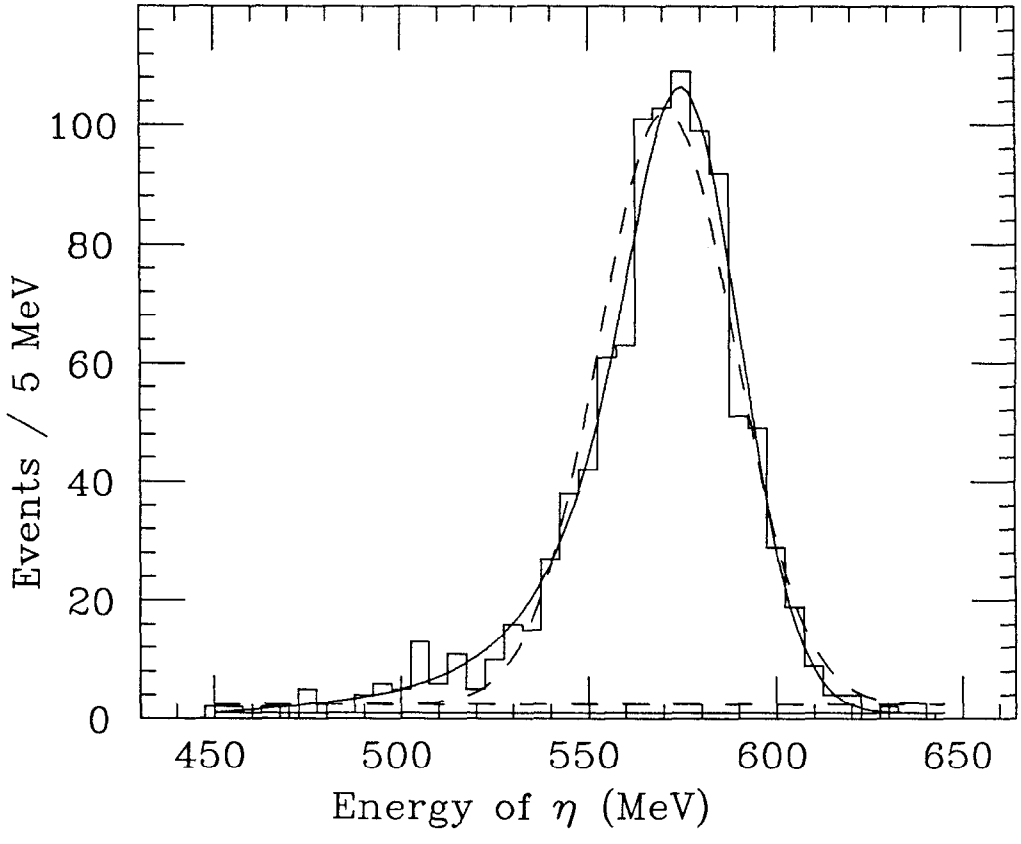

Fig. A.11 $\psi' \rightarrow \eta J/\psi$, $\eta \rightarrow \gamma\gamma$: energy of η fitted to line shape function (solid line) and Gaussian (dotted line). Fitted parameters:

Parameter	Lineshape Fit	Gaussian Fit
α	-2.8 $\pm$0.6 MeV	-5.34 $\pm$0.1 MeV
σ_0	2.7 $\pm$0.1%	3.25 $\pm$0.02 %
r	3.7 $\pm$0.7	
β	1.07 $\pm$0.04	
Conf. Lev.	0.390	0.000

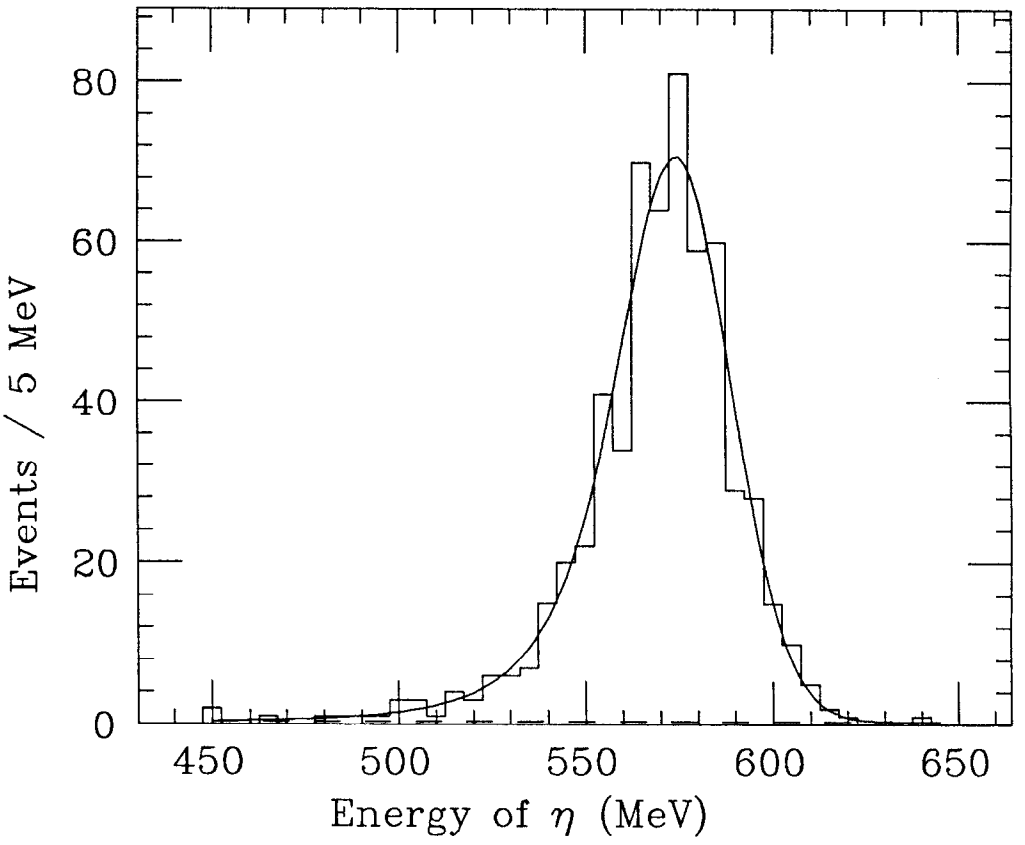

Fig. A.12 $\psi' \rightarrow \eta J/\psi$, $\eta \rightarrow \gamma\gamma$ (no equator or tunnel modules): energy of η fitted to line shape function (solid line). Best fitted values:

Parameter	Lineshape Fit
α	-3.3 $\pm$0.6 MeV
σ_0	2.59 $\pm$0.05%
r	5.4 $\pm$1.0
β	1.2 $\pm$0.2
Conf. Lev.	0.771

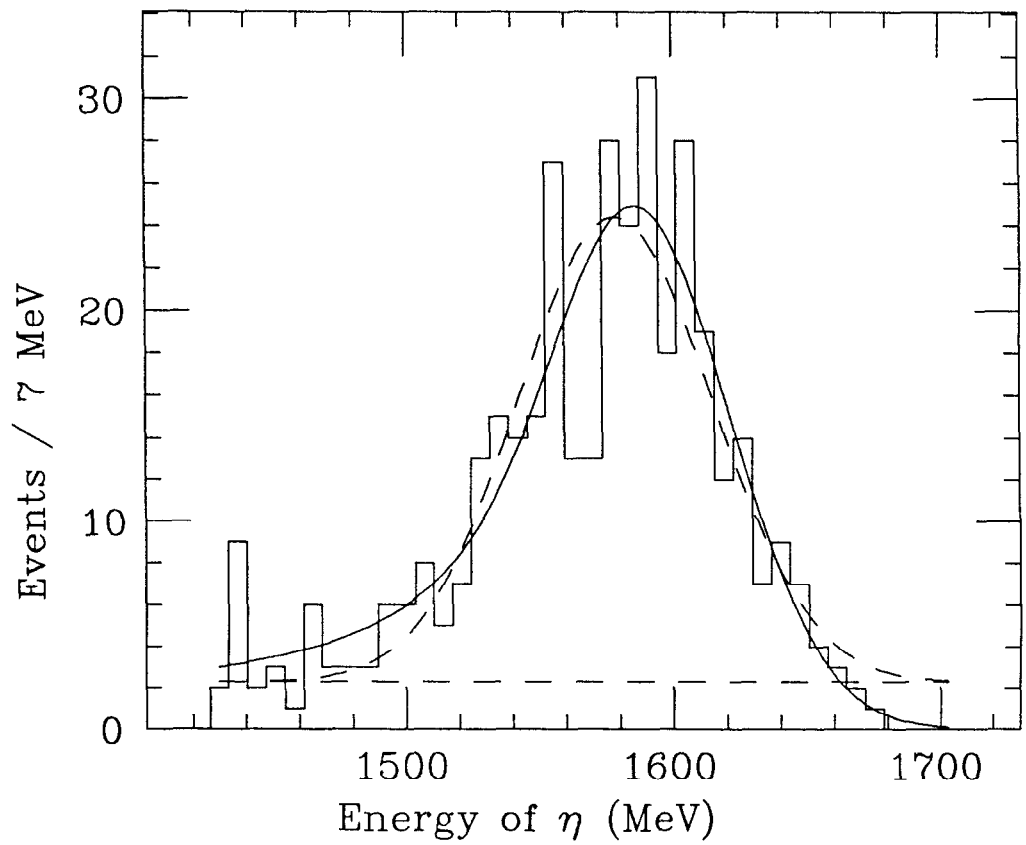

Fig. A.13 $J/\psi \rightarrow \gamma\eta$, $\eta \rightarrow \gamma\gamma$: Energy of η fitted to line shape function (solid line) and Gaussian (dotted line). Best fitted values:

Parameter	Lineshape Fit	Gaussian Fit
α	-3.3 $\pm$0.9 MeV	-7.6 $\pm$1.7 MeV
σ_0	2.9 $\pm$0.2%	3.0 $\pm$0.3 %
r	1.0 $\pm$0.8	
β	1.5 $\pm$0.3	
Conf. Lev.	0.232	0.004

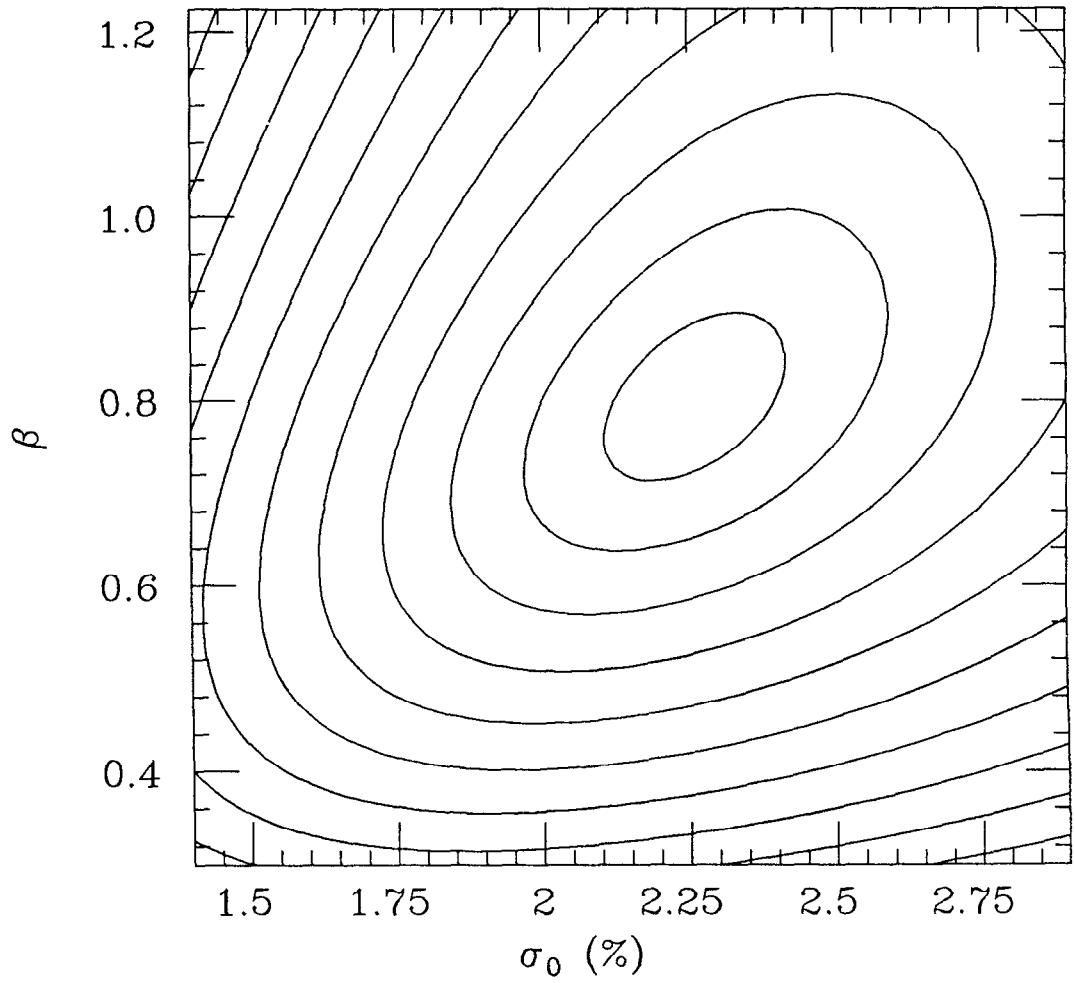

Fig. A.14 Likelihood function of fit to γ in $J/\psi \rightarrow \gamma\eta$ as a function of σ_0 and β. (Contours are spaced 1σ apart; first contour corresponds to 1σ.)

lihood of the fit to the gamma spectrum in $J/\psi \rightarrow \gamma\eta$ as a function of σ_0 and β. Thus, one must take care when using the results of these fits to use a consistent set of values of all of the line shape parameters – two different values of σ_0 may equally well describe the line shape function if accompanied by different values of r and β. In particular, it is not appropriate to draw any conclusions on the energy dependence of α or σ_0 . Although the fits to Gaussian line shapes have consistently lower confidence levels, the parameters of the Gaussian are free from such correlations, and one may compare values of α and σ_0 from different fits. Also, the Gaussian fits are important for the determination of the errors for kinematic fits in which all distributions are approximated by Gaussians. We show in Figs. A.15, A.16, and A.17 the variation of these parameters. We plot the parameters as functions of x, the energy of the γ being measured divided by the beam energy. For reference, we plot both the energy offset and the energy offset normalized by x. These variations are included in the systematic errors quoted for fitted quantities.

Reaction *	x	α	σ_0
$\psi' \rightarrow (\eta) J/\psi$	0.16 $\pm$0.05	-2.8$\pm$0.6 MeV	2.7$\pm$0.1 %
$\psi' \rightarrow (\eta) J/\psi$ (no eq. or tun.)	0.16 $\pm$0.05	-3.3$\pm$0.6	2.59$\pm$0.05
$J/\psi \rightarrow \gamma(\eta)$	0.52 $\pm$0.26	-3.3$\pm$0.9	2.9$\pm$0.2
$J/\psi \rightarrow (\gamma)\eta'$	0.90 $\pm$0	4.8$\pm$2.0	2.5$\pm$0.2
$J/\psi \rightarrow (\gamma)\eta$	0.97 $\pm$0	8.7$\pm$4.6	2.2 $\pm$0.3

* Energy measurement made of particle in parentheses.

Table A.4 Parameters for lineshape fits.

Reaction	r	β
$\psi' \rightarrow (\eta) J/\psi$	3.7±0.7	1.07±0.04
$\psi' \rightarrow (\eta) J/\psi$	5.4±1.0	1.2±0.2
$J/\psi \rightarrow \gamma(\eta)$	1.0±0.8	1.5±0.3
$J/\psi \rightarrow (\gamma)\eta'$	20±15	1.03±0.12
$J/\psi \rightarrow (\gamma)\eta$	8±12	0.65 ±.2

Table A.4 (cont.) Parameters for line shape fits.

Reaction	x	α	σ_0
$\psi' \rightarrow (\eta) J/\psi$	0.16±0.05	-5.3±0.1 MeV	3.25±0.02%
$J/\psi \rightarrow \gamma(\eta)$	0.52 ±0.26	-7.6±1.7	3.0±0.3
$J/\psi \rightarrow (\gamma)\eta'$	0.90 ±0	1.6±1.5	2.6±0.1
$J/\psi \rightarrow (\gamma)\eta$	0.97 ±0	0.1±3.2	2.5 ±0.3

Table A.5 Parameters for Gaussian fits.

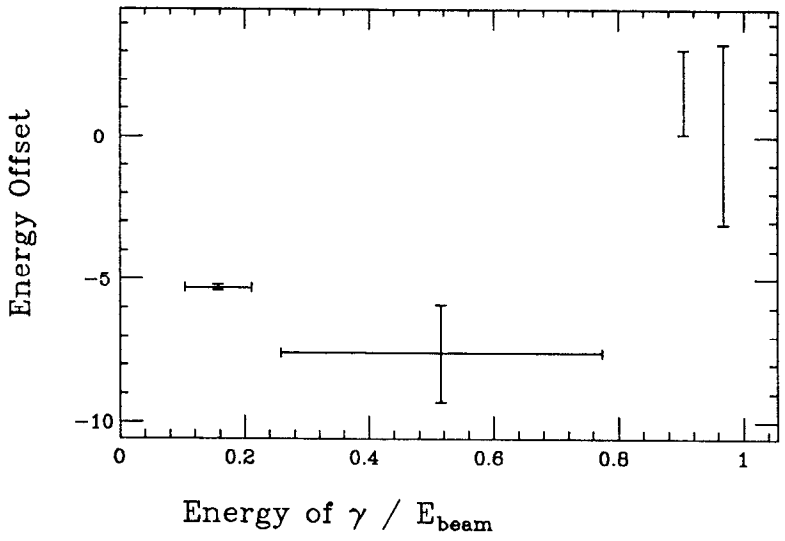

Fig. A.15 Variation of energy offset as a function of energy (normalized to beam energy).

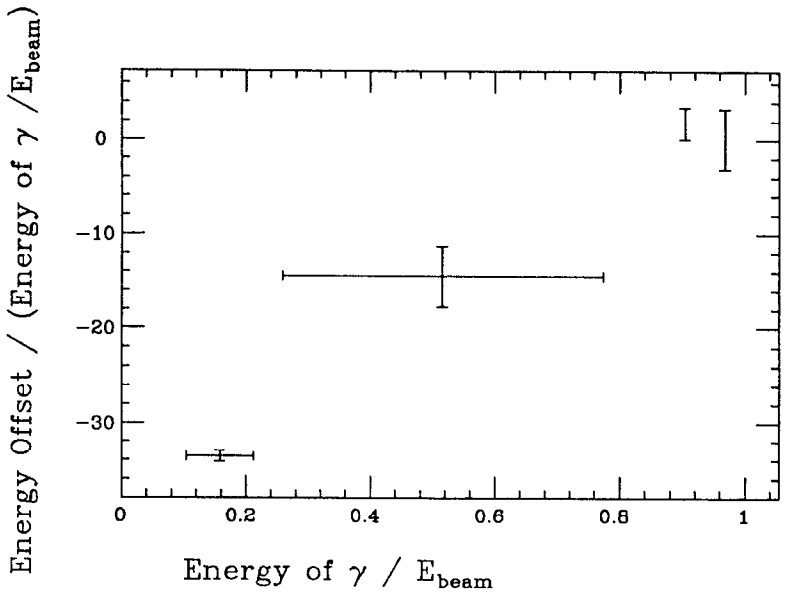

Fig. A.16 Fractional variation of energy offset as a function of energy (normalized to beam energy).

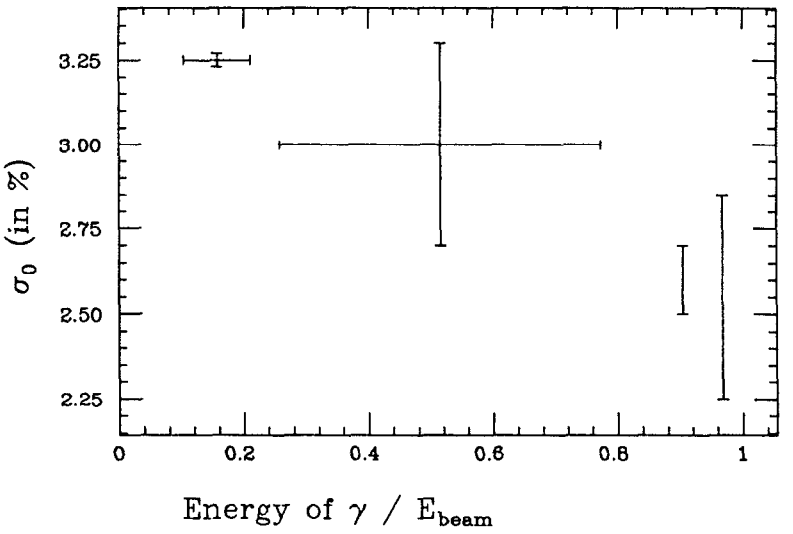

Fig. A.17 Variation of fractional resolution as a function of energy (normalized to beam energy).

References

1) Particle Data Group, *Rev. Mod. Phys.* **56** (1984) S1.

Appendix B

Monte Carlo

B.1 Introduction

This Appendix describes the aspects of the Crystal Ball Monte Carlo relevant to this study. In the reactions under investigation in this thesis, the first step of generating the four-vectors of the final state is straightforward since the initial, intermediate, and final particles are specified, and the final-state four-vectors are in large part determined by energy and momentum conservation if the number of particles in the final state is small enough. When the spin of the intermediate state is nonzero and kinematics are insufficient to completely determine all the four-vectors, the spin assumptions used to derive the angular distribution are noted at the appropriate point in the discussion. In some of the reactions studied here ($J/\psi, \psi' \rightarrow \gamma\eta, \eta \rightarrow \pi^0\pi^0\pi^0$ and $J/\psi, \psi' \rightarrow \gamma\eta', \eta' \rightarrow \eta\pi^0\pi^0$), the number of particles in the final state is sufficiently large that their angular distribution cannot be determined by kinematics alone despite the zero spin of the intermediate state. However, no evidence has been found for deviations from phase space in the angular distributions in the reactions $\eta \rightarrow \pi^0\pi^0\pi^{0[1]}$ or $\eta' \rightarrow \eta\pi^0\pi^{0[2]}$, and we accordingly generate the four-vectors of the decay products of the η and η' in the J/ψ and ψ' decays above according to phase space distributions. All events are generated with x = y = 0 and a distribution in z corresponding to a Gaussian-distributed bunch length of 3.1 cm.

Once the decays of all the intermediates have been calculated, the final state consists entirely of γ's. We wish to study the interaction of these γ's with the NaI (Tl) scintillator. The interaction of photons with matter is well-described by the Electron Gamma Shower code (EGS), although specifying the Crystal Ball geometry is somewhat complicated. The Crystal Ball implementation of EGS takes into account the varying shapes of the individual crystals. It also defines regions to account for the material surrounding each crystal as well as the material enclosing the hemispheres and the gap between them. It does not at the present time treat the endcap crystals, nor the beampipe and central detector. (The conversion probability for gammas in the beampipe and central detector is calculated separately and is discussed in the last section of this Appendix.)

B.2 Energy Resolution

In order to examine the response of the Monte Carlo to well-defined inputs, we generate sets of events containing one particle (either a γ or a π^0). These particles are distributed uniformly in solid angle with fixed momenta of 1700, 1300, 1000, 700, 500, 250, and 100 MeV/c.

Figure B.1 shows the observed Monte Carlo energy distribution for a γ with a dialed energy of 1700 MeV, using the sum of 13 crystals as a measure of the γ energy; Fig. B.2 shows the same distribution for a γ of 700 MeV. Both plots have been fitted with an NaI line shape function of the form described in Appendix A. Figure B.3 shows a plot of the dialed energy vs. σ for similar fits for Monte Carlo photons of the energies listed above. It will be noted that the Monte Carlo resolution is an almost linear function of energy; we parameterize the dependence by $\sigma = \sigma_0 E^{3/4}$ (E in GeV). Figure B.4 shows a plot of dialed energy vs. σ_0. The function is well fit by a constant value of $\sigma_0 = 1.5\%$. However, although studies of the data indicate the same functional form for σ, the value of σ_0 is substantially higher (although studies with a Crystal Ball prototype favor a value close to that derived from the Monte Carlo.) This discrepancy is discussed in Appendix E; we in

any event simply add a Gaussian-distributed fluctuation to the Monte Carlo crystal energies sufficient to bring σ_0 to 2.6%. Figure B.5 shows the distribution for 1700 MeV γ's after this correction.

In addition to this correction to the width, we also note that the central values of the fitted distributions are below the dialed values. This is to be expected inasmuch as part of the shower leaks out of the back of the crystal. This energy shift is not observed in the actual data since the central value of the Bhabha peak is fixed to be the beam energy (see Appendix E). We can make a similar correction to the Monte Carlo by "calibrating" the γ's at 1843 MeV to have the correct energy. This defines a single correction factor by which all crystal energies should be multiplied. The crosses in Fig. B.6 show the observed uncorrected energies; the diamonds show the observed energies after correction.

It will be recalled from Chapter 3 that the sum of 13 energy involves a position correction, PCORR, which is determined from Bhabha events. (All energies discussed above have had this correction incorporated.) If the Monte Carlo does not simulate the interstitial material between crystals, it is conceivable that the PCORR correction should not be applied to Monte Carlo showers. Figure B.7 shows a plot of $E_{max}/\sum_{i=1}^{13} E_i$ *vs.* $\sum_{i=1}^{13} E_i/E_{dialed}$, (analagous to Fig. 3.2) for Monte Carlo gammas of $E_{dialed} = 1843$ MeV, where $\sum_{i=1}^{13} E_i$ has been adjusted by the width and mean corrections described above. The line is a fit to the PCORR correction obtained from the data as shown in Fig. 3.2. It is seen that the PCORR correction obtained from Monte Carlo γ's follows the data PCORR closely with the possible exception of the endpoints. However, only a small fraction of photons have these extreme values of $E_{max}/\sum_{i=1}^{13} E_i$ as shown by the lower plot in Fig. B.7. Thus, we apply the PCORR correction to both data and Monte Carlo. For comparison, Figs. B.8 and B.9 show similar plots for γ's of other energies. It is seen that the PCORR correction function fits these distributions reasonably well, although there may be an upward shift for the lowest energy γ's.

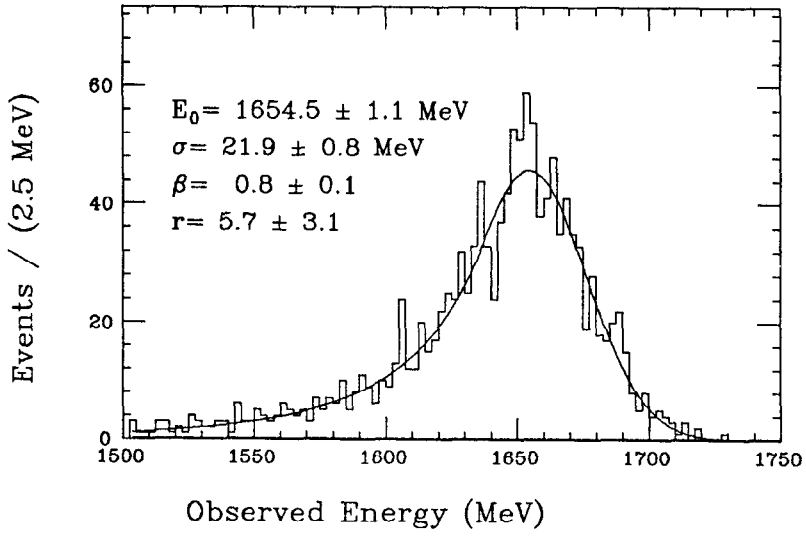

Fig. B.1 Energy distribution for 1700 MeV Monte Carlo γ: no corrections.

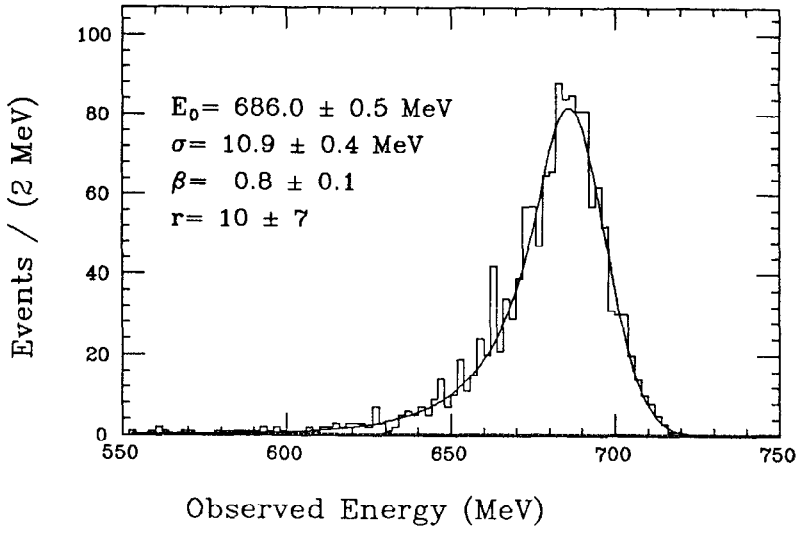

Fig. B.2 Energy distribution for 700 MeV Monte Carlo γ: no corrections.

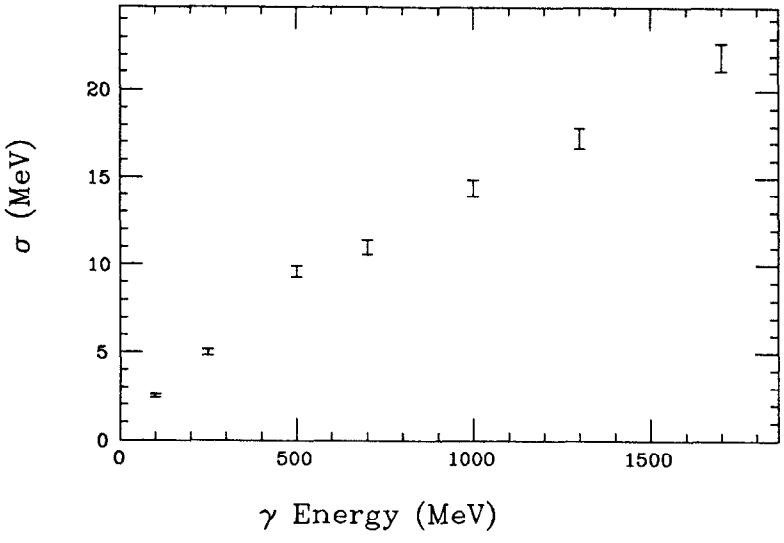

Fig. B.3 Monte Carlo energy resolution: no corrections.

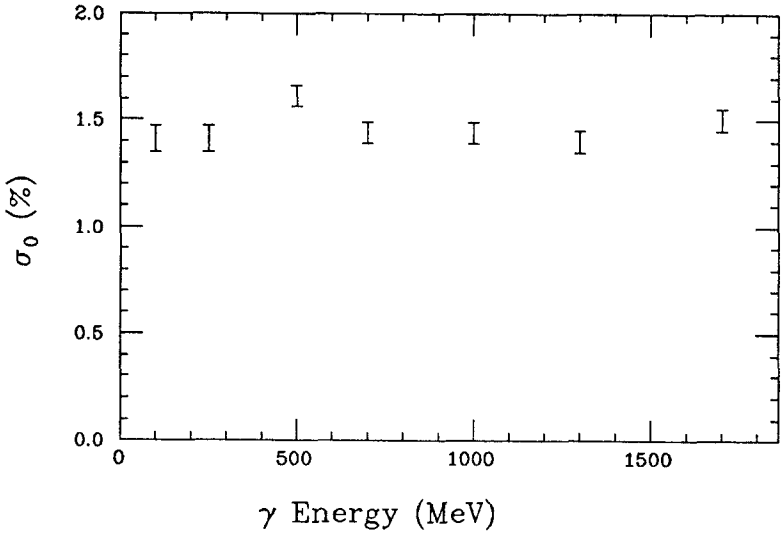

Fig. B.4 Coefficient of energy resolution: no corrections.

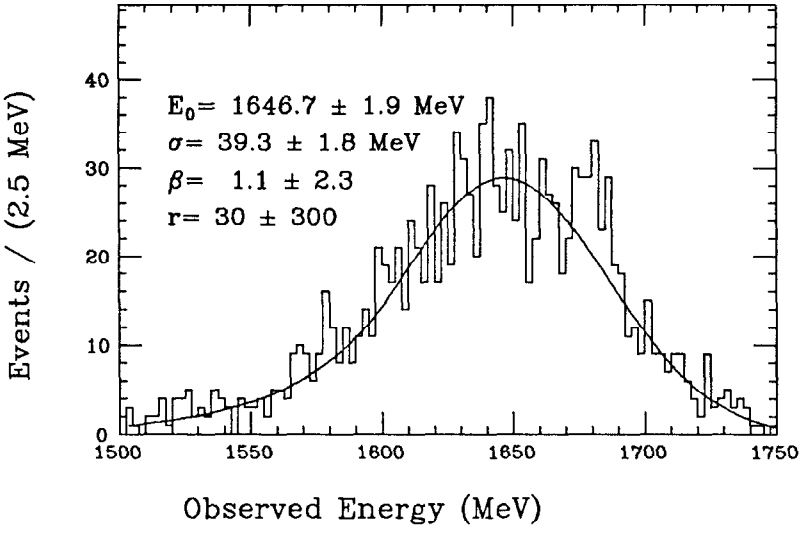

Fig. B.5 Energy distribution for 1700 MeV Monte Carlo γ: resolution correction.

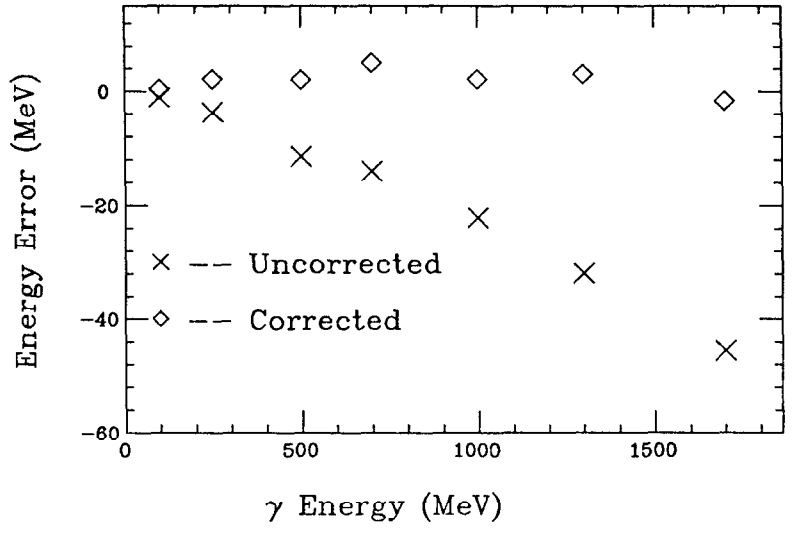

Fig. B.6 Peak energies before and after leakage correction.

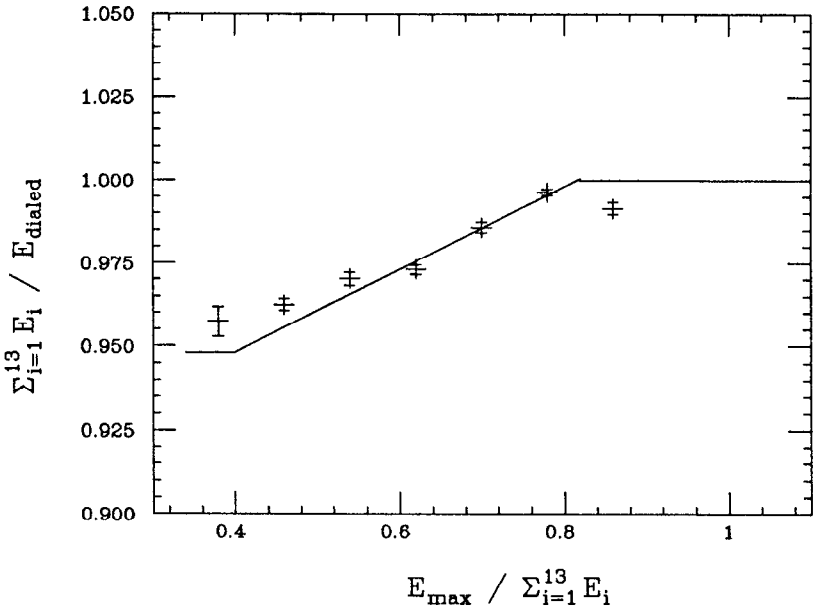

(a)

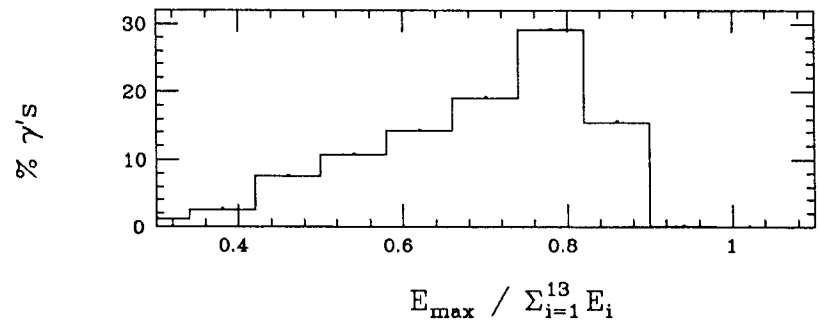

(b)

Fig. B.7 (a) $E_{max}/\sum_{i=1}^{13} E_i$ *vs.* $\sum_{i=1}^{13} E_i/E_{dialed}$ for 1843 MeV Monte Carlo γ's. (b) Distribution of $E_{max}/\sum_{i=1}^{13} E_i$

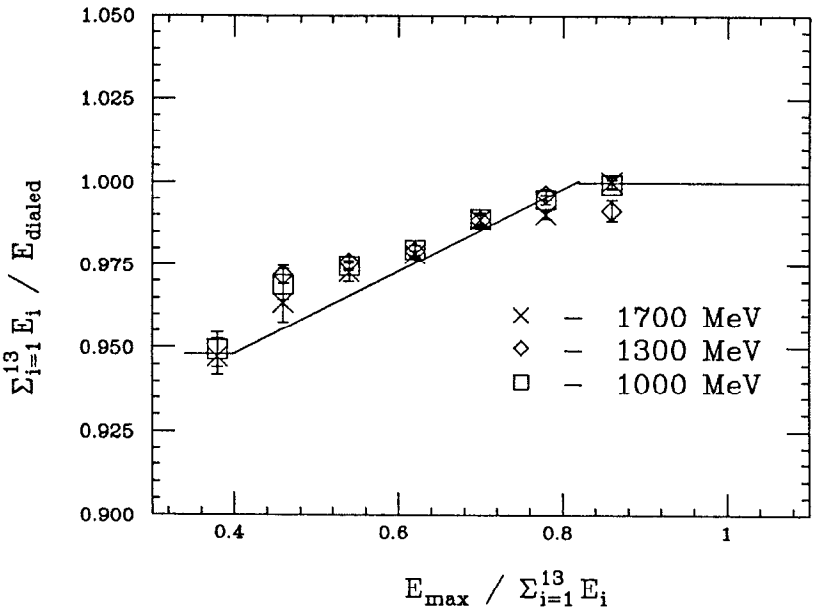

(a)

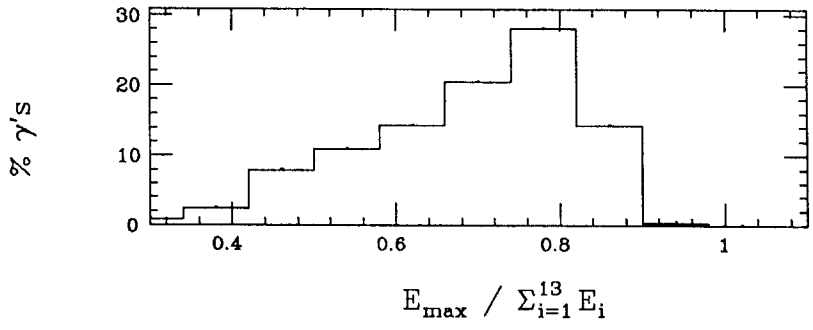

(b)

Fig. B.8 $E_{max}/\sum_{i=1}^{13} E_i$ *vs.* $\sum_{i=1}^{13} E_i/E_{dialed}$ for 1700, 1300, and 1000 MeV Monte Carlo γ's. (b) Distribution of $E_{max}/\sum_{i=1}^{13} E_i$.

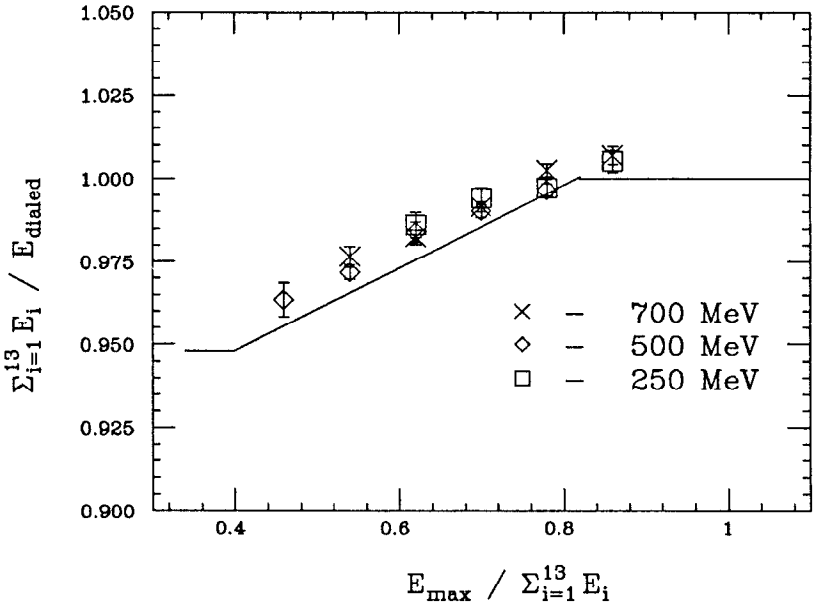

(a)

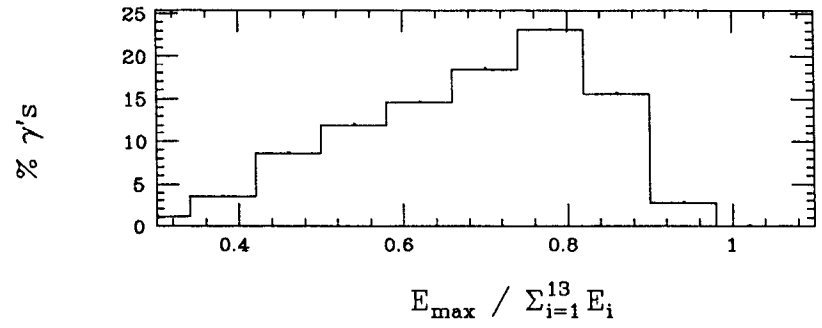

(b)

Fig. B.9 $E_{max}/\sum_{i=1}^{13} E_i$ *vs.* $\sum_{i=1}^{13} E_i/E_{dialed}$ for 700, 500, and 250 MeV Monte Carlo γ's. (b) Distribution of $E_{max}/\sum_{i=1}^{13} E_i$.

B.3 Angular Resolution

Using the same Monte Carlo datasets described in the previous section, we examine the difference between the dialed and observed directions of the γ's and π^0's. There is only one input particle in an event. However, the offline software may detect more than one track, due in the γ case to a split-off or in the π^0 case to a large opening angle between the two photons. Thus, we compare the dialed θ and ϕ to the θ and ϕ of the highest energy track in the event (where θ and ϕ denote the polar and azimuthal angles with the positron beam direction as polar axis). When using the π^0 Monte Carlos, we also require that the PIFIT mass of the highest energy track be greater than 90 MeV/c^2 inasmuch as we are interested only in merged π^0's. For each Monte Carlo dataset we plot the dialed θ minus the measured θ and fit the resulting distribution to a Gaussian. (Figures B.10 and B.11 show examples of such plots for the 1700 MeV γ and π^0 Monte Carlo datasets.) Similar plots are made for ϕ. Figure B.12 shows the dependance of the θ resolution for γ's as a function of energy. Figure B.13 shows an analagous plot for ϕ.* We note that the angular resolution improves with energy. Also, the GAMFIT directions are closer to the dialed directions than those determined by ESORT. The curve shows the best fit to a third-order polynomial which is used to calculate the angular errors for γ's in the kinematic fits. Figures B.14 and B.15 show the analagous plots for merged π^0's. Here the difference in angular resolution between the ESORT and PIFIT directions is more striking since ESORT chooses a direction pointing to the crystal with the highest energy, which may be far from the direction of the π^0. Again, the curve shows the function which is used to calculate the angular errors for π^0's in kinematic fits.

---

* When calculating the resolution in ϕ, the solid angle dependance must be removed. The quantity which is plotted is $\Delta(\phi \sin\theta)$.

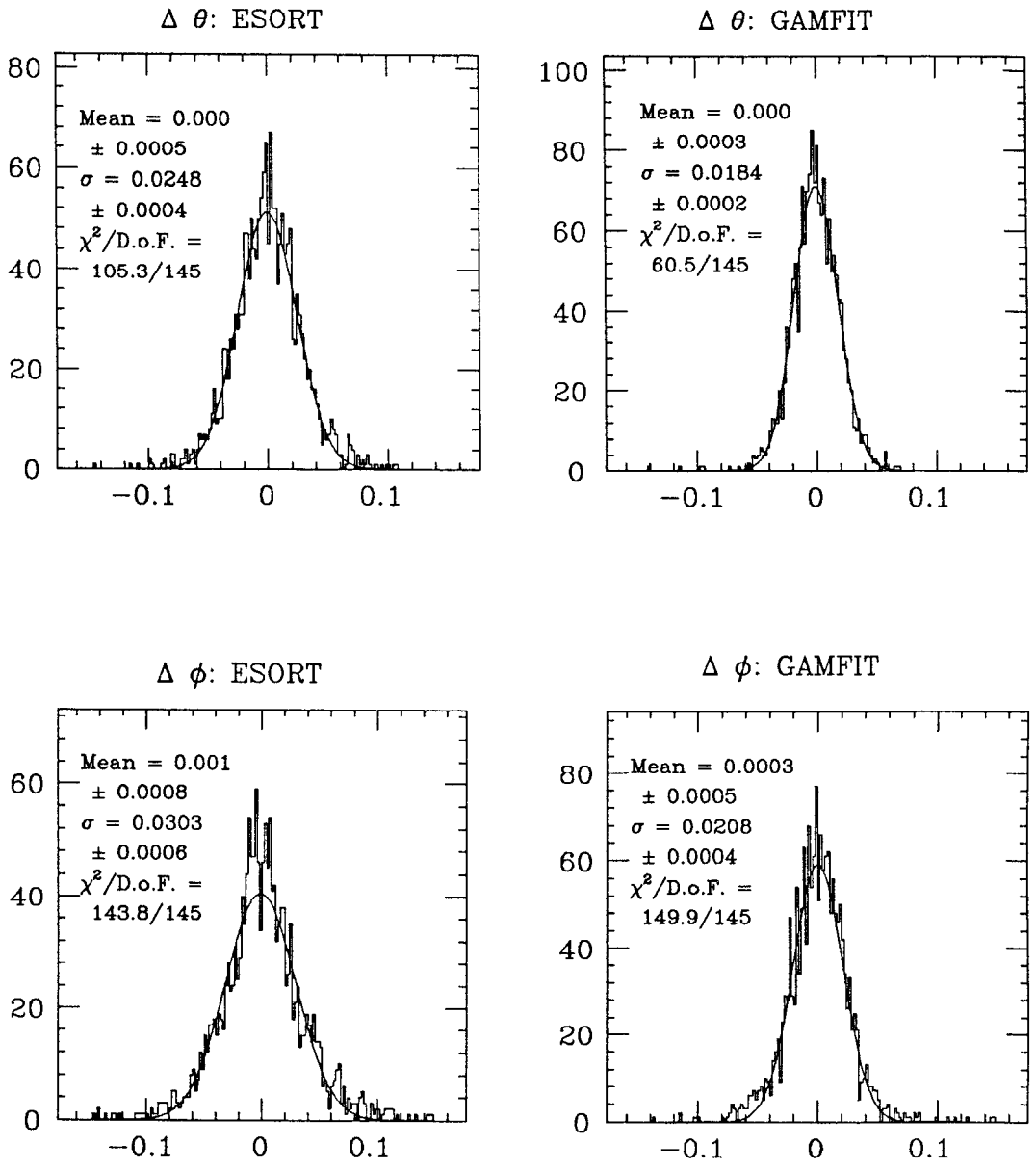

Fig. B.10 Samples of angular resolution fits (1000 MeV Monte Carlo γ's).

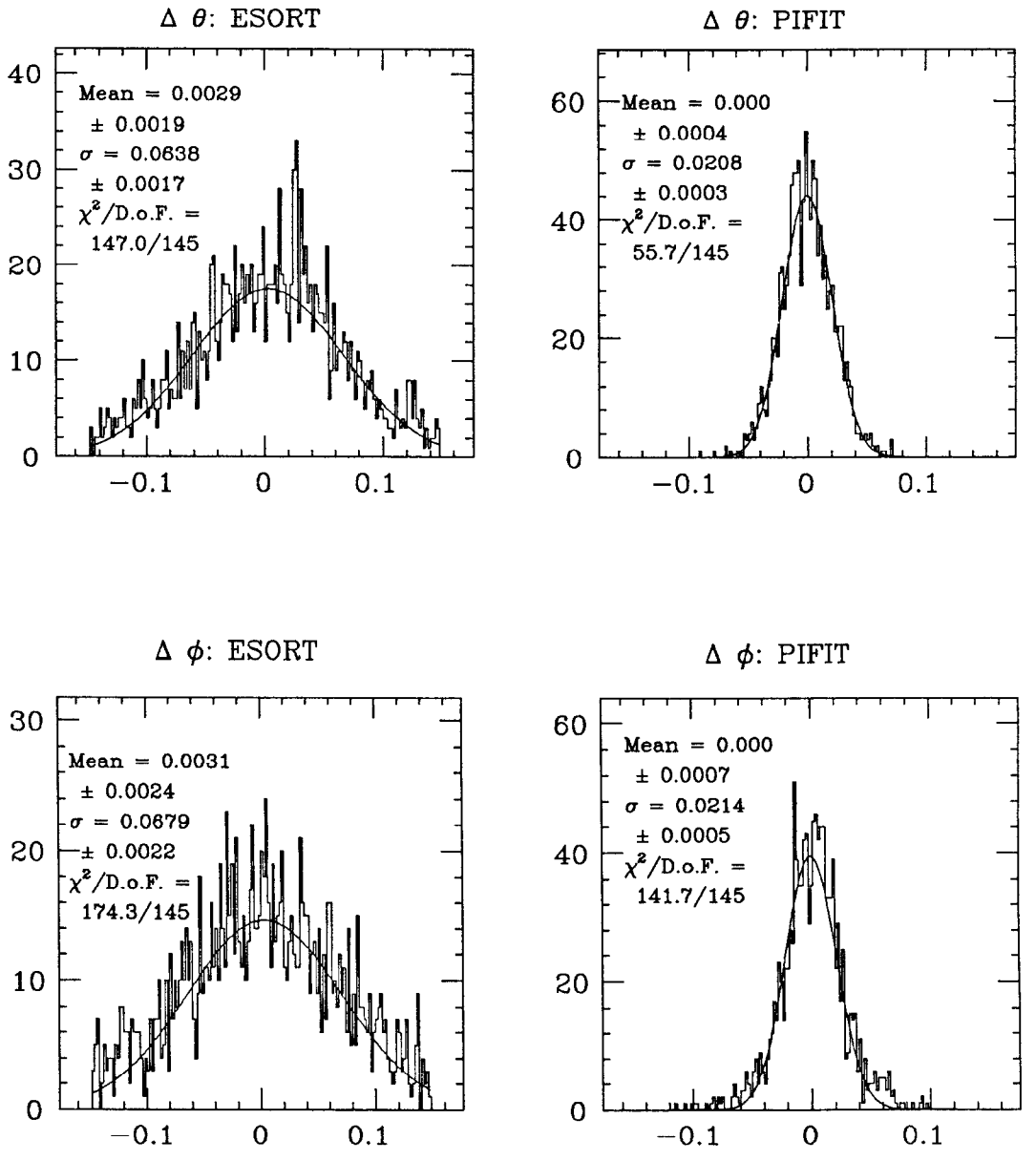

Fig. B.11 Samples of angular resolution fits (1000 MeV Monte Carlo π^0's).

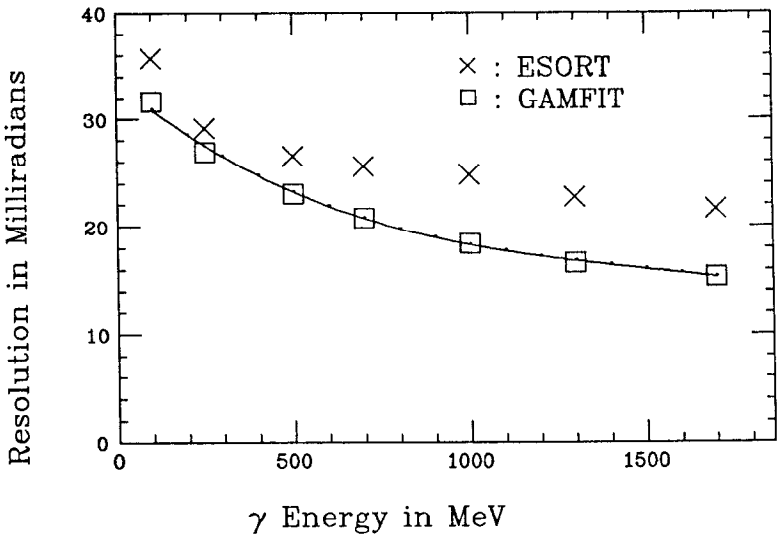

Fig. B.12 θ resolution of Monte Carlo photons.

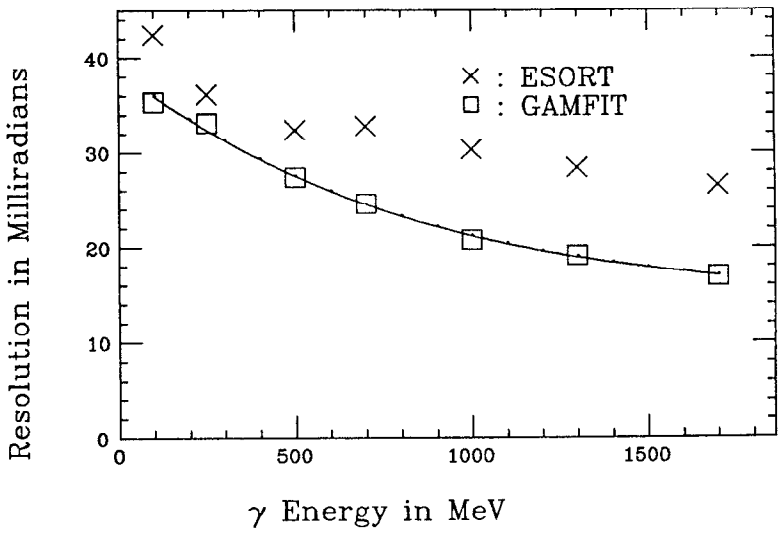

Fig. B.13 ϕ Resolution of Monte Carlo photons.

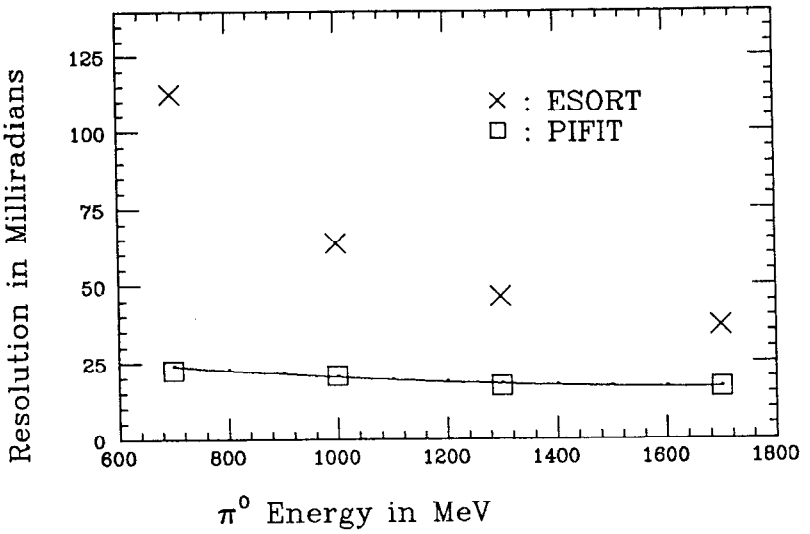

Fig. B.14 θ Resolution of Monte Carlo π^0's.

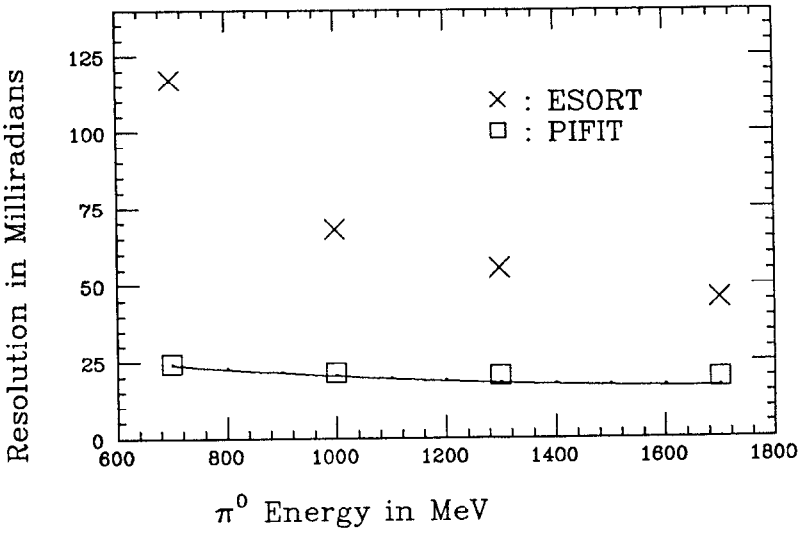

Fig. B.15 ϕ Resolution of Monte Carlo π^0's.

B.3.1 *Comparison With Data*

We first examine how well the Monte Carlo reproduces the angular acceptance of the detector. We require a sample of showering particles, and we use the reaction $e^+e^- \to \gamma\gamma$. From a subset of the ψ' sample we select events which have two neutral tracks, a visible energy within 300 MeV of the center of mass energy, and no endcap tracks. Figures B.16 and B.17 show plots of $\cos\theta$ *vs.* ϕ for the track in these events measured with both ESORT and GAMFIT. (ϕ is chosen to lie between $-\pi/2$ and $3\pi/2$ for these plots so as to make the structures at $\phi = 0$ and $\phi = \pi$ more evident.) The equator gap and the extent of the main Ball in $\cos\theta$ are visible in both plots. In addition, the quantization of the ESORT algorithm is visible in the first plot.† Figures B.18 and B.19 show analagous plots for a sample of 2000 MeV Monte Carlo photons distributed uniformly in ϕ and $\cos\theta$ out to $|\cos\theta| \leq 0.75$; Figures B.20 and B.21 shows the $\cos\theta$ projections for Monte Carlo photons generated over the entire solid angle but with lower statistics. Again, the equator gap and the extent of the Ball in $|\cos\theta|$ can be seen and agree with the plots obtained from the data.

Next, we examine how well the Monte Carlo reproduces the γ energy line shape. We generate 4000 Monte Carlo events of the decay $J/\psi \to \gamma\eta$ and subject them to the same cuts used to select this decay in the J/ψ data in Appendix A. Figure B.22 shows the energy spectrum of the direct photon for data and Monte Carlo fitted to a line shape function. (The data plot is identical to Fig. A.2.) The two distributions are in fair agreement, but the energy offset observed in the data (Appendix A) is not seen in the Monte Carlo. As a fraction of γ energy, this effect is slight, and we include it in our quoted systematic errors.

---

† The scatterplot in Fig. B.16 shows an increase in the density of points at large $|\cos\theta|$ as expected from a QED process. That this increase is not as noticeable in the scatterplot of Fig. B.17 is an artifact of the representation of the data. Since the ESORT directions are quantized, several photons entering the same submodule are plotted as a single point in the ESORT plot whereas they are shown as a cluster in the GAMFIT plot.

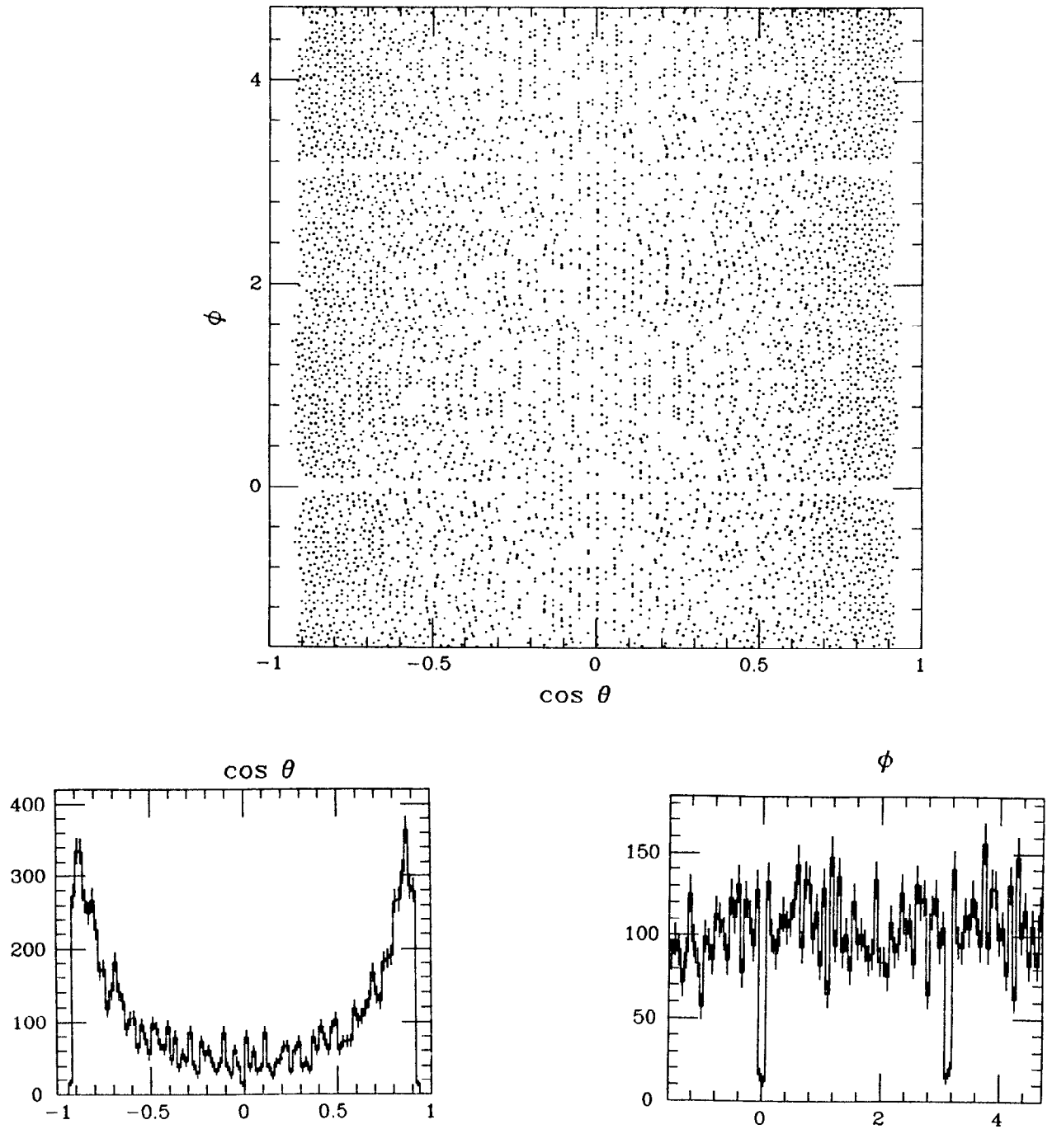

Fig. B.16 Angular distribution of photons in data: ESORT directions.

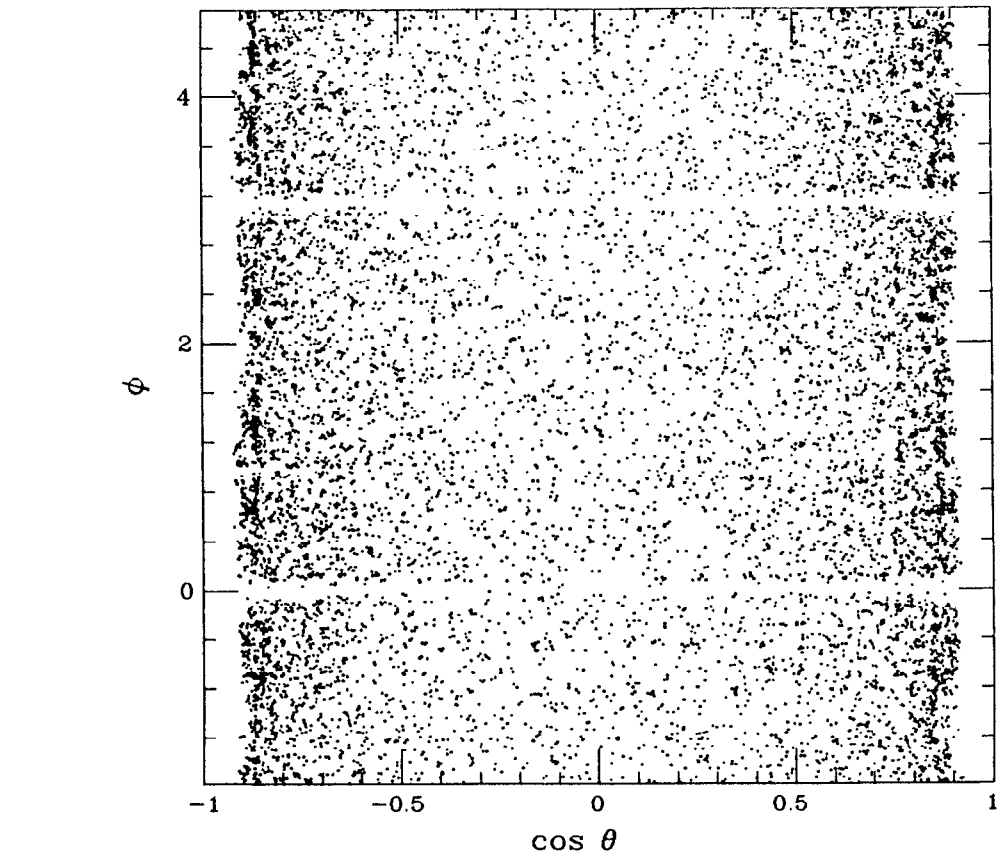

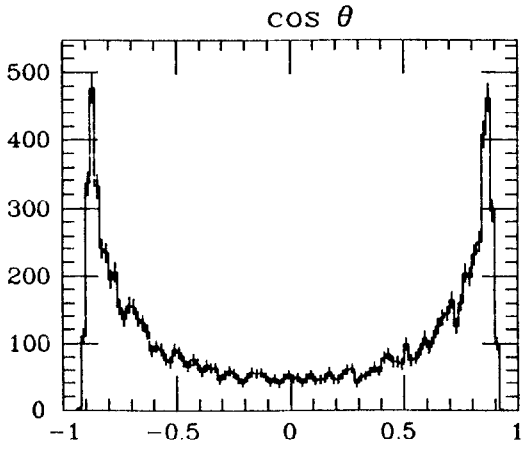

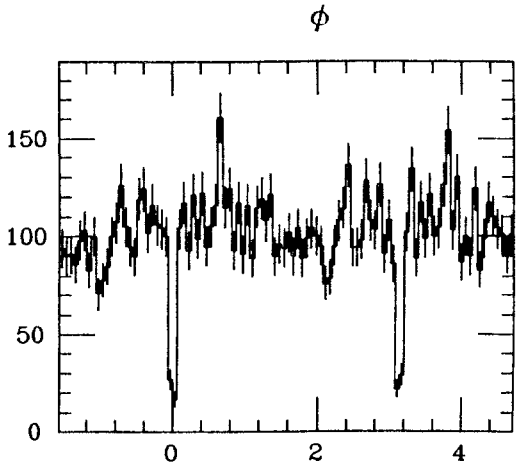

Fig. B.17 Angular distribution of photons in data: GAMFIT directions.

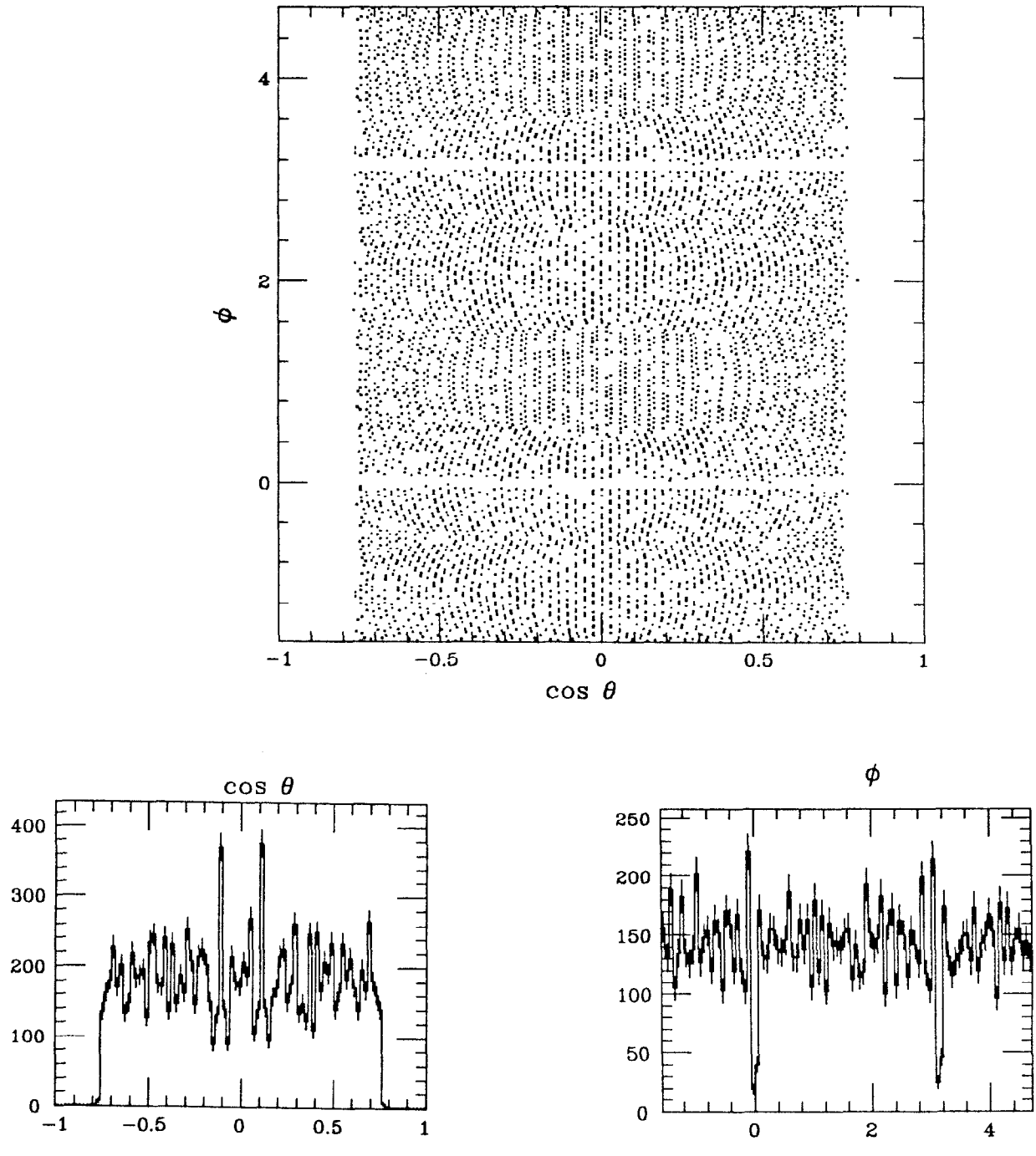

Fig. B.18 Angular distribution of photons in Monte Carlo: ESORT directions.

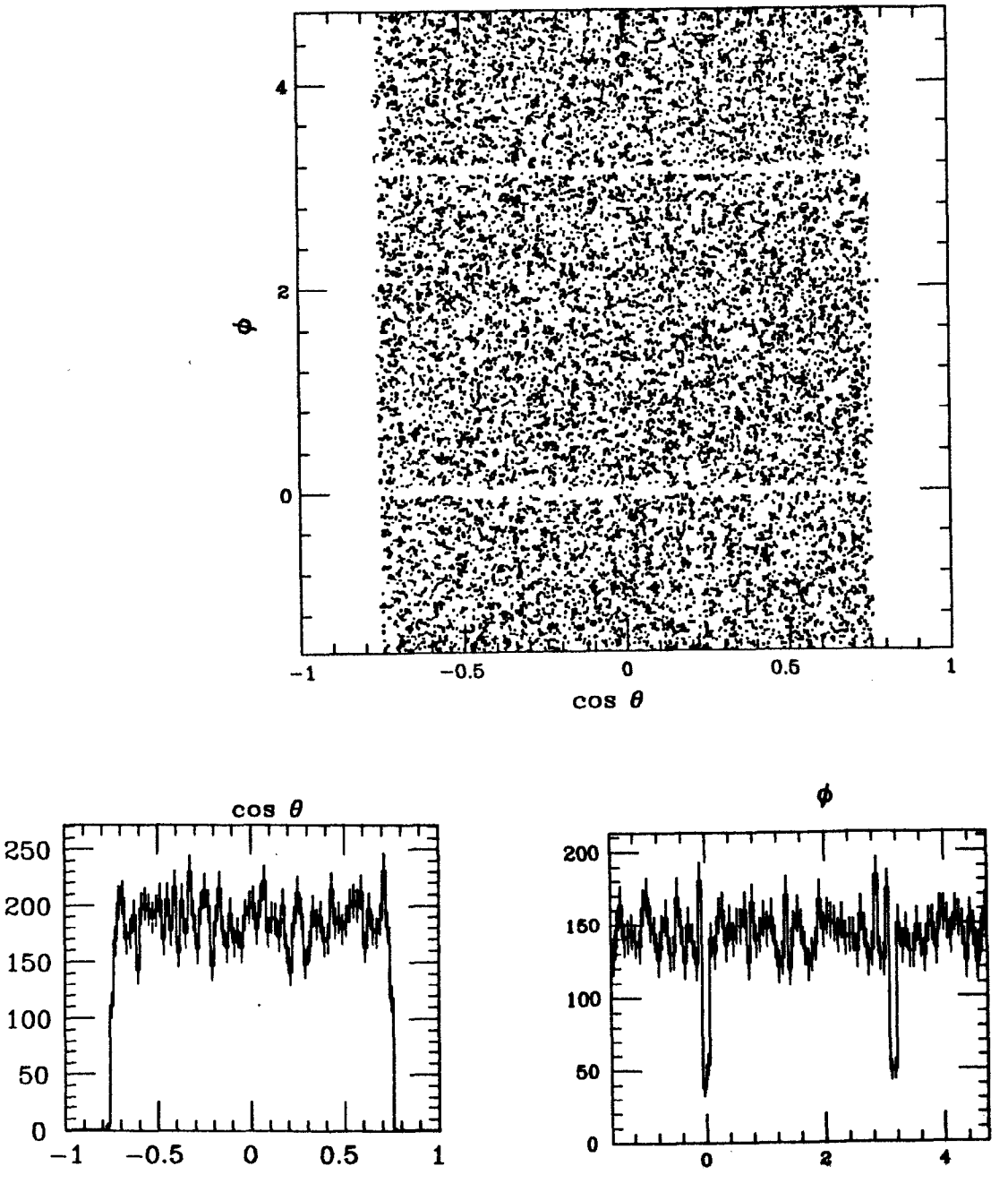

Fig. B.19 Angular distribution of photons in Monte Carlo: GAMFIT directions.

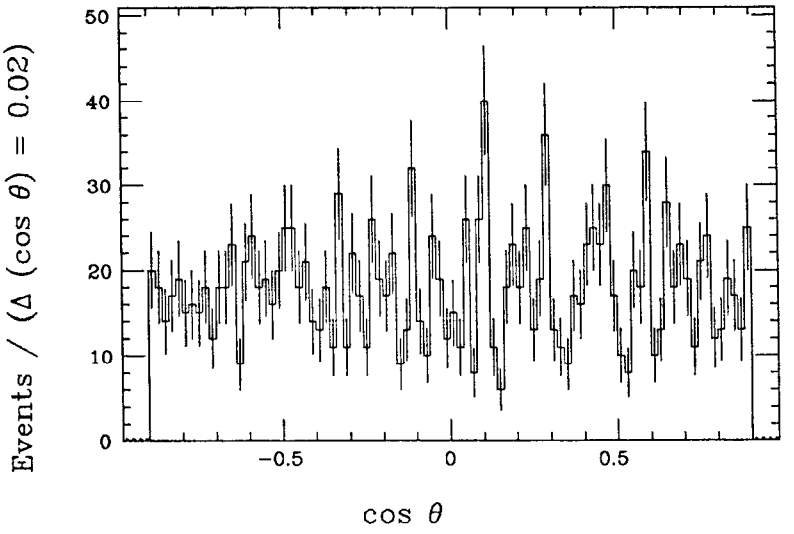

Fig. B.20 Angular distribution of photons in Monte Carlo: $\cos\theta$ projections: ESORT.

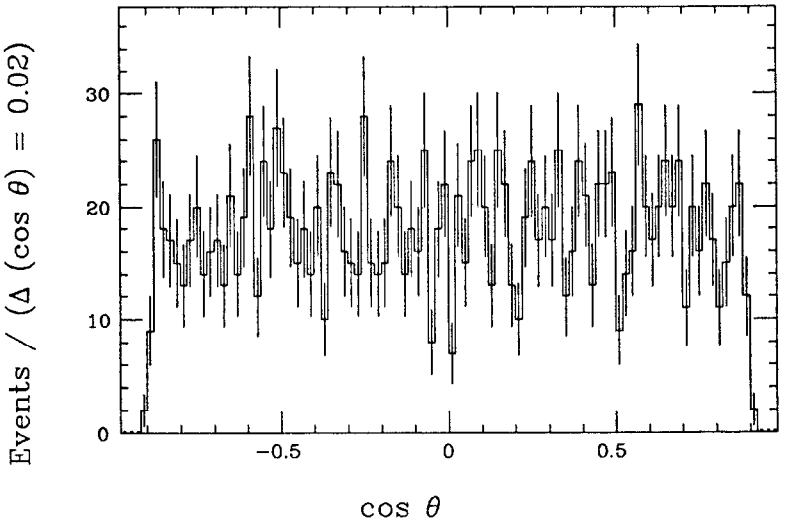

Fig. B.21 Angular distribution of photons in Monte Carlo: $\cos\theta$ projections: GAMFIT.

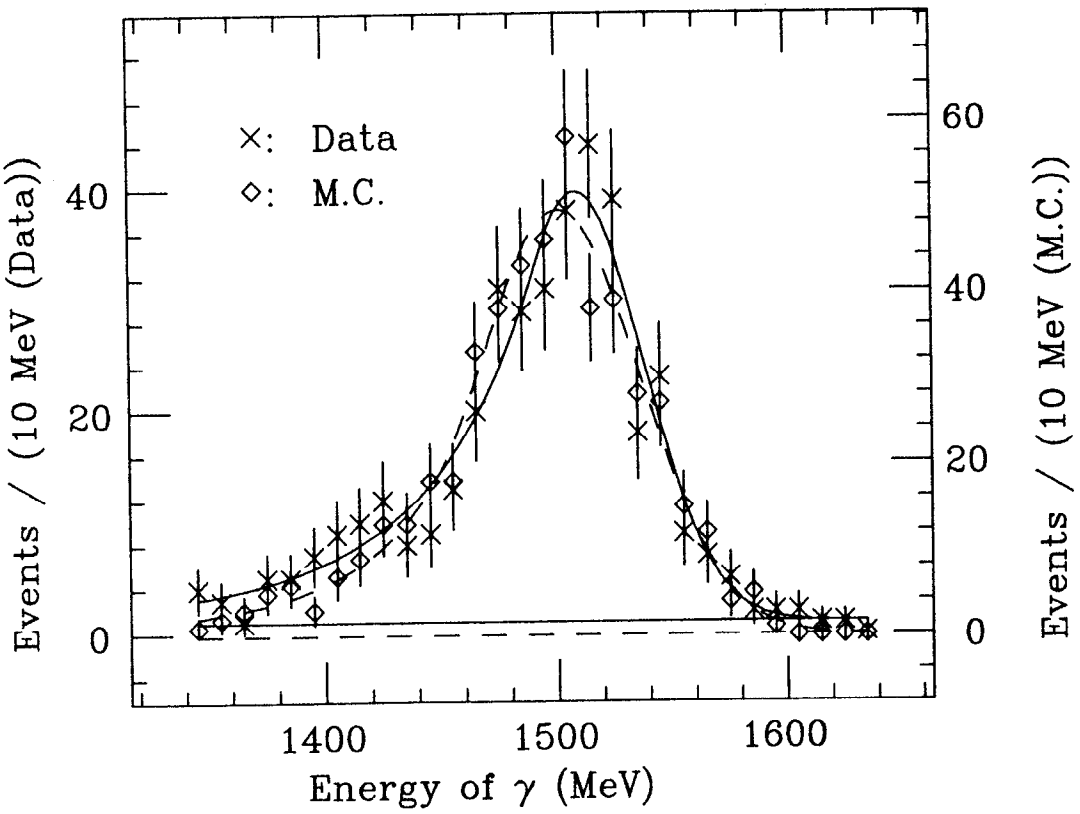

Fig. B.22 $J/\psi \to \gamma\eta$: Energy of direct gamma fitted to line shape function. Data: solid line. Monte Carlo: dotted line. Best fitted values:

Parameter	Data	Monte Carlo
α	8.7 ±4.6 MeV	1.0 ±2.5 MeV
σ_0	2.2 ±0.3%	2.6 ±0.2 %
r	8 ±12	4 ±5
β	0.65 ±0.23	1.1 ±0.2
Conf. Lev.	0.777	0.971

We next generate a Monte Carlo of 2000 events of the topology $\psi' \to \pi^0\pi^0 J/\psi$, $J/\psi \to e^+e^-$ and compare it with the ψ' data. We apply a set of cuts to both the Monte Carlo and the data to select events of the above topology. We select events with six tracks, no endcap tracks and no zero energy I.R. tracks, and a visible energy within 600 MeV of the center of mass energy; we place no restrictions on the number of charged tracks. We further require that the combined energies of the two highest energy tracks be between 2950 and 3190 MeV and that there be at least one pairing of the four lowest energy tracks consistent with two π^0's. We also place an overlap cut of $\cos\alpha < 0.85$ and a solid angle cut of $|\cos\theta| < 0.90$. Events passing these cuts are subjected to a kinematic fit requiring energy and momentum conservation but no constraints on the invariant mass of any pair of tracks. Figures B.23 - B.25 show plots for the pulls and confidence levels for the fits to data and Monte Carlo. The angular errors are consistent, although we see again that the Monte Carlo does not correctly reproduce the slight energy offset seen in the data.

B.4 Chamber Efficiencies and γ Conversion

The central detector simulation is performed separately from that of the main Ball. Chamber hits along the trajectory of a charged particle are generated according to the chamber efficiencies measured from Bhabha events. In this study the tagging probability for charged particles *per se* is not of primary concern since none of the final states contain charged particles. However, it is important that we correctly calculate the probability for overtagging and gamma conversion since this probability will enter our efficiency calculations as a multiplicative factor raised to a power equal to the number of γ's in the final state. A precise Monte Carlo treatment would incorporate all of the intervening material between the interaction point and the NaI in an EGS simulation and replace the γ by an e^+e^- pair if it converted. The algorithm actually used calculates the probability that a γ converts given its energy and the amount of material along its trajectory. If it does convert, it is replaced by a single charged particle at the point of conversion for the purposes

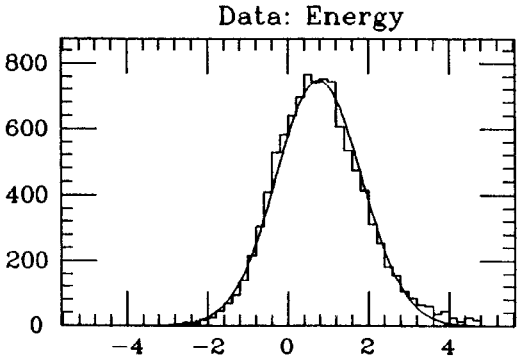

Mean = 0.77 ± 0.02
σ = 1.07 ± 0.02
χ^2/D.o.F. = 189/ 45

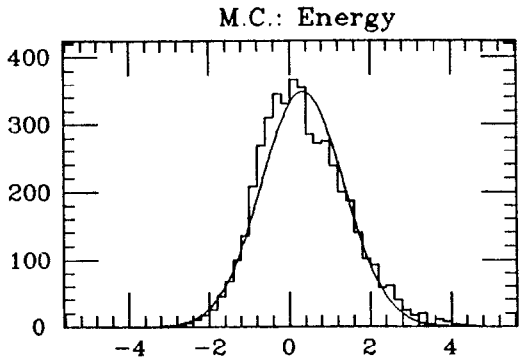

Mean = 0.33 ± 0.03
σ = 1.03 ± 0.02
χ^2/D.o.F. = 153/ 45

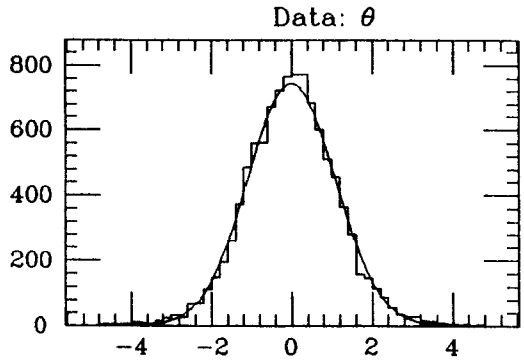

Mean = 0.01 ± 0.02
σ = 1.09 ± 0.01
χ^2/D.o.F. = 136/ 45

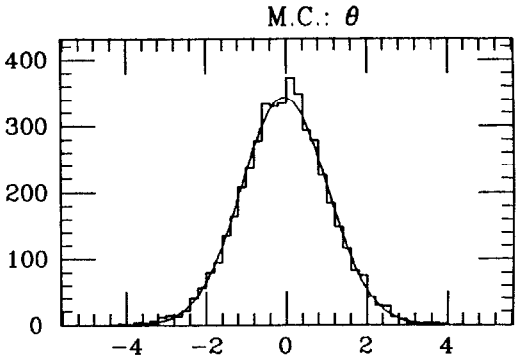

Mean = −0.05 ± 0.01
σ = 1.07 ± 0.01
χ^2/D.o.F. = 34/ 45

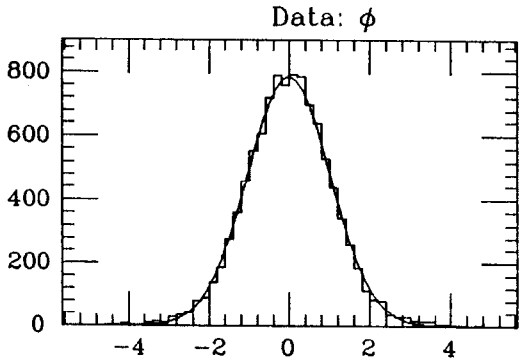

Mean = 0.02 ± 0.02
σ = 1.04 ± 0.02
χ^2/D.o.F. = 105/ 45

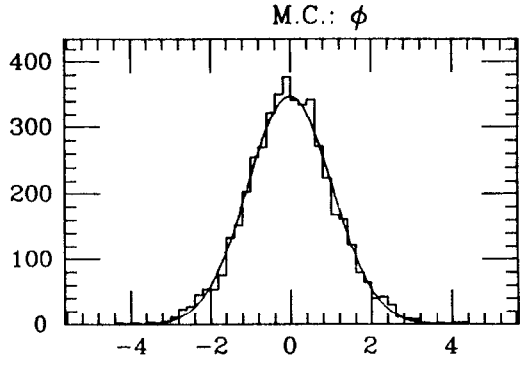

Mean = −0.02 ± 0.02
σ = 1.05 ± 0.01
χ^2/D.o.F. = 61/ 45

Fig. B.23 Pulls for kinematic fits to $\psi' \to \pi^0\pi^0 J/\psi, \pi^0 \to \gamma\gamma, J/\psi \to e^+e^-$ for data and Monte Carlo: tracks less than 1000 MeV.

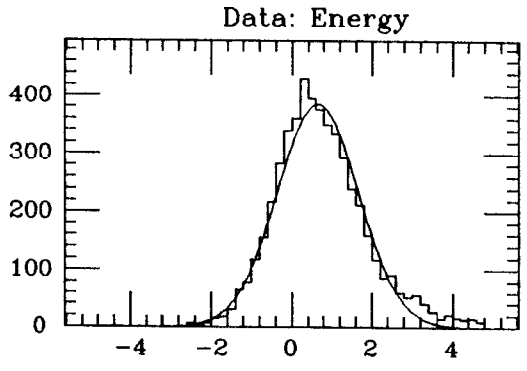

Mean = 0.65 ± 0.03
σ = 1.02 ± 0.02
χ^2/D.o.F. = 205/ 45

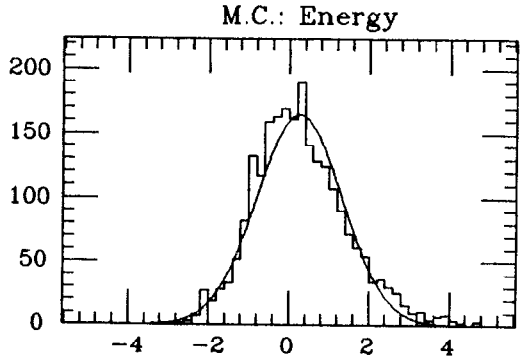

Mean = 0.26 ± 0.04
σ = 1.07 ± 0.03
χ^2/D.o.F. = 112/ 45

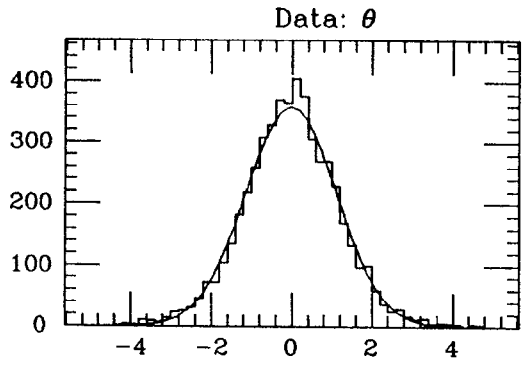

Mean = 0.02 ± 0.02
σ = 1.13 ± 0.02
χ^2/D.o.F. = 76/ 45

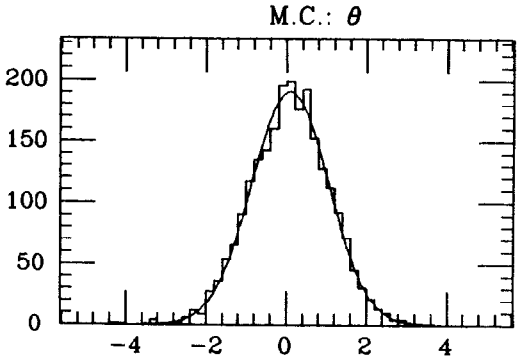

Mean = 0.09 ± 0.01
σ = 0.96 ± 0.01
χ^2/D.o.F. = 24/ 45

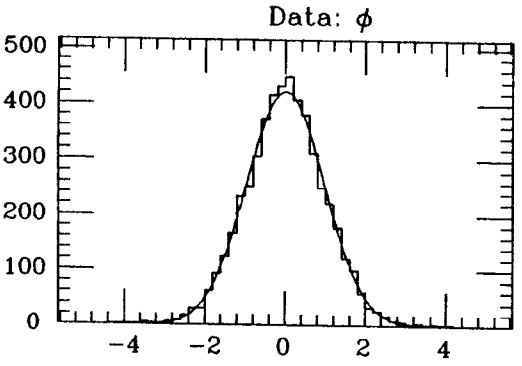

Mean = 0.00 ± 0.01
σ = 0.96 ± 0.01
χ^2/D.o.F. = 35/ 45

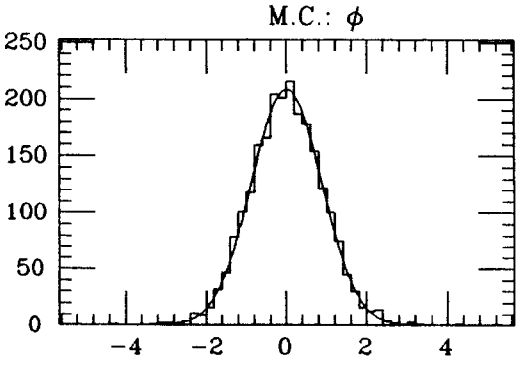

Mean = 0.00 ± 0.01
σ = 0.88 ± 0.01
χ^2/D.o.F. = 33/ 45

Fig. B.24 Pulls for kinematic fits to $\psi' \to \pi^0\pi^0 J/\psi, \pi^0 \to \gamma\gamma, J/\psi \to e^+e^-$ for data and Monte Carlo: tracks greater than 1000 MeV.

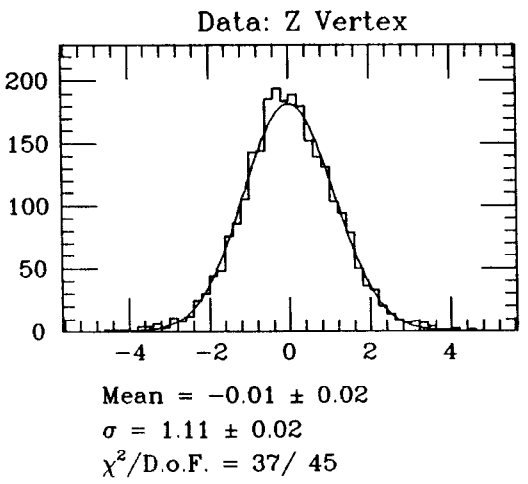

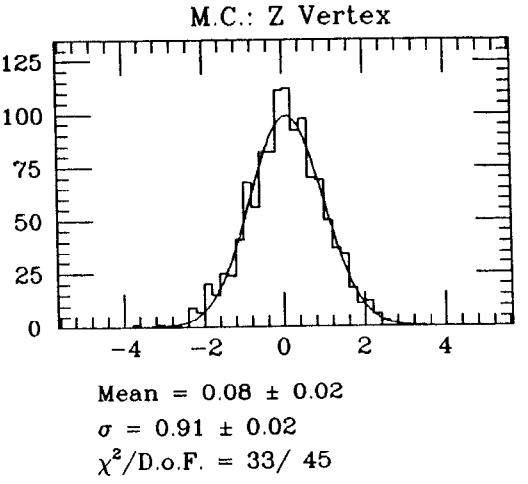

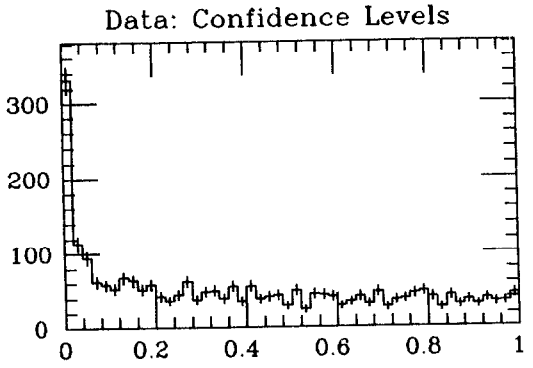

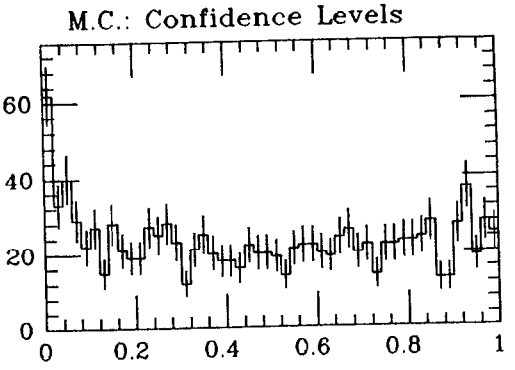

Fig. B.25 Pulls for kinematic fits to $\psi' \to \pi^0\pi^0 J/\psi, \pi^0 \to \gamma\gamma, J/\psi \to e^+e^-$ for data and Monte Carlo: z vertex and confidence levels.

of the chamber simulation but is treated as a γ in the NaI EGS simulation. Thus, the algorithm attempts to calculate the probability that a photon converts and is tagged as charged but does not account for the degradation in resolution due to converted photons which are not tagged charged. This is not a serious drawback since the Monte Carlo resolution is made to agree with that obtained from the data.

In investigating the overtagging and conversion of γ's, we wish to know

1. Is there an angular dependence in the conversion probability?
2. Is there a difference between the 1978/79 data and the 1981 data? One expects that the gamma conversion probability is higher for the 1981 data due to the introduction of the tube chamber.
3. How well does the Monte Carlo simulate these effects and the overall conversion probability?

In order to obtain the actual gamma conversion probability, we require a large, clean sample of gammas. We exploit the large branching ratio and distinct signature of the decay $\psi' \rightarrow \pi^0\pi^0 J/\psi, J/\psi \rightarrow e^+e^-$. This reaction has the additional advantage that the charged and neutral tracks can identified simply by their energies, since the e^+ and e^- will have energies of approximately 1500 MeV while the gammas will have 100-400 MeV apiece. We use the same cuts to select our sample as described in the previous section with the exception of the solid angle cut. Figure B.26 shows the distribution of missing mass opposite the four lowest energy tracks after these cuts. By accepting only those events that fall within the arrow shown on the plot, we obtain a sample of 2749 events with essentially no background. This yields a sample of over 10,000 γ's and 5000 charged particles.

In studying the neutral tagging efficiency, we accept only those events in which the two highest energy tracks have been correctly tagged as charged. Figures B.27 and B.28 show the ratio of low energy tracks tagged as neutral divided by the total number of low energy tracks as a function of $\cos\theta$ for the 1978/79 and 1981 datasets, respectively. We note that there is no discernible angular dependence in

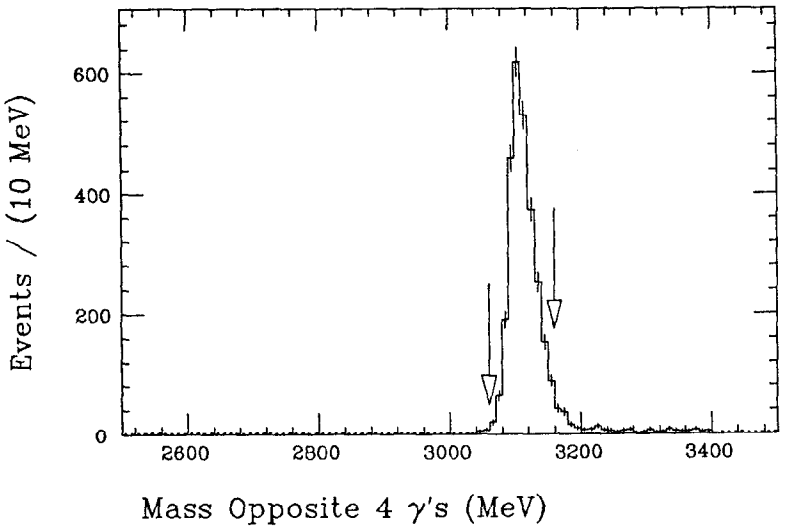

Fig. B.26 Missing mass opposite four lowest energy tracks after cuts in $\psi' \rightarrow$six tracks.

the efficiency for either dataset. However, the neutral tagging efficiency is slightly worse for the 1981 data than for the older data as anticipated due to the additional tube chamber. Figure B.29 shows the same plot for the $\psi' \rightarrow \pi^0\pi^0 J/\psi, J/\psi \rightarrow e^+e^-$ Monte Carlo. Again, there is no angular dependence, but the efficiency is somewhat higher for the Monte Carlo that the data. We assume that this discrepancy can be parameterized by a single correction factor (independent of angle). We divide the efficiencies for the Monte Carlo and data bin by bin and so make 20 measurements of this ratio. We average them to obtain ($\epsilon \equiv$ efficiency):

$$\frac{\epsilon_{old\ data}}{\epsilon_{Monte\ Carlo}} = 0.993 \pm 0.004 \qquad \frac{\chi^2}{\text{D.o.F.}} = \frac{23}{19}$$

$$\frac{\epsilon_{new\ data}}{\epsilon_{Monte\ Carlo}} = 0.983 \pm 0.004 \qquad \frac{\chi^2}{\text{D.o.F.}} = \frac{17}{19}$$

The χ^2 for each case indicate that our assumption is justified. We thus apply a

correction factor of $(0.993^n + 0.983^n)/2$ (where n is the number of γ's in the final state) to the Monte Carlo efficiencies for ψ' decays and 0.993^n for J/ψ decays (since the tube chamber was absent for the entirety of the J/ψ running). We include a systematic error of $\pm 0.5\%$ per photon.

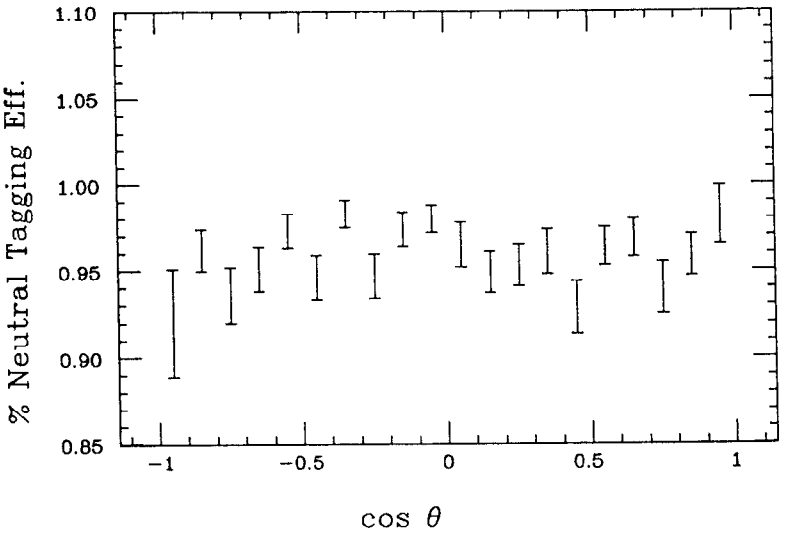

Fig. B.27 Neutral tagging efficiency: 1978/79 data.

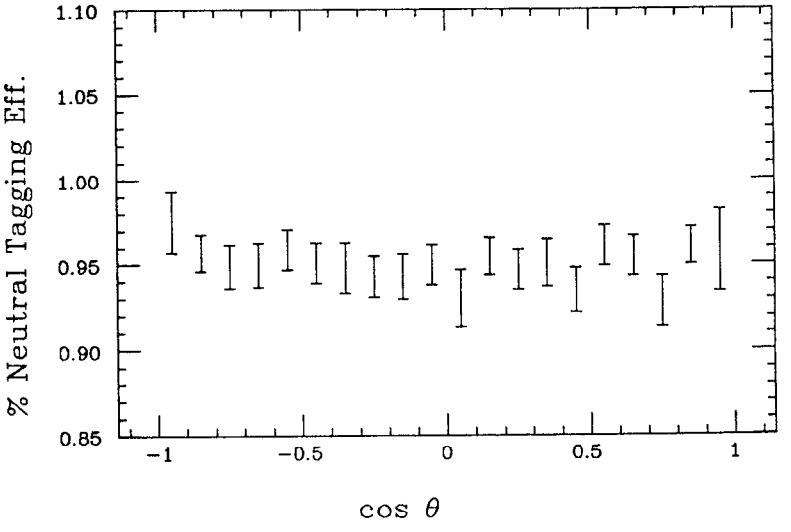

Fig. B.28 Neutral tagging efficiency: 1981 data.

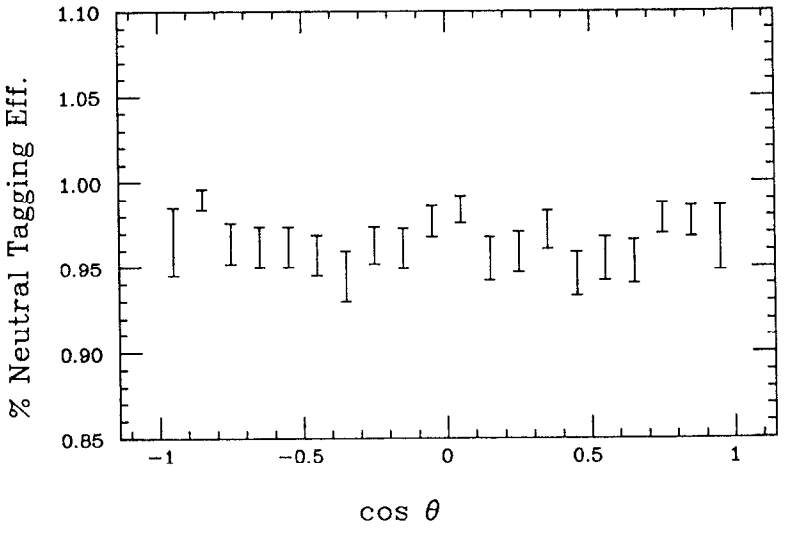

Fig. B.29 Neutral tagging efficiency: Monte Carlo.

References

1) C. Baglin *et. al.*, *Nucl. Phys.* **B22** (1970) 66.

2) M. Cerrada *et. al.*, *Nucl. Phys.* **B126** (1977) 189.

Appendix C

Shower Fitting Routines

We describe in this Appendix the shower fitting routines GAMFIT, PIFIT, and SMOMT that are used to fit γ and π^0 showers. Further details are given elsewhere by the authors of these algorithms.[1,2]

C.1 Descriptions of the Routines

GAMFIT[1] is used to determine the direction of a photon shower better than the standard offline software. Nearly 50,000 EGS photon showers are generated in order to derive the functional dependence of the energy in the incident crystal and its surrounding twelve neighbors on the direction and energy of the input photon. Although this is in principle a complicated function, a simplifying assumption is made that the probability distributions for energies in individual crystals are independent, and that the distribution for the neighbor crystals can all be fit by one functional form (an incomplete gamma function) as distinct from the central crystal (which is fit by a Gaussian). By examining Monte Carlos for several incident photon energies and directions, the dependence of the parameters of these functions on the energy and direction of the incident γ can be fit to simple functional forms. Given an observed shower, one can find the incident photon direction which maximizes the likelihood of the observed energy distribution. This defines the GAMFIT direction cosines; the energy of the shower is not determined by GAMFIT.

PIFIT[1] uses the same shower information as GAMFIT, but fits the convolution

of two γ showers instead of one. The sum of the energies of the two gammas is constrained to be the sum of the E_{13} energies of these two crystals, so that five parameters must be determined – the ratio of energies and two sets of direction cosines. With these quantities one can calculate the invariant mass of the two candidate γ's, allowing one to discriminate between a shower due to a single photon and two overlapping showers from the decay of a π^0. In the latter case the fitted energies and directions also provide an improved measurement of the four-vector of the π^0. PIFIT also performs a likelihood fit to a single photon distribution *a la* GAMFIT and returns a "pseudo chi-square" (the ratio of the likelihoods of the two hypotheses) which indicates how strongly the 2-γ hypothesis is favored over the 1-γ hypothesis. However, this quantity is highly correlated with the invariant mass value.

SMOMT[2] uses an algorithm distinct from that used in GAMFIT and PIFIT. Rather than determine the four-vector of the γ's making up a shower, GAMFIT calculates the second moment of the energy distribution, defined by

$$S = \frac{1}{E}\sum_{i=1}^{N} E_i(\hat{p}_i - < p >)^2 \qquad [C.1]$$

where the sum is over the crystals in a connected region, $E = \sum_{i=1}^{N} E_i$, $< p >$ is the first moment,

$$< p >= \frac{1}{E}\sum_{i=1}^{N} E_i\hat{p}_i \qquad [C.2]$$

and $\hat{p}_i$ is a unit vector pointing to the center of crystal i from the center of the Ball. It is reasonable to expect that the energy distribution of two overlapping showers will be less circular than that of a single shower and so will have a larger second moment (just as an ellipsoid has a larger moment of inertia than a sphere of equal mass). Thus, we expect that the second moment of a shower will be proportional to the invariant mass of the sum of the γ's that produced it. A detailed calculation

shows that the constant of proportionality is E^2. Thus, an estimate of the invariant mass of the γ's in a connected region is given by

$$M_X^2 = (S - S_\gamma)E^2 \qquad [C.3]$$

where S_γ subtracts the contribution to the shower mass due to a single γ. Figure C.1 shows the energy dependence of S_γ for a series of Monte Carlo single photon showers. We see that S_γ is roughly constant and take

$$S_\gamma = 0.007 \text{ radians}^2 \qquad [C.4]$$

(Figure C.1 and the value of S_γ quoted above are calculated for "extended" connected regions as defined in Appendix D. For connected regions as defined by the standard offline software, $S_\gamma = 0.004$ radians^2.)

SMOMT has an advantage over PIFIT in that it can calculate the invariant mass of a connected region with any number of γ's, whereas PIFIT is limited to connected regions with one or two. Also, SMOMT cannot be biased by the starting values for the likelihood fit, since no fit is performed. However, SMOMT does not separate γ's and π^0's as efficiently as PIFIT at high energies as shown below.

C.2 Monte Carlo Examples

We examine first the performance of these routines with Monte Carlo showers. Approximately 2000 single-particle events are generated for momenta of 1700, 1300, 1000, and 700 MeV for both γ's and π^0's (16000 events in all). The single particles in these events are distributed uniformly in $\cos\theta$ and ϕ. Cuts are made that require all generated tracks to have $|\cos\theta| < 0.8$ (measured from the generated z vertex), and no charged tracks (either from conversion or Dalitz decays of the π^0's). Additionally, we require there be only one connected region in the event inasmuch as we are not interested in this study in separated π^0's. Figure C.2 shows plots of the

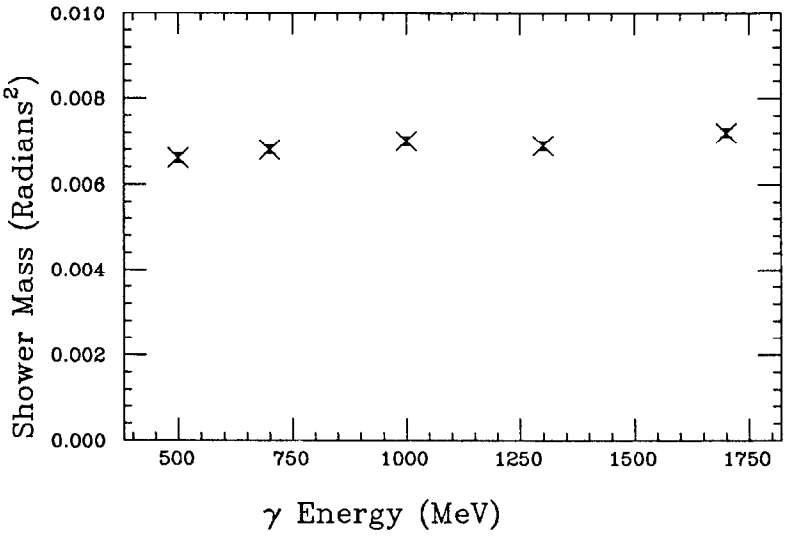

Fig. C.1 Energy dependence of S_γ from Monte Carlo.

invariant mass returned by PIFIT for γ's and π^0's. (The π^0 peak becomes smaller in successive plots due to the fact that a larger fraction of π^0's are separated at low energies. See Fig. 3.1.) We see that even at 1700 MeV/c the γ/π^0 separation is excellent. If we identify a shower with an invariant mass below 90 MeV/c^2 as a γ and above 90 MeV/c^2 as a π^0 (as shown by the arrows in Fig. C.2), the fraction of γ's called π^0's is 6% and the fraction of π^0's called γ's is 12%. In contrast, the SMOMT invariant mass peaks are not as separated (as shown in Fig. C.3). As a general rule, the SMOMT π^0 peak has roughly the same position and width as the corresponding PIFIT peak, but the γ peak occurs at higher invariant mass.

It will be noted that the PIFIT π^0 peak has a tail towards lower invariant masses even when the π^0 energy is relatively low. This is due in part to the fact that the starting direction of the low energy γ is slightly biased towards the starting direction of the high energy γ. Occasionally the low energy γ from the decay of a π^0

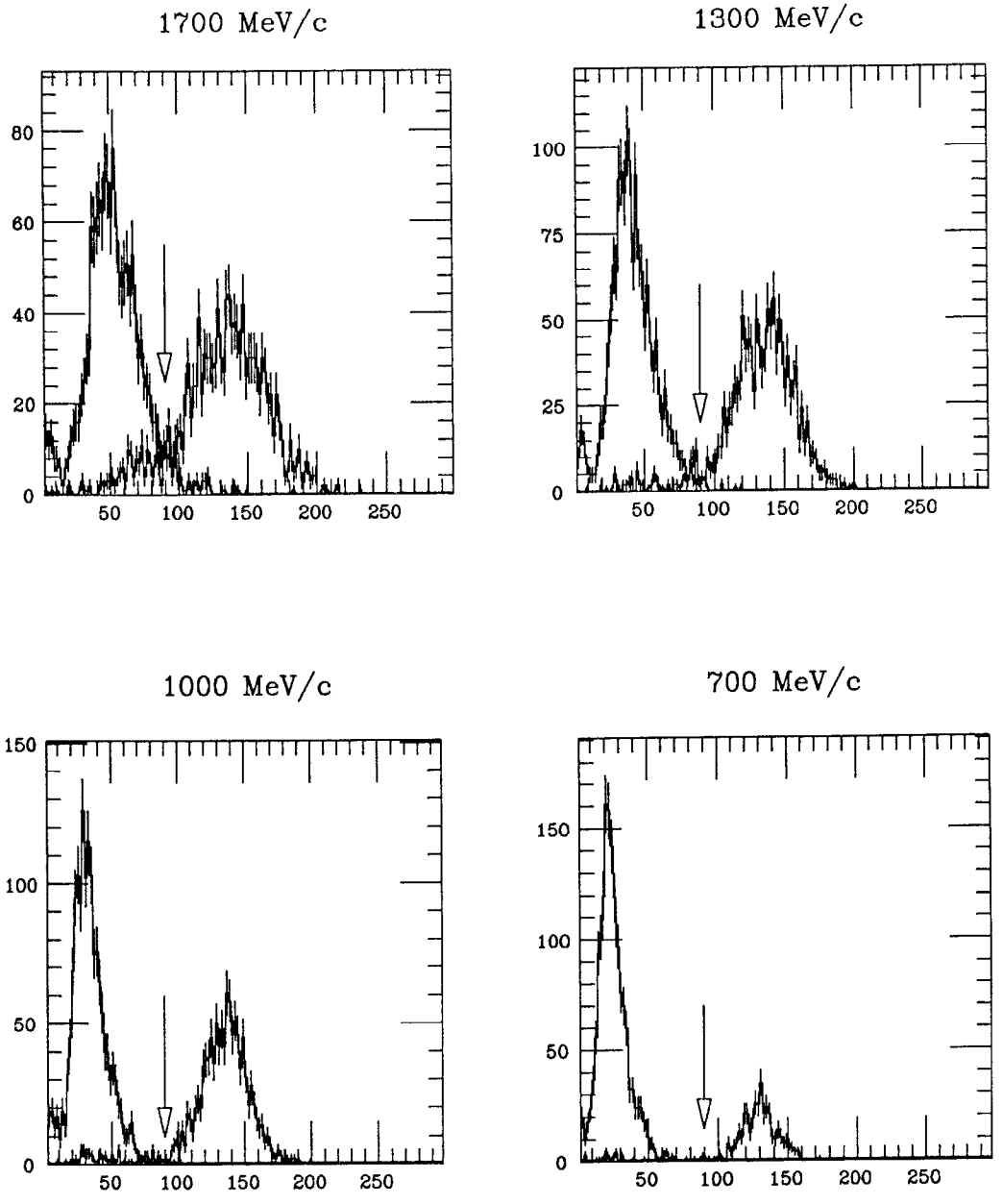

Fig. C.2 PIFIT masses : Monte Carlo γ's and π^0's with momenta between 700 and 1700 MeV/c.

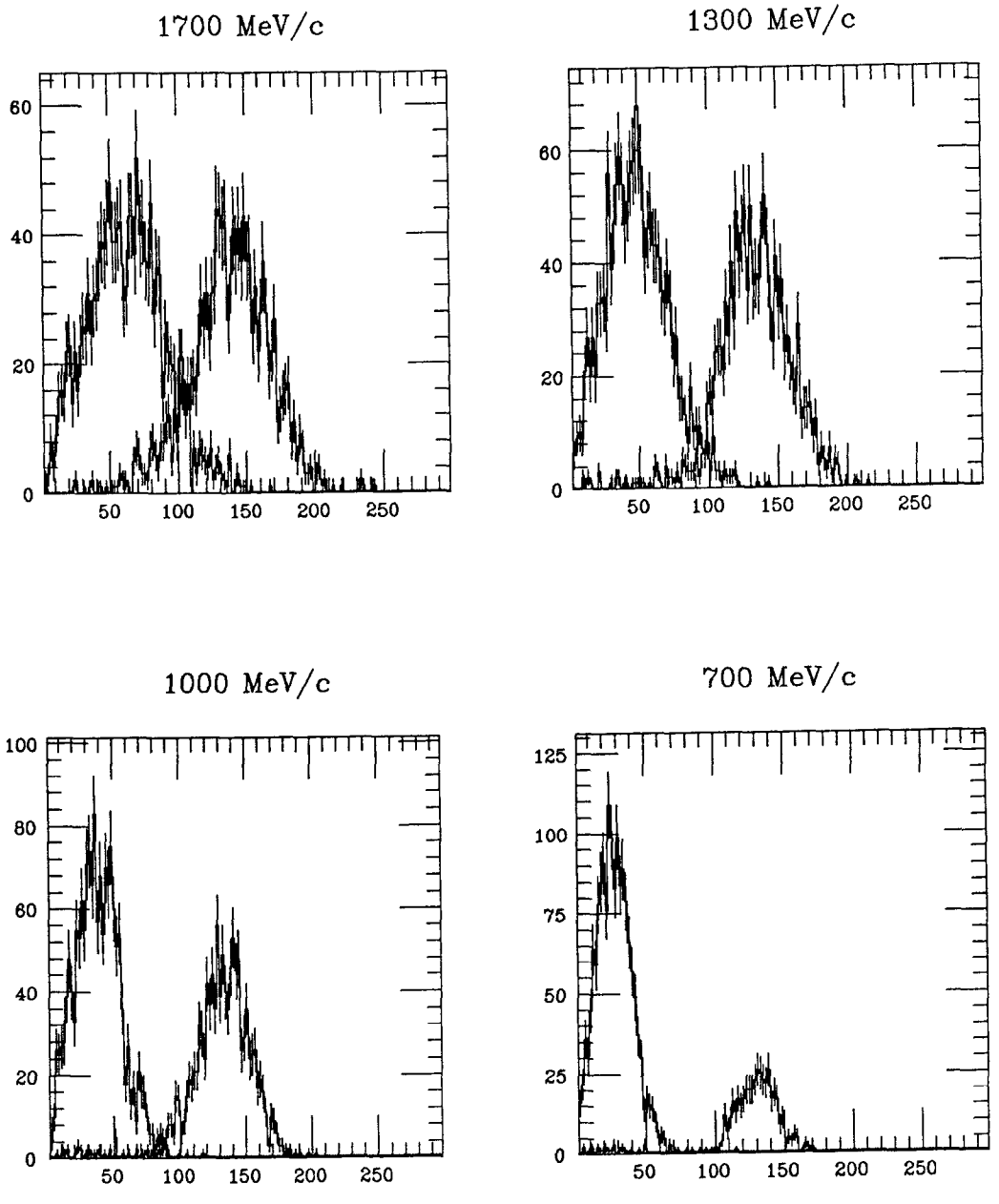

Fig. C.3 SMOMT masses : Monte Carlo γ's and π^0's with momenta between 700 and 1700 MeV/c.

will be so far from the high energy γ that it will not be detected by this algorithm. On the other hand, this γ may have a low enough energy that it is not flagged by the bumps discriminator. Thus, the high energy γ is flagged as a γ while the low energy γ remains unaccounted. Figure C.4 shows a Monte Carlo π^0 of this type. The stars show the dialed γ directions while the boxes show the initial PIFIT directions. Effects of this type are particularly pernicious in an analysis of the type described here since we require that the number of observed γ's be consistent with the constraints implied by C-parity conservation. In order to remedy this failing we adopt the following procedure. All connected regions which have not been flagged as π^0's by the 90 MeV/c^2 cut described above are searched for local maxima. (A local maximum is defined as a crystal which contains more energy than any of its three nearest neighbors.) If more than one such local maximum is found, PIFIT is called again with the starting γ directions defined by the local maxima. If the probability that this connected region contains two gammas is greater than that obtained from the previous call to PIFIT (as determined from the likelihood ratio) and the calculated invariant mass is greater than 90 MeV/c^2, we assume that this connected region actually contains a π^0 and replace the old PIFIT parameters. If there are more than two local maxima in a connected region, we use the PIFIT parameters from the one which yields the largest likelihood ratio.

Figure C.5 shows the distribution of PIFIT masses for the Monte Carlo γ's reevaluated with this procedure. Figure C.6 shows the corresponding plot for Monte Carlo π^0's. We see that this procedure occasionally misidentifies a γ as a merged π^0, but identifies a far larger number of merged π^0's correctly. Figure C.7 shows the same plot after this procedure has been applied to the J/ψ dataset. A clear π^0 peak is evident. Figure C.8 shows the invariant mass plots corresponding to Fig. C.2 after the above procedure has been applied. We see that the low invariant mass tail has been reduced for the high energy π^0's but not eliminated. Examination of the remaining events shows that they are due to asymmetric decays of the π^0 in which the low energy γ escapes detection either because it goes into a gap in the

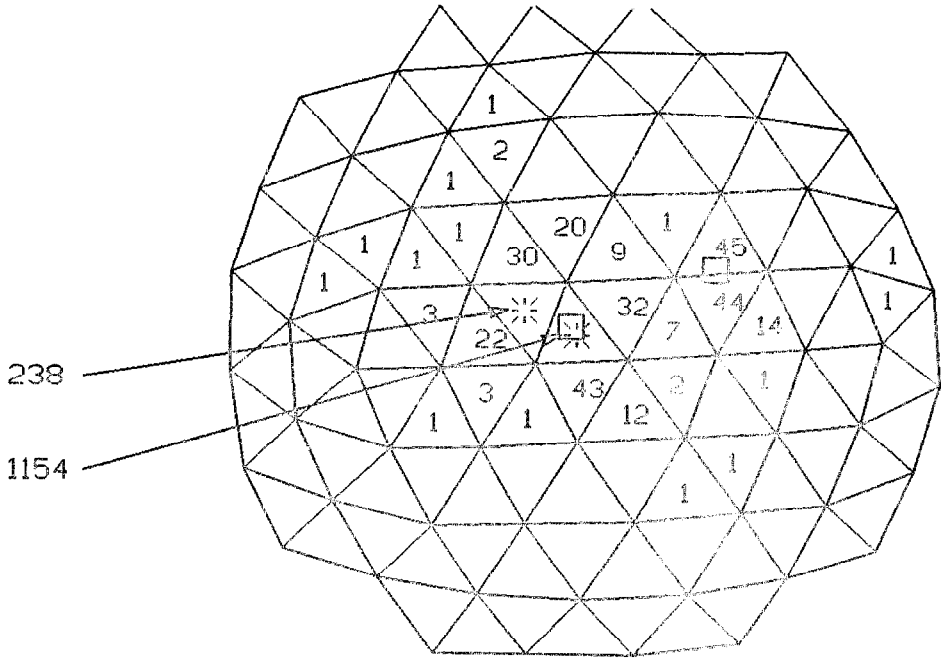

Fig. C.4 Monte Carlo π^0 shower with second gamma unflagged. (Boxes show dialed directions of photons; stars show directions of photons found by PIFIT.)

detector or it is so low energy that it does not deposit more than 10 MeV in any crystal and so does not pass the threshold to create a connected region. After this process, the fraction of γ's which are misidentified as π^0's increases to 7%, but the number of π^0's misidentified as γ's decreases to 8%.

C.3 Data Examples

We use two different reactions to illustrate the γ/π^0 separation in the data. First, the reaction $J/\psi \to \rho^0\pi^0, \rho^0 \to \pi^+\pi^-$ has a branching ratio of 0.4% , yielding a large sample of π^0's with energies in the range 1400 to 1500 MeV. (The π^0's are not monoenergetic due to the large width of the ρ^0.) From the entire produced J/ψ

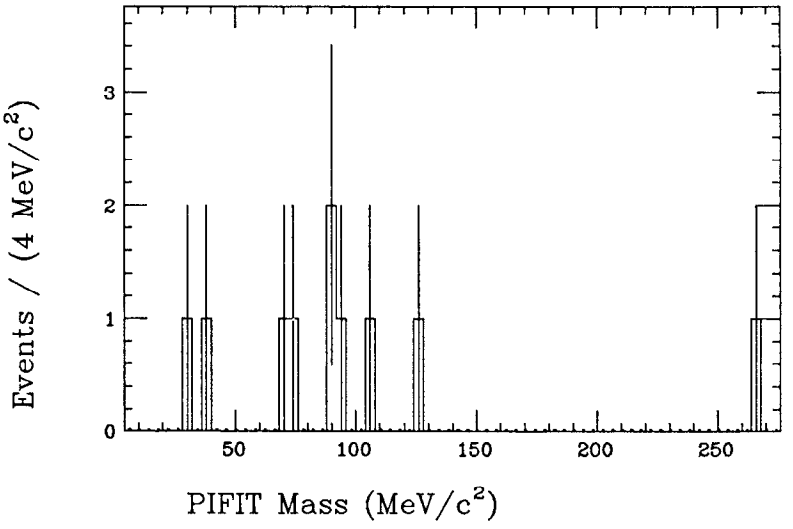

Fig. C.5 PIFIT masses of connected regions with two or more local maxima – γ Monte Carlos.

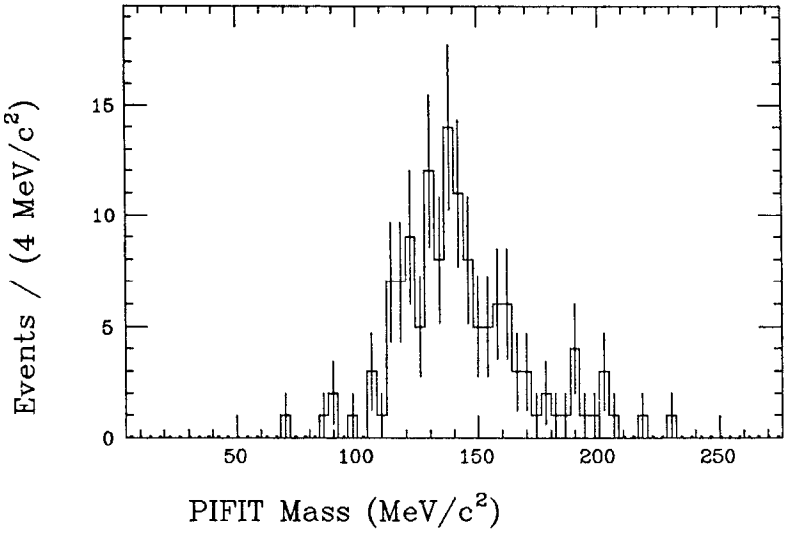

Fig. C.6 PIFIT masses of connected regions with two or more local maxima – π^0 Monte Carlos.

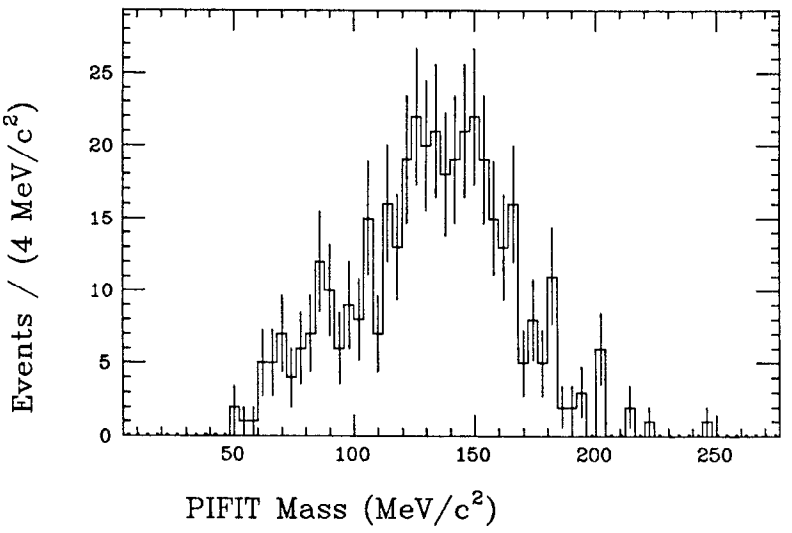

Fig. C.7 PIFIT masses of connected regions with two or more local maxima – J/ψ data.

sample, events are selected which have

1. three tracks of which two are tagged charged,
2. no zero energy I.R. tracks or endcap tracks,
3. all tracks in a plane, i.e., $|(\hat{u}_1 \times \hat{u}_2) \cdot \hat{u}_3| < 0.3$, where $\hat{u}_i$ is a unit vector pointing in the direction of track i,
4. Between 1400 and 1500 MeV in the neutral track.

Figure C.9 shows the PIFIT masses of the neutral track in the events so selected; Fig. C.10 shows the same distribution using the SMOMT masses. In addition to the π^0 peak, there is a small peak at low invariant masses due to contamination from other J/ψ decays (for instance, $J/\psi \to \gamma\eta'$, $\eta' \to \gamma\rho^0, \rho^0 \to \pi^+\pi^-$ where one of the γ's is lost) and from nonresonant processes (such as $e^+e^- \to \gamma\rho$).

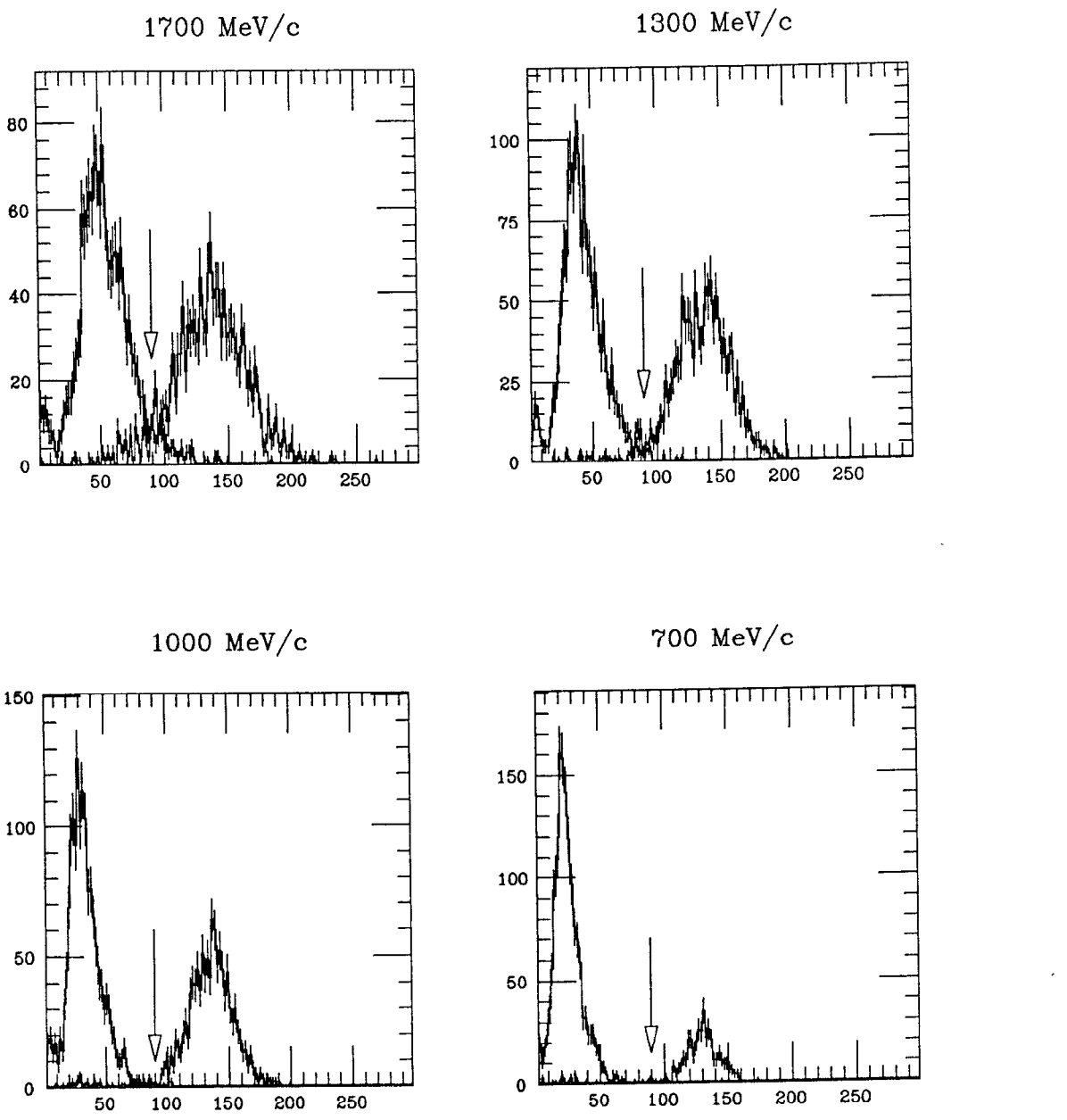

Fig. C.8 PIFIT masses after local maxima additions: Monte Carlo γ's and π^0's with momenta between 700 and 1700 MeV/c.

In order to study γ's of higher energy, we use the decay $\psi' \rightarrow \gamma\chi_0$, $\chi_0 \rightarrow \pi^0\pi^0$. The energies of the π^0's in this reaction are approximately one-half of the mass of the χ_0, or 1700 MeV. The largest background for this process is the QED reaction $e^+e^- \rightarrow (\gamma)\gamma\gamma$. We use as the parent sample the ψ' events which have been passed through all the neutral analysis described in Chapter 3 except the 3-γ connected region cut and the 200 MeV/c^2 SMOMT cut. We select events with three tracks and require the energy of the lowest track to be within 36 MeV of the expected energy of the transition photon to the χ_0. Figure C.11 shows the PIFIT distribution for the two high energy tracks. Two peaks corresponding to $e^+e^- \rightarrow (\gamma)\gamma\gamma$ and $\psi' \rightarrow \gamma\chi_0$, $\chi_0 \rightarrow \pi^0\pi^0$ are visible. Figure C.12 shows the same distribution for SMOMT masses.

We see in both these examples that PIFIT is able to separate γ's and π^0's up to 1.7 GeV. SMOMT is not as useful as a π^0/γ separator.* However, as noted previously, SMOMT is able to calculate the invariant masses of connected regions with more than one γ. In this regard, note that in neither Fig. C.10 nor Fig. C.12 does the SMOMT mass distribution extend much beyond 200 MeV/c^2. Since even the most energetic π^0's in the data samples under consideration here do not have SMOMT masses beyond 200 MeV/c^2, we conclude that any connected region which has an SMOMT mass beyond this threshold most probably contains more than two γ's. As described in Chapter 3, we eliminate events with such connected regions since we are unable to separate photon showers which are so closely overlapped.

* The plots shown here illustrate the SMOMT masses from a version of the SMOMT routine modified for use with the global shower algorithm. (See Appendix D.) The γ/π^0 separation of the standard version is somewhat better.

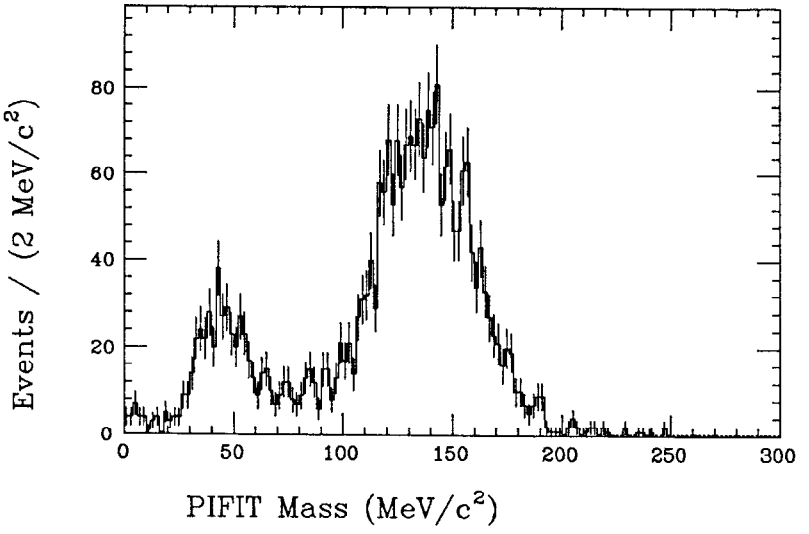

Fig. C.9 PIFIT mass of neutral track in $J/\psi \rightarrow \rho^0\pi^0, \rho^0 \rightarrow \pi^+\pi^-$.

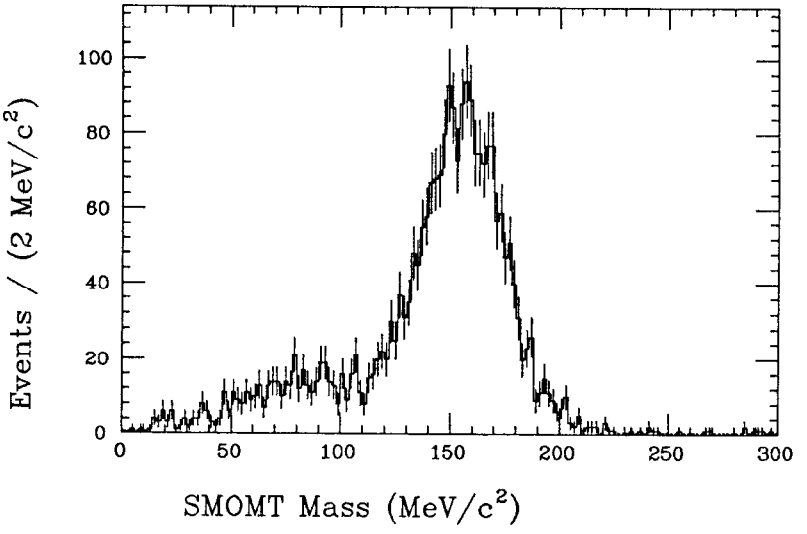

Fig. C.10 SMOMT mass of neutral track in $J/\psi \rightarrow \rho^0\pi^0, \rho^0 \rightarrow \pi^+\pi^-$.

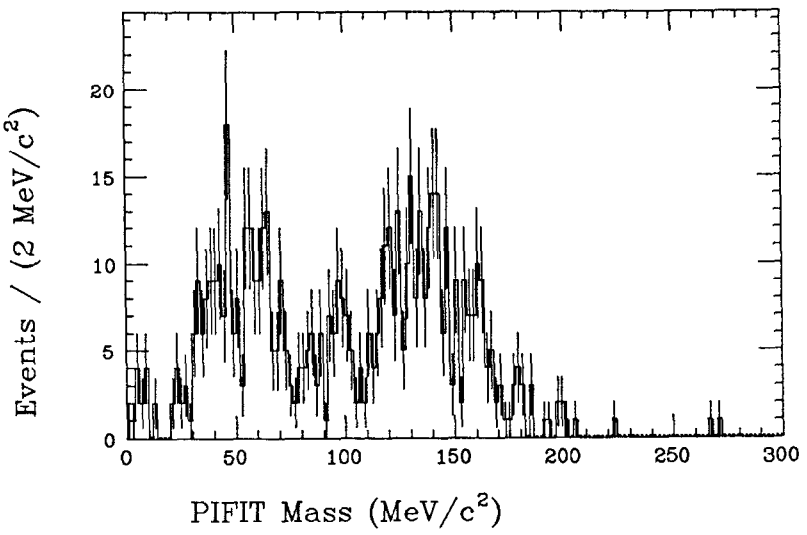

Fig. C.11 PIFIT masses of high energy tracks in $\psi' \rightarrow \gamma\chi_0, \chi_0 \rightarrow$ two neutral tracks.

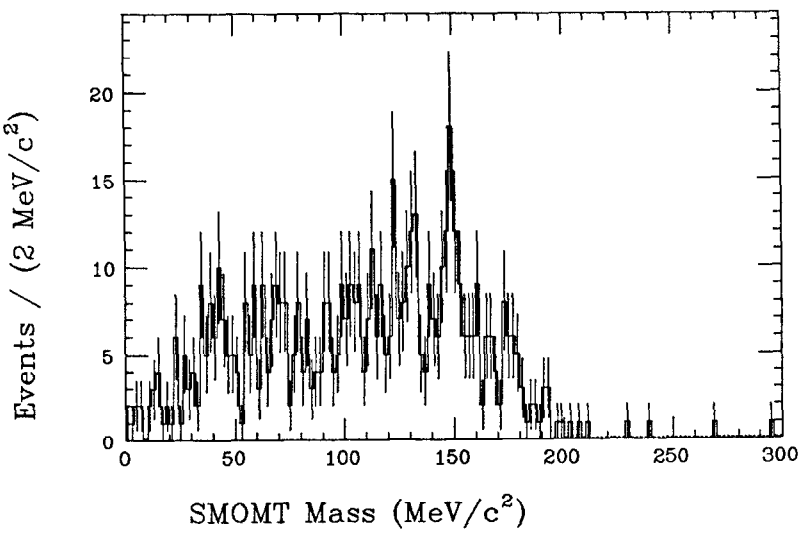

Fig. C.12 SMOMT masses of high energy tracks in $\psi' \rightarrow \gamma\chi_0, \chi_0 \rightarrow$ two neutral tracks.

References

1) R. Partridge, Ph.D. thesis, California Institute of Technology, 1984 (unpublished).

2) D. Antreasyan, Crystal Ball Note 321.

Appendix D

Global Shower Technique

D.1 Introduction

We describe in this appendix the concept and implementation of the global shower technique. This technique was developed to identify events in which the showers from γ's from several π^0's and/or η's overlap in the Ball. We do not reconstruct the four-vector of individual particles; rather, we attempt to calculate the invariant mass of their sum, as this is the quantity of interest in most studies. (The technique is similar to that used in jet studies at high energies with large calorimeters. It is impossible to disentangle the individual particles in a jet, but it is possible to calculate the invariant mass of the jet taken as a whole.) Consider as an example the decay $J/\psi \to \gamma\eta$, $\eta \to \pi^0\pi^0\pi^0$. Figure D.1 is a representation of a Monte Carlo event of this type. Each of the seven γ's is represented by a track number displayed in the crystal it enters, along with its energy. The direct γ, (i.e., the γ in the decay $J/\psi \to \gamma\eta$) is well-separated from the rest of the event. In contrast, five of the six γ's from the decay of the η are clustered together (as one expects from the small mass of the η relative to its energy in this decay). Figure D.2 shows the same event after it has been propagated through the detector simulation program. In the cluster containing five of the six γ's from the decay of the η, only three bumps are identified.

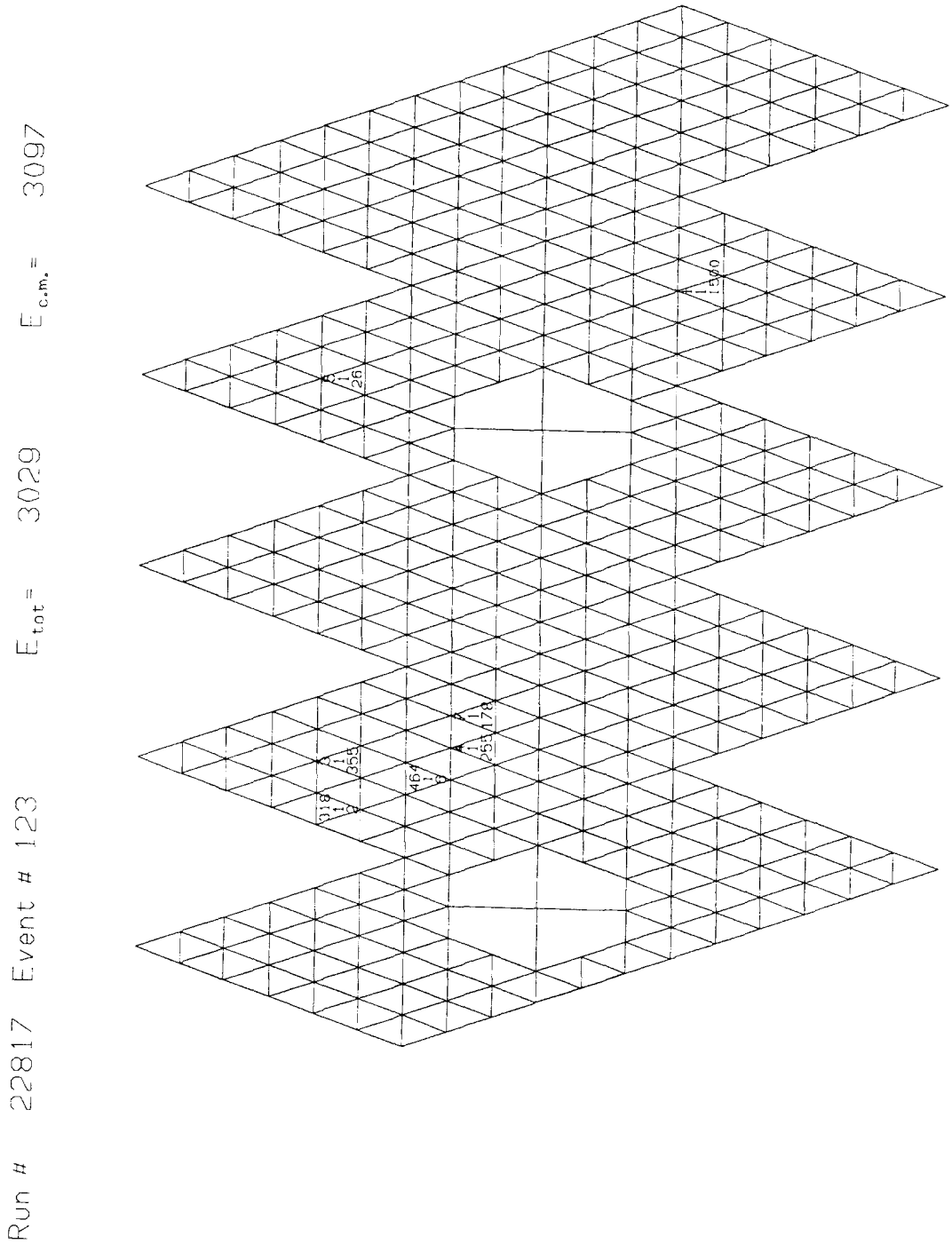

Fig. D.1 Monte Carlo simulation of $J/\psi \rightarrow \gamma\eta$, $\eta \rightarrow \pi^0\pi^0\pi^0$ before showering.

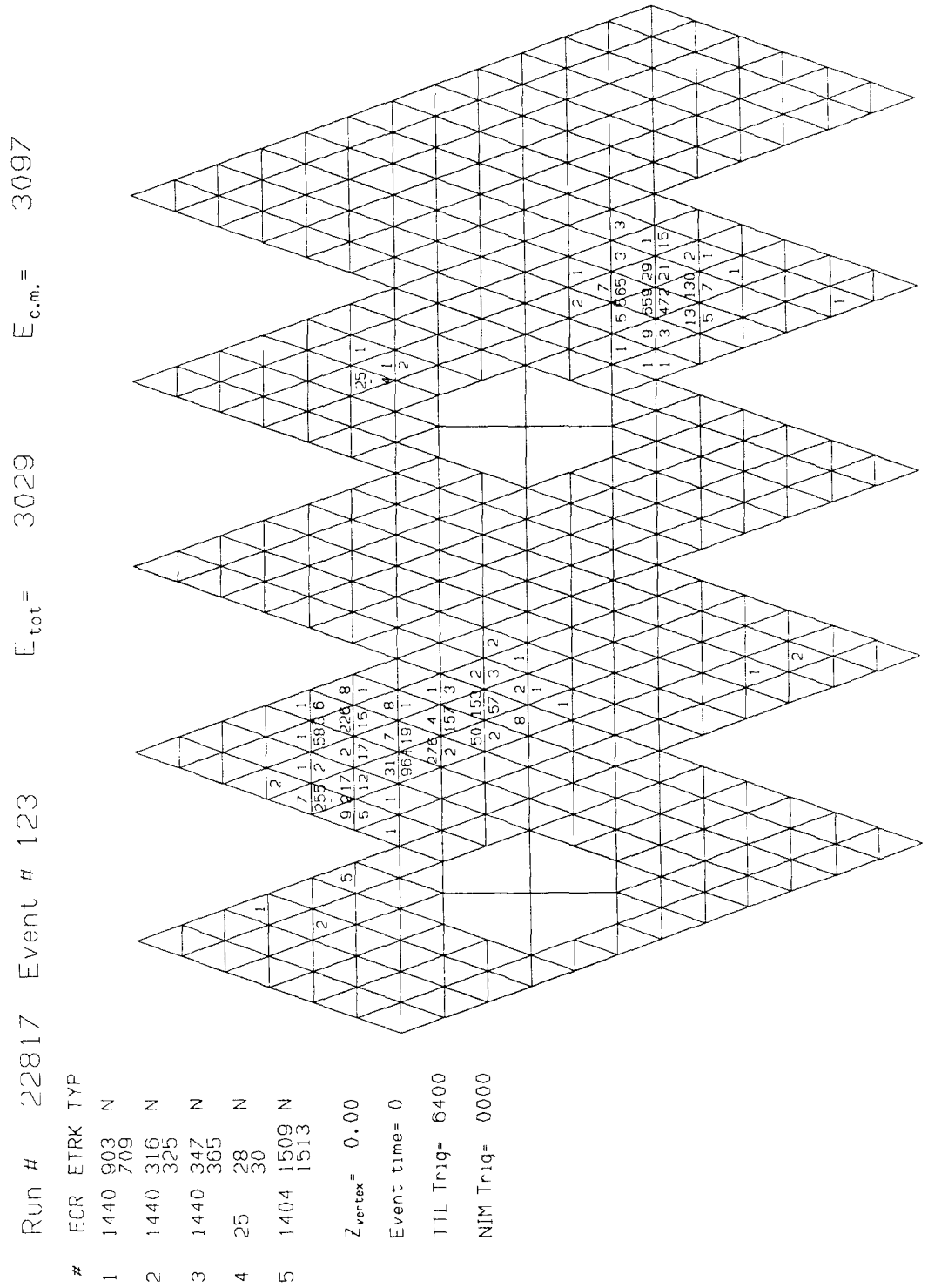

Fig. D.2 Monte Carlo simulation of $J/\psi \rightarrow \gamma\eta$, $\eta \rightarrow \pi^0\pi^0\pi^0$ after showering.

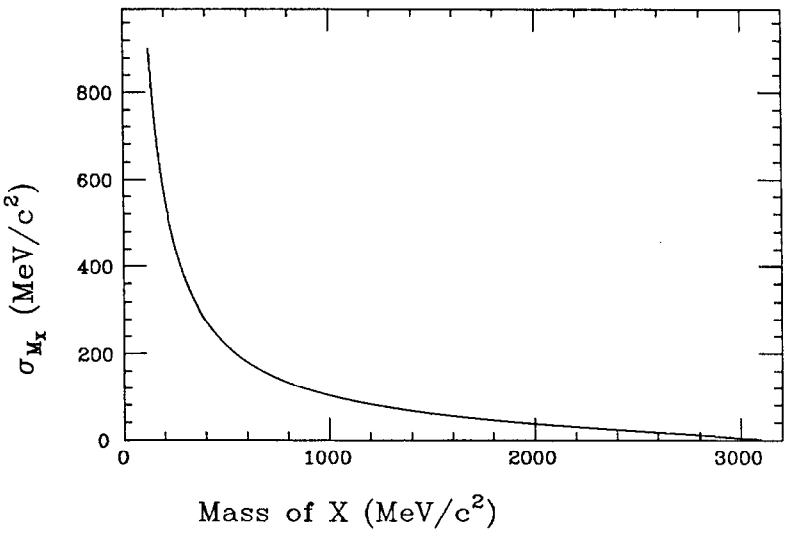

Fig. D.3 Resolution of mass opposite γ in $J/\psi \rightarrow \gamma$X.

These figures illustrate the problems inherent in identifying these events with a purely exclusive analysis. One could consider modifying the bump-finding algorithm to identify more efficiently these overlapping γ showers. However, the problem lies not in the extraction of the information, but the loss of the information itself. As Figs. D.1 and D.2 show, it is impossible to assign the energy in a given crystal to a given shower because the γ tracks lie so closely together. (A crystal may contain energy from as many as four different showers.) One can also consider a maximum likelihood fit of the observed energy distribution to several overlapping shower distributions along the lines of PIFIT. However, the number of parameters that need to be estimated is prohibitive.

Alternatively, one could consider identifying events of this type from the recoil mass opposite the direct photon. Figure D.3 shows a plot of the expected resolution of the mass opposite the direct photon in the decay $J/\psi \rightarrow \gamma$X as a function of the

mass of X assuming the energy resolution of the photon to be given by $\sigma = 0.026E^{3/4}$ (E in GeV). As can be seen from the figure, the resolution is 10 % of the mass value for $M_X = 1$ GeV and rapidly deteriorates as M_X approaches zero.

D.2 Algorithm

We adopt a different approach. We attempt to reconstruct the four-vector of the parent particle (the η in our example) from the crystal energies themselves without determining from which γ shower the deposited energy came (or even how many γ showers there were). Thus, we want to calculate the invariant mass of the 6-γ cluster in our example, or, otherwise stated, the invariant mass of all the deposited energy in the Ball except that associated with the direct photon. The algorithm consists of four steps:

1. redo production,
2. identify the direct photon candidate,
3. calculate the invariant mass of all other energy depositions in the event,
4. place cuts on the event sample to select certain topologies.

We describe each of these steps in detail below.

D.2.1 *Reproduction*

We begin with a dataset that has been selected by the standard production and neutral analysis software as described in Chapter 3 and Section 6.3. However, it is found that connected regions and bumps as defined in the standard production were not appropriate for the current analysis. In the first instance, a connected region as normally defined does not include crystals containing less than 10 MeV so that its energy is underestimated. In the second, the standard bumps discriminator is found to be too coarse. Thus, certain stages of the production are redone as described below.

First, the connected regions are extended by searching the Ball for any crystal which has not previously been assigned to a connected region. If such an unflagged crystal has in its three nearest neighbors a crystal that belongs to a connected region, the unflagged crystal is added to that connected region. If the unflagged crystal has in its three nearest neighbors more than one crystal which belongs to a connected region, the energy of the crystal is divided between the two largest energy connected regions in proportion to their energies. If no such crystal is found in the nearest three neighbors, the same procedure is applied to the next nine nearest neighbors. If none of the twelve neighbors of the crystal belongs to a connected region, the energy of the crystal is added to a residual energy sum which is distributed amongst all the connected regions at the end of the procedure in proportion to their energies. Finally, the "split-off" criterion described in Chapter 3 is used to find spurious connected regions. In contrast to the standard neutral analysis, the energy of the split-off is added to that of the connected region identified as its parent.

Second, the bumps step is redone in order to find "minibumps". A minibump is defined to be a crystal which has more energy than any of its three nearest neighbors. (In other words, a minibump is a local shower maximum.) A preliminary estimate of the energy of the minibump is made by summing the energies of the central crystal and its three neighbors. A minibump is not allowed to have less than 20 MeV with the exception that every connected region must have at least one minibump. ESORT is rerun to determine final energies.

D.2.2 *Identification of Direct Photon*

In order to tag the direct photon candidate, we note that the events we are trying to identify have the approximate topology shown in Fig. D.4. Because of the assumed low mass of the meson opposite the direct photon, the event will be "jet-like" with the shower from the direct photon on one side of the Ball and a cluster of photons in a small cone on the other. Thus, we take as the direct photon candidate that high energy connected region which is well separated from the rest

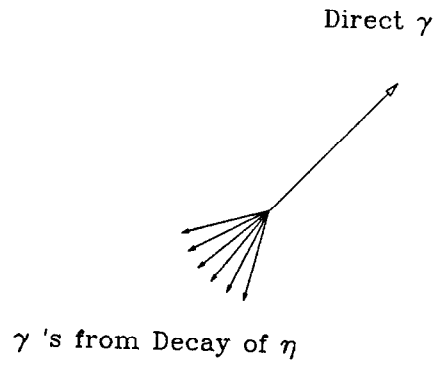

Fig. D.4 Approximate topology of events detected with global showers.

of the connected regions in the event. Specifically, the algorithm used is

1. An energy tensor is formed from the observed energies in the crystals. This tensor is diagonalized, and the eigenvector corresponding to the smallest eigenvalue is defined to be the "jet-axis".

2. Taking the jet axis to define a polar axis, we count the number of minibumps in the two hemispheres so defined. We call the hemisphere with the smaller number of minibumps the photon hemisphere and take as the direct photon candidate that connected region in the photon hemisphere with the largest energy. In the event that both hemispheres have the same number of minibumps, the direct photon candidate is taken to be that connected region which lies closest to the jet axis. It is essential that this algorithm correctly identify the direct photon. Events in which the direct photon identification is ambiguous are rejected.

3. In either case, we require that the direct photon candidate have an energy greater than 500 MeV and that it have more than twice the energy of the

second highest connected region in the photon hemisphere (in order to ensure there are no ambiguities in the identification of the direct photon). If the direct photon candidate does not fulfill these criteria, the event is rejected.

4. Figure D.5a shows the distribution of PIFIT masses of the direct photon candidate for the J/ψ dataset. For comparison, Fig. D.5b shows the same distribution for the $J/\psi \to \gamma\eta$, $\eta \to \pi^0\pi^0\pi^0$ Monte Carlo. We note a significant peak near the π^0 mass in the J/ψ data. This peak is due to those events in which the direct photon has been misidentified and events in which there is no direct photon (see below). In order to select events which are consistent with radiative decays, we require that the direct photon candidate have a PIFIT mass less than 90 MeV/c^2 (shown by the arrows in the plots). If it does not, the event is rejected.

Table D.1 shows the efficiency of this algorithm to identify the direct photon in the decays $J/\psi \to \gamma\eta$, $J/\psi \to \gamma\eta'$, and $J/\psi \to \gamma\mathrm{f}$ as determined from Monte Carlo.

Decay	% Correctly Identified	% Incorrectly Identified	% Rejected
$J/\psi \to \gamma\eta$, $\eta \to \pi^0\pi^0\pi^0$	98	0	2
$J/\psi \to \gamma\eta'$, $\eta' \to \eta\pi^0\pi^0$	95	2	3
$J/\psi \to \gamma\mathrm{f}$, $\mathrm{f} \to \pi^0\pi^0$	61	8	31

Table D.1 Monte Carlo Efficiency for tagging direct photon.

Note that there are decays of the J/ψ which are of the form $J/\psi \to \gamma + n\pi^0 + m\eta$ but which do not contain a monochromatic photon. ($J/\psi \to \omega\mathrm{f}$, $\omega \to \gamma\pi^0$, $\mathrm{f} \to \pi^0\pi^0$ is an example of such a decay.) There is no way to separate these events from the radiative decays in which we are interested; if they contain a high energy photon, they will contaminate the invariant mass plot.

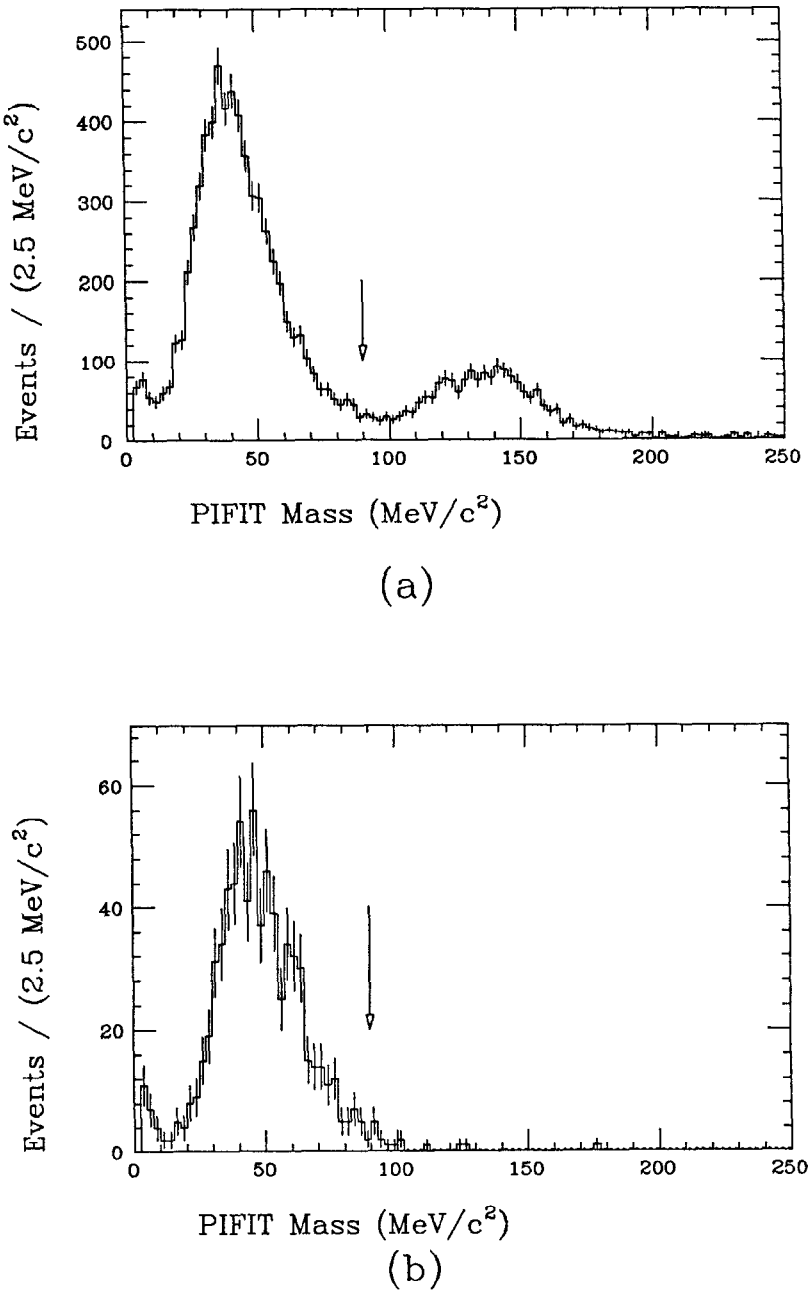

Fig. D.5 PIFIT masses for direct γ candidate. (a) J/ψ data. (b) $J/\psi \to \gamma\eta$ Monte Carlo.

D.2.3 *Invariant Mass Calculation*

Next, the invariant mass of all connected regions (except the direct photon connected region) is calculated. Each connected region is assigned an energy equal to the sum of the energies of the crystals comprising it, a direction corresponding to the weighted sum of these energies, and an invariant mass as determined from SMOMT (see Appendix C). Any connected region with an SMOMT mass below 90 MeV/c^2 is treated as a gamma and assigned an invariant mass of zero. The direct photon candidate is assigned a zero invariant mass regardless of its SMOMT mass. These "gamma" connected regions are assumed to contain only one photon and so are assigned direction cosines from GAMFIT. An energy correction is made for each connected region based on the residual energy sum and a rough PCORR correction. The event is fitted to energy-momentum constraints with increased energy errors for connected regions with nonzero invariant masses. The invariant mass opposite the direct photon (i.e., the global shower invariant mass) is calculated from these fitted quantities.*

D.2.4 *Additional Cuts*

At this point in the algorithm the global shower calculation is complete. However, we may choose to suppress background and/or enhance certain topologies through the use of cuts on quantities describing the entire event.

1. As emphasized previously, we do not attempt in this analysis to determine the four-vectors of the individual photons in an event. However, we can classify the event according to the structure in the showers it contains. For this purpose we utilize the minibumps defined earlier. An event from the decay

---

* Due to inaccuracies in the determinations of the invariant masses of the connected regions and round-off errors, the global shower invariant mass is sometimes negative or just slightly positive ($\leq$ 10 MeV/c^2). Such events are not included in plots of the global shower invariant mass.

$J/\psi \rightarrow \gamma\eta$, $\eta \rightarrow \pi^0\pi^0\pi^0$ is expected to have more minibumps than an event from $e^+e^- \rightarrow (\gamma)\gamma\gamma$ due to the larger number of γ's in the final state. On the other hand, an event from $J/\psi \rightarrow \gamma\eta$, $\eta \rightarrow \pi^0\pi^0\pi^0$ is expected to have fewer minibumps than an event from $J/\psi \rightarrow \gamma\eta'$, $\eta' \rightarrow \eta\pi^0\pi^0$ both due to the (possibly) larger number of γ's in the final state (depending on the decay mode of the η) and due to the larger mass of the η' which allows the gammas to be further separated than in the η decay. Note that due to shower fluctuations and overlaps, the number of minibumps does not correspond to the number of γ's in the final state. (The number of minibumps is typically higher.) However, this quantity can be used as a rough discriminator between different topologies. Figure D.6 shows the distributions of minibumps for $e^+e^- \rightarrow (\gamma)\gamma\gamma$, $J/\psi \rightarrow \gamma\eta$, $J/\psi \rightarrow \gamma\eta'$, and $J/\psi \rightarrow \gamma$f Monte Carlos. Note that due to the preliminary cut (noted in Chapter 3) which requires events to have three or more standard bumps, selected events almost always have at least three minibumps.

2. Analagous to the cut that requires the direct photon candidate to have a PIFIT mass less than 90 MeV/c^2, we can examine the largest PIFIT mass in the remainder of the event. An event from the decay $J/\psi \rightarrow \gamma\eta$, $\eta \rightarrow \pi^0\pi^0\pi^0$ in which several gammas overlap is expected to have at least one connected region in which two γ's from a π^0 overlap. In $e^+e^- \rightarrow (\gamma)\gamma\gamma$, on the other hand, there should be no connected region with a large PIFIT mass (although the SMOMT mass may occasionally be large due to the tail of the SMOMT γ distribution – see Appendix C). Figure D.7 shows the distribution for the largest PIFIT mass for the J/ψ data . Figure D.8 shows the same plot for the $J/\psi \rightarrow \gamma\eta$, $\eta \rightarrow \pi^0\pi^0\pi^0$ and $J/\psi \rightarrow \gamma\eta'$ Monte Carlos. As expected, there is a tendency for the $J/\psi \rightarrow \gamma\eta$ events to have a connected region of high PIFIT mass, and a cut requiring the highest PIFIT mass in the event to be above 90 MeV/c^2 preferentially selects these decays. However, Fig. D.8 also shows that this is not a good discriminator for $J/\psi \rightarrow \gamma\eta'$ decays.

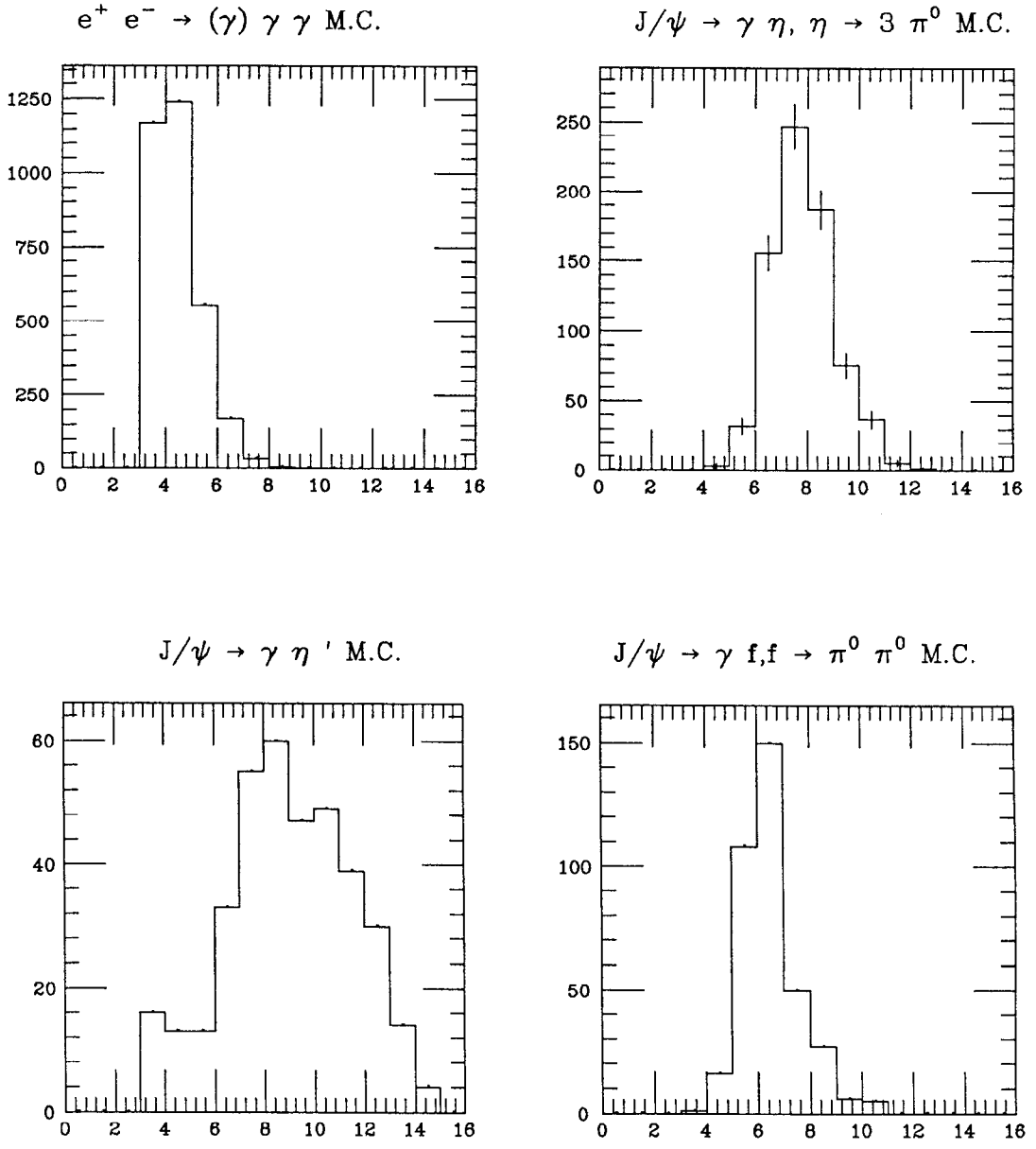

Fig. D.6 Distribution of minibumps from Monte Carlo.

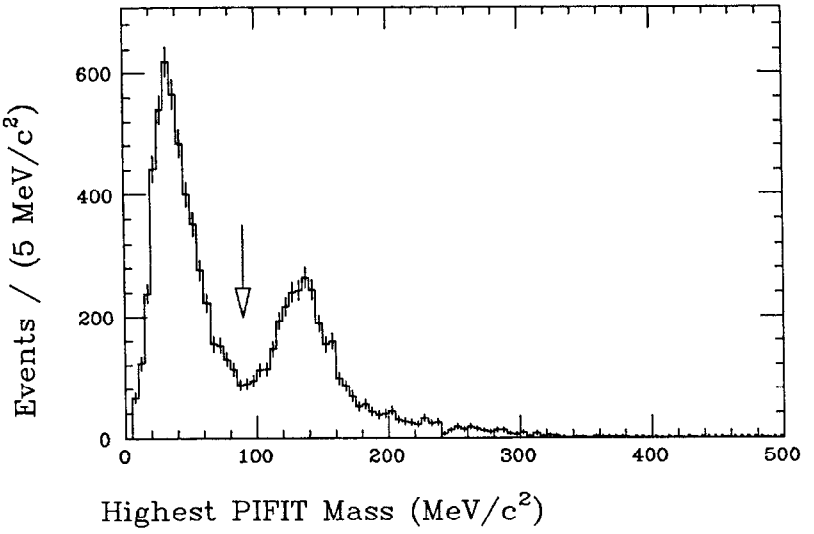

Fig. D.7 Distribution of largest PIFIT masses in event: J/ψ data.

3. Finally, we can examine the invariant masses formed by pairs of minibumps. Again, it should be emphasized that the minibumps provide only an approximate measure of the energies, directions, and number of γ's in the event. It is nevertheless useful to use these approximate measures to search for correlations. Figure D.9a shows the invariant mass distribution of all pairs of minibumps (except those associated with the direct photon connected region) for the J/ψ data. A peak at the π^0 mass is seen along with a small enhancement near the η mass. For purposes of illustration, we eliminate those γ's which contribute to pairs inside a π^0 window ($90 < m_{\gamma\gamma} < 150$) and calculate the invariant masses of all pairs of the remaining γ's, yielding Fig. D.9b. A clear η peak is now seen. We say that an event has an open η if it contains a pair of γ's with an invariant mass which falls into the η window shown by the arrows ($450 < m_{\gamma\gamma} < 600$). (*All* γ pairs are considered when making this cut;

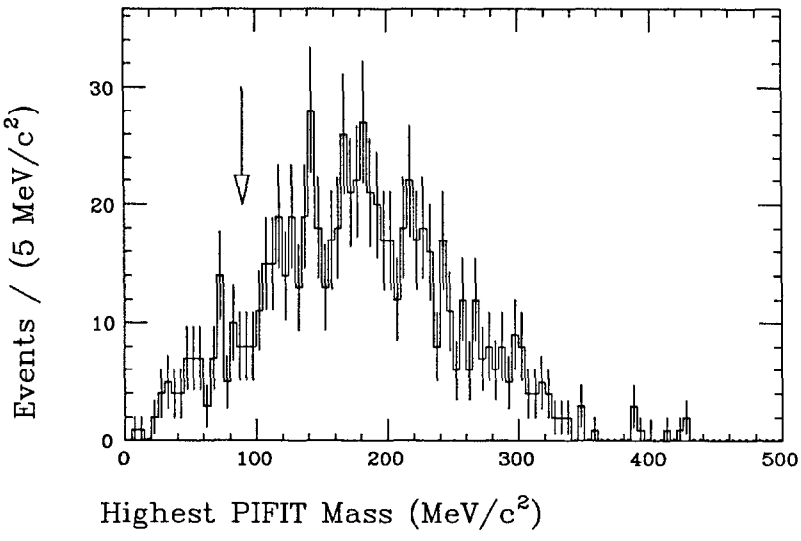

(a)

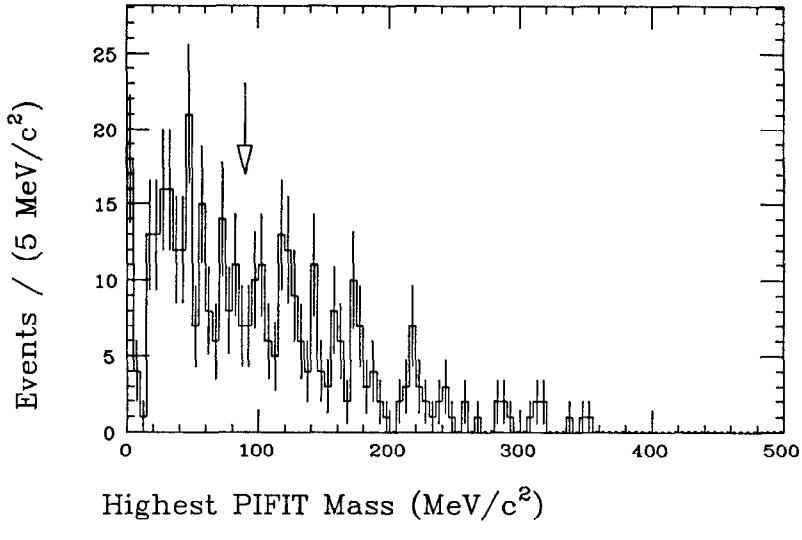

(b)

Fig. D.8 Distribution of largest PIFIT masses in event: Monte Carlo. (a) $J/\psi \to \gamma\eta$, $\eta \to \pi^0\pi^0\pi^0$. (b) $J/\psi \to \gamma\eta'$.

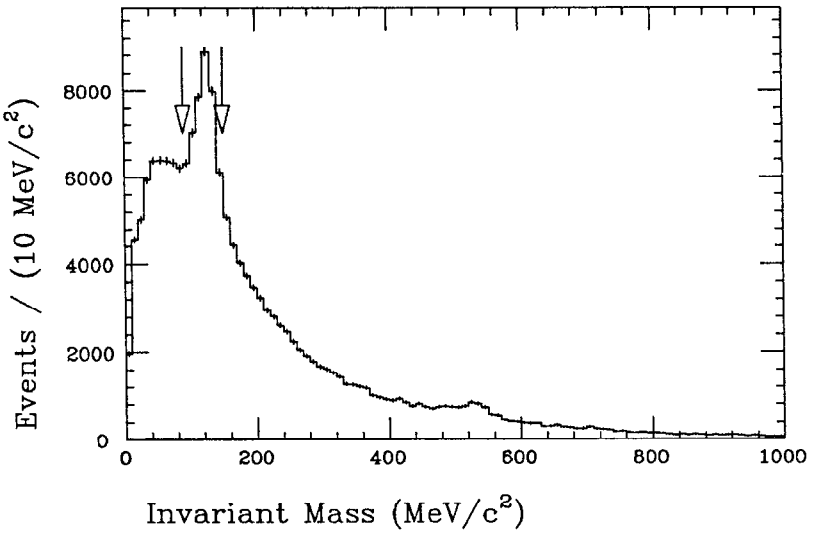

(a)

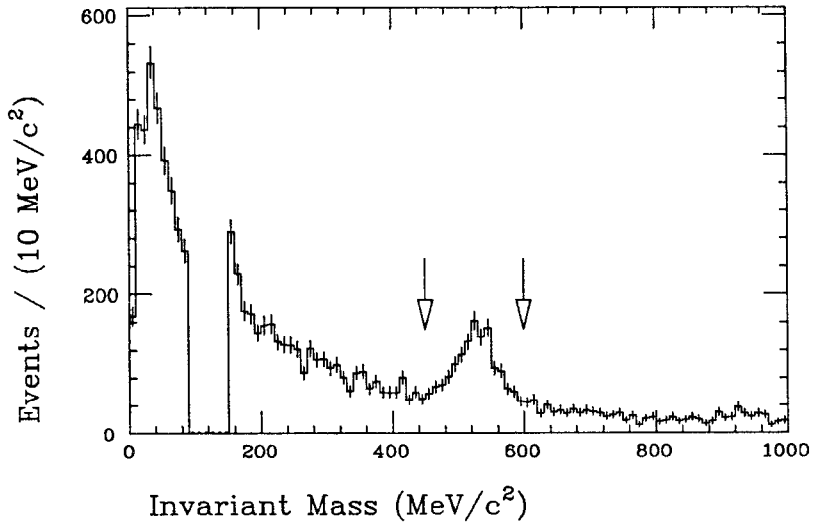

(b)

Fig. D.9 Distribution of invariant masses of all pairs of minibumps: J/ψ data. (a) Before π^0Cut. (b) After π^0Cut

the γ's forming π^0's were removed only to illustrate the boundaries of the η window.) This cut is useful when using the global shower technique to search for the decay $J/\psi \rightarrow \gamma\eta'$, $\eta' \rightarrow \eta\pi^0\pi^0$, $\eta \rightarrow \gamma\gamma$.

We can use combinations of these cuts to select certain topologies. Table D.2 shows the cuts that have been determined to enhance the decays listed. Although the notation refers to J/ψ decays, these cuts are also used for ψ' decays.

Decay	Number of Minibumps	Largest PIFIT Mass > 90.	Open η
$J/\psi \rightarrow \gamma\eta$, $\eta \rightarrow 3\pi^0$	$6 \leq$ NBMP ≤ 10	X	
$J/\psi \rightarrow \gamma\eta'$, $\eta' \rightarrow \eta\pi^0\pi^0$ $\eta \rightarrow 3\ \pi^0$ or $\gamma\gamma$	$6 \leq$ NBMP ≤ 13		
$J/\psi \rightarrow \gamma\eta'$, $\eta' \rightarrow \eta\pi^0\pi^0$ $\eta \rightarrow \gamma\gamma$	$6 \leq$ NBMP ≤ 10		X
$J/\psi \rightarrow \gamma$ f, f $\rightarrow \pi^0\pi^0$	$5 \leq$ NBMP ≤ 6	X	

Table D.2 Additional cuts for specific decays.

D.3 Examples

D.3.1 *Monte Carlo*

In order to study the largest neutral background at the ψ', we generate a Monte Carlo dataset of the Q.E.D. process $e^+e^- \rightarrow (\gamma)\gamma\gamma$ with the number of events selected to be equivalent to the luminosity accumulated in the ψ' sample. Figure D.10 shows the global shower mass for these events before any supplemental cuts; Figs. D.11 and D.12 show the same spectrum after the application of the cuts listed in Table D.2. It is evident that the Q.E.D. background is greatly suppressed by these cuts. Also note that although the combination of the cuts and the falling background does produce some structure in these spectra, the enhancements are small and are not near the regions of interest of the individual plots.

In order to model a typical signal, we generate a Monte Carlo dataset of decays of the form $\psi' \rightarrow \gamma$ X, X $\rightarrow \pi^0\pi^0\pi^0$ where M_X = 500, 900, 1300, 1700, 2100, 2500, 2900, and 3300 MeV/c^2. (100 events are generated for each value of M_X .) The first plot in Figure D.13 shows the invariant mass spectrum after application of the η cuts from Table D.2. Note that the efficiency of detection drops rapidly above $M_X \approx 2000$ MeV/c^2. This is due to the fact that at higher values of M_X the event becomes more isotropic, making the identification of the direct photon more difficult. Also note that there is a slight degradation of resolution for large values of M_X . The lower plot in Fig. D.13 shows the resolution of the global shower invariant mass as a function of M_X (compare Fig. D.3).

D.3.2 *Data*

Figure D.14 shows the global shower invariant mass distribution on the J/ψ after application of the η' cuts.† We see there is a broad accumulation of events above 1000 MeV/c^2. This is due to events in which there is no direct photon

† This plot is the same as Fig. 6.15 and is discussed in more detail in Chapter 6.

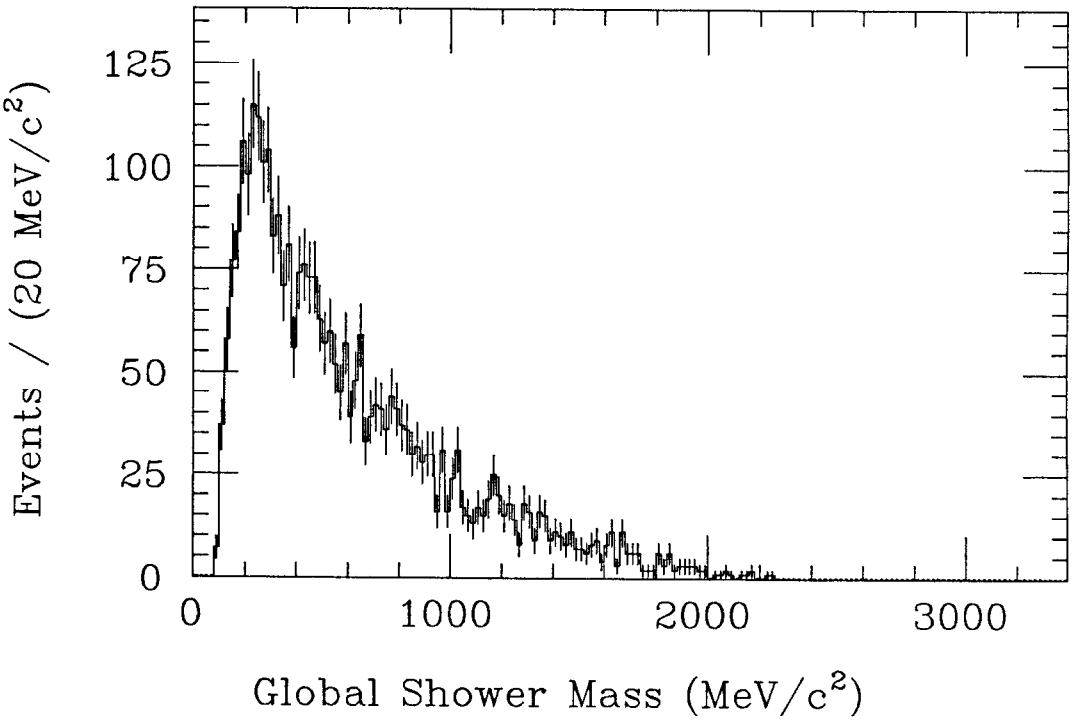

Fig. D.10 Global shower invariant mass distribution for $e^+e^- \rightarrow (\gamma)\gamma\gamma$ Monte Carlo.

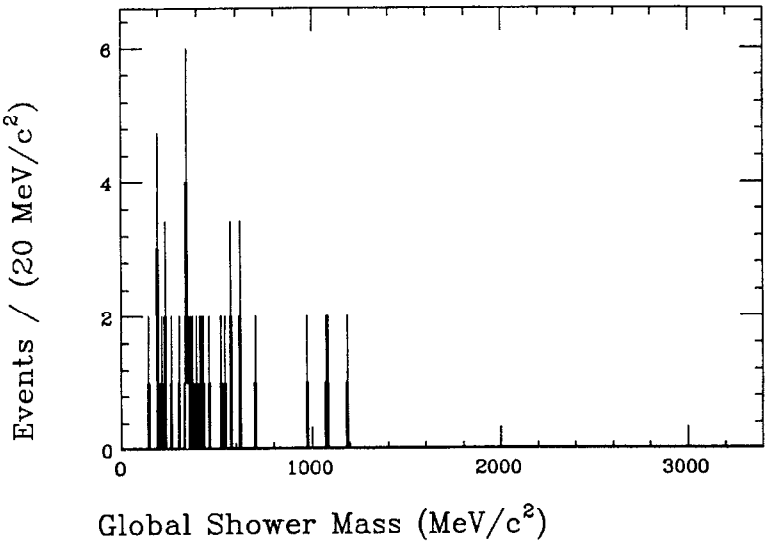

(a)

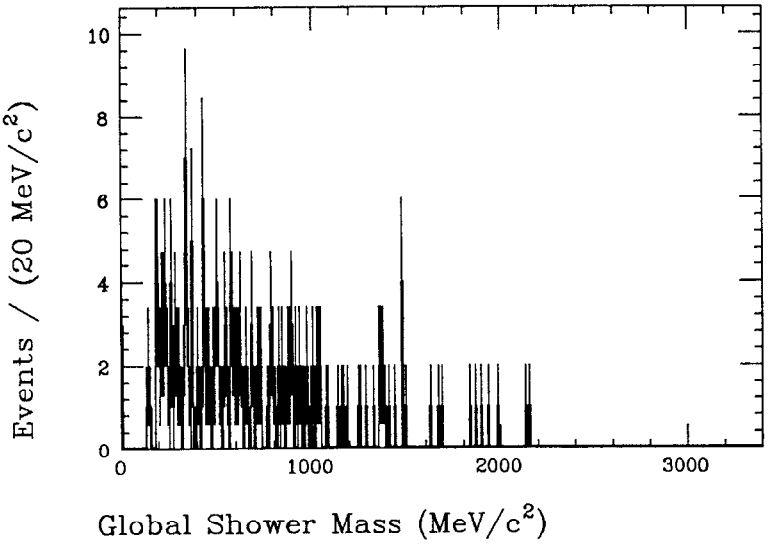

(b)

Fig. D.11 Global shower invariant mass distributions for $e^+e^- \rightarrow (\gamma)\gamma\gamma$ Monte Carlo. (a) η Cuts. (b) η' Cuts.

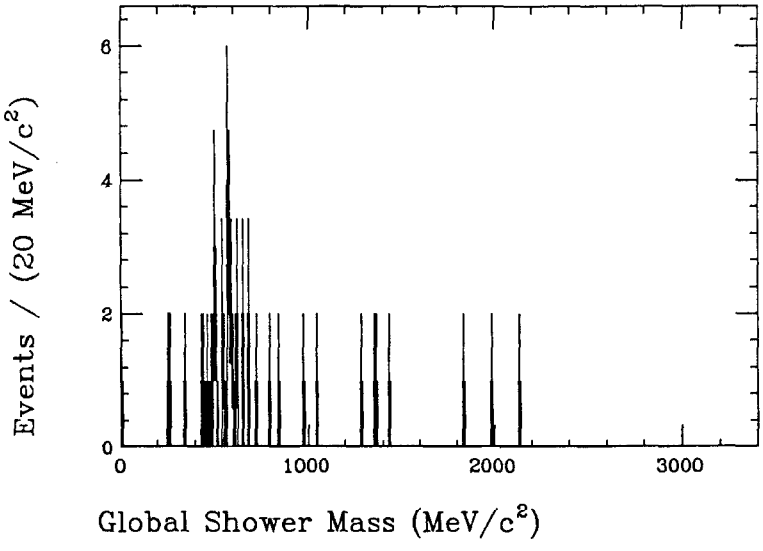

(a)

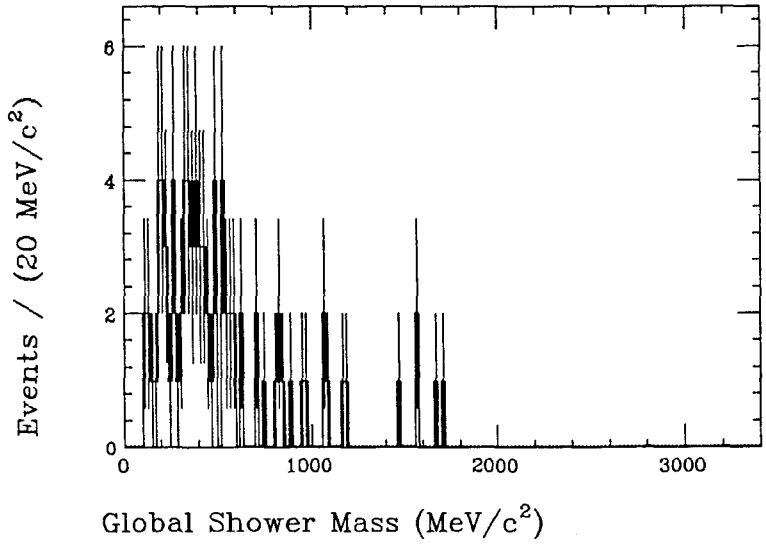

(b)

Fig. D.12 Global shower invariant mass distributions for $e^+e^- \rightarrow (\gamma)\gamma\gamma$ Monte Carlo. (a) η' Cuts, open η. (b) f Cuts.

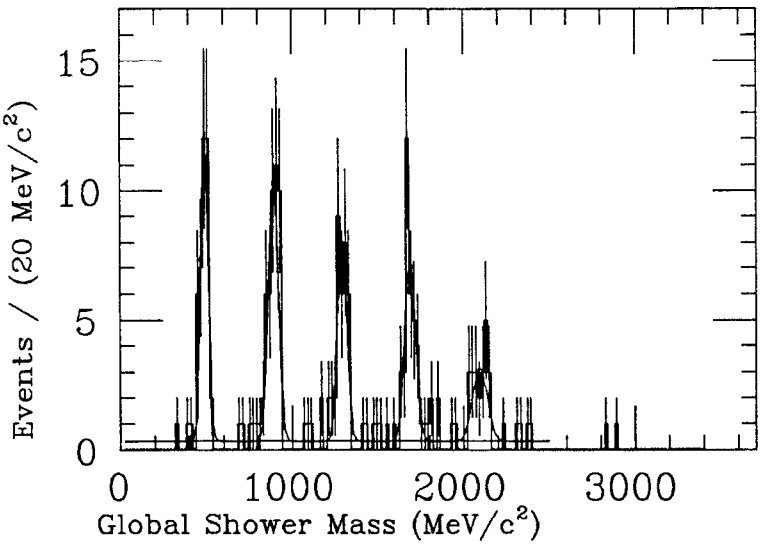

(a)

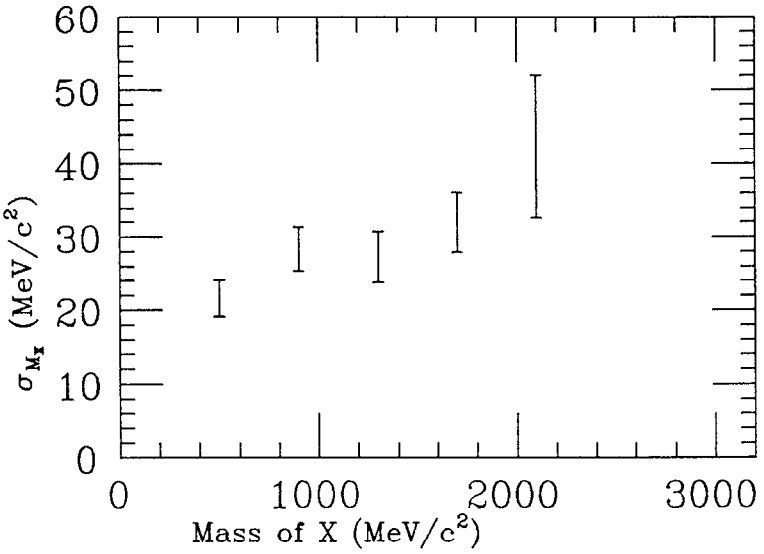

(b)

Fig. D.13 (a) Invariant mass plot for $J/\psi \rightarrow \gamma$X Monte Carlo. (b) Resolution of global shower method from $J/\psi \rightarrow \gamma$X Monte Carlo.

from the J/ψ (as in the decay $J/\psi \rightarrow \gamma\omega\pi^0\pi^0, \omega \rightarrow \gamma\pi^0$) or where the direct photon has been misidentified. Even though the cuts have been designed to select $J/\psi \rightarrow \gamma\eta'$, $\eta' \rightarrow \eta\pi^0\pi^0$ decays, we also see that there is substantial leakage from $J/\psi \rightarrow \gamma\eta$, $\eta \rightarrow \pi^0\pi^0\pi^0$. (Events from the decay $J/\psi \rightarrow \gamma\eta$, $\eta \rightarrow \gamma\gamma$ have been eliminated by the η' minibump cut. See Table D.2.) This illustrates one of the limitations of the global shower technique. Even though the efficiency of the global shower technique to detect certain topologies is high, one cannot reliably distinguish between final states containing different particles. This can be remedied to some extent in the present case by the imposition of the "open η" cut which requires that two minibumps have an invariant mass consistent with an η. (Fig. D.15.) We see that the η peak is substantially reduced. However, the detection efficiency for the η' drops by roughly 50%, and we have opted not to use this cut in the analysis presented in Chapter 6.

Although the efficiency for detecting the decay $J/\psi \rightarrow \gamma\,\mathrm{f}$ with the global shower technique is not particularly large (see Table D.1), this decay is useful for illustrating this method since it has been studied with an exclusive analysis elsewhere in this work (see Chapter 5). Figure D.16 shows the invariant mass spectrum for the J/ψ dataset after application of the cuts to select $J/\psi \rightarrow \gamma\,\mathrm{f}$, $\mathrm{f} \rightarrow \pi^0\pi^0$. We note that these cuts also pass a small fraction of the $J/\psi \rightarrow \gamma\eta$ and (perhaps) $J/\psi \rightarrow \gamma\eta'$ decays. We fit the structure around 1300 MeV/c^2 to a Breit-Wigner line shape plus a constant background in the range from 700 to 1900 MeV. We note several features of the fit. First, the fitted energy of the peak (1250 $\pm$10 MeV/c^2) is low compared with the Particle Data Group value of 1274 $\pm$5 MeV/c^2. This is typical of all measurements made with this technique, since the energies of overlapping showers cannot be as precisely determined as those of photons which are well-separated from the remainder of the event. (In particular, the position correction discussed in Chapter 3 cannot be precisely determined for overlapping showers.) Second, it is difficult to make an accurate determination of the width of the peak since the detection efficiency is not constant over such a large resonance. Finally,

a Monte Carlo of this decay yields an efficiency of 5.3% (including the branching ratio of the f to $\pi^0\pi^0$). Combining this with the 205 ± 18 events in the peak yields a branching ratio of $1.8 \pm 0.1 \times 10^{-3}$ (statistical errors only) consistent with the value obtained from an exclusive analysis in Chapter 5 ($1.7 \pm 0.1 \pm 0.5 \times 10^{-3}$). This is of course not an independent measurement, but a consistency check of the global shower technique.

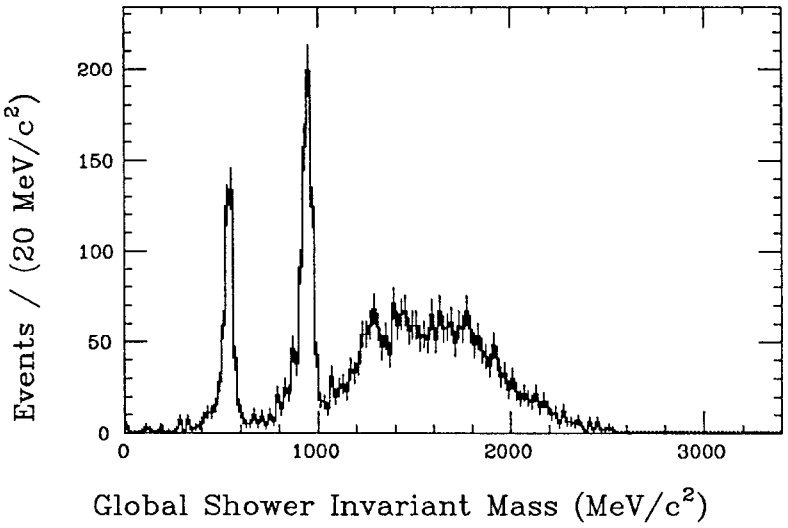

Fig. D.14 Global shower invariant mass on J/ψ: η' cuts.

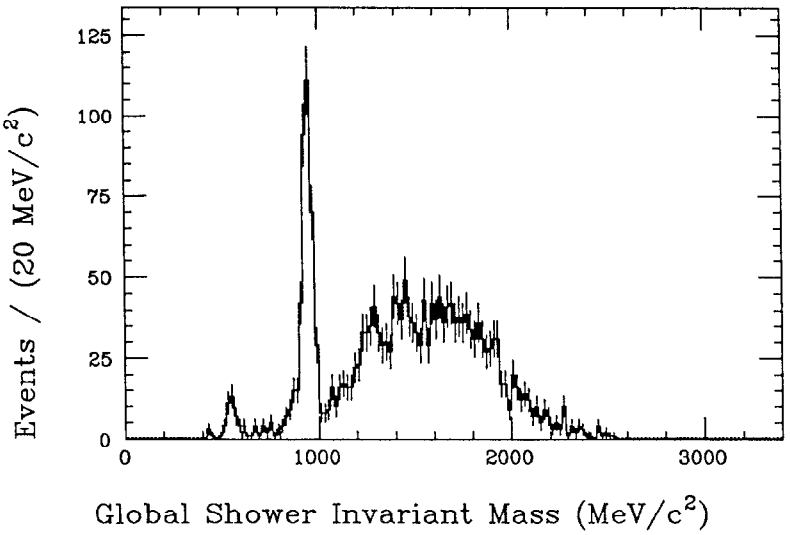

Fig. D.15 Global shower invariant mass on J/ψ: η' cuts with open η requirement.

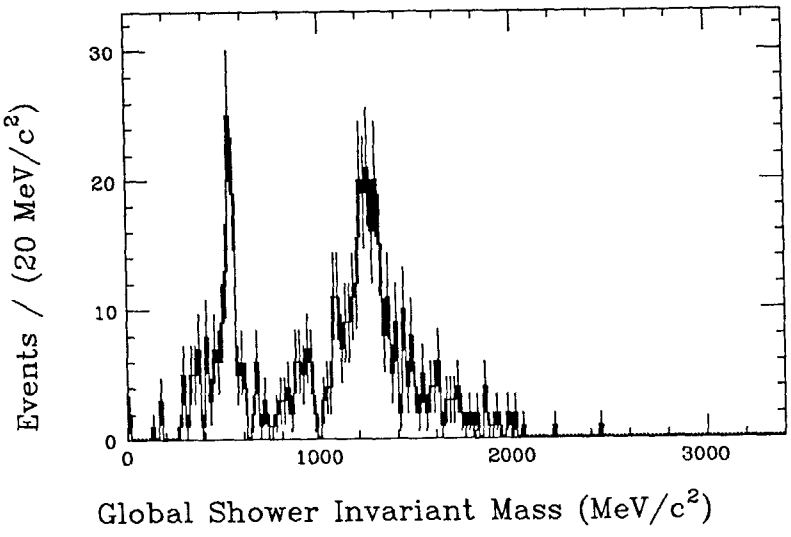

Fig. D.16 Global shower invariant mass on J/ψ: f cuts.

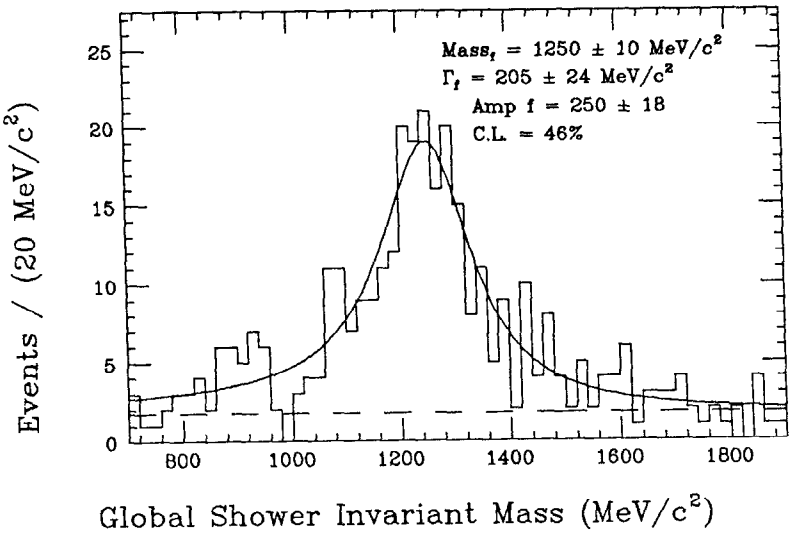

Fig. D.17 Global shower invariant mass on J/ψ: f cuts fitted to Breit-Wigner plus constant background.

Appendix E

NaI(Tl) Calibration

E.1 Introduction

In order to take full advantage of the resolution of NaI(Tl), it was necessary to calibrate the crystals frequently. Studies with a Crystal Ball prototype in a variety of test beams indicated that the response of the crystal-phototube combination was linear (see Fig. E.1).[1] If we take the response of both the low and high channels to be linear, we must determine a total of four constants. We choose these parameters to be

1. $P_{low\ channel}$: low channel pedestal,
2. $P_{high\ channel}$: high channel pedestal,
3. *Slope*: low channel slope,
4. *Ratio*: ratio of high channel to low channel (pedestal subtracted).

Calibration was a three-step process using both low energy calibration sources and Bhabha events from the raw data tapes. We describe the steps below.

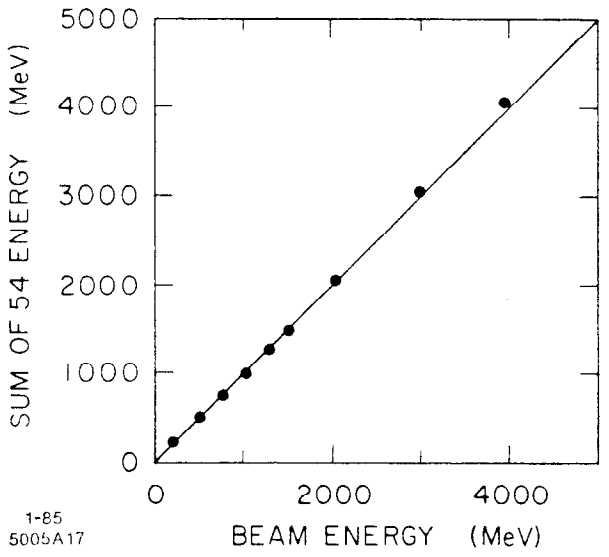

Fig. E.1 Test beam results from a Crystal Ball prototype.

E.2 Online Calibration

E.2.1 Cs^{137} *calibration*

Online calibration was performed approximately once every two weeks. First, pedestals for the low and high energy channels were determined by taking triggers generated by a pulser. Next, a 0.1 millicurie Cs^{137} source was placed at the center of each hemisphere. The transition

$$\begin{aligned} {}^{137}\mathrm{Cs} &\rightarrow \beta^- + {}^{137}\mathrm{Ba}^* \\ &\qquad \Big\downarrow \\ &\qquad\quad {}^{137}\mathrm{Ba} + \gamma(0.66\mathrm{MeV}) \end{aligned} \qquad [E.1]$$

yields a photon line of well-known energy. Calibration amplifiers were inserted into the integrate and hold circuits so that the experiment could trigger on these small

pulses; the pulse presented to the integration circuit was unaffected. As noted in Chapter 2, the smallest section of the Ball which could be used to generate a trigger was a set of nine contiguous crystals. Thus, a trigger was generated whenever the sum of the energies in a group of nine crystals passed a discriminator threshold ($\approx (1/2)E_\gamma$). Approximately 10,000 counts were taken for each group of nine. A histogram of the Cs^{137} spectrum was made for each crystal and fitted to a Gaussian plus a polynomial background. A sample spectrum is shown in Fig. E.2. Often, a photon Compton scattered off an electron in one crystal and deposited the remainder of its energy in a neighboring crystal. If the two crystals were in the same group of nine, a trigger was generated even though each crystal contained only a fraction of the photon's energy. Such events account for most of the background seen in Fig. E.2.

These pedestals and slopes made up the set of online constants. They were stored in a disk file on the online computer and were used to calculate energies for online displays and to determine the online data compression cut in terms of raw ADC counts. Also, the Cs^{137} spectra were permanently stored on disk in order to provide a performance monitor of the crystals.

E.2.2 *Van de Graaff Calibration*

The next step in the calibration was similar to the Cs^{137} calibration except that a higher energy photon than could be obtained with sources was used. A small Van de Graaff generator[2] was used to bombard a fluorine target with approximately 450 keV protons. This produced a monochromatic photon via the reaction

$$\begin{array}{l} {}^{19}\mathrm{F} + \mathrm{p} \rightarrow {}^{20}\mathrm{Ne}^* \rightarrow {}^{16}\mathrm{O}^* + \alpha \\ \qquad\qquad\qquad\qquad \big\lfloor\!\!\longrightarrow \quad {}^{16}\mathrm{O} + \gamma(6.131\mathrm{MeV}) \end{array} \qquad [E.2]$$

A photon of this energy typically produced a larger shower than could be contained in a single crystal. This complicated the analysis of the Van de Graaff data in that the determination of the calibration constant for a given crystal depended on the

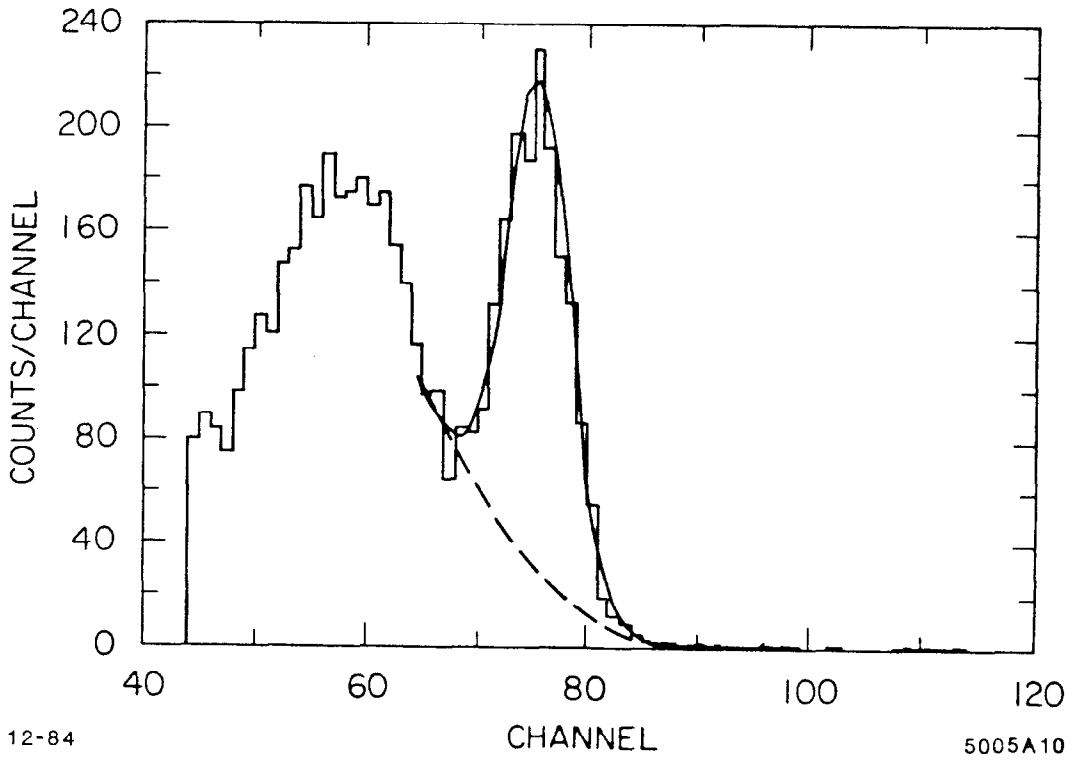

Fig. E.2 Typical Cs^{137} spectrum.

calibration constants of its neighbors. Thus, the following iterative procedure was used:

1. Each crystal was initially assigned the slope obtained from the Cs^{137} calibration.

2. For a given crystal i, the energies in i and the three crystals in the twelve neighbors of i with the largest energies were summed to obtain the measured energy. The slope assigned to crystal i was adjusted to make the peak of the energy distribution for crystal i agree with the known energy of the photon in reaction [E.2]. This process was repeated for every crystal in the Ball, i.e., i was varied from 1 to 720.

3. Step 2 was repeated three times at which point the procedure had converged for virtually all crystals.

The slopes so obtained were called the Van de Graaff slopes.

E.3 Offline Calibration

The final calibration constants used in the production of the data were obtained offline from the raw data tapes. $P_{low\ channel}$ and $P_{high\ channel}$ were obtained by averaging the pedestal peaks for each crystal in uncompressed events. (As noted in Chapter 2, the ADC counts for all crystals were written out one in every 128 events.) The *Ratio* constants were determined by performing a straight line fit to a plot of (low channel ADC counts minus low pedestal) *vs.* (high channel ADC counts minus high pedestal) for those events in which the energy in a given crystal fell into the range measured by both the low and high channels. The y-intercept of this line was constrained to be zero, and its slope was taken to be the ratio between the high and low channels.

The *Slope* constants were obtained from Bhabha events.* Using pedestals and

* The selection procedure does not use information from the inner detector, so the "Bhabha"

ratios obtained as described above and Van de Graaff slopes, a preliminary analysis was made of the raw data tapes to select events which contained two back-to-back connected regions each of which contained roughly the beam energy. In addition, in each of the connected regions it was required that 70% of the energy be in the central crystal. These events comprised the Bhabha sample which was analyzed by an iterative procedure similar to the one used to analyze the Van de Graaff data. Here, the initial slopes were taken to be the Van de Graaff slopes, and the measured energies were calculated from the sum of 13 algorithm described in Chapter 2. The measured energies on each side of the Bhabha events were constrained to be the beam energy, and five passes through the data were made.†

E.4 Resolution and Offset

Figure E.3 shows the measured energy distribution for a sample of Bhabha events using Van de Graaff and Bhabha slopes. The decrease in width of the distribution is clearly seen, and the final FWHM using the Bhabha constants is 4.7%. This is substantially larger than the $\approx$ 2.7% FWHM resolution obtained with a Crystal Ball prototype in high-energy test beams. The resolutions obtained from the studies described in Appendix A are also larger than those obtained with intermediate energy test beams (see Fig. E.4). Part of this discrepancy can be attributed to the fact that the test beam was directed at the centers of the crystal in the prototype tests, whereas the cuts used to obtain the Bhabha events could only approximately impose this condition. Also, the crystals in the prototype array were calibrated daily with the test beam as compared to the Bhabha samples which

sample actually includes both $e^+e^- \rightarrow e^+e^-$ and $e^+e^- \rightarrow \gamma\gamma$ events. Note that because QED distributions peak in the beam direction, the tunnel crystals are calibrated with far more events than the crystals in the "polar" regions of the Ball.

† The total energy of the event was not constrained to be the center-of-mass energy, so there was no correlation of the calibration constants for crystals in one part of the Ball with those on the opposite side.

were accumulated over periods of roughly two weeks.

Another discrepancy is the energy offset described in Appendix A. As outlined above, the final calibration constants were obtained from Bhabha events, so electrons and positrons at the beam energy were constrained to have the correct energy. However, the measured energies of low-energy photons in several well-constrained channels are slightly lower than the calculated energies. One possible explanation is that the measured energy of a shower is dependent on the position of the shower within the crystals since high energy showers penetrate deeper into the NaI(Tl). Figure E.5 shows the compensation curve of a typical crystal as measured by a Cs^{137} source placed at various positions along the crystal axis; Fig. E.6 shows the same curve averaged over all main Ball crystals excluding equator and tunnel curves. The arrows indicate the approximate positions of maxima of showers of 260 and 1842 MeV, respectively, corresponding to the energy of the photon in $\psi' \rightarrow \gamma\chi_0$ and the energy of a Bhabha electron at the ψ' energy. It is seen that the average response of a crystal at a depth corresponding to the low energy shower is indeed slightly lower than the response at the depth of a Bhabha shower.

However, in order to correctly account for the effect of compensation on the energy response, we should examine the distribution of the shower in the crystal rather than simply the shower maximum. Figure E.7 shows the longitudinal energy distributions of a γ shower of 260 MeV and an electron shower of 1842 MeV, respectively, in a slab of NaI(Tl) 16 radiation lengths thick and infinite in the transverse dimensions as calculated by the Electron Gamma Shower code (EGS). We see that the two showers sample roughly the same regions of the NaI(Tl) slab, although the "Bhabha" shower is centered somewhat deeper. To study what effect this has on the measured energy, we run two sets of 500 EGS showers simulating particles incident on a slab of NaI(Tl) as described above for an incident γ of energy 260 MeV. In the first we simply use the deposited energy as returned by EGS. In the second we modify the energy deposited at a given depth by a factor proportional to the compensation at that depth. Two similar sets of showers are run for an

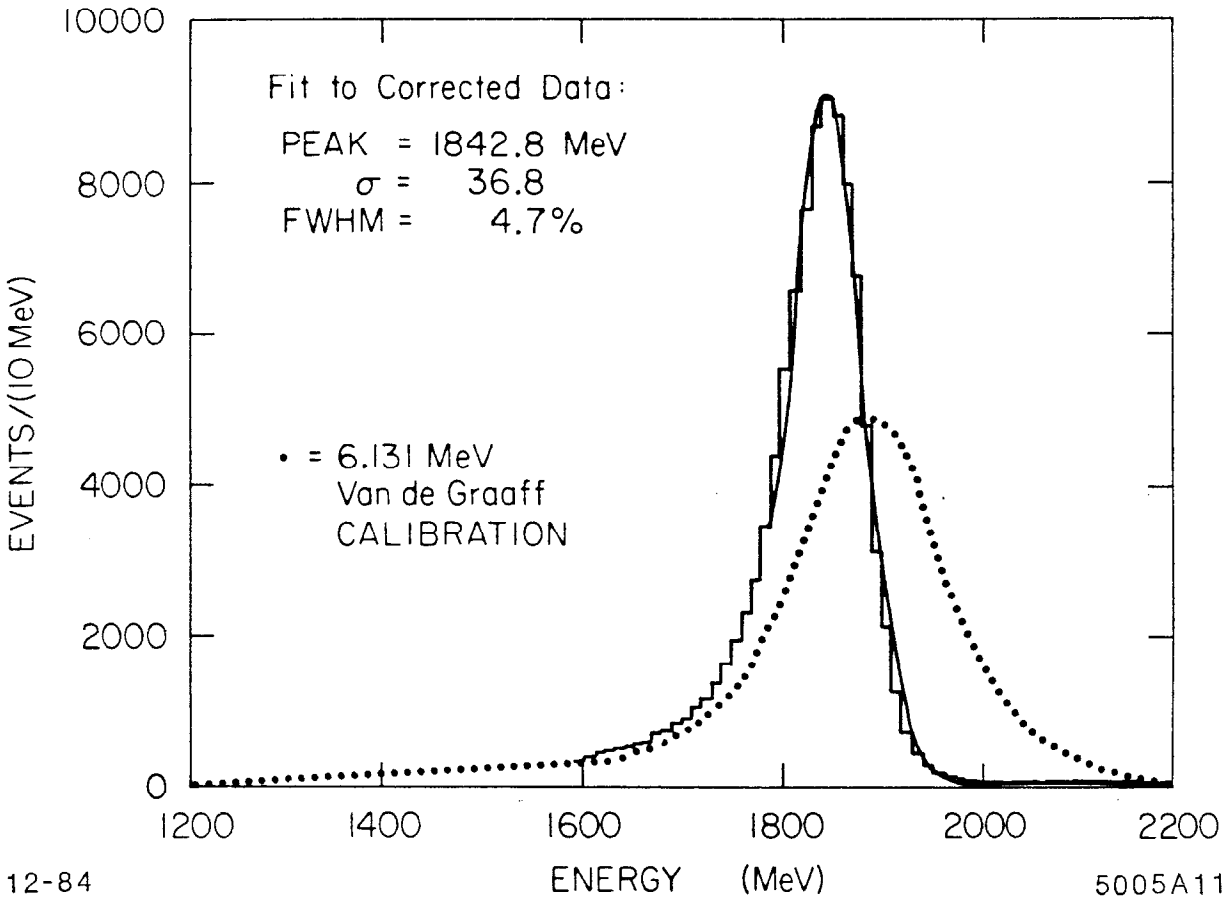

Fig. E.3 Sample Bhabha peak. Histogram shows data with Bhabha corrections; solid line shows best fit to line shape function. Dotted line shows fit to data without Bhabha correction.

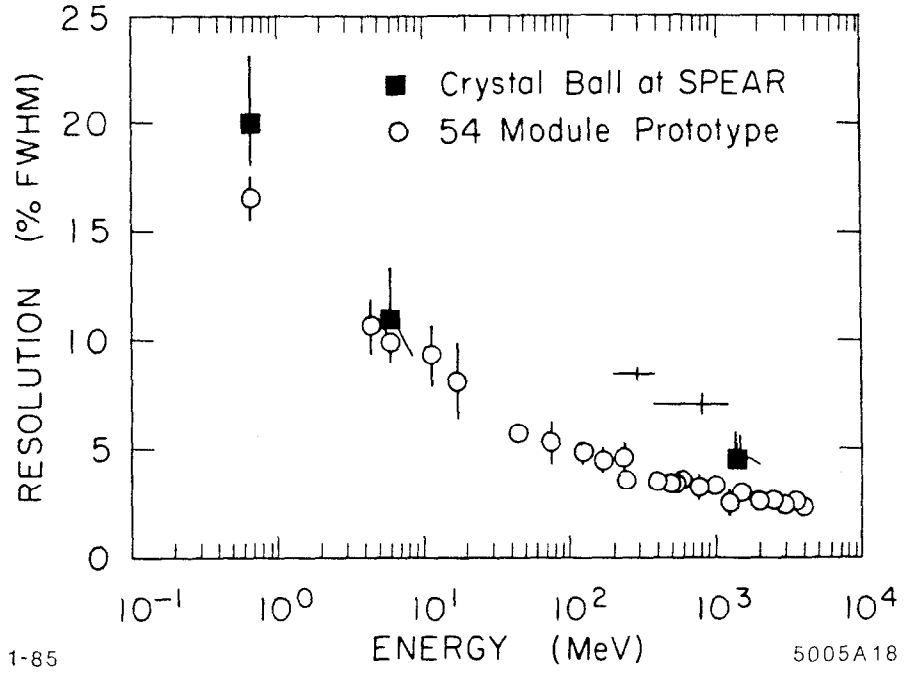

Fig. E.4 Crystal Ball resolution. Circles show test beam results from Crystal Ball prototype; boxes show resolutions from calibrations (Cs^{137} , Van de Graaff, and Bhabha); points with error bars show resolutions measured in this study. (Two high energy points overlap with Bhabha calibration.)

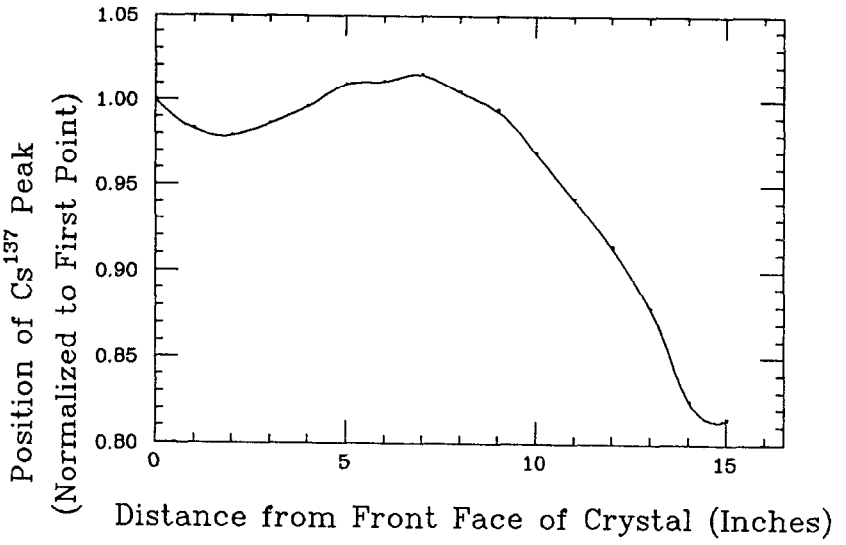

Fig. E.5 Typical compensation curve.

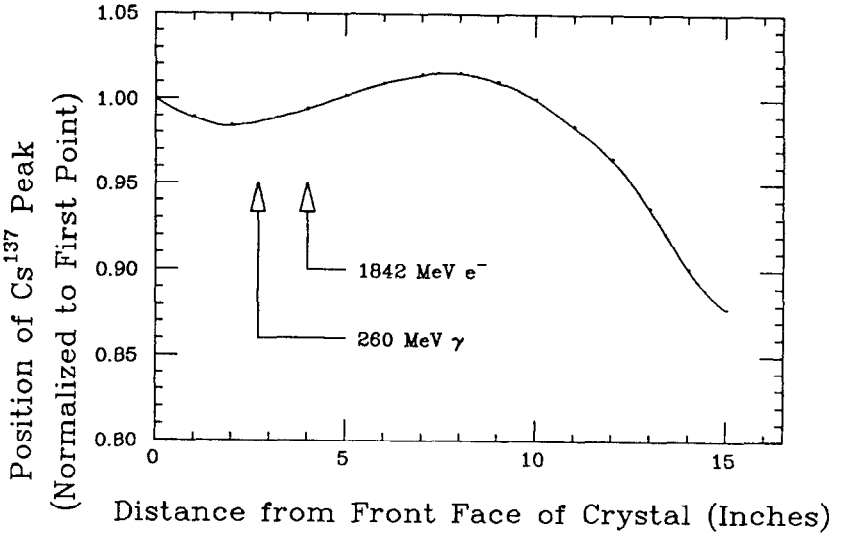

Fig. E.6 Average of compensation curves of all Crystal Ball crystals (excluding endcap, tunnel, and equator crystals). (Arrows show approximate positions of shower maxima of 260 MeV γ and 1842 MeV e^-.)

incident electron of energy 1842 MeV. In this simple simulation, several effects (lateral shower leakage, inert material in front of and between crystals, gaps between sections of the Ball) which are taken into account by the Crystal Ball Monte Carlo described in Appendix B are ignored. These effects all decrease the energy of the shower deposited in the NaI(Tl), so the means of the distributions in this study will be higher than those in Appendix B. Similarly, the resolutions in this study are smaller than those in the full Crystal Ball Monte Carlo. (For low energy photons, the observed width of the distribution is almost zero, since the full energy of these photons is deposited in a 16 radiation length slab.)

The results of these simulations are shown in Figs. E.8 and E.9 in which the spectra are fit to the line shape function described in Appendix A. It can be seen that the peak energies in the distributions based on the compensation-corrected EGS simulation (Fig. E.9) are lower than in the unmodified simulation (Fig. E.8). However, in order to properly simulate the effect of calibration, we must in each case multiply the observed energies by a correction factor which makes the central values of the Bhabha distributions coincide with the dialed Bhabha energy (as in Appendix B). The "calibrated" mean of the compensation corrected 261 MeV γ spectrum is slightly lower than the uncompensated spectrum (0.9 MeV), but not sufficiently lower to explain the $\approx$ 3 MeV shift seen in the data (see Appendix A).

In summary, the compensation correction is unable to account for the observed (negative) offset seen in the data, although it may be one component of the observed resolution. When a high-precision measurement of a photon energy is made (such as the energy of the transition photon in $\psi' \rightarrow \gamma\chi_0$), we simply apply an empirical energy correction derived from an independent channel (i,e., $\psi' \rightarrow \eta J/\psi$).

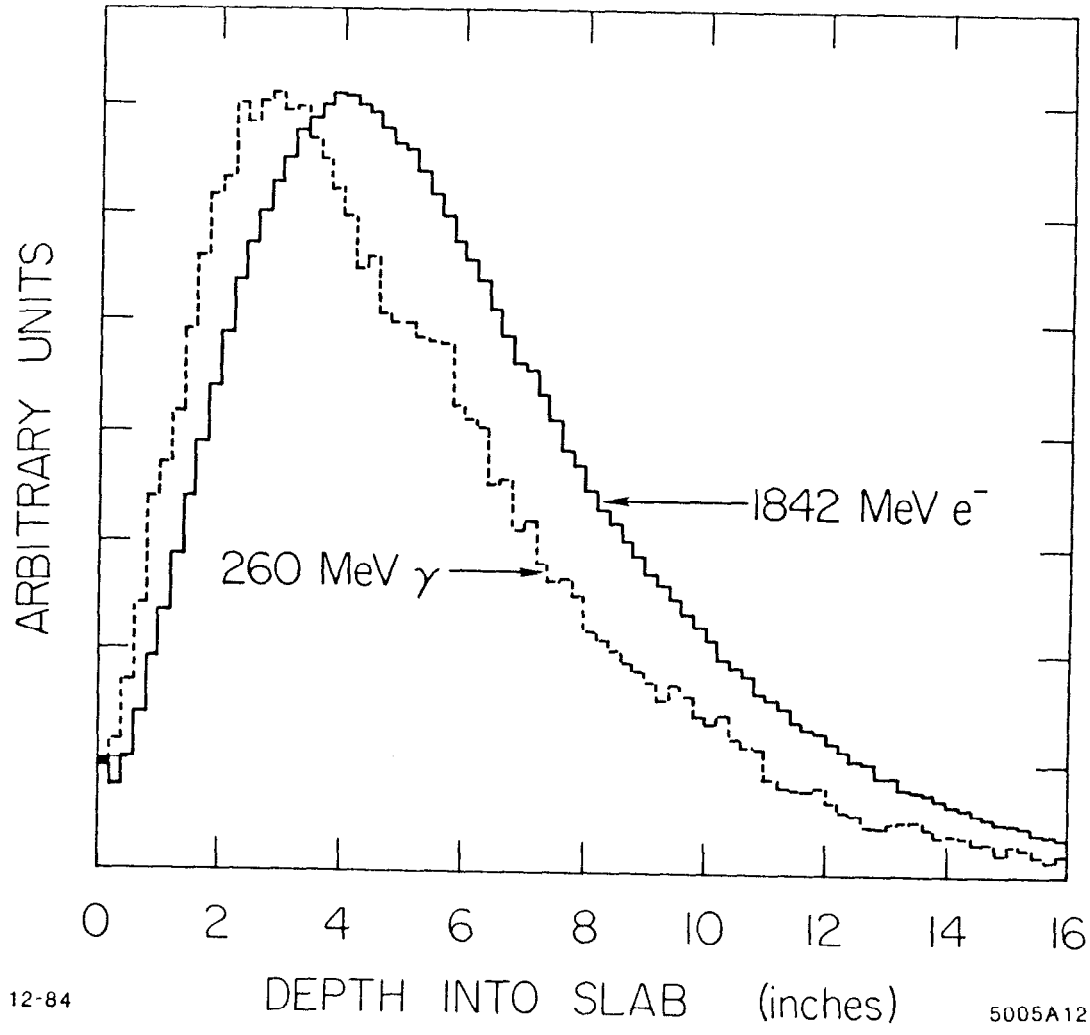

Fig. E.7 Longitudinal distribution of energy from an 1842 MeV e^- shower (solid line) and a 261 MeV γ shower (dotted line) in a 16 radiation length slab of NaI(Tl) (arbitrary normalization).

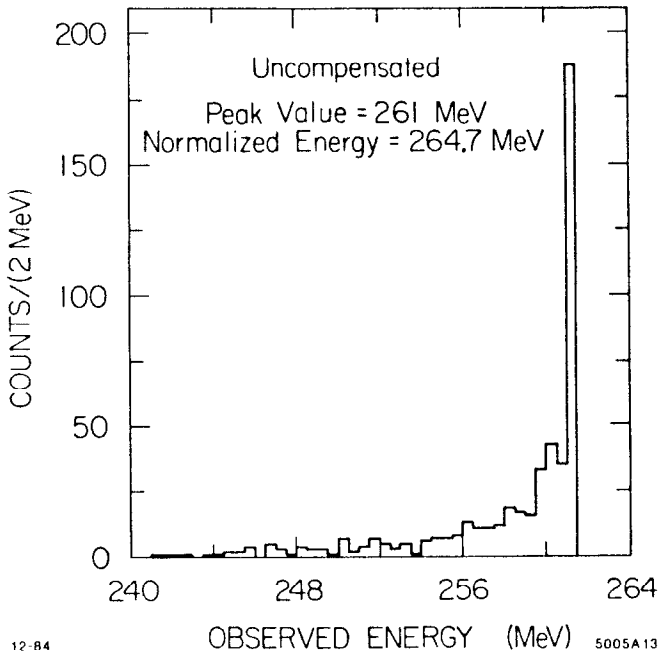

(a)

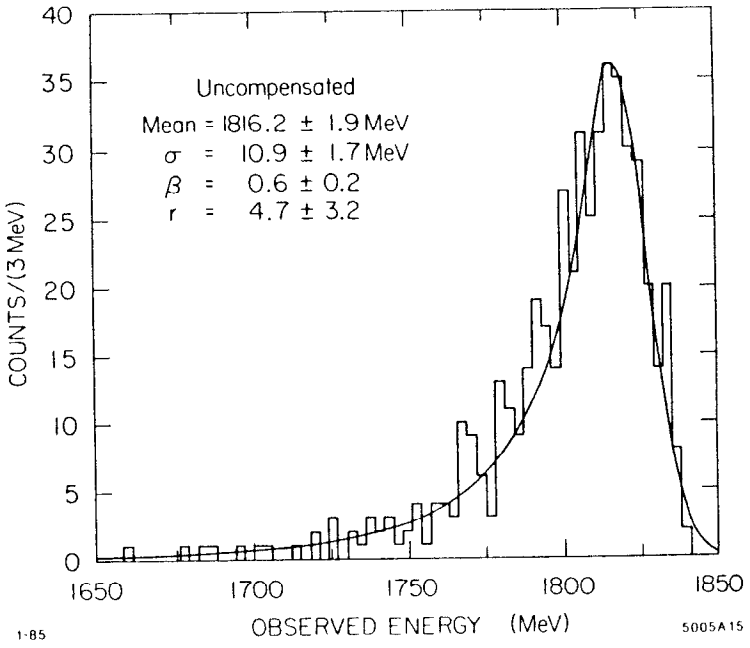

(b)

Fig. E.8 Deposited energies for (a) 260 MeV γ shower and (b) 1842 MeV e^- shower in a 16 radiation length slab of NaI(Tl).

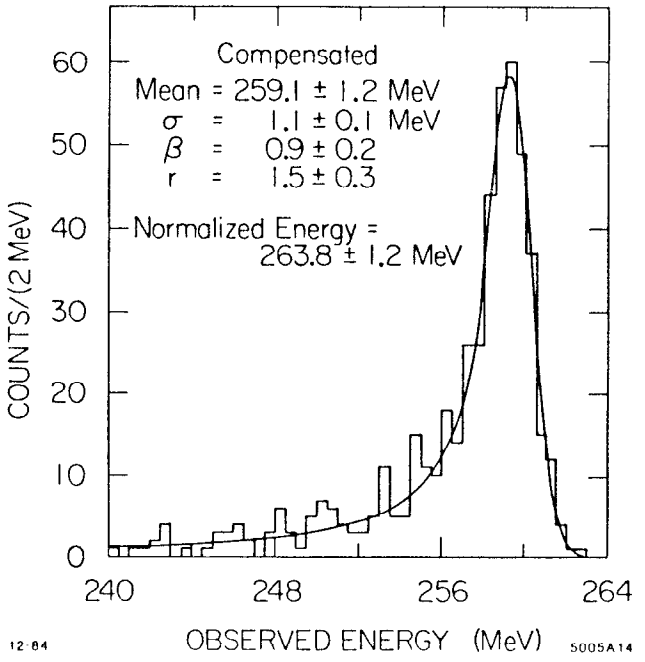

(a)

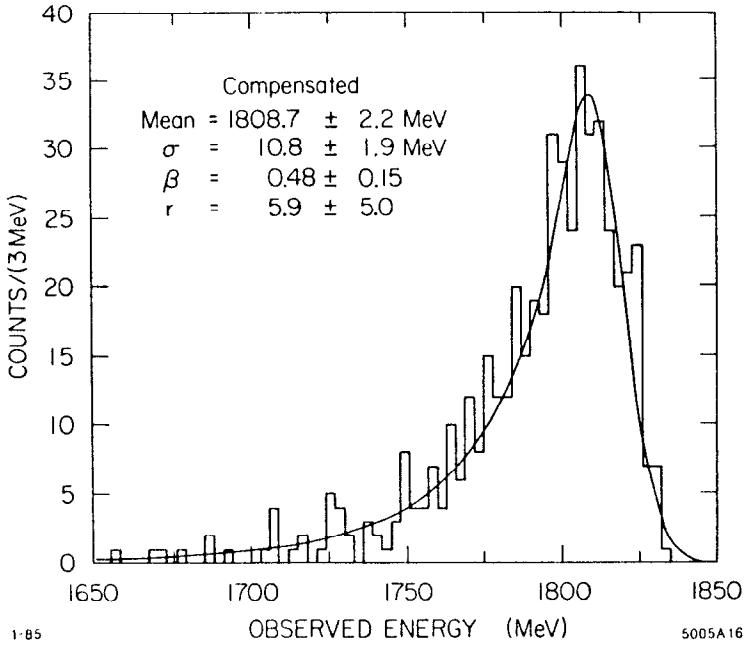

(b)

Fig. E.9 Deposited energies for (a) 260 MeV γ shower and (b) 1842 MeV e^- shower in a 16 radiation length slab of NaI(Tl) modified by compensation correction (see text).

References

1) Y. Chan *et. al.*, *IEEE Trans. on Nucl. Sci.* **NS-25** (1979) 333.

2) I. Kirkbride *et. al.*, *IEEE Trans. on Nucl. Sci.* **NS-26** (1979) 1537.